

Frustration and Randomness: Magnetic Studies of Organic Quantum Spin Liquids

THÈSE N° 8208 (2018)

PRÉSENTÉE LE 2 FÉVRIER 2018

À LA FACULTÉ DES SCIENCES DE BASE
LABORATOIRE DE PHYSIQUE DE LA MATIÈRE COMPLEXE
PROGRAMME DOCTORAL EN PHYSIQUE

ÉCOLE POLYTECHNIQUE FÉDÉRALE DE LAUSANNE

POUR L'OBTENTION DU GRADE DE DOCTEUR ÈS SCIENCES

PAR

Péter SZIRMAI

acceptée sur proposition du jury:

Prof. N. Grandjean, président du jury
Prof. L. Forró, Dr B. Náfrádi, directeurs de thèse
Prof. T. Giamarchi, rapporteur
Prof. P. Batail, rapporteur
Prof. H. M. Rønnow, rapporteur



ÉCOLE POLYTECHNIQUE
FÉDÉRALE DE LAUSANNE

Suisse
2018

To my wife, Viki

Abstract

Spin systems with strong magnetic interactions might remain disordered avoiding conventional magnetic long-range ordering due to zero-point quantum fluctuations, and supporting a Quantum Spin Liquid (QSL) state. Long-range quantum entanglement in QSLs promotes the emergence of non-local excitations and topological properties, unveiling unexplored quantum phenomena. The immense fundamental interest in this exotic phase of matter evinces the need for new crystalline designs and novel combinations of experimental methods in the study of QSLs.

The present PhD thesis focuses on two organic low-dimensional charge-transfer salt families that might host Quantum Spin Liquid states due to *geometrical frustration* and designedly introduced *randomness*. Using the combination of multi-frequency high-field Electron Spin Resonance (ESR) and Muon Spin Rotation (μ SR) techniques supplemented by ^1H Nuclear Magnetic Resonance and transport studies, I propose that organic frustrated magnetic systems are severely affected by the anion layers and by the weak antisymmetric exchange, the so-called Dzyaloshinskii-Moriya (DM) interaction.

Amongst crystalline hybrid conductor-rotor structures comprising Brownian rotator anion layers, I survey experimentally four different materials illustrating a variety of magnetic ground states depending on their dimensionalities and interactions with the rotor components. In quasi-one-dimensional weakly coupled spin chain systems, the presence of the controlled disorder originating from the slowing-down of rotators creates a spin-gapped or long-range antiferromagnetically ordered ground state depending on the spatial relation of the anion and the spin-bearing cation layers. Remarkably, inhomogeneous distribution of the disorder of the rotor stopping positions induces a broad distribution of the Néel temperatures at the microscopic length scales. In contrast, two quasi-one-dimensional distorted triangular lattice systems are identified as QSL candidates. In particular, low-temperature zero-field μ SR and high-field ESR measurements in $(\text{EDT-TTF-CONH}_2)_2^+[\text{BABCO}^-]$ (EDT-BCO) confirmed the absence of magnetic ordering down to 20 mK despite large, $J/k_B = 365$ K nearest-neighbor antiferromagnetic exchange interactions and a moderate anisotropy of $t'/t = 1.6$ of the inter-dimer transfer integrals. The linear field dependence of the ESR linewidth, i.e., the spectral density of the fluctuations, manifests fast spin excitations, reminiscent of motional narrowing. Despite a sizable DM interaction of 0.8 T suggested theoretically, the ESR lineshape remains unchanged down to 1.5 K, indicating the suppression of the effect of DM interaction. Longitudinal-field μ SR measurements reveal one-dimensional diffusive spin transport in EDT-BCO, and predominant fluctuations at the staggered component corresponding to the

Abstract

wave vector of $q = \pi/a$.

For comparison, I investigate the antisymmetric exchange in a nearly isotropic triangular lattice organic QSL candidate, κ -(BEDT-TTF)₂Ag₂(CN)₃ (κ -Ag, $J/k_B = 175$ K, $t'/t = 0.97$). The recently discovered sister compound of the first two-dimensional QSL (κ -(BEDT-TTF)₂Cu₂(CN)₃) displays a spin liquid-superconductor phase transition above a critical pressure of $p_c > 0.9$ GPa ($T_c = 5.2$ K). In κ -Ag, multi-frequency and angle-dependent ambient-pressure ESR studies found large antiferromagnetic fluctuations, and a staggered moment of $\mu_s = 6 \cdot 10^{-3} \mu_B$ at 2 K and at 15 T. Via globally fitting the field- and temperature-dependence of the ESR linewidth using the one-dimensional field theory of Oshikawa and Affleck, I assigned μ_s to a DM interaction of 1.2 T, weakly suppressed compared to its theoretical value of 5.5 T. Nevertheless, high-pressure multi-frequency ESR measurements reveal that the effect of the DM interaction is completely quenched with a moderate pressure of $p_{DM} = 0.3$ GPa, as a result of moving away from the spiral-ordered phase. Above p_{DM} , a linear field dependence and fast spin fluctuations are found, similarly to the ambient-pressure EDT-BCO. Furthermore, detailed analysis of the high-pressure ESR linewidth gives evidence of the effect of high pressure upon inherent charge fluctuations.

Key words:

Frustrated magnetism, Quantum Spin Liquids, Organic charge-transfer salts, Hybrid conductor-rotor systems, Electron Spin Resonance, Muon Spin Rotation

Résumé

Les systèmes de spins avec des interactions magnétiques fortes peuvent garder leur désordre et éviter l'ordre magnétique conventionnel grâce aux fluctuations de point zéro, et peuvent ainsi maintenir l'état Liquide de Spin Quantique (LSQ). L'enchevêtrement quantique à longue portée des LSQ promeut l'émergence des excitations non-locales et des propriétés topologiques dévoilant des phénomènes quantiques inexplorés. L'intérêt fondamental immense dans cette phase de la matière exotique démontre la nécessité de nouveaux modèles cristallins et de combinaisons originales de méthodes expérimentales dans l'étude des LSQ.

Cette thèse de doctorat se focalise sur deux familles de sels organiques de transfert de charges de basse dimensionnalité qui peuvent admettre des états LSQ grâce à la *frustration géométrique* et le *désordre* introduit par la construction de matériaux. Je propose que les systèmes organiques magnétiques frustrés sont sévèrement perturbés par les couches d'anions et par l'interaction d'échange antisymétrique faible, appelée interaction Dzyaloshinskii-Moriya (DM); pour ceci, différentes techniques sont combinées comme la Résonance de Spin Électronique (RSE) à multifréquence sous hauts champs magnétiques et la Spectroscopie de Spin de Muon (μ SR). Ces dernières sont complétées avec ^1H Résonance Magnétique Nucléaire (^1H -RMN) et l'étude de conductivité ainsi que le pouvoir thermoélectrique.

Parmi les hybrides de métaux moléculaires et de rotors moléculaires constitués de rotors browniens en tant que couches d'anions, j'examine expérimentalement quatre matériaux différents illustrant une variété des états fondamentaux en fonction de leur dimensionnalité et des interactions avec les composants rotors. Dans les systèmes de chaînes de spins faiblement couplées, la présence de désordre contrôlé crée des états fondamentaux ayant un gap de spin ou un ordre antiferromagnétique à longue portée en dépendant de la relation spatiale des couches d'anions et des couches de cations porteurs de spin. Remarquablement, la distribution inhomogène du désordre des positions angulaires de l'arrêt des rotors induit une distribution étendue des températures de Néel à une échelle microscopique. De l'autre côté, deux systèmes quasi-unidimensionnels de réseau triangulaire déformé sont identifiés comme des candidats LSQ. En particulier, des expériences μ SR à basse température sans présence du champ magnétique et des mesures RSE sous haut champ magnétique sur le cristal $(\text{EDT-TTF-CONH}_2)_2^+[\text{BABCO}^-]$ (EDT-BCO) confirment l'absence de l'ordre magnétique jusqu'à 20 mK malgré des interactions d'échange antiferromagnétiques fortes ($J/k_B = 365$ K) et l'anisotropie modérée des intégraux de transfert inter-dimères, $t'/t = 1.6$. La dépendance linéaire de largeur de raie RSE en fonction du champ magnétique manifeste des excitations rapides de spin rappelant le processus du rétrécissement par le mouvement. En dépit de

Résumé

l'interaction forte DM, calculée théoriquement valant $D/\mu_B = 0.8$ T, la forme de raie reste inchangée jusqu'à 1.5 K, indiquant la suppression des effets de l'interaction DM. Les mesures μ SR sous champs magnétiques longitudinaux révèlent que le transport de spin dans EDT-BCO est unidimensionnel et diffusif, et que les fluctuations prédominantes possèdent un vecteur d'onde de $q = \pi/a$.

En comparaison avec les matériaux précédents, j'étudie l'interaction d'échange antisymétrique dans κ -(BEDT-TTF)₂Ag₂(CN)₃ (κ -Ag, $J/k_B = 175$ K, $t'/t = 0.97$), candidat LSQ organique ayant un réseau triangulaire presque isotrope. Le composé frère récemment découvert du premier LSQ deux-dimensionnel (κ -(BEDT-TTF)₂Cu₂(CN)₃) exhibe une transition de phase liquide de spin-supraconducteur à une pression critique de $p_c > 0.9$ GPa ($T_c = 5.2$ K). Les études RSE à multifréquences et à dépendance d'angle à pression ambiante montrent des fluctuations antiferromagnétiques élevées, et un moment magnétique de $\mu_s = 6 \cdot 10^{-3} \mu_B$ à 2 K dans un champ magnétique de 15 T. Grâce à un ajustement global des fonctions de champ magnétique et de température de largeur de raie RSE, en utilisant la théorie unidimensionnelle de Oshikawa et Affleck, le moment μ_s est attribué à une interaction DM de 1.2 T, faiblement réprimée comparée à la valeur théorique de 5.5 T. Néanmoins, les mesures RSE à multifréquences et à hautes pressions dévoilent que l'effet de l'interaction DM est complètement éteinte sous une pression modérée de $p_{DM} = 0.3$ GPa, à cause de l'éloignement de phase d'ordre spirale. À des pressions plus hautes que p_{DM} , une dépendance linéaire du champ magnétique et des fluctuations rapides de spin sont identifiées, similairement au cas de EDT-BCO à pression ambiante. En outre, l'analyse détaillée de la largeur de raie RSE prouve l'effet de haute pression sur les fluctuations de charges.

Mots clefs :

Magnétisme frustré, Liquides de Spin Quantique, Sels organiques de transfert de charges, Systèmes hybrides de métaux moléculaires et de rotors moléculaires, Résonance de spin électronique, Spectroscopie de spin de muons

Contents

Abstract	i
Résumé	iii
Introduction	1
1 Geometrically frustrated magnets	5
1.1 Introduction	5
1.2 Historical background	7
1.3 Definition of QSLs	8
1.3.1 QSL state criteria	8
1.4 Experimental systems	9
1.4.1 Isotropic triangular organics	9
1.4.2 Kagomé: <i>an end to the drought</i>	12
1.4.3 Anisotropic triangular systems	12
2 Experimental techniques	15
2.1 Electron Spin Resonance	15
2.1.1 Basic principles	15
2.1.2 ESR instrumentation	17
2.1.3 ESR signals of low-dimensional systems	21
2.2 Muon Spin Rotation	26
2.2.1 Basic principles	26
2.2.2 Synchrotron sources	28
2.2.3 Muon spin rotation in magnetic materials	29
2.2.4 Muonium formation	31
2.2.5 Complementarity of ESR and Muon Spin Rotation	32
3 Towards disordered QSLs in molecular rotor systems	33
3.1 Structure and dynamics of molecular rotor systems	34
3.1.1 Microscopic insight	34
3.1.2 Crystalline rotor designs	35
3.2 Hybrid conductor-rotor systems with BCP rotators	36
3.2.1 A spin-gapped system	37

Contents

3.2.2	Antiferromagnetic ordering of a spin chain	40
3.3	Hybrid conductor-rotor systems with BCO rotators	46
3.3.1	Impeded motion in metallic state	47
3.4	A disordered Quantum Spin Liquid	51
3.4.1	High-temperature rotor dynamics	51
3.4.2	ESR measurements in quantum critical state	61
3.4.3	Muon Spin Rotation in quantum critical state	63
3.4.4	Spinon spectral density	68
3.4.5	Diffusive spin transport	69
3.4.6	Comparison of high-field and low-field quantum critical state	72
4	Antiferromagnetic fluctuations in a QSL candidate	75
4.1	Structure and NMR studies in triangular organics	75
4.1.1	Mott transition and superconducting state	77
4.1.2	Previous NMR investigations	78
4.2	Ambient-pressure AFM fluctuations	79
4.2.1	Low-field ESR measurements	79
4.2.2	High-field ESR measurements	83
4.2.3	Comparison with NMR and Muon Spin Rotation	97
4.3	High-pressure antiferromagnetic fluctuations	99
4.3.1	Charge fluctuations at high pressure	99
4.3.2	Pressure-tunable antiferromagnetic fluctuations	101
4.3.3	Absence of DM effect at moderate pressures	104
4.3.4	Quasi-continuous Mott transition	105
4.3.5	Low-temperature superconducting and metallic state	106
5	Conclusions & outlook	109
A	Versatile detection in HF-ESR	113
B	Comparison of magnetic torque measurements	117
	Acknowledgements	121
	Bibliography	123
	Curriculum Vitae	151

Introduction

"I think nature's imagination Is so much greater than man's, she's never going to let us relax"

Richard Feynman

Since the beginning of the twentieth century, research in condensed matter physics has been targeting the most urgent and the most utopian problems to support human progress and contribute to human knowledge [1]. Its results, from the discovery of superconductivity [2] (*Nobel Prize in Physics, 1913* [3]) to the foundation of semiconductor technology [4, 5] (*Nobel Prize in Physics, 1956*), contributed substantially to all present-day leading industrial sectors, such as health, information technology, and transportation [6]. These far-reaching outcomes would not have been conceivable without the cooperation with biologists, chemists, electrical and mechanical engineers, material scientists, and computer scientists. Symbiosis of scholars continues to facilitate to achieve the arising new opportunities, such as quantum computation [7] (*Nobel Prize in Physics, 2012* [8, 9]) and molecular machines [10] (*Nobel Prize in Chemistry, 2016* [11]).

The interdisciplinary approach is best exemplified through the evolution of the compelling research of organic molecular conductors in the last century (see Fig. 1) [12]. Since the 1911 historical proposal of McCoy and Moore that *it is possible to prepare composite metallic substances from non-metallic constituent elements* [13], the collaborative work of physicists and chemists generated an exponential expansion of the field. Alike for other crystal structures later, the hope of room-temperature superconductivity ignited an unprecedented interest. In 1964, Little [14] proposed a new mechanism, excitonic superconductivity, which promised an order of magnitude increase of the superconducting transition temperature (T_c). Nevertheless, this remains a dream in the twenty-first century. The overwhelming challenge he gave to synthetic chemists did not succeed but the ideas behind the concept led to a multiplied enthusiasm towards low-dimensional materials and physics, with the metallic conductivity and the low-temperature Peierls transition of a one-dimensional system, TTF-TCNQ [15, 16, 17, 18]. Thanks to the tremendous work, Jérôme *et al.* [19] succeeded to find organic superconductors amongst the Bechgaard salts [20] in $(\text{TMTSF})_2\text{PF}_6$ [21].

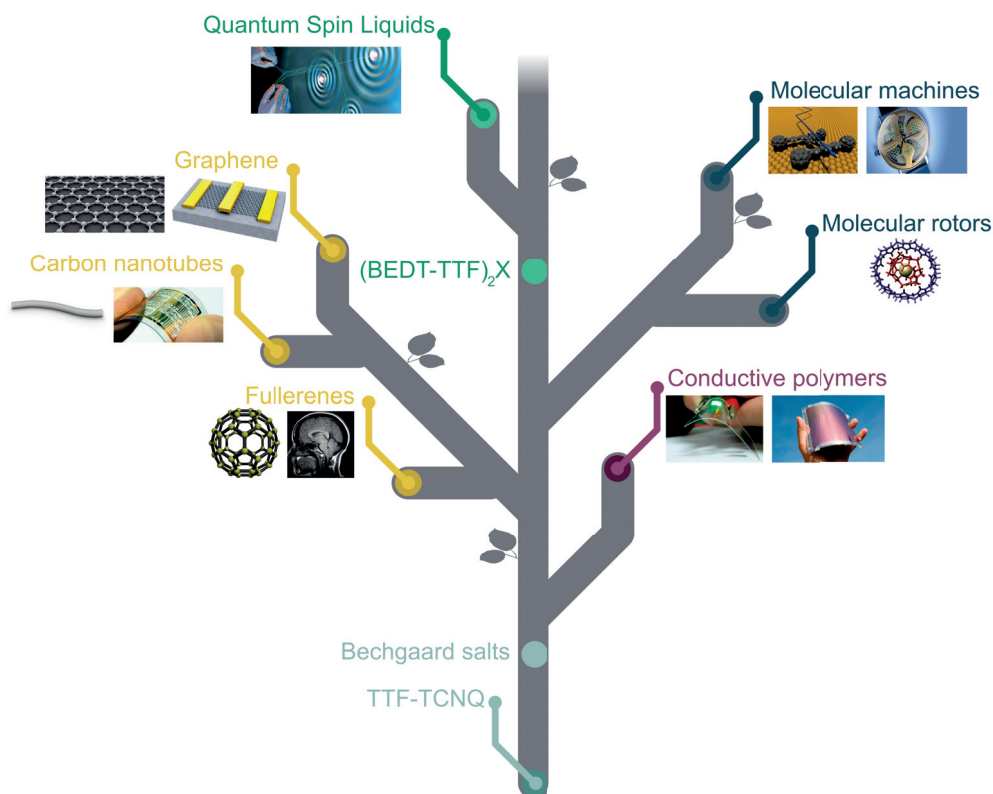


Figure 1 – Evolution of the interdisciplinary research in the 1970s initiated by the organic materials. Discovery of one-dimensional conduction in TTF-TCNQ followed by the observation of superconductivity in the Bechgaard salts launched enormous interest amongst organic chemists and condensed matter physicists. Conductive polymers opened a new avenue towards applications, such as OLEDs and organic photovoltaic cells. Fullerenes, carbon nanotubes, and graphene revolutionized our view of carbon, and helped us to explore novel opportunities, such as all-carbon logic circuits and magnetic resonance imaging contrast agents. Progress of organic chemistry inspired the design of molecular gyroscopes (using molecular rotors), Feynman's nanocar, and entire complex molecular machines. Owing to innovation in computer technology, Quantum Spin Liquids emerge as potential solutions for topological quantum computing¹.

These seminal investigations established a long-lasting trial-and-error effort of crystal design for the observation of complex phenomena in organic systems. One of the most successful family is that of the dimerized $(\text{BEDT-TTF})_2\text{X}$ charge transfer salts, which reached the highest T_c amongst organic conductors under hydrostatic pressures [22] and allows the exploration of phase diagrams resembling to that of high- T_c superconductors [23]. This material family presented the first-ever candidates of the two-dimensional Quantum Spin Liquids (QSL) in 2003 [24], sought since the 1973 proposal of Anderson [25] (*Nobel Prize in Physics, 1977*).

Amongst the organic materials, the successful synthesis of thin films of conducting polyacetylene by Heeger, McDiarmid, and Shirakawa [26] (*Nobel prize in Chemistry, 2000* [27]) founded a new direction, the broad branch of conductive polymers. Applications of organic polymers

are widespread due to the cost-effective manufacturing using solution-processing [28]. These are present from the more specific uses, such as electromagnetic shielding of electronic circuits [29] and anti-static coating materials to prevent electrical discharge exposure [30] to the more general ones, such as organic light emitting diodes (OLED) [31, 32], organic field-effect transistors (OFET) [33], and organic solar cells [34].

In the quest for one of the organic compounds, the polyenes, Kroto, Curl, and Smalley were prompted to identify the buckminsterfullerenes (C_{60} and C_{70}) for the first time in 1985 [35] (*Nobel Prize in Chemistry, 1996* [36]). Their finding corrected the list of carbon allotropes in chemistry textbooks, and it broadened the scientific community, opening completely new avenues. Fullerenes were investigated in organic photovoltaics [37] and as magnetic resonance imaging contrast agents [38]. The boom of the carbon research era could not peak in the nineties, as Iijima [39] identified the carbon nanotubes, finding the one-dimensional allotrope. In 2003, with the appearance of more and more complex systems, such as logic circuits [40, 41], the nanotubes were believed to be the ultimate members of the family. The playful approach of Novoselov and Geim [42] (*Nobel Prize in Physics, 2010* [43]) to make thinner and thinner layers of graphite and to get to the single-layer thick carbon structure, graphene, completed the allotropes. Graphene caused a global explosion, and took closer us to the dream of spintronic devices [44], transparent screens [45], a number of energy storage solutions [46], ultrafiltration [47], and fast and efficient bioelectric sensory devices [48].

Maturation of the material engineering in organic chemistry accelerated the reach-out for structures with increasing complexity. Inspired by the visionary talk of Feynman (*Nobel Prize in Physics, 1965*) [10], Sauvage, Stoddart, and Feringa pioneered the synthesis of molecular motors, and nanoobjects, such as nanocars [62]. Capable of performance of useful work, these molecular-sized machines would signify the last giant leap in the miniaturization of useful machines [11]. To control the internal dynamics of components, the key need for the development of new crystal engineering strategies started a new path, the creation of molecular rotors. After rewarding experiments in solution, Kelly achieved unidirectional motion by energy supply [63]. Recent undertakings led to three-dimensional crystalline rotor arrays reaching a rotation frequency of 430 GHz at room temperature [64]. Within hybrid structures, uniquely designed molecular rotors accomplished to interact with conducting molecular slabs [65], foreseeing a new synergy with the rich physical properties of the system.

Within my four-year-long endeavor into the ever-blooming field of organic charge transfer salts, I explored two low-dimensional frustrated magnetic material families that are expected to host quantum spin liquid states due to the strong frustration and in the presence of well-controlled disorder. In my experimental quest for complex behavior and structures with the realm of topological quantum computation [66], I took advantage of the unique multi-frequency, high-field, and high-pressure Electron Spin Resonance (ESR) instrumentation available in our laboratory. My ESR investigations were supplemented by Muon Spin Rotation

¹Sources of photos: Artwork by Andrew Lilja, Lateral Magazine [49], and Ref. [50, 51, 52, 53, 54, 55, 56, 57, 58, 59, 60, 61]

Introduction

(μ SR) experiments in large-scale facilities, in the ISIS Rutherford Appleton Laboratory (United Kingdom, Didcot) and in the Paul Scherrer Institute (Switzerland, Villigen).

In this thesis, I will first introduce the geometrically frustrated magnetic systems from a theoretical and experimental point of view (Chapter 1), and I will give an introduction to the experimental methods and characteristics of the information provided for low-dimensional organic systems (Chapter 2).

In Chapter 3, I survey and deeply scrutinize the ground state of four different hybrid conductor-rotor systems. I offer a first-ever demonstration that the magnetic character of these hybrid systems is crucially affected by the presence of the rotor components (as anion layers) advancing spin-gapped, ordered antiferromagnetic, and spin-liquid ground states. My ESR and μ SR investigations unravel that one of these frustrated magnetic crystalline materials, $(\text{EDT-TTF-CONH}_2)_2^+[\text{BABCO}^-]$, manifests a triangular-lattice quasi-one-dimensional disordered QSL state induced by the intrinsic disorder stemming from the randomized stopping positions of the rotors.

Within the $(\text{BEDT-TTF})_2\text{X}$ material family, I investigate the low-temperature magnetic properties of κ - $(\text{BEDT-TTF})_2\text{Ag}_2(\text{CN})_3$, a recently identified pressure-tunable quantum spin-liquid candidate [67]. My detailed ambient- and high-pressure ESR studies (presented in Chapter 4) find large field-induced and angle-dependent antiferromagnetic fluctuations at low temperatures. I assign these effects to a sizable Dzyaloshinskii-Moriya interaction and to the vicinity of a spiral-ordered phase [68, 69]. I demonstrate that the effect of the antisymmetric exchange interaction is tunable by pressure, leading to a long-range quantum-entangled state in the absence of antiferromagnetic fluctuations at high pressure. I propose a temperature-, field- and pressure-dependent phase diagram that resolves a number of long-standing issues in the understanding of the phase diagram of the triangular lattice organic QSLs [70, 71].

Despite numerous proposals [72, 73], I do not believe that the (organic or inorganic) quantum spin liquids would appear in topological quantum computers in the near future or the incipient molecular machines would deliver drugs efficiently in the human body within the next ten years. Nevertheless, I firmly hold that the present-day low-temperature condensed matter physics research will lead to fundamentally new industrial applications, will usher novel research areas for another generation of scholars, and will resolve the most urgent problems, such as energy-need and the slowed-down evolution prospects of information technology.

1 Geometrically frustrated magnets

In the following, I will give an introduction to the theory of frustrated magnetic systems. I will discuss the key definitions used in the field of frustrated magnetism, and I will present its historical evolution. To demonstrate the expansion seen in the last 15 years, I will provide a non-exhaustive list of experimental realizations of quantum spin liquids in two-dimensional systems.

1.1 Introduction

The term *geometrical frustration* was first described in the context of spin glasses [76]. Therein, it was used to demonstrate that simultaneously satisfying all exchange processes might become impossible due to the presence of locally competing interactions. For example, the Ruderman–Kittel–Kasuya–Yosida (RKKY) interaction gives an oscillating interaction in metals,

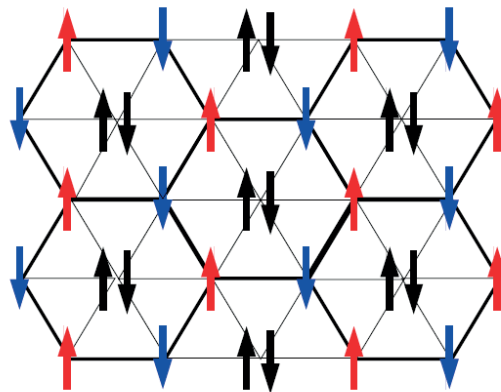


Figure 1.1 – Degenerate ground states of the Ising model on the triangular lattice demonstrating the residual entropy of the system. If the spins are determined on the honeycomb sublattice (thick solid line), the energy of the system does not change if the spins in the center of the hexagons point up or down. Figure taken from Ref. [74, 75].

Chapter 1. Geometrically frustrated magnets

which can be antiferromagnetic and ferromagnetic as the distance changes. In the case of CuMn or AuFe, the homogeneously distributed dilute Mn or Fe ions lead to the competition between antiferromagnetic and ferromagnetic interactions on the lattice. At low temperatures, this results in quenched disorder of the magnetic system. Thus, the complexity and rich physics of the spin glass systems stem from the combination of frustration and disorder [77, 78].

In pure, disorder-free systems the frustration might emerge as a result of the geometry of the interactions or due to geometry of the lattice. In this case, the general definition of *geometrical frustration* is modified: a simple pattern of the extended systems cannot be defined using local conditions [79, 80]. Theoretically these systems can be studied considering a periodic Hamiltonian. In the Heisenberg model of magnetism the Hamiltonian reads

$$\mathcal{H} = \sum_{(i,j)} J_{ij} \vec{S}_i \vec{S}_j. \quad (1.1)$$

Here, the summation is done over the nearest neighbors, J_{ij} is the magnetic interaction between the \vec{S}_i and \vec{S}_j spins and the spins \vec{S}_i are unit vectors or components of the quantum spin. If all the J_{ij} interactions are ferromagnetic, all exchange interactions can be satisfied, therefore, geometrical frustration cannot take place. The presence of antiferromagnetic interactions, however, does not necessarily imply that the system becomes frustrated. Bipartite lattices, e.g., the square lattice, can be split into two sublattices where interactions are only in-between the sublattices. The Néel configuration can thus minimize the energy, and a high Néel temperature is expected [81].

The geometry of the interactions might lead to frustration even on square lattices. In the $J_1 - J_2$ model, the ratio of the nearest neighbor J_1 interactions and the next-nearest neighbor J_2 interactions determines whether a Néel configuration can stabilize. For large enough J_2 interactions ($J_2 > J_1/2 > 0$), the degeneracy of the system becomes infinite, where a continuous parameter tunes the degeneracy. The first experimental investigations were performed in the vanadate system, $\text{Li}_2\text{VO}_2\text{SiO}_4$. Nuclear Magnetic Resonance (NMR) [82] and Muon Spin Rotation (μSR) [83] confirmed that a collinear magnetic state is developed with a complex behavior just above the transition temperature. An other family of systems with a disordered state is given by the spin ice systems, where classical spins sit on a pyrochlore lattice, e.g, $\text{Dy}_2\text{Ti}_2\text{O}_7$ or $\text{Ho}_2\text{Ti}_2\text{O}_7$ [84].

The triangular motif induces frustration due to the geometry of the lattices in the triangular and kagomé structures. In the antiferromagnetic Ising model, the triangular lattice possesses large residual anisotropy, i.e., the number of degenerate states per lattice sites remains significant even at very low temperatures. A simple reasoning can point out the existence of the large number of degenerate ground states, if we handle the triangular lattice as a centered honeycomb lattice (see Fig 1.1). Once we satisfy all the antiferromagnetic interactions on the honeycomb lattice, all the spins at the center of the honeycombs can be independently set, giving a degeneracy of $2^{N/3}$ for N spins, and a residual entropy of $S/N \approx 0.2310$. The exact

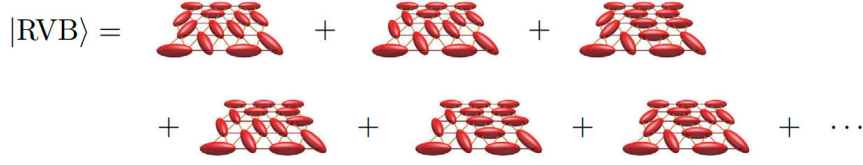


Figure 1.2 – A Resonating Valence Bond state on the spin-1/2 triangular lattice. Ellipsoids indicate spin-zero singlet states of two $S = 1/2$ spins. Figure taken from Ref. [87].

residual entropy was first calculated by Wannier [85], and a much simpler derivation was given by Moessner *et al.* [86] by counting the dimer coverings of the honeycomb lattice.

Within the well-known Heisenberg model (see Eq. 1.1), the energy of both triangular motif structures is proportional to

$$\vec{S}_1 \cdot \vec{S}_2 + \vec{S}_2 \cdot \vec{S}_3 + \vec{S}_3 \cdot \vec{S}_1 = \frac{1}{2} (\vec{S}_1 + \vec{S}_2 + \vec{S}_3)^2 - \frac{3}{2}, \quad (1.2)$$

which can be minimized with $\vec{S}_1 + \vec{S}_2 + \vec{S}_3 = \vec{0}$. For triangular lattices, this leads to a three-sublattice state with 120° between the spins. For the kagomé, this condition does not restrict extensively the possible configurations [75].

1.2 Historical background

To identify the ground state of these frustrated structures, a number of theoretical proposals were discussed in the last decades. Anderson and Fazekas [25] were the first to propose the so-called *Resonating Valence Bond* (RVB) model as a possible ground state of the spin-1/2 triangular lattice [88]. This model resolves the symmetry breaking of a single dimer covering by the virtue of describing the system as a superposition of all different pairings at the wavefunction level (see Fig 1.2). It was shown later by Huse and Elser [89] and Bernu *et al.* [90] that three-sublattice long-range ordering takes place in the triangular lattice. The kagomé remains a good candidate for the RVB state [91, 92], along with RVB solutions of many model Hamiltonians [86, 93].

The idea of an RVB state was boosted by the discovery of high-temperature superconductivity, proving that the Gutzwiller projection of a Fermi liquid can lead to an RVB state [94, 95]. This connected the RVB state to the high- T_c systems, and suggested that doping of an RVB system would induce the formation of a superconducting state. Furthermore, Anderson [94] suggested that the cuprate superconductors demonstrate the existence of the '*long-sought*' *Quantum Spin Liquids* (QSLs). Therein, it was proposed that the *spinon* quasiparticles give the underlying mechanism in the QSLs.

These exotic excitations remain, to date, widely proposed and searched signatures of the QSL state [70, 87]. In contrast to spin-1 magnons obeying Bose-Einstein statistics [96], these are

fractionalized, spin-1/2 quasiparticles [97]. Both gapless fermionic spinons [98] and gapped QSLs with bosonic spinons were identified [99]. Later, Wen [100] constructed hundreds of spin liquids, and found two more classes of QSL statistics: rigid spin liquids and algebraic spin liquids. Kitaev's honeycomb lattice model [101], and his proposal for the '*fault-tolerant*' quantum computation based on QSLs showed the validity of the QSL concepts [87].

1.3 Definition of QSLs

The complexity of the QSL systems can be exposed by the difficulty of giving a simple positive definition of the state [70]. The traditional definition of QSLs resides on the observation of the absence of magnetic ordering even at the lowest possible temperatures due to the high degeneracy [87]. To provide an experimental relation, Ramirez [102] introduced an empirical measure of the frustration:

$$f = \frac{|\theta_{CW}|}{T_c}. \quad (1.3)$$

Here, T_c is the transition temperature and θ_{CW} is the Curie-Weiss temperature. The latter is found from the fit of the macroscopic susceptibility $\chi \propto 1/(T - \theta_{CW})$, and, as the first order correction to the Curie law, it gives a simple estimate of the magnetic interactions. This frequently used parameter sets the scale, and identifies a spin liquid state if f is large enough, that is, $f > 10$.

A more advanced theoretical description can be given by identifying a QSL as a system with anomalously high degree of entanglement [103, 104]. In other words, QSLs cannot be described as product states of any finite spatial arrangements [87]. From an experimental point of view, this definition is challenging to test. In most cases, it requires the confirmation of separate signatures using multiple experimental techniques, such as, NMR, μ SR, thermal conductivity, specific heat, or macroscopic susceptibility [105]. In some cases, such as for 3D Coulomb phase U(1) QSLs, the observation of a *smoking-gun* feature can be found using neutron scattering experiments [87].

1.3.1 QSL state criteria

Up to now, I only focused on one crucial ingredient in the quest for the QSL magnetic systems, the frustration [106, 107]. Two further criteria can be defined to find a QSL candidate: (i) small S spin state and (ii) the proximity of the Mott transition [108, 87]. The spin-1/2 state (which was indirectly assumed above) ensures the increased fluctuation in our system. The closeness of the metallic state, i.e., a *weak* Mott insulator state can support the presence of higher order terms, such as the ring-exchange interaction, and can lead to Fermi-surface QSLs [109, 110]. It is necessary to emphasize that these general observations are not always fulfilled, e.g., larger S spin systems can still behave as effective spin-1/2 systems because of strong single-ion terms splitting, and might remain in a highly quantum-like order [87, 111, 112]. Furthermore,

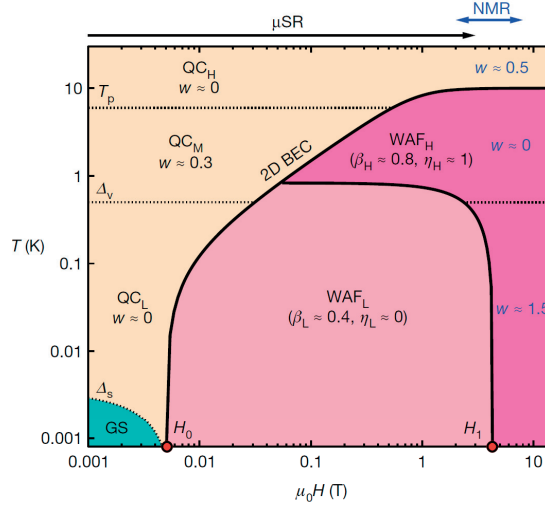


Figure 1.3 – The first experimentally determined magnetic field-temperature phase diagram of an isotropic triangular organic QSL, κ -Cu shown as obtained from μ SR, NMR, and thermodynamic measurements. Two distinct quantum critical points are found at H_0 and at H_1 . The boundaries between the phases and the critical properties are determined from μ SR. The quantum critical (QC) and the weakly antiferromagnetic (WAF) regions are subdivided based on the critical parameters (L:low, M:intermediate, H:high). GS is the proposed gapped-spin-liquid regime. Figure taken from Ref. [71].

inorganic kagomé systems are strong Mott insulators, and these can be described by purely Heisenberg physics [70, 113].

1.4 Experimental systems

Despite the numerous theoretical models investigated in detail, the theoretical approximations either oversimplify the complexity of the experimentally identified QSL candidates, or give too important restrictions to the real systems. This discrepancy and the complexity of experimental challenges underlined in Section 1.3 provoke that only a handful of QSL candidates were studied extensively enough to provide satisfactory evidence of the QSL state. Among two-dimensional, triangular motif systems, sufficient information is available in the inorganic kagomé lattice herbertsmithite, $\text{ZnCu}_3(\text{OH})_6\text{Cl}_2$ [114], and in the organic spin-1/2 triangular systems, κ -(BEDT-TTF) $_2\text{Cu}_2(\text{CN})_3$ (κ -Cu) [24] and β' - $\text{Me}_3\text{EtSb}-[\text{Pd}(\text{dmit})_2]_2$ (dmit) [115].

1.4.1 Isotropic triangular organics

The first convincing two-dimensional QSL state was identified in the triangular lattice layered system, κ -(BEDT-TTF) $_2\text{Cu}_2(\text{CN})_3$ [24]. Both the κ -Cu and dmit systems possess organic, layered structures, with one hole per dimer (see Fig. 1.4a,b). The dimers form a $S = 1/2$ triangular lattice structure with large exchange couplings of $J(\kappa - \text{Cu})/k_B \approx 250$ K [24] and $J(\text{dmit})/k_B \approx 220 - 250$ K [116], and very weakly anisotropic exchange integrals of $t'/t(\kappa - \text{Cu}) \approx$

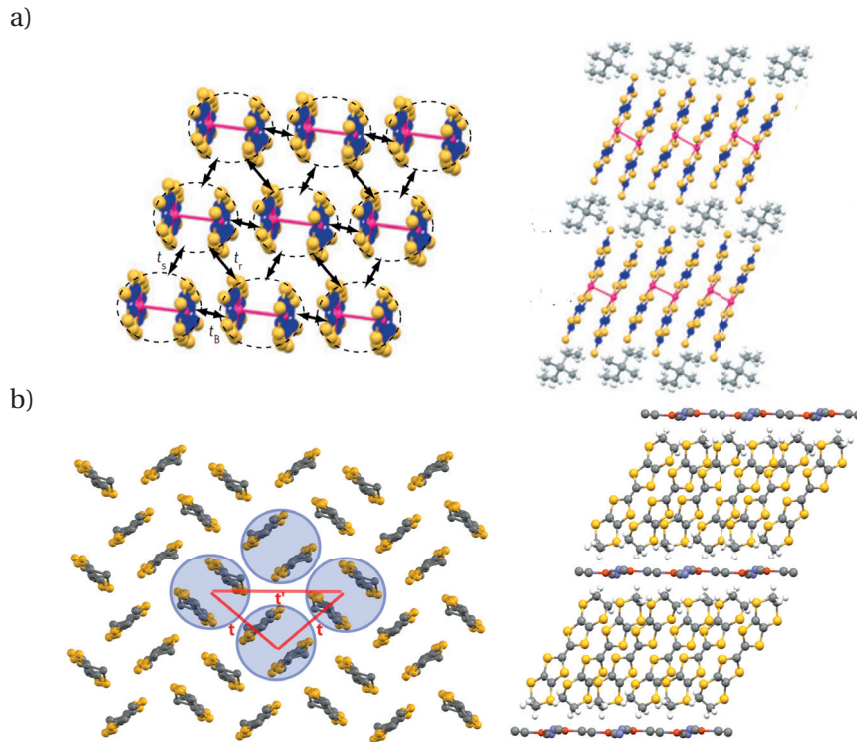


Figure 1.4 – Crystal structures of the firstly discovered isotropic triangular organic QSL candidates. Top view (left) showing the strong dimerization with one electron with one spin-1/2 at each dimer. Side view of the crystal structure displaying the two-dimensional magnetic layers separated by nonmagnetic layers (right). *a)* β' -Me₃EtSb-[Pd(dmit)₂]₂, the overlap integrals are similar, and yield exchange interactions of 220-250 K [115, 116, 117] *b)* κ -(BEDT-TTF)₂Cu₂(CN)₃, the prime example of isotropic triangular organic QSLs, possesses a strong, $J/k_B \approx 250$ K exchange interaction [24, 118, 119].

1.06 [124, 71, 24] and $t'/t(\text{dmit}) \approx 0.92$ [116, 125]. ¹H NMR and ¹³C NMR data confirmed in both organic systems the absence of magnetic ordering down to $10^{-4} J/k_B$ [24, 117, 119]. Together with detailed zero-field μ SR studies in κ -Cu [71, 126], it was proven that spin fluctuations persist down to 20 mK. This remarkable result could not be complemented with neutron scattering data, as the latter is typically prohibited in organic materials due to the large scattering from hydrogen.

Regarding the emergence of low-temperature excitations, thermodynamic evidence was provided by low-temperature specific heat data, which showed a significant $c_v \propto \gamma T$ linear-in-temperature contribution, pointing to a gapless state. In a Mott insulator, the presence of such a term could only be assigned to the spinon Fermi sea [127, 128]. In the determination of the γ term from c_v , however, some difficulties are posed by the presence of the Schottky contribution. Via thermal conductivity (κ) data, it was undoubtedly shown that dmit sustains delocalized *mobile*, fermionic spinons, and a spin-gapped state was described in κ -Cu [129, 130]. In κ -Cu, thermal conductivity studies of Yamashita *et al.* [130] revealed a phase transition at ~ 6 K, predicted early on from ¹H NMR data [24]. This anomaly was later identified from lattice effects and entropy release [131], microwave properties [132], and using ultrasonic

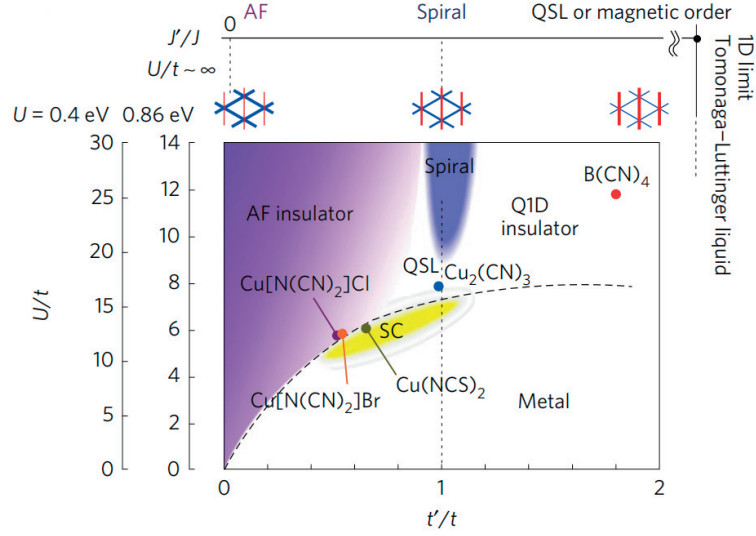


Figure 1.5 – Schematic phase diagram of κ -(ET)₂X charge-transfer salts (AF: antiferromagnet, SC: superconductor). Phases are drawn on the basis of theoretical estimates of the half-filled Hubbard models [120, 121]. $U = 0.4$ eV provides consistent picture, and $U = 0.86$ eV is taken from *ab initio* calculations [122]. $U/t \rightarrow \infty$ limit in the phase diagram is the anisotropic spin-1/2 $J - J'$ Heisenberg model drawn based on theoretical estimates with notable simplifications to show good continuity of the considered model [123]. Figure taken from Ref. [69].

wave propagation technique [133]. The anomaly was assigned to a crossover to a quantum disordered state [24], an instability of the QSL state [134, 135, 136], or to a phase transition to a paired-electron crystal [137]. Similarly, an instability of the QSL state was recognized in dmit at ~ 1 K from ¹³C NMR data, and it was related to a pairing instability [136, 117]. Due to the large J exchange coupling in these systems, these changes are believed to stem from subtleties of the Hamiltonian [87].

To better assess the low-temperature magnetic properties of κ -Cu, Pratt *et al.* [71] performed a detailed μ SR study to determine the magnetic field-temperature phase diagram of κ -Cu (see Fig 1.3), which revealed that a spin-gapped phase exists at very low temperatures. In addition, a rather complex magnetic phase diagram was unveiled. This demonstrated that a phase transition takes place from the quantum critical state to an antiferromagnetic state at a low field of ~ 5 mT with strongly suppressed magnetic moment as a result of two-dimensional Bose-Einstein condensation of the spin excitations [138]. The gapped and the weakly antiferromagnetic phases are assumed to be separated by a quantum critical point [139]. The small energy gaps and the field-induced anomalies, however, remained unexplained [68]. Surprisingly, magnetic torque measurements did not find the weakly antiferromagnetic phase and the numerous phase transitions, which was interpreted as a difference in the time scales relevant for the experiments [140].

The presence of spin-1/2 Cu²⁺ impurities and the closeness of the superconducting transition

complicate the systematic studies in κ -Cu. To overcome these difficulties, a QSL sister compound, κ -(BEDT-TTF)₂Ag₂(CN)₃ has been recently synthesized [67] and identified as a *strong* Mott insulator due to the negative chemical pressure compared to κ -Cu. As this material was the subject of my PhD research project, a more detailed discussion will be given in Chapter 4.

Recently, a strongly spin-orbit coupled rare-earth isotropic triangular system, YbMgGaO₄ was discovered with a gapless spinon Fermi surface [141, 142].

1.4.2 Kagomé: *an end to the drought* [143]

Herbertsmithite, the end member of the paratacamite family, was found to be an almost ideal example of the spin-1/2 kagomé structure, where the μ SR and neutron scattering measurements confirmed the absence of magnetic order down to 20 mK and 35 mK in powder and in single crystal samples, respectively [114, 144, 145, 146]. Gapless fractionalized, spinon excitations were found [146], despite the presence of 5-10% impurities resulting from Zn in the kagomé layer and Cu in-between the layers. The observed gapless behavior without sharp features could not be reconciled with most theories [147]. For a complete description, the presence of further neighbor interactions or the perturbation due to the Dzyaloshinskii-Moriya (DM) interaction (see Section 2.1.3) had to be assumed [148]. ESR measurements found that the DM interaction reaches as high as 8% of the magnetic coupling ($D \approx 0.08J$). It was demonstrated experimentally from NMR data [149] that the QSL state only persists up to a small (~ 1.5 T) magnetic field, and a spin-solid state is formed due to the large DM interaction.

1.4.3 Anisotropic triangular systems

Non-ideal triangular lattice systems provide a unique insight into the relevance of the geometrical frustration. Namely, the organic and inorganic materials, such as, Cs₂CuCl₄, κ -(BEDT-TTF)₂B(CN)₄ (κ -B), and κ -H₃(Cat-EDT-TTF)₂ (κ -H) display QSL behavior despite the absence of isotropic exchange coupling. These systems and the QSL state induced in X-ray irradiated two-dimensional κ -(BEDT-TTF)₂Cu[N(CN)₂]Cl [150] demonstrated that the phase diagram of the QSL states has to be reconsidered (see Fig. 1.5)

The first anisotropic QSL candidate was Cs₂CuCl₄ with an exchange coupling ratio of $J'/J \approx 1/3$, which was found to indicate a rather low frustration parameter of $f \approx 8$, ordering at $T_N = 0.46$ K [151, 152]. The observation of a broad continuum in the dynamical structure factor measured by neutron scattering confirmed that, instead of a magnon-like spectrum, a spinon continuum can be identified [151]. The detailed phase diagram found an extended QSL state [153], and a quantitative theory [154] could explain both the neutron scattering and the dynamical magnetic susceptibility data [155] by the virtue of coherently bound two-spinon states, that is, *triplons*, resulting in significant transverse dispersion.

The two organic systems, κ -B and κ -H are much less investigated. Both are quasi-one-dimensional systems with moderate anisotropies of $t'/t(\kappa - B) \approx 1.8$ [69] and $t'/t(\kappa - H) \approx$

1.48 [156], and the temperature dependence of their macroscopic susceptibilities are well described by the anisotropic triangular lattice curves [157, 158]. Torque magnetometry showed κ -H to be a QSL with a constant, Pauli susceptibility down to $J/10^4$ indicating a gapless Fermi surface state. In contrast, ^1H NMR data in κ -B displayed a clear phase transition to a spin-gapped phase at $T_c \approx \frac{1}{30}J/k_B$.

2 Experimental techniques

In this Chapter, I will present two experimental methods used during my PhD thesis for magnetic studies of geometrically frustrated magnetic systems: Electron Spin Resonance (ESR) and Muon Spin Rotation (μ SR). I will introduce the basic principles for both spectroscopic techniques, and I will give a brief overview of the signatures of magnetically ordered and disordered states in the quest for a low-temperature quantum critical state. As we will see, both techniques have their own advantages and disadvantages, and their combination offers a way to unravel magnetic properties with an unprecedented precision. I will show that even if traditionally μ SR is combined with NMR to study QSLs, ESR technique provides a more sensitive alternative to NMR on the disordered state and the spin-anisotropies.

2.1 Electron Spin Resonance

ESR (or EPR=Electron Paramagnetic Resonance), which was developed in 1944 by Yevgeny Zavoisky [159], is a contactless spectroscopic technique widely used for studies in biology, chemistry, and in physics [160]. Owing to its unique sensitivity down to 10^{12} spins, traditional ESR spectrometers provide a versatile and powerful method for studies, e.g., of free radicals, chemical reactions [161], and the ground state of correlated electron systems [162, 163]. With the development of fields of quantum computation [164, 165, 166] and spintronics [167, 44], and the continuous miniaturization of modern ESR detection schemes [168, 169], it remains an important tool in modern laboratories.

2.1.1 Basic principles

Interaction of an external \mathbf{B}_0 magnetic field and a μ magnetic moment is described by the Zeeman Hamiltonian [170], which reads [171, 172]

$$\mathcal{H}_{\text{ext}} = -\boldsymbol{\mu} \cdot \mathbf{B}_0. \quad (2.1)$$

Chapter 2. Experimental techniques

For an electron in a solid, the μ magnetic moment is a sum of the orbital (\mathbf{L}) and spin angular momentum (\mathbf{S}) contributions, hence, it reads

$$\boldsymbol{\mu} = -\frac{\mu_B}{\hbar} (g_L \mathbf{L} + g_S \mathbf{S}) = -\frac{\mu_B}{\hbar} g_J \mathbf{J}. \quad (2.2)$$

Here, μ_B is the Bohr magneton, $g_L = 1$ and $g_S \approx 2.0023$ are the g -factors [173], g_J is the Landé g -factor, and $\mathbf{J} = \mathbf{L} + \mathbf{S}$ is the total angular momentum. Thus, in a magnetic field $\mathbf{B}_0 = B_0 \mathbf{z}$, the allowed energy level splittings are

$$\Delta E = g_J \mu_B J_z B_0. \quad (2.3)$$

Here, J_z can take the values $J_z = -J, -J+1, \dots, J$.

Using Eq. 2.1 and Eq. 2.2, the time dependence of the quantum mechanical expectation value of \mathbf{J} can be given as an equation of motion, as

$$\frac{d\langle \mathbf{J} \rangle}{dt} = \frac{i}{\hbar} \langle [\mathcal{H}_{\text{ext}}, \mathbf{J}] \rangle = \gamma \langle \mathbf{J} \rangle \times \mathbf{B}_0. \quad (2.4)$$

In the last step, we used the Ehrenfest theorem [174] and the gyromagnetic ratio (γ): $\boldsymbol{\mu} = \gamma \mathbf{J}$. Similarly to the classical case, Eq. 2.4 shows a precession of $\langle \mathbf{J} \rangle$ around the applied magnetic field with the Larmor frequency $\omega_L = \gamma B_0$.

Bloch equations

In an ESR experiment, a transition is induced by microwaves between the different energy levels of Eq. 2.3, yielding a resonance condition of $\hbar\omega = \Delta E$. The induced transition is achieved via switching on a linearly polarized alternating magnetic field, B_x . To simplify the calculations, B_x can be broken to two circularly polarized components, rotating in the opposite directions. Close to the resonance, only the one rotating in the same direction as $\langle \mathbf{J} \rangle$ is of importance to induce transition: $\mathbf{B}_1 = B_1 [\mathbf{i} \cos(\omega t) - \mathbf{j} \sin(\omega t)]$. In the laboratory frame

$$\frac{d\langle \mathbf{J} \rangle}{dt} = \gamma \langle \mathbf{J} \rangle \times [\mathbf{B}_0 + \mathbf{B}_1]. \quad (2.5)$$

In the frame rotating with \mathbf{B}_1

$$\frac{\partial \langle \boldsymbol{\mu} \rangle}{\partial t} = \langle \boldsymbol{\mu} \rangle \times [\mathbf{k}(\gamma B_0 - \omega) + \mathbf{i}\gamma B_1]. \quad (2.6)$$

Eq. 2.6 emphasizes that if $\gamma B_0 = \omega_L \approx \omega$, $\boldsymbol{\mu}$ rotates around the x -axis with periodically changing magnetic potential energy. This oscillation would cause a continuous spin-flip in the absence of friction. The simplest model to describe a relaxation process can be given by assuming exponential relaxation of the magnetization, which was first implemented in the Bloch equations

as follows [175]

$$\begin{aligned}\frac{dM_z}{dt} &= \gamma(\mathbf{M} \times \mathbf{B})_z + \frac{M_0 - M_z}{T_1} \\ \frac{dM_x}{dt} &= \gamma(\mathbf{M} \times \mathbf{B})_x - \frac{M_x}{T_2} \\ \frac{dM_y}{dt} &= \gamma(\mathbf{M} \times \mathbf{B})_y - \frac{M_y}{T_2}.\end{aligned}\tag{2.7}$$

Here, \mathbf{B} is the effective magnetic field, M_0 is the equilibrium magnetization through the z -axis, and two relaxation times are included. T_1 is the spin-lattice or longitudinal relaxation time representing the energy transfer to a reservoir (usually the lattice). T_2 is the so-called spin-spin or transverse relaxation time measuring the loss of phase coherence of spins.

The solutions of the Bloch equations can be given for the real (χ') and imaginary part (χ'') of the complex dynamic susceptibility (χ) as

$$\chi = \chi' - i\chi''.\tag{2.8}$$

In the reference frame, the solution reads

$$\begin{aligned}\chi' &= \frac{\chi_0\omega_0}{\mu_0} T_2 \frac{(\omega_0 - \omega) T_2}{1 + (\omega - \omega_0)^2 T_2^2} \\ \chi'' &= \frac{\chi_0\omega_0}{\mu_0} T_2 \frac{1}{1 + (\omega_0 - \omega)^2 T_2^2}.\end{aligned}\tag{2.9}$$

Here, χ' is the elastic or dispersive and χ'' is the inelastic or dissipative response of the system, which are connected by the Kramers-Kronig theorem [172].

2.1.2 ESR instrumentation

The World War II boosted the development of the microwave instrumentation, leading to the first continuous-wave ESR (1944 [159]) and NMR (1945 [176]) experiments. With the development of the Fourier transform NMR technique (1965 [177]) and later on the first commercially available pulsed (1987 [178]) and the first high-field ESR spectrometers (1996 [179]), the instrumentation went through a significant progress over the previous decades [180]. In the following, I will discuss two designs available in our laboratory. Firstly, a commercial low-field spectrometer (Bruker Elexsys E500) will be presented covering the frequencies of S-band ($f = 4.1$ GHz yielding a $g = 2$ resonant field of $B_{\text{res}} = 0.15$ T), X-band ($f = 4.1$ GHz, $B_{\text{res}} = 0.33$ T), and Q-band ($f = 35$ GHz, $B_{\text{res}} = 1.2$ T) at temperatures from $T = 1.8$ K to $T = 500$ K. Later on, I will discuss the home-built high-frequency ($f = 52 - 420$ GHz, $B_{\text{res}} = 1.8 - 15$ T) and high-pressure ($p = 0 - 1.6$ GPa) setup built and continuously developed in our laboratory operating from $T = 1.5$ K to 300 K [181, 182].

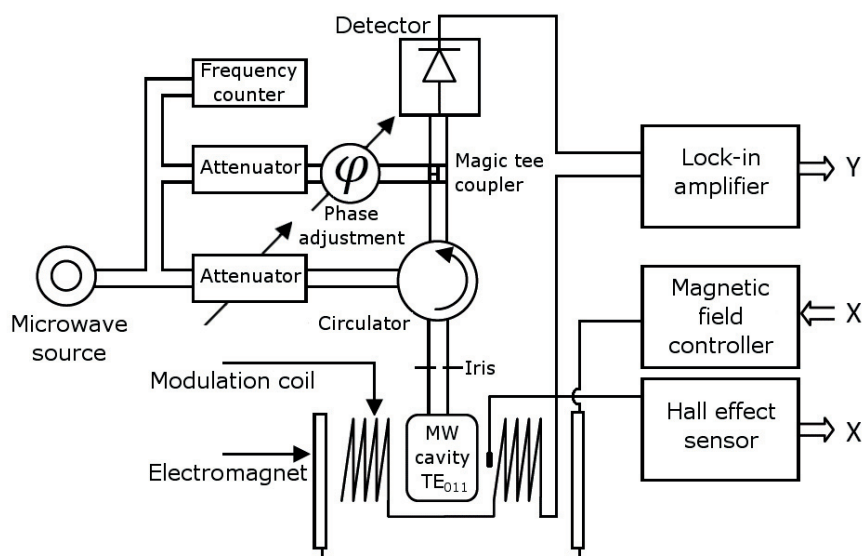


Figure 2.1 – Block diagram of a continuous-wave X-band ESR spectrometer utilizing homodyne detection scheme. Figure adapted from Ref. [171].

Low-frequency ESR setup

As seen previously, a minimal ESR experiment would require a sweeping magnetic field and a microwave (MW) source, supplemented with a detector. In practice, a number of similar complications arise that must be resolved: *i)* only a small amount of the MW power is absorbed, *ii)* the MW frequency must be precisely controlled, and *iii)* the detected signal is very weak compared to the background noise.

At our low-frequency setup (see Fig. 2.1), the MW source is a phase-locked Gunn diode with a maximal output power of 200 mW [183]. This power is transmitted by MW waveguides to three different components. One part provides information about the precise frequency using a frequency counter, the second part is sent directly to the detector after tunable attenuation, and the third component arrives at the circulator. This ferrite element is a three-port device in which the MW entering at a port can only leave at the next port. Thus, the MWs coming from the MW source are sent to the cavity, and the MW radiation reflected from the cavity leaves towards the detector.

The MW cavity resolves the issue of low MW absorption by the virtue of working at critical coupling. In this state, the resonant cavity functions as an impedance-matched load on the transmission line [184]. There is no reflection from the cavity off-resonance [185]. The figure of merit of sensitivity of the cavity to perturbations is the quality factor (Q). As in mechanical oscillators, the Q -factor (typically in the range of 5000-10000 in X-band spectrometers) measures the efficiency of the energy storage: $Q = 2\pi \cdot E(\text{stored}) / E(\text{dissipated per MW cycle})$ [186]. In the frequency domain, it defines the width ($\Delta\nu$) of the MW mode at a given frequency (ν):

$Q = \nu/\Delta\nu$. To decrease the noise in the ESR experiment, and to achieve maximal sensitivity, the automated frequency control (AFC) unit maintains the load-matching conditions.

When the electron spins become resonant, additional MW power is absorbed, and the critical coupling is lost leading to a slight reflection from the MW cavity. This power is transmitted to the detector biased with the reference signal. After a φ phase shift of the reference, in constructive interference conditions, the measured signal is $I_{\text{ESR}} \propto \chi''\sqrt{P}$, where P is the reflected power.

To further improve the signal-to-noise ratio, we use lock-in technique via modulating the sweeping magnetic field using modulation coils in the MW cavity. The ESR signal is a derivative Lorentzian curve (see Fig. A.1).

High-frequency ESR setup

The need for high-field ESR (HF-ESR) spectrometers was raised as early as in 1957 by G. Feher to make use of the significant increase of sensitivity with the frequency [187]. HF-ESR, as compared to low-frequency ESR provides an improvement of the g -factor resolution proportional to the multiplication of the frequency assuming that the linewidth (ΔB_{pp}) of the signal does not change. In general, a g -factor difference, Δg , can be resolved in B magnetic field if

$$\frac{\Delta B_{\text{pp}}}{2B} < \frac{\Delta g}{\bar{g}}, \quad (2.10)$$

where \bar{g} is the average g -factor in the material. This means that the high-field limit will be reached at different fields in different materials. Furthermore, systems with large zero field splittings can be studied using HF-ESR [188, 189]. In the following Chapters, I will give examples of multi-frequency studies where the large magnetic fields are required to provide information on the Hamiltonian of magnetic materials.

Fig. A.3 depicts the scheme of our HF-ESR spectrometer utilizing quasi-optical technique [190, 191], a flexible solution to modify the front-end optics in our system [192]. This approach means that quasi-optical elements, such as polarizers (in our case, wire grids), beam splitters (rotating grids), and Faraday rotators (ferrite passive phase shifter) are implemented. The MW source is a tunable signal generator with frequencies from 0 to 23 GHz. The output frequency (typically used ~ 13.1 GHz) is passively multiplied by frequency doublers leading to an order of magnitude power loss at each multiplication. Two different cascaded multiplier chains are operated at our HF-ESR spectrometer, together granting a quasi-continuous frequency coverage from 50 to 432 GHz (see Appendix A and Fig. A.2). As there are MW power losses due to the doublers and the setup was optimized for 210 GHz operation, the signal-to-noise ratio does not increase with the frequency as expected theoretically, instead, it has a maximum at 312 GHz (see Fig. A.2).

Following the MW source, a corrugated horn helps us to transform the MW waveform to a

Chapter 2. Experimental techniques

single-mode Gaussian beam propagating in free space. As in low-frequency ESR, a homodyne detection scheme is used, i.e., the MWs are split into two parts, one of them serving as reference arm and the other traveling to the sample positioned into the superconducting magnet. The latter component suffers a phase shift by a translatable mirror to achieve the constructive interference condition. An elliptical mirror focuses the MWs into a corrugated pipe in the Variable Temperature Insert of the magnet. If the resonant conditions are satisfied, a portion of one of the circularly polarized components in the linearly polarized light is absorbed. This provokes the appearance of the other linearly polarized component at the reflected signal, i.e., it functions in induction mode [193]. A wire grid, serving as a circulator reflects all of the original, linearly polarized component but it transmits the signal-carrying MWs to the detector. The detector is a bolometer that measures the incoming MW power of the ESR signal.

Apart from the standard magnetic field modulation technique, frequency modulation can be employed for the detection of the ESR signals owing to the lack of resonating MW components (see Appendix A) [181]. Furthermore, chopping of the MWs (achieved by setting a pulsed MW waveform) can be used for the detection of broad signals with large intensity without the need of field modulation (see Fig. A.1) [164]. These additional characteristics demonstrate that this spectrometer design serves as a versatile tool for ESR experiments, and allows our laboratory to push the limits of the technique to remain in the forefront of present-day material research.

High-frequency high-pressure ESR setup

In condensed matter systems, hydrostatic and chemical pressures are exceptional tools that allow to alter the system, and are frequently applied for the investigation of the materials. Even if ESR is highly sensitive to phase transitions, high-pressure ESR measurements did not become widespread due to a large number of difficulties in the design of such systems [194, 195]. Most commercial ESR instruments use resonating structures, as described in Section 2.1.2, which should be fitted to the high-pressure withstanding, nonmagnetic structures, in a size compatible with the space restrictions of the electromagnets, and combined with magnetic field modulation. These technical challenges were overcome using two methods: either by using high-dielectric materials to reduce the active volume [196], or by using a combination of diamond-anvil cells with specialized microwave resonating structures [197]. Due to the lack of resonating structures in high-field ESR spectrometers, they grant a significant simplification in the setup design. The first ESR setup allowing high-frequency high-pressure operation in a broad temperature range was designed in our laboratory [181], and will be presented below.

In a clamped-type piston cylinder pressure cell using a nonmagnetic beryllium copper (BeCu) body, the magnetic field modulation is placed on the outer side. This leads to an upper limit of ~ 300 - 500 Hz for the modulation frequency and a rather small modulation amplitude. Nevertheless, the pressurized volume (filled with Daphne 7373 oil as pressure transmitting medium) behaves as an oversized cavity, enhancing significantly the signal-to-noise ratio. This volume is penetrable for MWs through a diamond window providing a pressure seal and a plug, and it is closed at the bottom with the piston, its top flat surface serving as a MW

mirror. The ESR sample is placed on the top of the mirror to further optimize the sensitivity. The whole body is coupled to an oversized corrugated waveguide. As a consequence of the small, 1.5 mm-in-diameter diamond window, the setup operates best at frequencies 210 GHz or higher. In practice, the overall sensitivity loss is only an order of magnitude compared to the ambient-pressure ESR measurements.

2.1.3 ESR signals of low-dimensional systems

In the following, I will examine the characteristics of the ESR signals arising in the different viable low-temperature states in low-dimensional systems. In particular, I will focus on the ESR properties of states viable within the Mott-Hubbard model [198, 199]. In the limit of large overlap (t) and weak on-site interaction (U), the system becomes metallic, and gives rise to the so-called Conduction Electron Spin Resonance (CESR) signal [200, 201]. In contrast, for large on-site interaction ($U \ll t$), a magnetically ordered state might emerge if the exchange interaction, $J = 4t^2/U$ is strong enough. As we saw in Section 1.1, despite the strong J interaction, some systems may remain in a quantum disordered state, providing unique observations of collective magnetic excitations.

ESR signal of conduction electrons

In three-dimensional metallic systems, if the free-electron gas model holds, the Pauli spin-susceptibility measured by ESR (see Eq. 2.9) is proportional to the electronic density of states at the Fermi level, $D(E_F)$. Thus, after calibration, the absolute spin-susceptibility enables the determination of $D(E_F)$. In its dimensionless form the susceptibility reads [173]

$$\chi_0(\text{Pauli}) = \mu_0 \frac{g^2}{4} \mu_B^2 D(E_F) \frac{1}{V_c}, \quad (2.11)$$

where V_c is the volume of the unit cell. In a metal with inversion symmetry, the spin-lattice relaxation might occur as a result of momentum scattering by phonons in case the ions in the lattice induce spin-orbit coupling [44]. The so-called Yafet relation [202] states that the spin-conserving scattering probability and the momentum scattering time are equivalent. As perturbation theory can show it, the admixing of the spin-up and spin-down states stemming from the spin-orbit interaction leads to a Δg g -factor shift of the CESR signal as compared to its free electron value. Thus the ΔB_{pp} linewidth, as a measure of the spin relaxation time must satisfy the generalized Elliott-Yafet relation in simplest metals [167, 203]

$$\Delta B_{pp} = \frac{\varepsilon_0 \omega_{pl}^2}{\gamma} \frac{\alpha_1}{\alpha_2^2} (\Delta g)^2 \rho. \quad (2.12)$$

Here, ε_0 is the vacuum permeability, ω_{pl} is the plasma frequency, $\alpha_{1,2}$ may vary between 1...10 depending on the metals, and ρ is the resistivity.

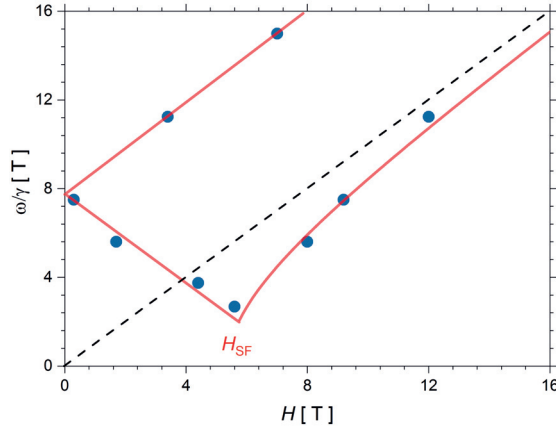


Figure 2.2 – Typical easy-axis antiferromagnetic resonance magnetic field-frequency mode diagram measured in a double-perovskite system, $\text{Ca}_2\text{MnTeO}_6$ ($T_N = 42$ K) [208]. Solid lines depict the calculated mode diagram. Remarkably, a large DM interaction causes the appearance of an energy gap provoking a continuous spin reorientation close to the spin-flop field, H_{SF} .

The identification of a CESR signal in a metal relies on a number of benchmarks [162, 167]: *i*) the measured spin-susceptibility must match the Pauli spin-susceptibility expected in the given system *ii*) the temperature-dependence should differ from the Curie-temperature dependence ($\chi_0(\text{Curie}) \propto 1/T$) *iii*) the linewidth should follow the Elliott-Yafet mechanism [202, 204, 205] *iv*) the relation of ΔB_{pp} and the g -factor must follow the Elliott-Yafet relation.

Nevertheless, the case of one- and two-dimensional organic conductor systems exhibits different characteristics pointing to the invalidity of the Elliott-Yafet mechanism, due to the different topology of the Fermi surface [206, 207]. In these systems we only require the first two benchmarks of the CESR to be confirmed.

ESR in magnetically ordered phases

If the magnetic interactions lead to ordering at low temperatures, the ESR signal below the transition deviates from the paramagnetic one observed above the transition due to the non-negligible spin interactions. Multi-frequency ESR studies provide direct information on the frequency-magnetic field mode diagram of a given material, and are capable to determine the exchange anisotropies. Close to the transition temperature, the ESR signal becomes complicated, and the critical region can only be described by dynamical scaling theories [209, 210]. Well below the transition temperature, an effective magnetic field can be defined by the sum of the applied magnetic field and the internal field. Although this assumption simplifies the treatise, the complexity of the problem can be illuminated by the simplest case of ferromagnetic materials without exchange anisotropies: owing to the spontaneous magnetization of the material, the sample shape affects the resonance frequency through the demagnetization factor.

In antiferromagnets (AFM) below the Néel temperature (T_N), two sublattice magnetizations (A and B) are to be handled. Thus, Eq 2.5 for the magnetization of the material can be written as a system of two coupled dynamic equations that read [210]

$$\begin{aligned}\frac{d\mathbf{M}_A}{dt} &= -\gamma\mathbf{M}_A \times (\mathbf{H}_0 + \mathbf{H}_{e,A} + \mathbf{H}_{a,A} + \mathbf{H}_1) \\ \frac{d\mathbf{M}_B}{dt} &= -\gamma\mathbf{M}_B \times (\mathbf{H}_0 + \mathbf{H}_{e,B} + \mathbf{H}_{a,B} + \mathbf{H}_1).\end{aligned}\quad (2.13)$$

These modified equations of motion comprise the magnetic fields originating from the exchange (\mathbf{B}_e) and the anisotropy fields (\mathbf{B}_a), which were absent in the paramagnetic case. In its general form, the anisotropy energy becomes

$$E_a = \frac{1}{2}K_1(\beta_A^2 + \beta_B^2) + \frac{1}{2}K_2(\gamma_A^2 + \gamma_B^2), \quad (2.14)$$

where K_1 and K_2 ($0 < K_1 < K_2$) are the easy-intermediate and easy-hard anisotropy energies, and α_A , α_B , β_A , and β_B are the direction cosines of the magnetization. Thus, the angle dependence of Eq. 2.14 implies a strong angle dependence of the antiferromagnetic resonance (AFMR) modes calculated from Eq. 2.13.

For uniaxial anisotropy ($K_2 = K_1$) and in the case of an applied magnetic field (\mathbf{H}_0) parallel to the easy axis, the solutions are expressed as

$$\begin{aligned}\frac{\omega_{\pm}}{\gamma} &= H_{\text{SF}} \pm H_0 && \text{if } H_0 < H_{\text{SF}} \\ \frac{\omega}{\gamma} &= \sqrt{H_0^2 - H_{\text{SF}}^2} && \text{if } H_{\text{SF}} < H_0 < H_E \\ \frac{\omega}{\gamma} &= H_0 - H_A && \text{if } H_E < H_0,\end{aligned}\quad (2.15)$$

where the + and – signs stand for the two sublattices, and H_{SF} is the spin-flop field at which the anisotropy energy becomes equal to the Zeeman energy. For an applied field perpendicular to the easy axis, the modes are

$$\begin{aligned}\frac{\omega_1}{\gamma} &= \sqrt{H_0^2 + H_{\text{SF}}^2} \\ \frac{\omega_2}{\gamma} &= \sqrt{1 - \left(\frac{H_0}{H_{\text{SF}}}\right)^2}.\end{aligned}\quad (2.16)$$

If the crystal structure lacks the inversion symmetry, the contribution of the antisymmetric exchange interaction is expected to be non-zero between neighbouring spins. This term, the so-called Dzyaloshinskii-Moriya interaction was first taken into account to explain the weak ferromagnetic properties of hematite, $\alpha\text{-Fe}_2\text{O}_3$ [211, 212, 213]. This interaction can be expressed phenomenologically as

$$\mathcal{H}_{\text{DM}} = \sum_{(i,j)} D_{ij} \vec{S}_i \times \vec{S}_j, \quad (2.17)$$

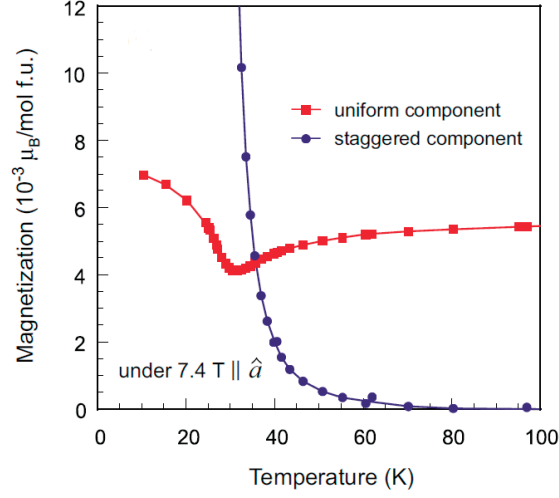


Figure 2.3 – Temperature dependence of the staggered and the uniform component of the magnetic moment in κ -Cl as measured by the shift of the ^{13}C -NMR data, and coinciding with the increase of the noncollinear angle measured from the magnetic-field axis (not shown here). It reveals the emergence of the staggered magnetization as high as at ~ 60 K, at temperatures much higher than the $T_{\text{N}} = 23$ K Néel temperature. Note that the applied 7.4 T field was applied in the \hat{a} direction, i.e., forming an angle of 45° with the DM interaction. Figure taken from Ref. [215].

where \vec{D}_{ij} is the Dzyaloshinskii-Moriya (DM) vector between spins \vec{S}_i and \vec{S}_j . This component induces the originally antiparallely aligned spins to form a canting angle of the order of $\varphi = D/J$, where D and J are the amplitudes of the leading DM and exchange interaction terms. This canting modifies the AFMR modes and makes the general description more complicated, as the symmetry of the crystal structure is to be considered. In general, the shape of the AFMR modes remains similar to the one defined in Eq. 2.15 and Eq. 2.16, if the value of D/J is low enough, and the corresponding canting is small (see Fig. 2.2) [214]. Relevantly, the zero-energy mode at H_{SF} vanishes, appearing at higher energies approximately proportional to the amplitude of the DM vector. In fact, the jump of the free energy minimum is replaced by a continuous spin reorientation.

Antiferromagnetic fluctuations

As discussed in Section 1.4.2, a large enough DM interaction might destroy the quantum disordered state [148]. As it was seen in NMR studies [149], the presence of the DM interaction leads to a phase transition towards an ordered state at large enough magnetic fields. This is therefore reasonable to expect that at magnetic fields close to a field-induced phase transition antiferromagnetic fluctuations might appear already above T_{N} , as signatures of increasing staggered magnetization. In fact, the interplay between the DM and Zeeman interactions changes the antiferromagnetic transition to a crossover phase at finite fields. The staggered

magnetization, \mathbf{M}_s , functions as an internal field of the system which can be expressed as

$$\mathbf{h} = \frac{\mathbf{D}}{J} \times \mathbf{H}. \quad (2.18)$$

This \mathbf{h} internal field should provoke a resonance field shift of the ESR signal. Furthermore, \mathbf{M}_s decreases the transverse spin relaxation rate, T_2 , which is supposed to be resulting in a broadening of the ESR signal [216].

To quantify the effects of the staggered magnetization in low-dimensional strongly correlated systems, we can rely only on calculations on the antiferromagnetic Heisenberg $S = 1/2$ spin chains, no calculations are available for isotropic or anisotropic Heisenberg triangular-lattice antiferromagnets.

In one-dimensional $S = 1/2$ spin chains, it was established using a field theory that the temperature and magnetic field dependence of the g -factor shift from the paramagnetic value reads [217, 218, 219]

$$\begin{aligned} \Delta g_{\text{sf}} &= Fz[z - \text{Re}(G)] \\ \Delta B_{\text{pp}} &= \eta_0 + FzB\text{Im}(G). \end{aligned} \quad (2.19)$$

Here, $z = \Gamma(\frac{1}{4}) / (\frac{3}{4})$ and $\Gamma(x)$ denotes the gamma function, and

$$\begin{aligned} G(B, T) &= \frac{\Gamma\left(\frac{1}{4} - i \frac{g\mu_B B}{2\pi k_B T}\right)}{\Gamma\left(\frac{3}{4} - i \frac{g\mu_B B}{2\pi k_B T}\right)} \\ F(B, T) &= c^2 \sqrt{\frac{\pi}{128}} \frac{J}{k_B T} \sqrt{\ln\left(\frac{\lambda J}{k_B T}\right)}. \end{aligned} \quad (2.20)$$

Here, c is an angle- and crystal-dependent parameter determining the staggered field from the DM interaction. The parameter λ in the logarithmic term compensates for the subleading terms [220]. In the high-field limit, these equations give a linear-in-field increase of both of the g -factor shift and the ESR linewidth. In the low-field limit, the g -factor shift and the ESR linewidth follow a simple quadratic-in-field dependence that is expressed as

$$\begin{aligned} \Delta g_{\text{sf,low}} &\approx 0.34 g_e^2 \mu_B^2 \frac{Jc^2 B^2}{(k_B T)^3} \ln\left(\frac{J}{k_B T}\right) \\ \Delta B_{\text{sf,low}} &\approx 0.69 g_e \mu_B \frac{Jc^2 B^2}{(k_B T)^2} \ln\left(\frac{J}{k_B T}\right). \end{aligned} \quad (2.21)$$

In this case, the ratio of the two ESR measurables gives a simple value:

$$\frac{\Delta B_{\text{sf,low}}}{\Delta g_{\text{sf,low}}} \approx 2 \frac{k_{\text{B}} T}{g_e \mu_{\text{B}}}. \quad (2.22)$$

Remarkably, this ratio is independent of the field, and linear in temperature.

Despite the lack of an extensive theory, several attempts were made to investigate the effect experimentally in a truly two-dimensional organic antiferromagnet, κ -(ET)₂Cu[N(CN)₂]Cl (κ -Cl) [216, 215, 221]. These ¹³C-NMR and ESR studies confirmed that in a nominally paramagnetic phase field-induced magnetism can appear above the T_{N} transition temperature. Combined with molecular field calculations giving a qualitative proof of the effect, the NMR study of Kagawa *et al.* [215] demonstrated that the NMR shift can be separated into a staggered and a uniform magnetization component. It was evidenced that both \mathbf{M}_{s} and the noncollinear angle of the dimers start to grow below 60 K (see Fig. 2.3). Due to the symmetry configuration needed for NMR studies that require that the inner and outer ¹³C sites sit in a symmetrically equivalent position, the NMR measurements were performed in a direction where \mathbf{h} is not maximal. For ESR measurements, the crystals were oriented in the direction exactly perpendicular to the DM interaction, leading to significantly larger staggered fields. In addition, as the DM interaction in the subsequent layers of κ -Cl form an angle of 90°, the layers with maximal \mathbf{M}_{s} and with $\mathbf{M}_{\text{s}} = 0$ were measured at the same time providing a direct proof of the role of the DM interaction. Although it was observed that the theory developed for spin-1/2 chains gives an approximately good description of the observed behavior, the quantitative agreement was not tested.

Above I stressed that the measurements were performed in a two-dimensional system. Although the solution of this simplified model is already challenging, the interlayer interactions are to be considered in this system [222, 223]. Relevantly, the comparison of ESR and resistivity measurements determined the interlayer interaction to be at the range of dipole-dipole interaction, thus, it can be regarded to be weak enough [222, 224].

2.2 Muon Spin Rotation

2.2.1 Basic principles

As for electrons in the ESR experiment, the application of muons (μ^+) in μ SR studies is based on their precession in a B magnetic field¹. Regarding the muon source used for experimental work, we can differentiate three different cases. As it is known from the famous example of relativistic time dilation, muons from the cosmic rays are present on the surface of Earth, and this source was and is still used for a number of large-scale experiments, such as the imaging of volcano chambers [225].

¹As the mass of the muons differs from that of electrons ($m_{\mu} \approx 207 m_e$), the gyromagnetic ratio of the muons is $\gamma_{\mu} \approx 135 \text{ MHz/T}$, resulting in a correspondingly smaller Larmor frequency.

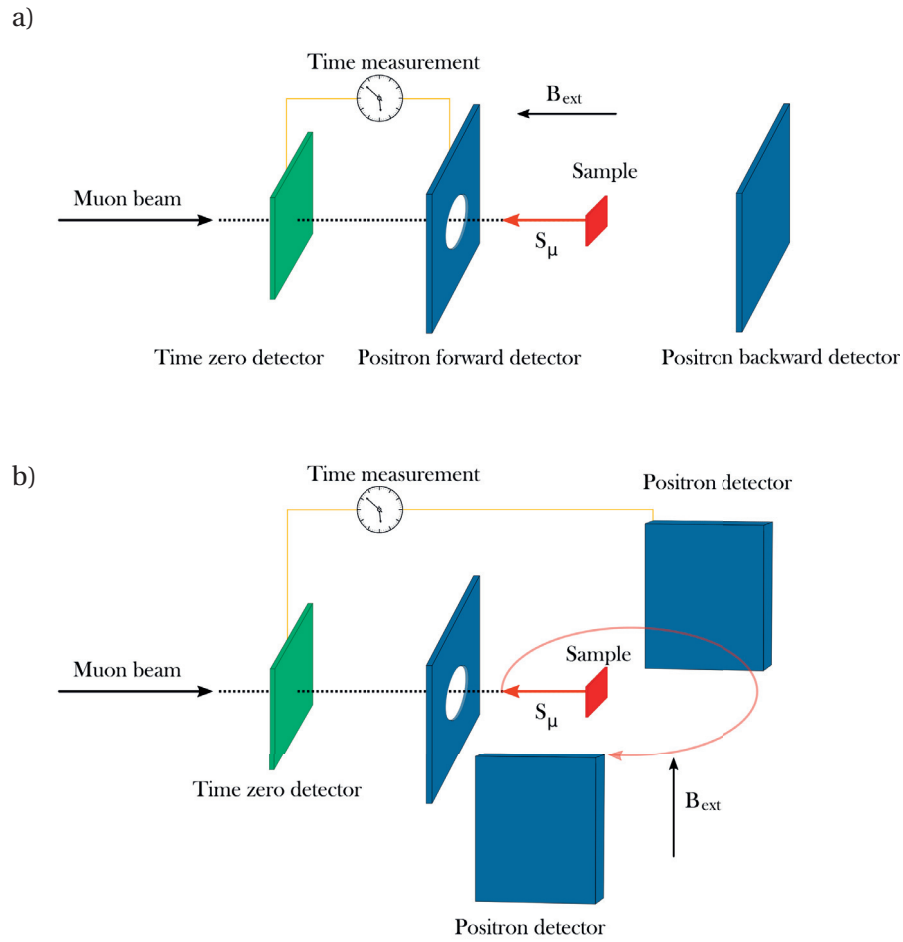
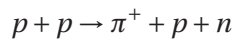
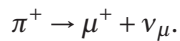


Figure 2.4 – Typical experimental setups for μ SR experiments showing the relative orientations of the muon beam and the positron detectors. In a μ SR experiment, the Cartesian coordinate Z is parallel to the original muon spin orientation (S_μ), as determined by the muon beam orientation. The muon spin precesses around the external field, B_{ext} . Thus, in longitudinal field and zero-field experiments, $P_Z(t)$ can be measured using the forward and backward detectors (see *a*). In a transverse field experiment, the $P_X(t)$ (and equivalently, $P_Y(t)$) is relevant in the time measurement (see *b*).

This natural source, however, is insufficient for μ SR studies, and continuous-wave (CW) and pulsed synchrotron sources are used for performing material characterization [226]. In both cases, surface muons are produced using a graphite target for the high energy proton beams, which results in the collision



producing fast decaying pions (π^+):



Here, ν_μ stands for the muon neutrino. The zero spin of the π^+ implies that the μ^+ and ν_μ spins and momentum must be opposite to satisfy the two-body decay. Given the negative

Chapter 2. Experimental techniques

helicity of the neutrino, the parity is violated, and the momentum and spin of the muon are in opposite directions. This leads to effectively 100% spin-polarized muons, thus, no magnetic field is required to achieve a sizable spin polarization, in contrast to NMR and ESR techniques.

As the muon arrives in the sample, it loses a significant fraction of its initial kinetic energy by a large number of collisions due to the Coulomb interaction (it slows down from 4 MeV to a few keV), and it stops at an interstitial site. Once implanted, the muon has a lifetime of $\tau_\mu = 2.2 \mu\text{s}$ while it decays as

$$\mu^+ \rightarrow e^+ + \nu_e + \bar{\nu}_\mu.$$

In this rather complicated three-body process, observation of the electron neutrino, ν_e , and the muon antineutrino, $\bar{\nu}_\mu$, is impossible, so the positron is detected. The latter has a preferential direction to fly away, parallel to the muon spin orientation. This asymmetry can be resolved in the backward and forward detectors [227]:

$$A(t) = \frac{N_F(t) - \alpha N_B(t)}{N_F(t) + \alpha N_B(t)}, \quad (2.23)$$

where $N_F(t)$ and $N_B(t)$ are the numbers of the forward- and backward-detected muons, respectively, and α is an experimental parameter compensating the slightly different forward and backward detector configurations depending on a number of experimental factors. In practice, $A(t)$, the asymmetry contains all the relevant information regarding the material properties. For a given detector configuration with a fix covered solid angle and detector efficiency, it has a theoretical maximum value $A_{\text{max}} < 1$. This maximum is close to 0.25 in all facilities ², however, to avoid confusion, I will use the relative muon polarization, $P(t) = A(t)/A_{\text{max}}$ for the presentation of the μSR data.

2.2.2 Synchrotron sources

Given the significant costs, the μSR studies are limited to four sites in the world. CW sources are available at Paul Scherrer Institute (PSI $S\mu\text{S}$) in Switzerland and at TRIUMF in Canada, whereas pulsed sources are available in KEK in Japan and at the ISIS Rutherford Appleton Laboratory in United Kingdom. In a CW experiment, each muon is identified with the corresponding positron it decays into. For pulsed sources, the muons arrive in pockets with large intensity during a very short time (~ 80 ns at the ISIS), and the time is measured from the arrival of the pocket until the detection of the positron. The CW source provides an exceptional precision of time, and it can be used down to very short times. In contrast, the pulsed source can be used for longer timescales to identify low-frequency oscillations. Hence, in our μSR studies we used the combination of these techniques to provide a more complete mapping and understanding.

²It is $A_{\text{max}}(\text{PSI}) = 0.25$ in PSI and $A_{\text{max}}(\text{ISIS}) = 0.27$ in ISIS typically at the relevant instruments.

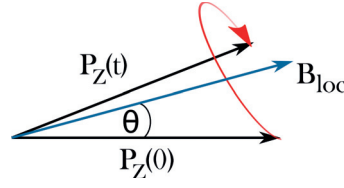


Figure 2.5 – The spin of the μ^+ implanted in the sample precesses around an arbitrarily oriented \mathbf{B}_{loc} local magnetic field. θ is the constant angle formed by the spin and \mathbf{B}_{loc} , i.e., $\sin^2(\theta) = (B_x^2 + B_y^2)/\mathbf{B}_{\text{loc}}^2$ and $\cos^2(\theta) = B_z^2/\mathbf{B}_{\text{loc}}^2$.

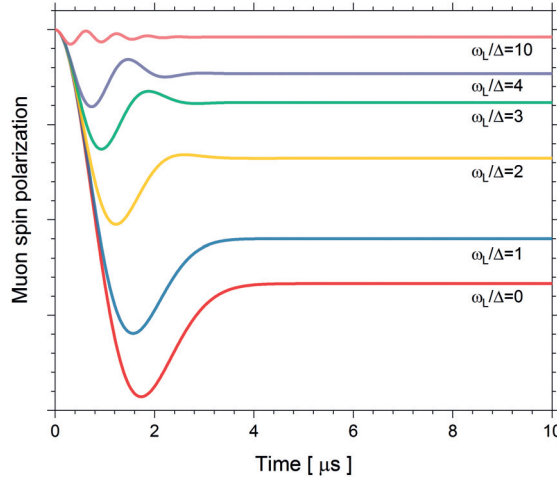


Figure 2.6 – Kubo-Toyabe muon polarization function in a Gaussian internal field distribution at different values of the B_{ext} external field applied parallel to the muon spin orientation (longitudinally). Note the minimum at $\Delta \cdot t \approx \sqrt{3}$ ($\Delta/\gamma_\mu = 1$ MHz) in the zero-field case. Adapted from Ref. [79].

2.2.3 Muon spin rotation in magnetic materials

Depending on the relative orientation of the muon spin and the applied magnetic field, the μSR experiments are identified as zero-field (ZF), transverse field (TF), or longitudinal field (LF) measurements. As shown in Fig. 2.4, the corresponding $P_\alpha(t)$ polarizations are detected in the three cases.

Zero-field μSR experiments

The ZF and LF μSR experiments are performed using similar setups, as shown in Fig. 2.4a. In a static local magnetic field, \mathbf{B} , the muon spin rotates around \mathbf{B} , and it yields (see Fig. 2.5)

$$P_z(\mathbf{B}, t) = (\sin^2(\theta)) + (\cos^2(\theta)) \cos(\gamma_\mu |\mathbf{B}_{\text{loc}}| t). \quad (2.24)$$

In a powdered ordered magnet, this field is centered at a constant value, ω_0/γ_μ with a distribution width of Δ/γ_μ , thus, the distribution is $p(B) = \mathcal{N}(\omega_0/\gamma_\mu, (\Delta/\gamma_\mu)^2)$, yielding a polarization

of [228, 229]

$$P_z(t) = \frac{1}{3} + \frac{2}{3} \exp\left(-\frac{\Delta^2 t^2}{2}\right) \cos(\omega_0 t). \quad (2.25)$$

Here, the constant, 1/3-component originates from the muons in the direction of the magnetic field, and the rotating part is an indication of magnetic ordering. In the absence of ordering, i.e., in the paramagnetic state, the internal magnetic field distribution comes from the nuclear dipole contribution centered at zero: $p(B) = \mathcal{N}(0, (\Delta/\gamma_\mu)^2)$. The so-called Kubo-Toyabe function³ then reads [230, 231]

$$P_z(t) = \frac{1}{3} + \frac{2}{3} (1 - \Delta^2 t^2) \exp\left(-\frac{\Delta^2 t^2}{2}\right). \quad (2.26)$$

As shown in Fig. 2.6, Eq. 2.26 describes a function that is a Gaussian at short times, and displays a minimum value at $\Delta \cdot t \approx \sqrt{3}$, indicative of an oscillation around the nuclear dipole fields. In general, these nuclear dipole fields are quite weak with $\Delta/\gamma_\mu \approx 0.1$ mT. For $t \rightarrow \infty$, the Kubo-Toyabe function converges to 1/3 (known as the 1/3-tail).

For the dynamic local fields, the *strong collision* model is used that assumes that all memory of the previous time evolution is lost after a given collision. Each collision takes place after a characteristic time of τ_c , i.e., with a characteristic frequency of $\nu = 1/\tau_c$. In case of slow dynamical processes, the Kubo-Toyabe evolution is preserved between the collisions, and the overall time dependence follows $P_z(t) \propto \exp(-(2/3)t/\tau)$ decay of the 1/3-tail. Generally, the exact $P_z(t)$ function is too complicated and it is calculated numerically, except for simple cases, e.g., the Abragam [232] and the generalized Abragam formula, i.e., the Keren function [233].

The Abragam formula, which was first calculated for the NMR lineshape, provides analytical form for moderately dynamic processes with $\Delta \cdot \tau \approx 1 - 5$ [234], and it is given as

$$P_z(T) = \exp\left(-\frac{2\Delta^2}{\nu^2} [\exp(-\nu T) - 1 + \nu T]\right). \quad (2.27)$$

For $\nu/\Delta \gg 1$, i.e., in the fast fluctuating limit Eq. 2.27 converges to

$$P_z(t) = \exp\left(-\left(\frac{2\Delta^2}{\nu}\right)t\right) = \exp(-\lambda_z t). \quad (2.28)$$

Here, the relaxation rate, $\lambda_z = 2\Delta^2/\nu$ is in the motional narrowing limit known from NMR, and the $P_z(t)$ is a relaxation function with very slow depolarization in fast fluctuating spin systems [229].

The coexistence of static and dynamic fields is standardly described with the multiplication of the corresponding functions [234].

³The same function is sometimes called static Gaussian Kubo-Toyabe function to emphasize that it originates from a Gaussian field distribution.

Longitudinal-field μ SR experiments

Longitudinal-field μ SR measurements are crucial to identify the quasi-static processes [229] and, particularly in QSLs, the nature of the spin excitations.

In the static limit, the LF Kubo-Toyabe function takes the integral form

$$P_z(\omega_L, \Delta, t) = 1 - \frac{2\Delta^2}{\omega_L^2} \left[1 - \exp\left(-\frac{1}{2}\Delta^2 t^2\right) \cos(\omega_L t) \right] + \frac{2\Delta^4}{\omega_L^3} \int_0^t \exp\left(-\frac{1}{2}\Delta^2 \tau^2\right) \sin(\omega_L \tau) d\tau. \quad (2.29)$$

As shown in Fig. 2.6, Eq. 2.29 defines an oscillating function form with a frequency of ω_L . Once the applied magnetic field, $B = \omega_L/\gamma_\mu$ becomes large enough ($\omega_L \gg \Delta$), the relaxation disappears [79].

In the fast fluctuating limit, there is no field-dependence at low fields. At high fields, as it was shown by Keren [233, 79], the relaxation rate in Eq. 2.28 can be substituted by

$$\lambda_z(\omega_L) = \frac{2\Delta^2\nu}{\omega_L^2 + \nu^2}. \quad (2.30)$$

The markedly different LF dependence in the static and in the dynamic cases provides a method to differentiate them.

Transverse-field μ SR experiments

Application of a transverse magnetic field (\mathbf{B}_\perp) does not create repolarization of the muon asymmetry, instead, it acts as the applied magnetic field in NMR and ESR experiments, thus, it detects T_2^* -processes. In the time domain, it yields a signal oscillating with the Larmor frequency $\omega_L = \gamma_\mu B_\perp$ (see Fig. 2.4b).

Furthermore, weak transverse field experiments are readily applicable to measure the ordered magnetic fraction in magnetic materials, as only the paramagnetic component rotates around \mathbf{B}_\perp , and the frozen part continues to precess around the internal magnetic field.

2.2.4 Muonium formation

In some chemical environments, the positively charged muon may form a neutral, atomic-like muonium state with an electron: $\text{Mu} = \mu^+ e^-$. In this form, the Hamiltonian reads [227]

$$\mathcal{H} = \hbar\gamma_\mu \mathbf{I} \cdot \mathbf{B} + \hbar\gamma_e \mathbf{S} \cdot \mathbf{B} + A\mathbf{S}\mathbf{I}. \quad (2.31)$$

Here, \mathbf{I} and \mathbf{S} are the muon- and electron-spin operators, and A is the hyperfine coupling constant. Thus, this represents a two-level state with a triplet and a singlet state. In large enough magnetic fields, the muon and the electron spin can be decoupled leading to the repolarization of the initial asymmetry [235]. For isotropic muonium, the repolarization

follows

$$P_z(\omega_L) = \frac{1 + 2 \left(\frac{\omega_L}{\omega_{L,0}} \right)^2}{2 \left[1 + \left(\frac{\omega_L}{\omega_{L,0}} \right)^2 \right]}. \quad (2.32)$$

Here, $\omega_{L,0} = 21.4$ MHz ($B_0 = 0.1585$ T) for free muonium, and a large B_0 indicates localized wave function, a small B_0 represents radical formation [236].

In particular, a so-called muonated radical state is formed in organic materials [237]. Here, the hyperfine interaction of the muon and the free electronic spin can be used for the description of the molecular dynamics. As the spin-lattice relaxation is affected by the molecular motion, and it might provoke fluctuations of the isotropic and anisotropic part of the hyperfine interaction, LF data can be utilized to gain information about the dynamical processes [238, 239].

In metals, the muonium formation is not possible as the μ^+ is screened by the surrounding electrons within the Thomas-Fermi screening length [227]. Thus, in metallic systems, the muon is expected to remain in the μ^+ state.

2.2.5 Complementarity of ESR and μ SR

As I reviewed above, ESR is ideal to detect small spin-anisotropies with high precision. μ SR, however, is a local probe, and it provides a mapping of all the possible q -vectors. Furthermore, μ SR does not require the application of magnetic field, hence the system can be measured in an unperturbed environment, giving a unique tool for magnetic measurements. Nevertheless, via the implantation of muons into the structure, the crystal structure is locally modified. In some cases, this local effect was experienced to be rudimentary to the ground state. For example, in KCuF_3 , in a quasi-one-dimensional spin-1/2 chain system, susceptibility measurement was prevented by the local distortion induced by the muon [240]. A further complication of μ SR stems from the unknown μ^+ positions, leading to uncertainty in the analysis of the results, despite the growing interest and successes of the density functional theory (DFT) calculations. In organic systems, this problem is even more relevant due to the large number of possible muon sites, increasing the challenges of numerical methods. In addition, the formation of Mu is a further difficulty, as any conclusion regarding the calculation of the magnetic volume ratio of the long-range ordered phases must take into account the effect of the presence of muonium.

3 Towards disordered QSLs in molecular rotor systems

In Chapter 1, I pointed out that the observation of a quantum critical state does not only require the geometrically frustrated crystal structure and a perfect isotropy of the frustrated magnetic couplings: a number of additional unique material properties are needed to be combined to preserve the QSL behavior at very low temperatures and to host a quantum-entangled state in a correlated electron system. For example, a frequently cited aspect in one- and two-dimensional experimental realizations of QSL candidates is the interplay between magnetic interaction and quenched disorder originating from several distinctive forms, e.g., due to impurities or structural disorder in the magnetic or in the separating layers. To date, however, the disorder came from unintentional imperfections, non-stoichiometric compositions, or from intentionally introduced, destructive defects [150].

In this Chapter, I will present crystalline hybrids of molecular rotor and molecular conductor structures that provide examples of creating mechanical disorder in a fundamentally new way. Relevantly, these materials accommodate at low temperatures slowed down rotors with well-defined stopping positions leading to a complex but controllable low-temperature state. These materials host a vast number of ground states from bulk antiferromagnetic long-range order to the quantum disordered limit. In the following, I will present structural, transport, ^1H NMR, ESR, and μSR studies in this material family. Especially, I will enlighten the magnetic properties of $(\text{EDT-TTF-CONH}_2)_2^+[\text{BABCO}^-]$, a QSL candidate discovered during my PhD research project.

During my research project, I performed the ESR and μSR measurements in the four presented crystalline systems. The ^1H NMR experiments were done by Pawel Wzietek, and he performed the analysis with my contribution. Transport data were acquired by Andrea Pisoni, Edoardo Martino, Konstantins Mantulnikovs, and Luka Ćirić, and I analyzed all these measurements in detail. These experimental results are added to the present thesis to facilitate the global understanding, and to exhibit the complexity of the studied compounds.

3.1 Structure and dynamics of molecular rotor systems

In his visionary talk in 1959, Feynmann proposed building small machines from atoms, such as an infinitesimal machine like an automobile [10]. This complex challenge motivated and inspired the field of organic chemistry to construct molecular machines at the molecular scale. It was achieved via two major routes: one involved the usage of topological entanglement, i.e., mechanical bonds, the other was based on isomerisable (unsaturated) bonds. The pioneers of the two methods, Jean-Pierre Sauvage, James Fraser Stoddart, and Bernard (Ben) L. Feringa were awarded by the Nobel Prize in Chemistry in 2016 "*for the design and synthesis of molecular machines*" [11], such as molecular shuttles [241], molecular elevators [242], and the nanocar [62]. These molecular motor systems [243] are designed to perform movements as a result of external stimuli, e.g., chemical stimulus or light irradiation [244, 245, 246]. In the absence of energy transfer, molecular machines can be constructed as amphidynamic crystals, i.e., systems with a large molecular motility combined with significant phase order [247]. The function to be fulfilled by the rotator and the stator components determines the required crystal structure of each part. In particular, Brownian molecular rotors are designs that are activated by temperature, and that inherently show dipole fluctuations measured by a parametric angle, and demonstrate unidirectional rotations [248, 249].

3.1.1 Microscopic insight

Crystalline molecular rotors provide a unique playground to test the ensemble average behavior of separate molecular parts. The most common technique to study the peculiarities of the rotor systems is ^1H and ^{13}C NMR [247]. In NMR spectroscopy, the spin-lattice relaxation, T_1 , can be dominated by certain dynamic processes if other parts of the crystal are fairly static [64]. If the motion results from a single process, the correlation time of the rapid motion, τ_c , can be determined from the temperature dependence of T_1 via fitting the spin-relaxation time to the Bloembergen-Purcell-Pound (BPP) theory [250, 251], which reads

$$\frac{1}{T_1} = K \left[\frac{\tau_c}{1 + \omega_L^2 \tau_c^2} + \frac{4\tau_c}{1 + 4\omega_L^2 \tau_c^2} \right]. \quad (3.1)$$

Here, $K = (2/3)\gamma^2 \mathbf{B}_{\text{nuc}}^2$ is a constant, corresponding to dipolar interactions related to the relative positions of the participating nuclei with $\mathbf{B}_{\text{nuc}} \propto r^{-6}$ nuclear dipole field, where r is the distance of the two nuclei carrying the dipole moment. Clearly, the relaxation is most efficient if $\tau_c = 1/\omega_L$ leading to a minimum in the spin-relaxation time (see, for example Fig. 3.3). To unravel the microscopic origin of the BPP fitting, NMR studies benefit from the well-established density functional theory (DFT) molecular calculations.

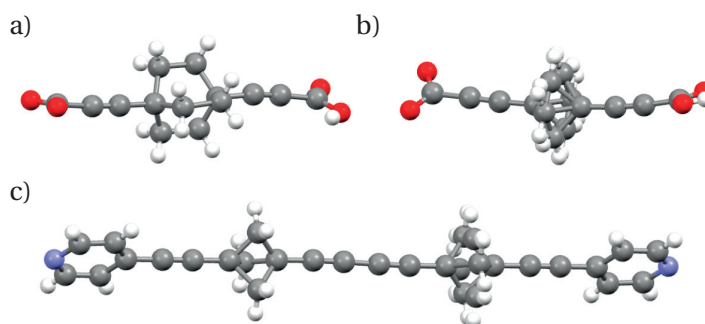


Figure 3.1 – Rotator designs. *a*) BABCO⁻ based on the BCO rotator possessing three different conformational forms leading to a $D_3 \rightleftharpoons D_{3h} \rightleftharpoons D_3$ chirality switch with an energy barrier of 50 K [65, 252]. *b*) HO₂C-CC-BCP-CC-CO₂⁻, based on the BCP rotator. *c*) Building block of crystalline arrays based on the BCP rotator [253].

3.1.2 Crystalline rotor designs

Recently, two rotor components were found to provide ultra-fast rotation at room temperature and enhanced rotor functionalities [65]. The 1,4-bis(ethynyl)-bicyclo[2.2.2]octane (BCO) and 1,3-bis(ethynyl)bicyclo[1.1.1]pentane (BCP) were designed in multiple different forms as shown in Fig. 3.1 [253].

Crystallized rod-like molecules based on BCP or BCO display unusual coupling of the nearby molecules. Due to strong H \cdots H bonds, the neighboring rotors show synchronous gearing motion, and the nearest neighbors function as cogwheel pairs [252, 253]. As the sliding and freely gearing wheels exhibit an energy difference, the sliding one leading to too strong hydrogen bonds, their ratio in the crystal structure remains small. Remarkably, the crystal can be reversibly transformed into a non-gearing design by the virtue of thermal relaxation [254].

The BIBCO molecules that take advantage of the I⁻-based halogen bonding using the BCO component, present a uniquely large rotation frequency due to the ideal crystalline array. The disordered (430 GHz at room temperature) and the ordered layers (77 GHz) possess separate rotational barriers, as found from NMR data and DFT calculations [65]. In a similar halogen bonding-based structure, it was demonstrated through the observation of a phase transition that the number of equilibrium positions largely depends on the available space [255]. In the insulating [*n*Bu₄N⁺]₂[BABCO][BABCO⁻]₂ structure, the BABCO molecules exhibit similar rotation frequencies with two different sites stemming from the disordered and the ordered molecules. In contrast, this Brownian motion is largely braked (leading to two orders of magnitude slower rotation) by the presence of an organic conductor layer in (EDT-TTF-CONH₂)₂⁺[BABCO⁻] [65] (see Fig. 3.7). This slow rotation was explained to result from two channels. Firstly, the BABCO units are placed into an environment with strong H \cdots H bonds leading to a rather large rotational barrier. In addition to this pathway, the low-dimensional electron gas with a large number of degrees of freedom serves as a bath for the dissipation of the energy [65].

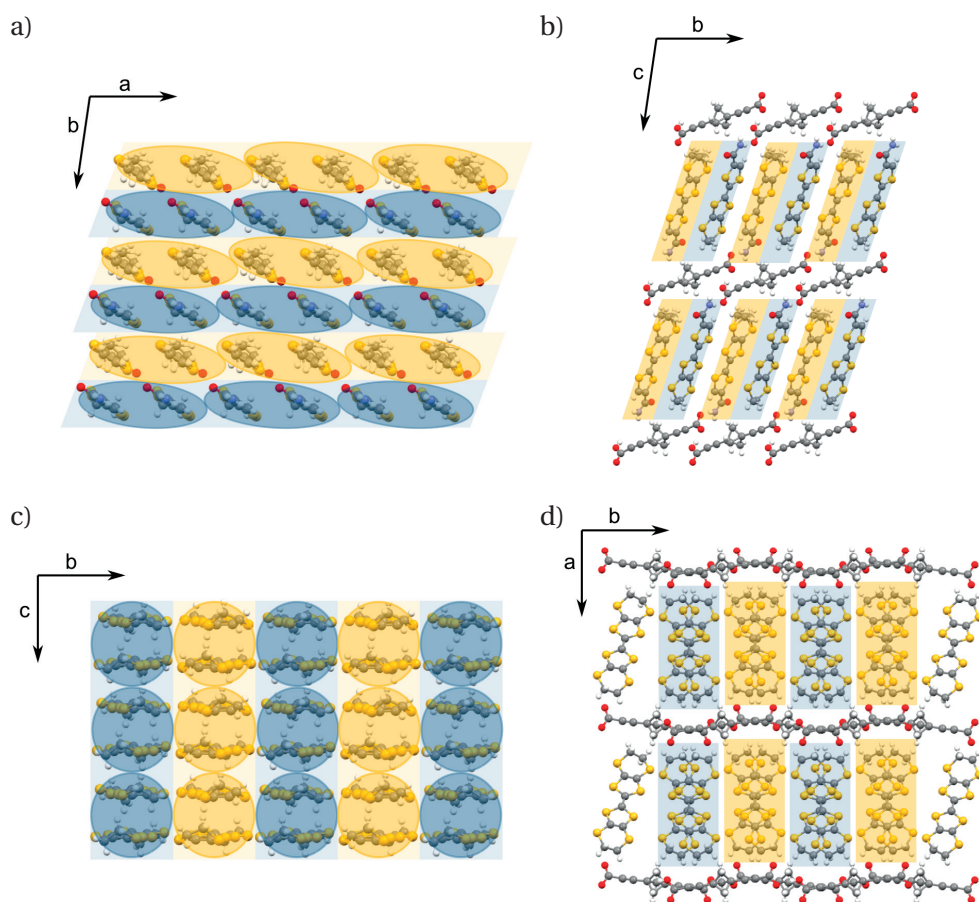


Figure 3.2 – Hybrid conductor-rotor materials with BCP rotators. *a)-b)* Top and side view of the crystal structure of $[\text{EDT-TTF-CONH}_2]_2^+ [\text{HO}_2\text{C-CC-BCP-CC-CO}_2^-]$ showing a dimerized system displaying gapped spin-ladder behavior. Note the closeness of the BCP rotor components to the spin-ladder. *c)-d)* Top and side view of the structure of $[\text{BEDT-TTF}]_2^+ [\text{HO}_2\text{C-CC-BCP-CC-CO}_2^-]$ revealing a strongly dimerized, spin-chain (or weakly coupled rectangular) behavior affected by the BCP rotators.

In the following, I will discuss the crystal structures of my four-year-long study of hybrid conductor-rotor systems.

3.2 Hybrid conductor-rotor systems with BCP rotators

The observation of quantum dissipation in a hybrid system (see above) commenced investigations in a new organic material family, that of the crystalline hybrids of molecular conductors and molecular rotors [65, 256]. This interest stems from the unique interaction of the conducting layer and the molecular rotors, which induces coupling between the Brownian motion of the rotors and the Fermi sea of the conducting system. Thus, it opens the way towards studying the role of rotor systems within the rich phase diagram of organic charge transfer salts.

3.2. Hybrid conductor-rotor systems with BCP rotors

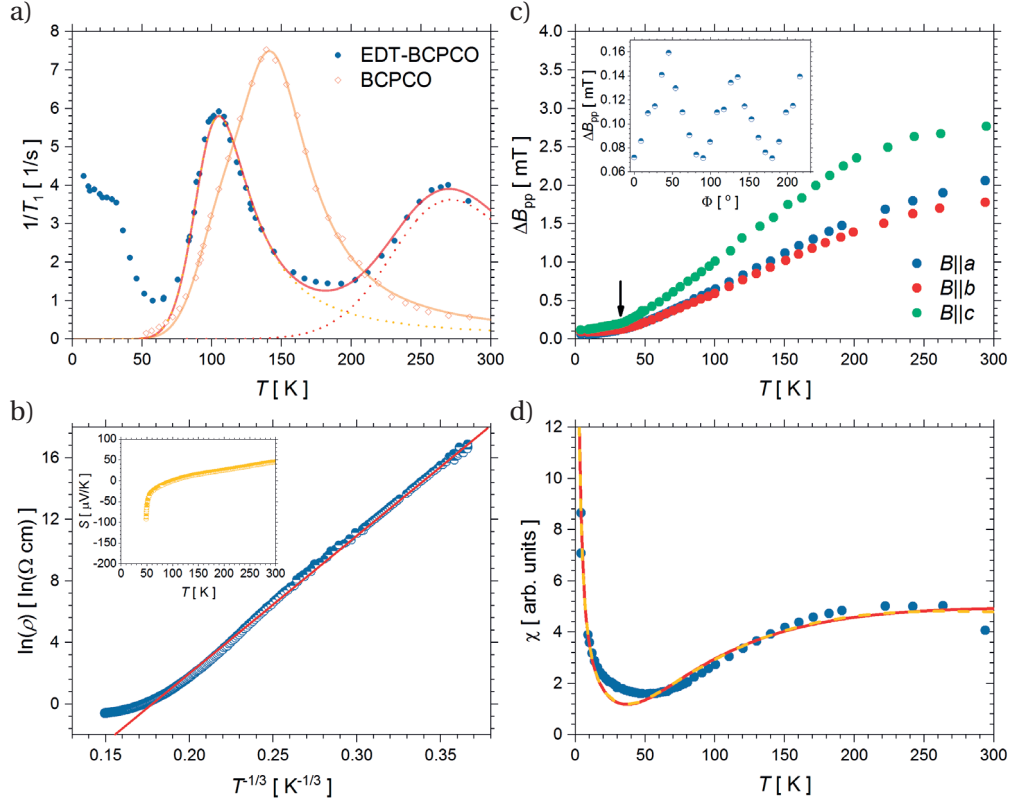


Figure 3.3 – *a*) Inverse ^1H -NMR spin-lattice relaxation rate in crystallized $(n\text{-Bu}_4\text{N}^+)\text{HO}_2\text{C-CC-BCP-CC-CO}_2^-\cdot\text{H}_2\text{O}$ (BCPCO) and in the hybrid system $[\text{EDT-TTF-CONH}_2]_2^+[\text{HO}_2\text{C-CC-BCP-CC-CO}_2^-]$ (EDT-BCPCO). Solid lines are fit to the BPP theory (Eq. 3.1) with two rotational barriers. Dotted lines present the two separate rotational minima in T_1 . *b*) Resistivity of the hybrid system. Solid line is a fit to the VRH model. Inset: Seebeck coefficient pointing to a transition around 50 K. *c*) ESR linewidth in the principal crystallographic directions. The arrow denotes the change of the slope of the linewidth. Inset: The angle dependence of the ESR linewidth at 5 K illustrates that the narrow ΔB_{pp} originates only from the dipole-dipole interactions. *d*) Spin-susceptibility of the hybrid system as measured by ESR spectroscopy demonstrating a gapped, exponential-like decrease. Yellow and red lines are fits to the spin-susceptibility using the low-dimensional antiferromagnetic spin-gapped and the strong-rung spin-ladder models together with a low impurity concentration.

3.2.1 $[\text{EDT-TTF-CONH}_2]_2^+[\text{HO}_2\text{C-CC-BCP-CC-CO}_2^-]$, a spin-gapped system

The crystalline hybrid system $[\text{EDT-TTF-CONH}_2]_2^+[\text{HO}_2\text{C-CC-BCP-CC-CO}_2^-]$ possesses a layered structure (see Fig. 3.2), where dimers of the EDT-TTF-CONH₂ molecule jointly donate one electron to the HO₂C-CC-BCP-CC-CO₂⁻ rotor. According to the DFT calculations, the dimers are created from the equivalent EDT-TTF-CONH₂ molecules, i.e., from *A* – *A* and *B* – *B* pairs. The strong H ··· H bonds between the EDT-TTF-CONH₂ dimers and the rotors lead to a strong interaction between the two layers and it induces cooperative behavior between them.

Comparison of the present layered structure and the crystalline rotor comprised only of the (HO₂C-CC-BCP-CC-CO₂⁻) molecules ($(n\text{-Bu}_4\text{N}^+)\text{HO}_2\text{C-CC-BCP-CC-CO}_2^-\cdot\text{H}_2\text{O}$) should provide detailed and relevant information on the nature of the searched interaction. As shown in

Chapter 3. Towards disordered QSLs in molecular rotor systems

Fig. 3.3a, the spin-lattice relaxation rate (T_1^{-1}) measured using ^1H NMR, indicates that two different rotational barriers are present in both systems. Fit to the BPP theory (see Eq. 3.1) reveals that in the insulating material, the two, coupled rotational barriers are $E_{a,1}/k_B = 600$ K and $E_{a,2}/k_B = 1160$ K. In contrast, the two thermally activated Arrhenius processes in the hybrid system possess barriers of the size of $E_{a,1}/k_B = 650$ K and $E_{a,2}/k_B = 1750$ K.

The ratio of the two different sites with slightly different rotational barriers in the two systems are of interest for the identification of the rotational modes. As measured by the intensity ratio of the two corresponding fits to the Arrhenius processes, a rather similar ratio is found in the two systems: $I_1/I_2 \approx 2/3$. The characteristically different rotational barriers, however, reveal differing origins of the rotational modes. In $(n\text{-Bu}_4\text{N}^+)\text{HO}_2\text{C-CC-BCP-CC-CO}_2^-\cdot\text{H}_2\text{O}$, the coupled rotational barriers stem from perpendicularly oriented, interacting BCP rotators, rotating separately on orthogonal axes. In the conducting hybrid system, only the lower rotational barrier is present due to the BCP. The higher barrier is an indication of jumps in-between two equilibrium positions of the EDT-TTF- CONH_2 molecules corresponding to two different conformations (as confirmed from X-ray diffraction data). Below 50 K, the molecular rotation is completely stopped in both systems, only a slowly growing, impurity-related signal can be identified at low temperatures in the hybrid sample.

The inverse effect, i.e., the impact of the rotors upon the conducting layer can be accounted for by transport and ESR measurements. The strong two-dimensionality of the conducting system is well demonstrated by the temperature dependence of the resistivity as shown in Fig. 3.3c. Whereas the DFT calculations suggest a two-dimensional hole-doped metallic band structure, owing to the strong disorder resulting from the presence of the rotor components, the in-plane resistivity is best described by the two-dimensional Variable Range Hopping model, which reads [257]

$$\rho(T) = \rho_0 \exp \left[\left(\frac{T_0}{T} \right)^{\frac{1}{d+1}} \right], \quad (3.2)$$

where $d = 2$ is the dimensionality of the system¹.

Temperature dependence of the Seebeck coefficient (S , thermoelectric power) exhibits hole-doped metallic-like behavior above $T = 50$ K, as it occurs to possess a weak temperature dependence that approaches towards 0 (see Fig. 3.3c). Below 50 K, however, S changes sign and becomes unmeasurably large. Quite remarkably, this transition takes place at a similar temperature where the Brownian motion of the rotor components is seen to be stopped in NMR data demonstrating that the influence of the rotors plays a crucial role in the charge carrier dynamics. As in most organic materials [258], this transition might result from two different scenarios: *i*) it may be an indication of a metal-insulator transition induced by the rotors or *ii*) the high-temperature small Seebeck coefficient could point to a disorder-induced S of a semiconductor where the interplay with the rotational component leads to a disordered

¹The parameter $T_0 = \xi^3/D(E_F)$, where $D(E_F)$ is the density of localized states and ξ is the hopping range.

charge carrier diffusion.

To distinguish these two possibilities, X-band ESR measurements were carried out in [EDT-TTF-CONH₂]₂⁺[HO₂C-CC-BCP-CC-CO₂]⁻. The ESR measurements are summarized in Fig. 3.3c and d. The temperature-dependent spin-susceptibility, $\chi_s(T)$, provides substantial information to determine the nature of exchange coupling in low-dimensional, magnetically coupled systems [259]. As it can be seen in Fig. 3.3d, the ESR intensity shows a clear exponential-like decrease below 200 K, and a Curie-component at very low temperatures stemming from a small $S = 1/2$ impurity concentration [260, 261]. The impurity-dominated term comes into play only below 50 K where the ¹H NMR data showed the stopping of the rotor components. As χ_s becomes dominated by the first term, the ESR linewidth, ΔB_{pp} , shows a clear change of the slope at the same temperature range. With the increase of the rotation frequencies at higher temperatures, the ESR linewidth, as a measure of the fluctuation rate, continues to grow as a function of temperature. At the lowest temperatures, as it is demonstrated in the inset of Fig. 3.3c, ESR measurements can only detect the impurity-related signal. Thus, the ESR measurements identify the transition at 50 K as the appearance of an impurity-dominated behavior. These observations clearly exclude a possible metal-insulator transition as assumed from the thermoelectric power data.

Relevantly, the rapid suppression of χ_s may be related to a strongly dimerized low-dimensional antiferromagnetic system following a temperature dependence [262]

$$\chi_s(T) = \mu_0 \cdot \frac{3}{4} \cdot g^2 \mu_B^2 \cdot \left(\frac{N_{\text{imp}}}{T} + N_{\text{spin-gap}} \sqrt{\frac{\Delta}{k_B T}} \exp^{-\frac{\Delta}{k_B T}} \right). \quad (3.3)$$

Here, the singlet-triplet gap, Δ , is found to be $\Delta/k_B \approx 180$ K, lower than it was in a 1:1 acid/zwitterion hybrid [263]. The ratio of the impurity concentration and the spin-gap term is measured to be $N_{\text{imp}}/N_{\text{spin-gap}} = 1.1\%$, which demonstrates a very low impurity concentration. Thus, χ_s proves the low-dimensional magnetic behavior. This intriguing observation can be satisfied by a number of different spin models amongst the dimerized systems [264]. Notably, two well-established alternatives are *i*) the alternating spin-chain systems, where the subsequent antiferromagnetic interactions within the spin chain have interaction strengths of J and αJ with $0 < \alpha < 1$ and *ii*) the spin-ladder models where two parallel spin chains characterized by the J_{rail} interaction, are coupled via the interchain interaction of size J_{rung} . Analytic expressions fitted to χ_s for the alternating chain and the spin-ladder models [265] showed clearly that the best fit is achieved when using the strong-*rung* ladder model, revealing that the interchain interactions are rather strong in this system. As depicted in Fig. 3.3d, $J_{\text{rail}}/k_B = 305$ K and $J_{\text{rung}}/k_B = 340$ K (with an impurity concentration of $N_{\text{imp}}/N_{\text{spin-ladder}} = 1.5\%$) yield a similar overall description as the spin-gap model defined in Eq. 3.3. Notably, the absolute spin-susceptibility measured by the two models in Fig. 3.3d differs only by 20%, i.e., it is well below the precision of the ESR spin-susceptibility calibration.

Structurally, the alternating chain model would only be viable if the BCP rotators provided

sufficient local alternation of the exchange interaction to maintain a quasi-continuous perturbation along the chain. Nevertheless, DFT calculations confirm that the described strong-rung spin-ladder model might be a valid explanation. It was shown that for every second chain the $A - B$ interactions along the chains are comparable to the $A - A$ and $B - B$ interactions within the chain, whereas every other second $A - B$ interactions are significantly lower. Thus, even if it were tempting to relate the large interchain coupling to a rectangular model, based on the DFT results I propose that the strongly interacting A and B chain pairs build up a gapped spin-ladder compound. As the larger $A - B$ interactions are closer to the BCP rotator component, the disorder might contribute to the absence of low-temperature magnetic ordering.

To conclude, this material demonstrates that the BCP rotator affects substantially the low-temperature behavior of the system and leads to a gapped spin-liquid spin-ladder compound.

3.2.2 [BEDT-TTF]₂⁺[HO₂C-CC-BCP-CC-CO₂⁻], an antiferromagnet with $T_N = 20$ K

As shown in Fig. 3.2, the hybrid system [BEDT-TTF]₂⁺[HO₂C-CC-BCP-CC-CO₂⁻] has a similar layered structure with one hole per dimer of [BEDT-TTF]₂, and the same anion rotators, [HO₂C-CC-BCP-CC-CO₂⁻]. DFT calculations showed that the dimerization takes place again in-between the $A - A$ and $B - B$ dimers, and the system becomes one-dimensional with a moderately strong interchain coupling. This theoretical finding is in good agreement with the measured transport properties. The electrical resistivity can be fitted to an activated behavior, $\rho(T) = \rho_0 \exp(E_a/k_B T)$, with an activation energy of $E_a/k_B \approx 2200$ K, as depicted in Fig 3.4*b*. The Seebeck coefficient gives a large value close to room temperature, and grows continuously with cooling. Below 280 K, it is not measurable anymore.

In the observed strongly one-dimensional insulator state, ESR and ¹H-NMR data identify the evolution of a low-temperature magnetic state. To emphasize this, here, I focus on $(T_1 T)^{-1}$, the NMR inverse spin-lattice relaxation rate multiplied by the temperature. In general, the spin contributions to $(T_1 T)^{-1}$ can be written as [266, 267]

$$(T_1 T)^{-1} = \frac{2\gamma_n^2 k_B}{g^2 \mu_B^2} \sum_{\mathbf{q}} |A_0|^2 \frac{\chi''(\mathbf{q}, \nu_n)}{\nu_n}, \quad (3.4)$$

where γ_n is the nuclear gyromagnetic ratio, A_0 is the contact coupling, and $\chi''(\mathbf{q}, \nu_n)$ is the dynamical electron spin-susceptibility. In the simplest cases, $(T_1 T)^{-1}$ can be considered to be proportional to the electronic spin-susceptibility: $(T_1 T)^{-1} \propto \chi_0(\omega)$.

Fig 3.4*a* presents $(T_1 T)^{-1}$ as a function of temperature, and it reveals two relevant temperature regimes: one above 100 K and one below it. In accordance with this, the best fit to this spin-susceptibility is achieved with the sum

$$\chi_0 \propto \frac{1}{T + \theta_{CW}} + \frac{1}{T - T_N} + \chi_{KT}. \quad (3.5)$$

3.2. Hybrid conductor-rotor systems with BCP rotators

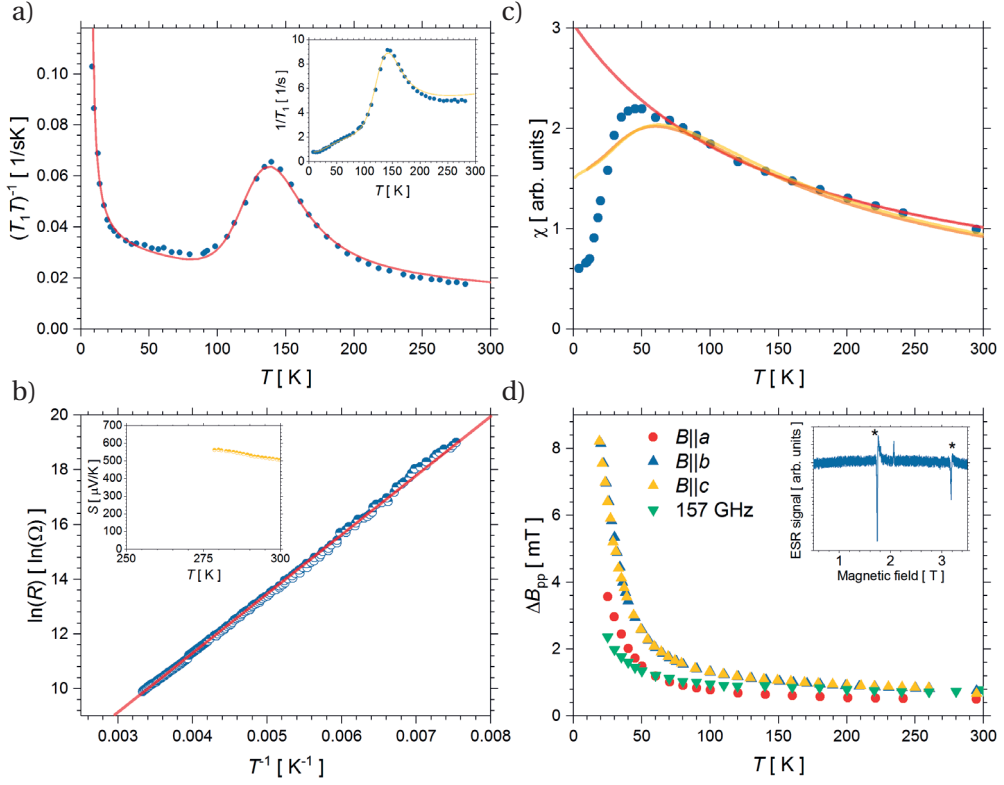


Figure 3.4 – Experimental results in the hybrid system $[\text{BEDT-TTF}]_2^+ [\text{HO}_2\text{C-CC-BCP-CC-CO}_2]^-$. *a)* Temperature dependence of the nuclear spin lattice relaxation rate divided by temperature, $(T_1 T)^{-1}$, from $^1\text{H-NMR}$. Solid line is a fit as explained in the text. Inset: Inverse spin-lattice relaxation rate. Solid line is the same fit as in the main figure. *b)* Arrhenius plot of the resistivity of the hybrid system. Solid line is a fit to an activated behavior with $\Delta/k_B = 2200$ K. Inset: Seebeck coefficient measured close to room temperature presenting large values. *c)* Spin-susceptibility as measured by X-band ESR. Solid lines are Curie-Weiss fit with $\theta_{\text{CW}} = -150$ K (red), the Bonner-Fisher curve (yellow) with $J/k_B = 97$ K (see Eq. 3.6), and the rectangular model (brown) with $J_1/k_B = 94$ K and $J_2/J_1 = 7\%$. *d)* ESR linewidth above the Néel temperature in the principal crystallographic direction $B \parallel a$ at 9.4 GHz and 157 GHz frequencies indicating antiferromagnetic fluctuations. Inset: Antiferromagnetic resonance at 157 GHz and at 3 K. The asterisks denote the two AFMR modes that disappear above T_N . The third line comes from an impurity and is not perturbed by T_N .

Here, the first term corresponds to the antiferromagnetic interactions (with $\theta_{\text{CW}} = 350$ K) highlighting the strong antiferromagnetic fluctuations. The second term tests the critical regime above the antiferromagnetic transition (with a fitted $T_N = 5$ K), and the third term (χ_{KT}) is a fit to the BPP theory at high temperatures.

To see the relevance of the terms independently, the corresponding temperature regimes need to be investigated separately. At the high-temperature regime, around 150 K, the spin-lattice relaxation points to a minimum related to a rotational barrier of $E_a/k_B \approx 970$ K indicating similarities with the case presented in Section 3.2.1 (see the inset of Fig 3.4a). Here again, the low-temperature rotational barrier is found to remain unperturbed by the presence of the conducting molecular layer, and the barrier at higher temperatures appears to be completely

missing below 300 K. This missing T_1 -minimum is in line with a single crystallographic position of the BCP rotators in the hybrid system. Below 100 K, once the rotational component is frozen out, the inverse spin-lattice relaxation is dominated by the local electronic magnetization, and the antiferromagnetic state starts to play a role.

Multi-frequency ESR data confirmed the high-temperature emergence of antiferromagnetic fluctuations and the low-temperature antiferromagnetic ordering. As depicted in Fig. 3.4c, the spin-susceptibility can be well approximated with a Curie-Weiss term at high temperatures with $\theta_{CW} = -150$ K pointing to strong antiferromagnetic nearest-neighbor interactions. Nevertheless, it was shown that the Curie-Weiss temperature may be an overestimate of the strength of the exchange coupling [158], and it can only provide qualitative information in low-dimensional systems. As it was seen in other uniform Heisenberg spin-1/2 chains, the Bonner-Fisher curve can be used to give a theoretical estimate of the exchange coupling J along the chain [268]. To fit χ_s , I apply a numerical estimate using a Padé polynomial in the form [269]

$$\chi = \frac{N_A g^2 \mu_B^2}{4k_B T} \cdot \frac{1 + \sum_{n=1}^5 \left(\frac{J}{k_B T}\right) N_n}{1 + \sum_{n=1}^6 \left(\frac{J}{k_B T}\right) D_n}. \quad (3.6)$$

Here, the N_n and D_n coefficients are tabulated in Ref. [269]. As explained in Section 3.2.1, due to the small sample size, the absolute spin-susceptibility determined experimentally ($\chi_s = 9.4 \cdot 10^{-4}$ emu/mol) is not precise enough to directly compare to the absolute χ_s given in Eq. 3.6. Instead, the ESR spin-susceptibility was used as an output for numerical fitting. As shown in Fig. 3.4d, the best fit gives $J/k_B = 97$ K (with only 10% difference in the fitted absolute value). DFT calculations showed that the interchain interaction is non-zero in the present system, too. Thus, it would be expected that the interchain interaction, J' , might contribute to the spin-susceptibility. Fitting χ_s to the rectangular $J_1 - J_2$ model [270, 271], demonstrated that a similarly good fit can be achieved to describe the peak structure with $J_1/k_B = 94$ K and the ratio $J_2/J_1 = 7\%$. The rather weak interchain coupling is in agreement with the DFT results. In contrast to $[\text{EDT-TTF-CONH}_2]_2^+ [\text{HO}_2\text{C-CC-BCP-CC-CO}_2]^-$, the BCP rotators are structurally positioned in a way that there is no asymmetry in every second $A - B$ dimer interactions, the spin-ladder model can be excluded.

The measured χ_s reaches a maximum around 45 K, and short-range ordering commences to appear below this temperature. In parallel, both the resonant field shift (not shown) and the ESR linewidth (see Fig. 3.4d) indicate antiferromagnetic fluctuations below 50 K. Despite the unique sensitivity of ESR, it is intriguing that the antiferromagnetic fluctuations appear at temperatures as high as at 150 K. For example, in $(\text{TMTSF})_2\text{X}$ ($\text{X} = (\text{AsF}_6, \text{PF}_6, \text{Br})$) three-dimensional fluctuations were only detected 2 K above T_N [272]. Nevertheless, in the spin-chains δ - $(\text{EDT-TTF-CONMe}_2)_2\text{X}$ ($\text{X} = (\text{AsF}_6, \text{Br})$) [273, 274] the linewidth was found to manifest an increase at similarly high temperatures. Therein, it was found to be independent of the structural transition at 10 K. Here, as well, it can be speculated not to stem from the presence

of the BCP rotators.

To explain the emergence of antiferromagnetic fluctuations at these very high temperatures, two models may be quoted [274]. In the case of dipole-dipole fluctuations, the critical temperature dependence would follow a power-law behavior, where the power μ of the ΔB_{pp} -increase is determined by the dimensionality d of the fluctuations $\mu = 3 - \frac{d}{2}$ [275]. However, the measured broadening has a too weak temperature dependence, much slower than any power-law shooting to infinity at T_N . Nevertheless, the dimensionality of the linewidth increase can be determined when comparing the temperature dependencies in the three crystallographic directions. The similarity of the T -dependence of the three directions indicates that the fluctuations are three-dimensional.

Alternatively, as I presented in Section 2.1.3, the low-field Oshikawa-Affleck theory would be able to describe the critical region (see Eq. 2.21) arising due to quantum fluctuations for systems with staggered magnetization. As I will explain in detail in the case of EDT-BCO (Section 3.4) and for κ -Ag (Chapter 4), symmetry considerations imply that the *staggered* DM component is absent in the crystallographic b direction due to the presence of a glide symmetry operation, only a *uniform* DM can be found here. Thus, ΔB_{pp} measured in this direction gives the highest contribution to the staggered magnetization. Hence, it would be expected to have a strong ($\Delta B_{pp} \propto B^2$) field dependence. This is absent as it is visible from the comparison of ΔB_{pp} at 9.4 GHz and at 157 GHz (see Fig. 3.4d).

Thus, both of the mentioned models fail to explain quantitatively the T -dependence of ΔB_{pp} while approaching T_N . Like in δ -(EDT-TTF-CONMe₂)₂AsF₆ [274], it cannot be concluded where this non-trivial temperature dependence of the broad fluctuating regime stems from. In the present case, it is intriguing that the fluctuations appear already at temperatures of J/k_B , the large coupling measured in the chain direction. Thus, the observed linewidth increase might be related to the strong interchain antiferromagnetic fluctuations that result in bulk three-dimensional antiferromagnetic order only at temperatures below the interchain exchange interaction. In fact, both DFT calculations and fits to χ_s showed that the interchain J' is only an order of magnitude smaller than J . In this unfrustrated, rectangular system, it is not surprising that the two-dimensionality does not prevent the formation of an antiferromagnetically ordered system.

The ESR linewidth has a maximum at ~ 20 K, and it starts to decrease below it, revealing a phase transition, which turns out to be a three-dimensional antiferromagnetic state with $T_N \approx 20$ K. Angle-dependent studies at 9.4 GHz uncovered that the low-temperature ESR signal (not shown here) does not follow the crystallographic orientation of the studied sample, therefore, it is not an intrinsic impurity in the crystal. Differently from the low-temperature paramagnetic signal found in δ -(EDT-TTF-CONMe₂)₂AsF₆ [276] and in (EDT-TTF-CONH₂)₆⁺[O₂C-CC-BCO-CC-CO₂⁻](CH₃OH)₂ (see Section 3.3.1), the low-temperature paramagnetic signal is independent of the crystal structure, it only senses the formation of a three-dimensional AFM state.

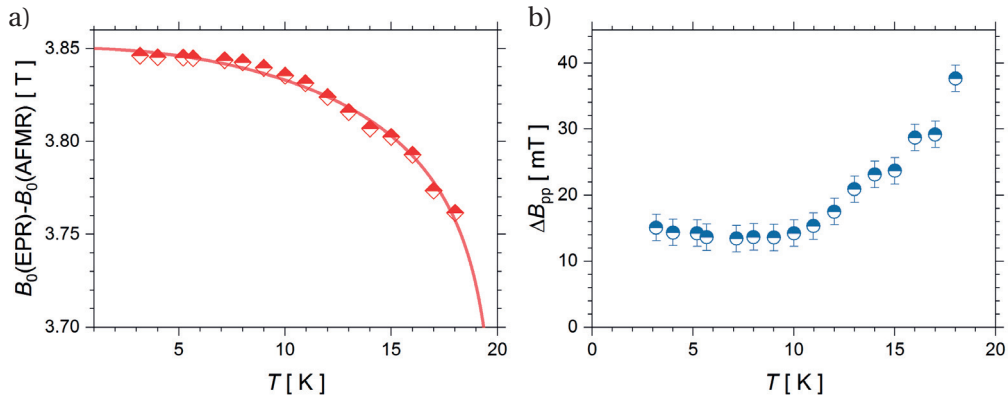


Figure 3.5 – Temperature dependence of one of the AFM resonance modes in [BEDT-TTF]₂⁺[HO₂C-CC-BCP-CC-CO₂]⁻ at 157 GHz in the $B \parallel b$ direction. *a)* Temperature dependence of the resonant field of the AFM resonance mode as compared to the $g = 2$ EPR position. The solid line is a fit to the local internal field using Eq. 3.7 indicating a low-temperature behavior with $\alpha = 1.8$. Note that the broadening of AFMR prevents the determination of β that is most relevant close to T_N . *b)* Temperature dependence of the linewidth of the AFM resonance mode revealing constant linewidth up to $T = 10$ K, and a critical T -dependence close to T_N .

It is noticeable that T_N measured by ¹H-NMR ($T_N = 5$ K) and that measured by ESR ($T_N = 20$ K) differ significantly. Both methods detect the bulk antiferromagnetic order, however, single crystals were measured in ESR, whereas ¹H-NMR studies required polycrystalline samples. The quite large T_N -difference could be explained by different defect concentrations in the samples with different morphology. Nevertheless, this explanation is not plausible in this system, as both low-temperature ¹H-NMR and ESR revealed a small defect concentration. Furthermore, T_N did not show sample-to-sample variation in high-field ESR data. This demonstrates that the observed differences do not stem intrinsically from the difference of the crystal morphology. Instead, it was demonstrated that the susceptibility, measured by ¹H-NMR, can be better fitted with a distribution of T_N values within the crystal. Thus, the long-range ordering does not take place at a fixed temperature but in a wide temperature range. Remarkably, this striking effect is probably provoked by the random, independent stopping positions of the BCP rotators, leading to low-temperature quenched disorder, and ordering temperatures differing at microscopic length scales.

Low-frequency ESR was unable to detect the AFM resonance modes below T_N . Favorably, the AFMR modes could be followed using the high-frequency setup. At 157 GHz, two AFMR lines were found in the $B \parallel b$ direction at magnetic fields much lower than the resonant field expected for paramagnetic impurities with $g = 2$ (see the inset of Fig. 3.4*d*). To unravel in detail the characteristics of the AFM state, temperature-dependent studies were performed at 157 GHz. Fig. 3.5 presents the temperature evolution of the resonant field and the AFMR linewidth. The AFMR remains unperturbed up to 10 K with a nearly constant position and linewidth. Both measurables start to reveal a critical behavior above this temperature, and explode close to T_N . The low-temperature change of the resonant field, as a measure of the

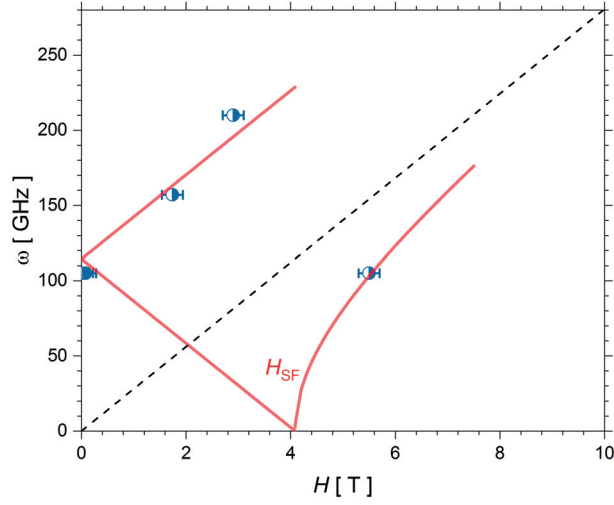


Figure 3.6 – Magnetic field-frequency mode diagram of an AFM resonance mode in $[\text{BEDT-TTF}]_2^+ [\text{HO}_2\text{C-CC-BCP-CC-CO}_2^-]$ measured at $T = 6$ K in the $B \parallel b$ direction. Solid lines are fits to Eq. 2.15, with a spin-flop field of $H_{\text{SF}} = 4.1(1)$ T. Dashed line corresponds to the resonant field of $g = 2$ EPR signals. Note that the second AFMR found at 157 GHz could not be identified at other frequencies. The error bars correspond to the width spread of each signal.

local internal field, was fitted to the conventional expression of

$$\frac{B_{\text{loc}}(T)}{B_{\text{loc}}(0)} = \left[1 - \left(\frac{T}{T_N} \right)^\alpha \right]^\beta. \quad (3.7)$$

Here, $B_{\text{loc}}(T)$ and $B_{\text{loc}}(0)$ measure the local internal field at temperature T and zero temperature, respectively. α and β describe the $T \rightarrow 0$ and $T \rightarrow T_N$ temperature dependence of the local internal field, respectively. Eq. 3.7 approximates well the Brillouin function in the vicinity of T_N and at very low temperatures via fitting the two components with the α and β critical exponents. Due to the critical increase of the linewidth in the vicinity of T_N , only α can be determined from the AFMR T -dependence, which was found to be best described with $\alpha = 1.8$ as shown in Fig. 3.5.

The multi-frequency ESR method proved to be a powerful tool in the AFM state, as it unveiled the magnetic field-frequency mode diagram. Fig. 3.6 displays both the resonant field positions and the calculated mode dispersion (using the expressions given in Eq. 2.15) corresponding to data along the easy-axis, in this case, in the $B \parallel b$ direction. It is evident that the AFMR was hindered in the low-frequency measurements (limited to < 1.5 T) due to the large spin-flop field, $H_{\text{SF}} \approx 4.1$ T. Quite remarkably, the presented data covers three different branches, which makes the determination of the separate branches exceptionally precise. In addition, the mode dispersion calculation confirms that the DM interaction is rather weak in the system. In fact, the mode dispersion close to the spin-flop field is expected to show a gap in the presence of DM, which is absent in the present case.

To summarize, the three-dimensional antiferromagnetic ordering in this spin-chain system is

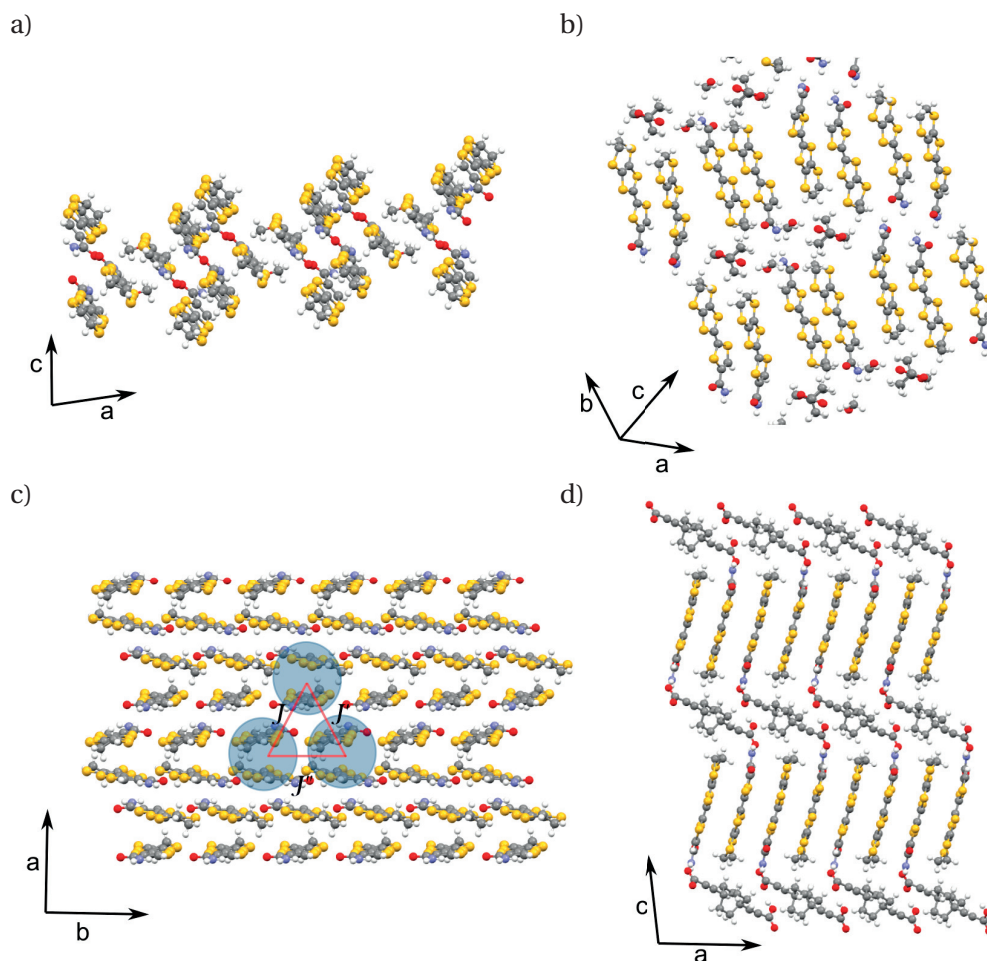


Figure 3.7 – Hybrid conductor-rotor materials with BCO rotator. *a)-b)* Top and side view of the crystal structure of $(\text{EDT-TTF-CONH}_2)_6^+[\text{BABCO}^-](\text{CH}_3\text{OH})_2$ indicating strong interaction of the cation layer with the BCO rotators. *c)-d)* Top and side view of the the crystal structure of $(\text{EDT-TTF-CONH}_2)_2^+[\text{BABCO}^-]$ having a strongly dimerized ($A-B$), two-dimensional anisotropic triangular lattice structure possessing strong $J : J' : J'' = 216 \text{ K} : 131 \text{ K} : 356 \text{ K}$ exchange couplings [65]².

set by the quenched disorder due to the stopped rotor positions, resulting in microscopically distributed ordering temperatures.

3.3 Hybrid conductor-rotor systems with BCO rotators

As in the case of the BCP rotators, the BCO rotators provide, as well, vast possibilities to unravel both the role of the low-temperature disorder and the high-temperature viscous motion of the components. If the BCO rotator is placed into a structurally restricted space, or its rotation is slowed down by cooling, it might result in an increased disorder compared to the BCP rotator. Furthermore, it has been shown that the BCO rotator has three different conformational

² a^* , b^* , and c^* are close to the a , b , and c directions, as $\alpha = 90^\circ$, $\beta = 97^\circ$, and $\gamma = 90^\circ$.

3.3. Hybrid conductor-rotor systems with BCO rotators

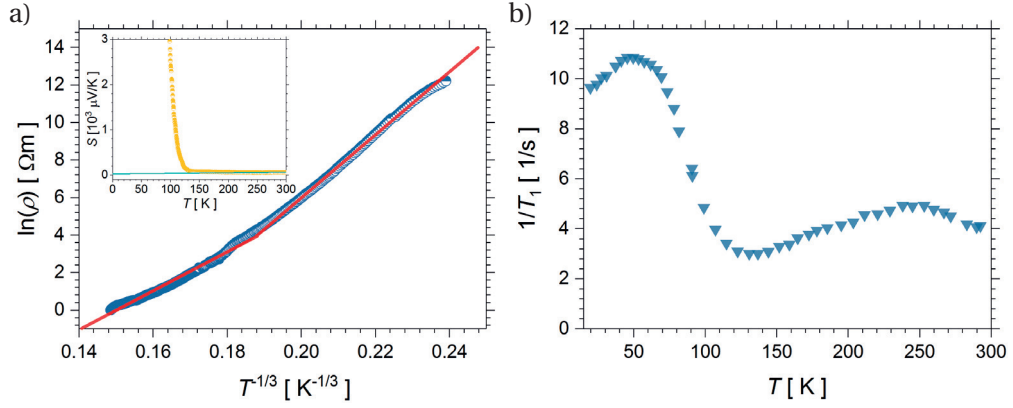


Figure 3.8 – Transport properties of $(\text{EDT-TTF-CONH}_2)_6^+[\text{BABCO}^-](\text{CH}_3\text{OH})_2$. *a*) Resistivity is shown to fit to the VRH both below and above the metal-insulator transition ($T_{\text{MI}} = 120$ K). Inset: Seebeck coefficient indicating metallic behavior above T_{MI} and a sudden increase below it. Solid line is a fit above T_{MI} highlighting the metallic behavior. *b*) Inverse $^1\text{H-NMR}$ spin-lattice relaxation exhibiting impeded motion in the metallic phase followed by a release of rotor motion below T_{MI} .

forms [277]. One is related to the D_{3h} point symmetry, and the other two to the right- and left-twisted D_3 symmetries. This torsional motion of the three blades drives the $D_3 \rightleftharpoons D_{3h} \rightleftharpoons D_3$ chirality switch with an approximately 50 K barrier [252], which gives additional, random disorder in the BCO-based hybrid conductor-rotor materials. As we will see in the following, this additional complexity will contribute to reach even more complicated systems.

3.3.1 Impeded motion in $(\text{EDT-TTF-CONH}_2)_6^+[\text{BABCO}^-](\text{CH}_3\text{OH})_2$

$(\text{EDT-TTF-CONH}_2)_6^+[\text{O}_2\text{C-CC-BCO-CC-CO}_2^-](\text{CH}_3\text{OH})_2$ differs from the other three compounds described in the present Section, as it only carries one spin per three dimers of $(\text{EDT-TTF-CONH}_2)_2$. Clearly, in an insulator state, it reduces the possibility of the formation of a magnetic state given that it is rather far from the half filling, thus, the probability of nearest neighbors possessing a spin decreases significantly. Regarding the anion layer, the structure hosts two additional $(\text{CH}_3\text{OH})_2$ groups for each $[\text{O}_2\text{C-CC-BCO-CC-CO}_2^-]$.

Electrical resistivity, measured on single crystals, is depicted in Fig. 3.8*a*. In accordance with the disorder and randomness expected from the structure, $\rho(T)$ follows the Variable Range Hopping model, as described by Eq. 3.2. This behavior can be assigned to the disorder due to the rotor motion. In agreement with this disordered state, at high temperatures the Seebeck coefficient is low (with $S = 57 \mu\text{V/K}$ at room temperature). The thermoelectric power remains low and constant down to ~ 120 K, where it shoots to infinity. As in Section 3.2.1, in the present BCO-based system either a metal-insulator transition takes place at $T_{\text{MI}} = 120$ K or a disorder-related phenomenon is observed from the thermoelectric power.

The metal-insulator transition is easily followable from $^1\text{H NMR}$ measurements. At the high-temperature metallic state, the rotor motion is impeded by the quantum dissipation of the conducting layer. This impeded motion leads to the featureless temperature dependence of

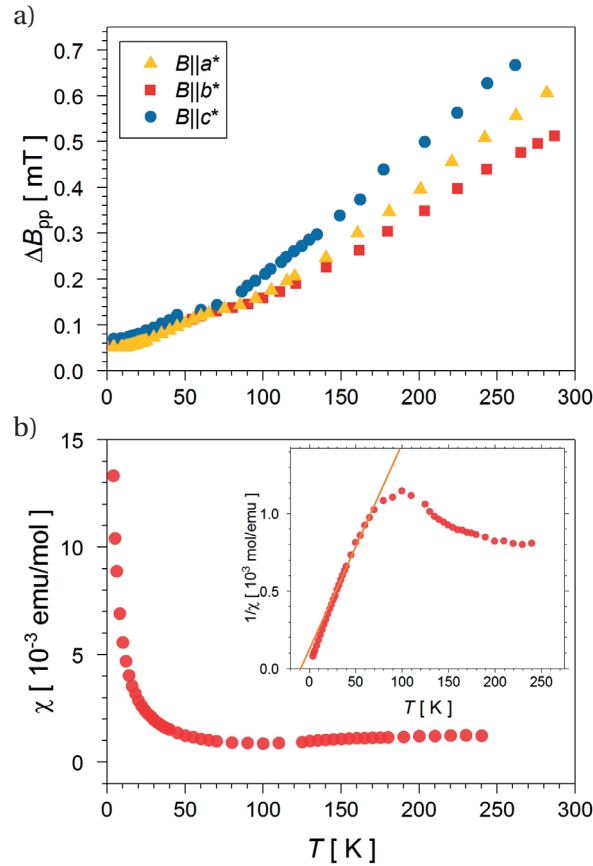


Figure 3.9 – ESR measurables in $(\text{EDT-TTF-CONH}_2)_6^+[\text{BABCO}^-](\text{CH}_3\text{OH})_2$. *a)* X-band ESR linewidth in the main crystallographic directions. The metallic phase is seen to demonstrate a linear increase of the linewidth, reminiscent of high-dimensional metallic temperature dependence. Note the change of slope at the metal-insulator phase transition. *b)* Spin-susceptibility as measured by X-band ESR. Down to 120 K, χ is constant indicating metallic Pauli spin-susceptibility. Inset: Inverse spin-susceptibility. The solid line is a linear fit to the $1/\chi$ below 70 K showing Curie-Weiss-like antiferromagnetic fluctuations with $\theta_{\text{CW}} = -9$ K.

the ^1H NMR spin-relaxation time $T_1^{-1}(T)$ in the absence of any motion-related maximum. The electronic spin contributions are thus more relevant at high temperatures. This is further shown by $(T_1 T)^{-1}$, which stays constant at high temperatures. Below 120 K, however, a rather peculiar decrease of T_1 is seen due to the disappearance of the blocked rotor motion in the insulating state.

ESR measurements were performed both at X-band and using the high-frequency setup. The spin-susceptibility measured at X-band is plotted in Fig. 3.9*b*. Clearly, χ_s does not change significantly above 120 K, which accounts for a metallic-like Pauli spin-susceptibility at high temperatures with $\chi_s \approx 38$ states/(eV·unit cell). This low-spin susceptibility is in good agreement with the small Seebeck coefficient and the surprisingly featureless resistivity. Below 120 K, χ_s changes character, and it follows a Curie-Weiss temperature dependence with a rather low $\theta_{\text{CW}} = -9$ K. This change is a direct proof that a metal-insulator transition shows up

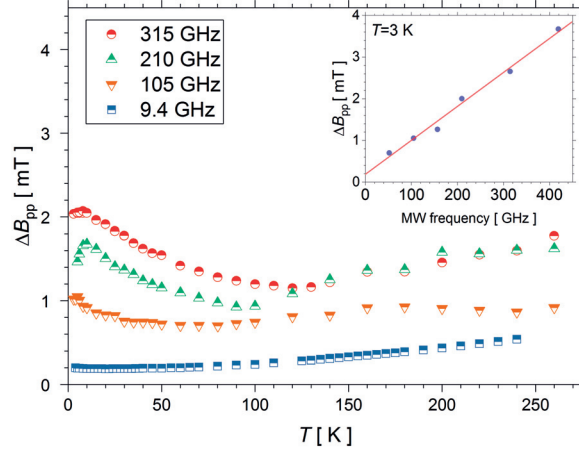


Figure 3.10 – ESR linewidth of $(\text{EDT-TTF-CONH}_2)_6^+[\text{BABCO}^-](\text{CH}_3\text{OH})_2$ at several different frequencies. Below the metal-insulator transition, the slope change is clearly observed. At 15 K, ΔB_{pp} exhibits a maximum probably due to partial magnetic ordering below this temperature. Inset: Frequency dependence of the ESR linewidth revealing linear field dependence related to paramagnetic impurity lines.

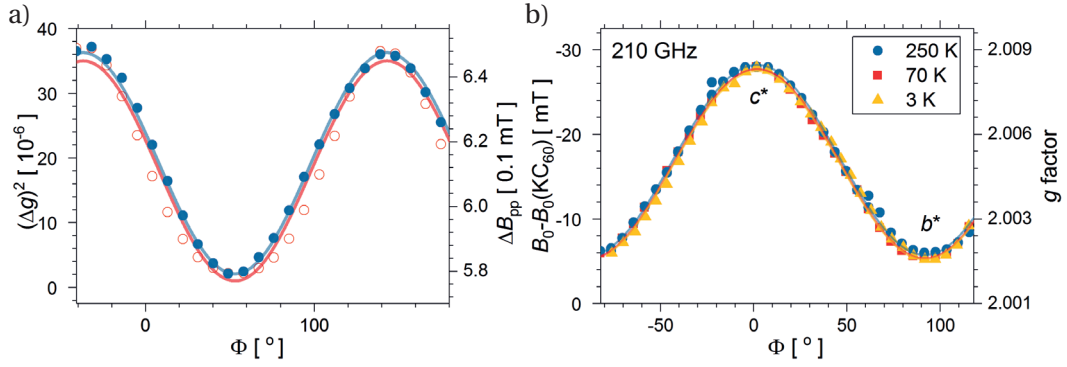


Figure 3.11 – Angle dependence of the ESR line in $(\text{EDT-TTF-CONH}_2)_6^+[\text{BABCO}^-](\text{CH}_3\text{OH})_2$. *a)* X-band studies at room temperature contrasting $(\Delta g)^2$ and ΔB_{pp} . Good agreement is found demonstrating the validity of the Elliott-Yafet relation given in Eq. 2.12. *b)* Resonant field and g -factor as found at 210 GHz at different temperatures. At all temperatures, the angle dependence remains unchanged indicating that the material does not go through structural changes, and the same paramagnetic lineshape is followed throughout the experiment. Solid lines are sinusoidal fits to the data.

around 120 K.

The observed phase transitions can be followed from the multi-frequency ESR linewidth. In order to provide a meaningful comparison, the presumed effect of twinned crystals must be excluded. Indeed, at all temperatures, the ESR linewidth exhibits a slow broadening as a function of frequency, as shown in Fig. 3.10, displaying a multi-frequency comparison. The ESR line only stops to broaden above 157 GHz, where the two twinned crystallites with slightly different g -factor anisotropy become separated. In this sense, the 210 GHz and the 315 GHz temperature dependencies of the ESR linewidth are to be compared to correctly identify the low-temperature behavior.

Chapter 3. Towards disordered QSLs in molecular rotor systems

At the high-temperature metallic state, the slope of the linewidth as a function of temperature increases with temperature, and the signal is almost frequency-independent, which is most pronounced when comparing data at 210 GHz and at 315 GHz. This two-dimensional metallic state can thus be described within the Elliott-Yafet spin-relaxation mechanism, i.e., the spin relaxation happens due to the spin orbit coupling. As the resistivity measurements are affected by the disorder of the system, the ESR linewidth cannot be compared to the resistivity to confirm the validity of the mechanism. Nevertheless, the proportionality of $\Delta B_{pp} \propto (\Delta g)^2$ is expected to be satisfied at high temperatures. As shown in Fig. 3.11a, the correspondence is clearly observed at room temperature. In addition, Fig. 3.11a proves that the spin-orbit related component of the ESR linewidth remains low.

At the metal-insulator transition, the slope of $\Delta B_{pp}(T)$ switches at the temperature of the proposed metal-insulator transition, 120 K. Although at X-band the slope change is rather weak, at high frequencies the change is more clearly identifiable. The low-temperature insulator state displays a decreasing ΔB_{pp} with increasing temperature. In contrast, at high temperatures the ΔB_{pp} increases together with the temperature. The low-temperature frequency dependence demonstrates that the linewidth increases proportionally to the frequency, which is a clear insulating behavior originating from very weakly coupled spins. Given that at these temperatures the Brownian motion of the BCO rotors is frozen, especially at the frequency of the ESR measurements, the ESR line originates from $S = 1/2$ spins at large distances from each other. This observation is further confirmed from the $T = 3$ K frequency dependence of the ESR linewidth shown in the inset of Fig. 3.10.

At 15 K, $\Delta B_{pp}(T)$ displays a small maximum, the most clearly seen at the highest ESR frequencies, 210 GHz and 315 GHz. The maximum, together with a sudden drop of the spin concentration (i.e., $\chi \cdot T$) at 9 K measured by the ESR spin-susceptibility indicates that some of the spins order antiferromagnetically.

It is interesting to ask whether the ESR signal at high temperatures and at low temperatures come from the same origin, or the low-temperature signal is only a measure of the purity of the crystal, and this signal is not incorporated into it crystallographically. Angle-dependent ESR measurements, depicted in Fig. 3.11, show that both the high- and the low-temperature signal preserves the crystallographic symmetry, the same origin can be related to all of these temperatures. Thus, the slow low-temperature increase and the maximum of the low-temperature linewidth provides a way to track the partial antiferromagnetic ordering of the system. This points to a microscopically phase-separated material as observed in other organics [278, 279]. It shows that due to the disorder provoked by the BCO rotators, most of the spin system remains in an unordered state but small parts of the crystal develop antiferromagnetic ordering. Remarkably, this model is consistent with the description used to explain the partial antiferromagnetic state in δ -(EDT-TTF-CONMe₂)₂AsF₆ [276], where the sample-dependent defects were found to be responsible to the suppression of frustration. Here, the disorder is intrinsic, originating from the anion layer. Thus, the system remains mostly in a paramagnetic phase together with an antiferromagnetically ordered component. Due to the rather complex structure

with significant amount of paramagnetic islands in $(\text{EDT-TTF-CONH}_2)_6^+ [\text{BABCO}^-](\text{CH}_3\text{OH})_2$, it was not possible to find the AFM resonance modes despite extensive search for the signals.

3.4 $(\text{EDT-TTF-CONH}_2)_2^+ [\text{BABCO}^-]$, a disordered spin liquid

In the following, I will present the hybrid system that turned out to be the first experimental realization of a mechanical disorder-induced two-dimensional QSL material.

3.4.1 High-temperature rotor dynamics above $T_{\text{MI}} = 75 \text{ K}$

The present EDT-BCO and the previous system share the same rotator component based on BCO, which, together with the same acceptor layer, could imply similarities of the physical properties. In contrast to its (CH_3OH) -containing counterpart presented in the previous section, $(\text{EDT-TTF-CONH}_2)_2^+ [\text{O}_2\text{C-CC-BCO-CC-CO}_2^-]$ (EDT-BCO) creates a structure where each molecular dimer hosts one hole, resulting in a spin-1/2 distorted triangular lattice (see Fig. 3.7). Extended Hückel Theory (EHT) [65] and DFT calculations showed that the dimerization is strong in the system, the spin-independent hopping integral in-between the *A*- and *B*-cations of the dimer are three times larger than any other integrals. Thus, assuming a distorted triangular lattice formed of dimers of inequivalent EDT molecules yields exchange integrals of $J : J' : J'' = 216 \text{ K} : 131 \text{ K} : 356 \text{ K}$ as shown schematically in Fig. 3.7, which predicts a strong distortion in the quasi-one-dimensional regime.

From a structural point of view, the EDT-BCO possesses *Pa* symmetry, a monoclinic primitive unit cell. Therefore, a glide symmetry operation is present in the system that involves a reflection along the *a* – *c* plane and a translation along the *a* axis in the *a* – *b* plane, i.e., in the plane of the EDT layer. This operation leads to the equivalent positions of $(x, y, z) \rightarrow (x + \frac{1}{2}, -y, z)$. Notably, there is no symmetry operation in the crystal structure that would move an *A* cation to a *B* one. In fact, the lengths of the double bonds in-between the central carbon atoms on the *A* cation (1.33 Å) is substantially different from the length of the corresponding bond on the *B* cation (1.40 Å)³. This difference is more pronounced than the one found in δ -(EDT-TTF-CONMe₂)₂Br, where the lengths of the carbon double bonds on the cations are 1.35 Å and 1.39 Å [280]. Accordingly, the charge disproportionation is expected to be larger in EDT-BCO. Remarkably, ¹³C NMR studies found in δ -(EDT-TTF-CONMe₂)₂Br that this discrepancy leads to an effective alternation of molecules with one hole and neutral molecules with a fitted charge ratio of 9:1 [280]. In the present system, these results imply that a strongly one-dimensional charge-ordered behavior becomes a possible scenario.

The structural similarities are well represented by the transport properties of EDT-BCO depicted in Fig. 3.12. Here again, the Seebeck coefficient shows a low value at high temperatures, and it shoots to infinity around 75 K. As in the cases considered above, this may unveil a metal-insulator transition, or it may show the presence of sizable disorder measured at high

³X-ray diffraction analysis was performed at 200 K [65].

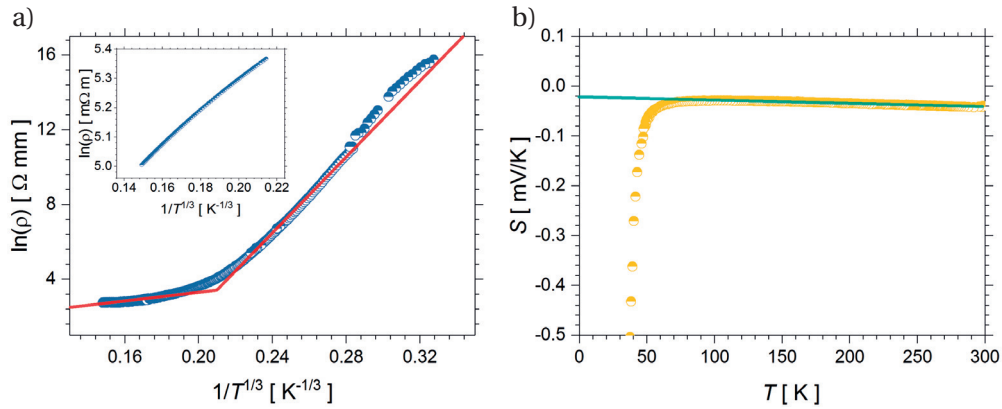


Figure 3.12 – Transport properties of EDT-BCO revealing similarities with $(\text{EDT-TTF-CONH}_2)_6^+[\text{BABCO}^-](\text{CH}_3\text{OH})_2$ (see Fig. 3.8). *a*) Resistivity shows VRH behavior, and a metal-insulator transition around 75 K. Inset: Out-of-plane resistivity pointing to a strongly two-dimensional structure in EDT-BCO. Both measurements were carried out on a single crystalline sample cut by Focused Ion Beam (FIB) technique. *b*) Seebeck coefficient in EDT-BCO. Solid line is a fit to the high-temperature metallic-like temperature dependence.

temperatures as a low contribution to the Seebeck coefficient.

To further investigate the unusual high-temperature behavior, resistivity measurements were combined with ¹H-NMR and μSR measurements. Interestingly, the resistivity cannot be described within the VRH model using a single T_0 in Eq. 3.2, a much better fit is achieved by fitting it to two different T_0 values, one below, and one above 35 K. This is a first experimental signature that the disorder, probably provoked by the BCO rotators is more significant in this system than in the $(\text{CH}_3\text{OH})_2$ -containing counterpart. Resistivity measurements in the plane of the EDT layer, in the $a - b$ plane, and perpendicular to it, in the c axis direction, present a large, temperature-independent anisotropy (see the inset of Fig. 3.12). This is a direct experimental proof that the system is a strongly two-dimensional one with weak coupling in-between the layers.

As in the (CH_3OH) -containing counterpart, the high-temperature metallic state is expected to result in quantum dissipation due to the viscous motion of the BCO rotator components. This impeded motion was indeed found in Ref. [65], and it was the very first observation of such a uniquely coupled behavior. Nevertheless, follow-up ¹H-NMR studies provide a further insight into the rotor dynamics both in the high-temperature metallic and the low-temperature insulator regime. It was confirmed through NMR measurements that the $1/T_1$ above the metal-insulator transition can be assigned to the rotor layer. In contrast to the insulator compound, $[n\text{Bu}_4\text{N}^+]_2[\text{BABCO}][\text{BABCO}^-]_2 \cdot \text{H}_2\text{O}$, where both disordered BABCO and ordered BABCO⁻ sites were seen experimentally [65], the variable temperature ¹H NMR spin relaxation time is not thought to detect two different BCO rotator positions. Instead, a single [BABCO⁻] position is known to exist in the present material. Thus, a single dynamic process is followed in EDT-BCO, corresponding to a single barrier.

⁴The fitted activation energy has significant uncertainty, as the peak of T_1^{-1} is not followed above its maximum.

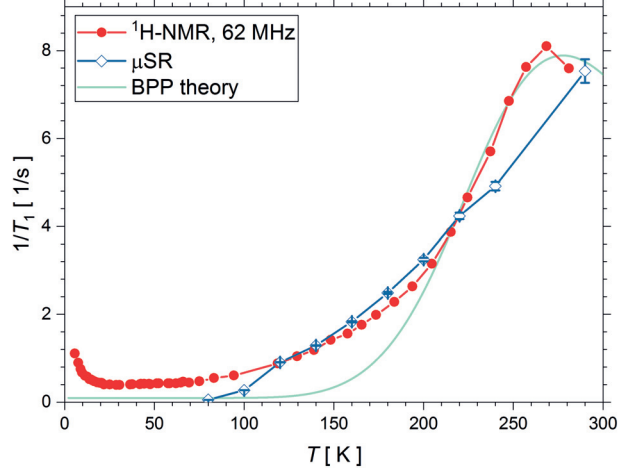


Figure 3.13 – Comparison of the spin lattice relaxation time measured by ^1H NMR and those calculated from μSR assuming a single-barrier BPP relaxation as explained in the text. The solid line is a fit to the ^1H -NMR T_1^{-1} using the BPP theory with an activation energy of $E_a/k_B \approx 1400 \text{ K}^4$, $\tau_0 = 6.4 \cdot 10^{-7} \text{ s}$ or an attempt frequency of $A = 1.5 \text{ MHz}$. At room temperature, the frequency of the rotation is in the MHz regime. Note that the usual peak expected at the NMR spin relaxation time is above room temperature, which signifies that a considerable ambiguity remains on the exact determination of the fitting parameters.

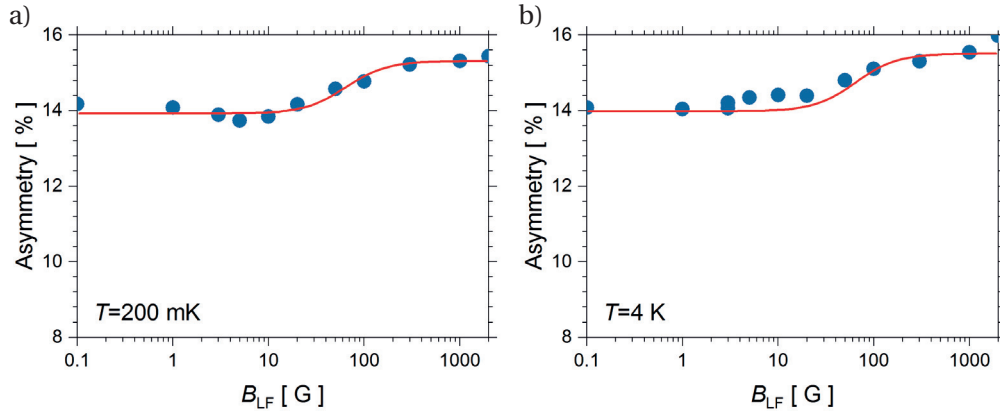


Figure 3.14 – Repolarization of the initial muon polarization in longitudinal fields at $T = 200 \text{ mK}$ (a) and $T = 4 \text{ K}$ (b). The solid red lines are fits to the isotropic Mu contribution as described by Eq. 2.32 in Section 2.2.4, with a low hyperfine coupling of $B_{\text{hyp}} = 6.5 \text{ mT}$. Note that the field dependence measured at higher fields cannot be used due to the field-dependent changes in the muon beam position.

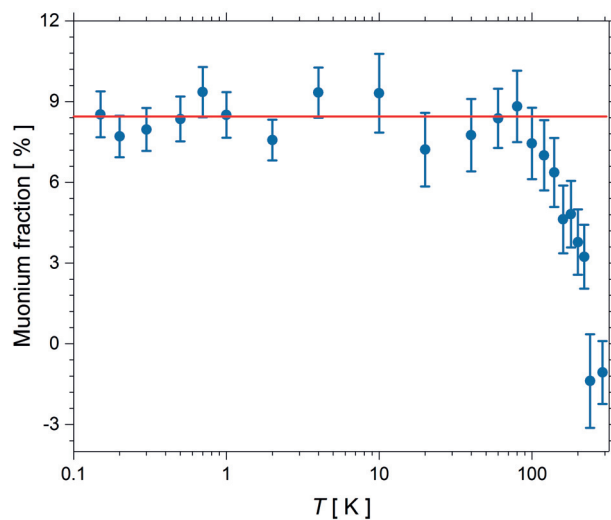


Figure 3.15 – Temperature dependence of the estimated muonium fraction as determined from longitudinal field dependences as shown in Fig. 3.14. At high temperatures, the absence of muonium formation indicates a high enough mobility, corresponding to a metallic state.

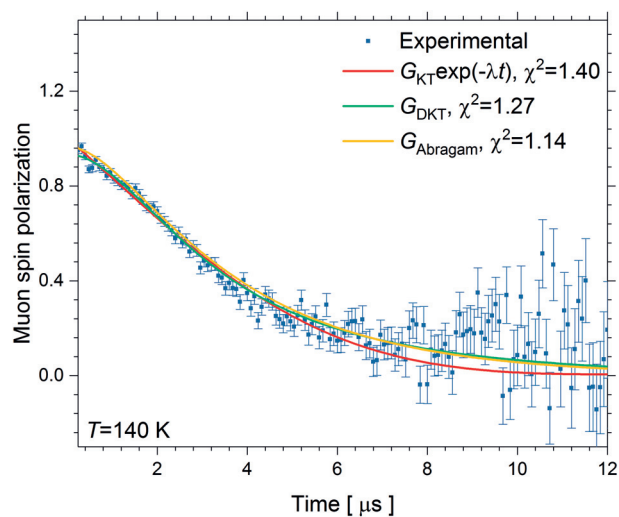


Figure 3.16 – Comparison of fits of the μ SR relaxation times at 140 K exhibiting a better fit with the dynamic Kubo-Toyabe relaxation function ($\chi^2 = 1.27$) and the Abragam function ($\chi^2 = 1.14$) than the fit to Eq. 3.10 ($\chi^2 = 1.40$) used at the low-temperature insulating regime.

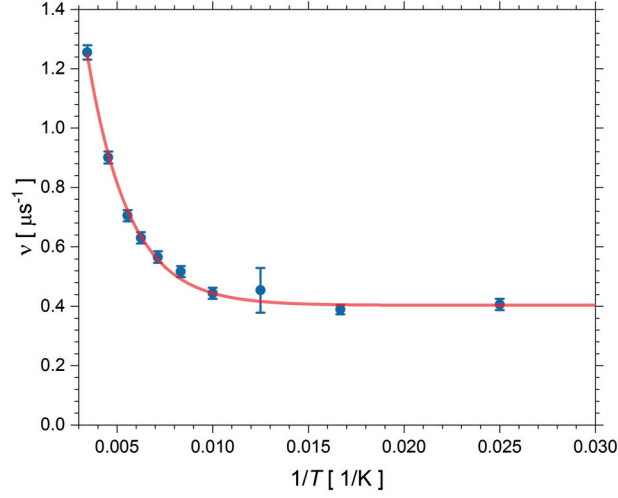


Figure 3.17 – μ SR fluctuation rate as a function of temperature from the dynamic Kubo-Toyabe relaxation fit of the data. The solid line is a fit to $\nu = \nu_0 + (1/\tau_0) \cdot \exp(E_a/k_B T)$, with $\nu_0 = 0.40(1) \mu\text{s}^{-1}$, $E_a/k_B = 462(26) \text{ K}$, and $\tau_0 = 2.4(2) \cdot 10^{-7} \text{ s}$.

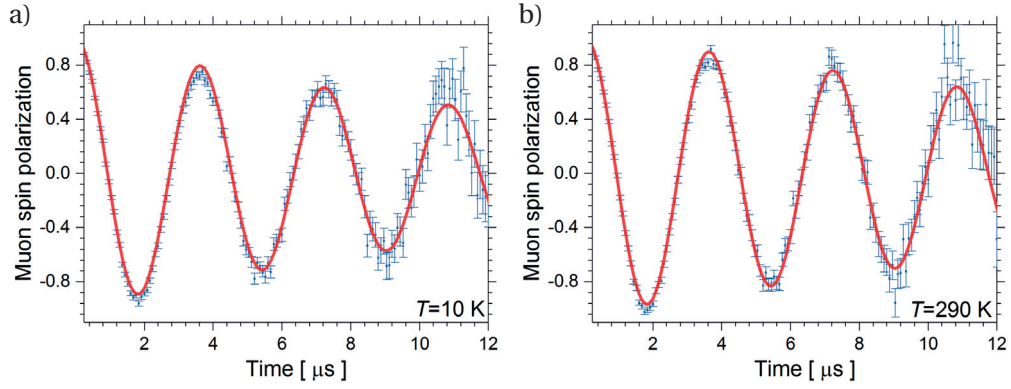


Figure 3.18 – Weak transverse field data at $T = 10 \text{ K}$ (a) and at $T = 290 \text{ K}$ (b). At $T = 10 \text{ K}$, an exponentially relaxing envelope gives the best fit with $\lambda = 0.062 \mu\text{s}^{-1}$. At $T = 290 \text{ K}$, the Abragam relaxation function gives a better description with a field distribution of $\Delta = 0.169(3) \mu\text{s}^{-1}$ and a correlation time of $\tau_c = 1.7(9) \mu\text{s}^{-1}$. Note that the wTF relaxation is smaller than the ones fitted at zero-field, as the relaxation at ZF is induced by two components of the local magnetic field [229].

To test the development of T_1^{-1} , the BPP theory (Eq. 3.1) is fitted to the temperature dependence, and it is shown in Fig. 3.13. In accordance with the above structural considerations, only one peak is seen. Below 50 K, however, T_1 starts to slowly decrease. This change is a definite manifestation of magnetism-related low-temperature spin relaxation. Furthermore, this low-temperature change cannot be present in a metallic state, thus the NMR data determines a lower bound for a possible metal-insulator transition. ^1H -NMR is not capable to provide a precise measure of the metal-insulator state as it was possible in the case of (CH₃OH)-containing material, as the rotor dynamics is largely frozen out at the temperature range close to 75 K.

An alternative identification of the metal-insulator transition can be proposed using μ SR data. As it was discussed in Section 2.2.4, the muonium formation is only possible in insulators, and it is frequently observed in organic systems due to the large number of unsaturated bonds [226, 227]. To determine the muonium fraction, longitudinal-field dependence of the μ SR spectra was measured at the ISIS facility at a broad temperature range. In addition, the determined Mu fraction was corroborated with low-temperature μ SR data measured at a continuous source in PSI to ensure that absolute values are correctly determined. Fig. 3.14 depicts fits to example repolarization curves at $T = 200$ mK and at $T = 4$ K. The fitted hyperfine coupling at all temperatures is $B_{\text{hyp}} = 6.5(1)$ mT. This low value indicates a muonium radical with a localized wavefunction, which is plausible in an organic insulator with a large number of unsaturated bonds [236].

Fig. 3.15 summarizes the muonium fraction from the fitted repolarization curves. It exhibits the presence of a sizable muonium fraction at low temperatures as an indication of decreased mobility and a weak Mott insulator state. Nevertheless, it has a significant temperature dependence providing a clear evidence of the mobility increase. At the highest temperatures, the muonium fraction goes to zero due to the large enough mobility. This data therefore gives a further proof of the metal-insulator transition.

To give a better insight into the rotor dynamics measured by ^1H -NMR, high-temperature μ SR measurements were performed. Given the large unit cell and the complicated crystal structure of EDT-BCO, a number of muon stopping sites can be identified in the structure both close to the EDT layer and close to the BCO molecular rotator layer. Thus, comparison of the muon spin relaxation with the spin-lattice relaxation time of the ^1H NMR data is possible at high temperatures. As presented in Section 2.2, in a μ SR experiment, the asymmetry of the forward and backward detectors is plotted. Our ZF measurements above the metal-insulator transition ($T_{\text{MI}} = 75$ K) find that the low-temperature fitting function (see below, Eq. 3.10) must be replaced by a dynamic function representing fluctuations in the intermediate regime. In Fig. 3.16, the ZF μ SR depolarization at 140 K is displayed comparing three different fitting functions. The low-temperature product form (Eq. 3.10) is contrasted with the Abragam formula (Eq. 2.27) and with the dynamic Kubo-Toyabe function [227, 234]

$$A(t) = G_{\text{DKT}}(\Delta, \nu, t) + A_{\text{bg}}, \quad (3.8)$$

where ν measures the fluctuations in our system in a strong collision model in a system without memory. The fits and the observation that the LF dependence (not shown here) does not follow the longitudinal field dependence of the dynamic Kubo-Toyabe function demonstrate that the high-temperature dynamics is best described by the moderately dynamic process defined by Eq. 2.27. To further confirm the different dynamics of the low-temperature and the high-temperature data, weak transverse field (wTF) data were acquired. Fig. 3.18 gives a comparison of high- and low-temperature weak transverse field fits. Remarkably, the low-temperature wTF muon depolarization can be best interpreted with an exponential depolarization, whereas the room temperature depolarization manifests the validity of Abragam relaxation. As highlighted

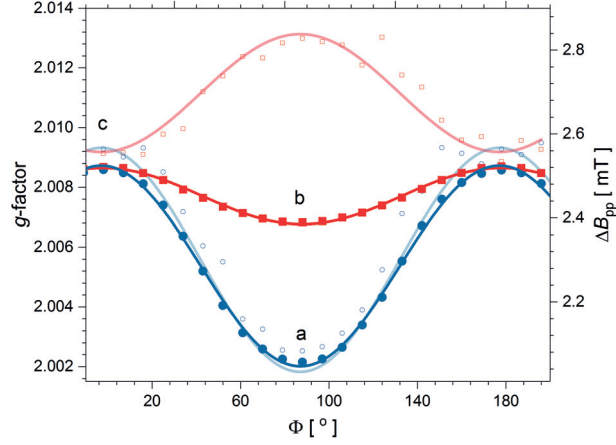


Figure 3.19 – Angle dependence of the g -factor (full circles and squares) and the room-temperature X-band ESR linewidth (empty circles and squares) in EDT-BCO. Solid lines are sinusoidal fits to the data.

above, the metal-insulator transition is close to the temperature where the rotation of the BABCO^- molecules stop completely. Thus, I relate the change of the muon relaxation to both the metal-insulator transition and to the interaction with the rotor layer. The observed dynamic fluctuation rate, ν , is a measure of the rotor dynamics at the high temperature regime⁵.

Comparison of the μSR results with the NMR data is the easiest by the virtue of comparing the correlation time determined from ^1H -NMR and that measured by μSR assuming a single-barrier BPP theory to fit the whole temperature range above 75 K⁶. In Fig. 3.13, I show the $(T_1^{-1})_{\mu\text{SR}}$ calculated from the μSR data. Here, the K constant is a fitting parameter, as the average distance of the nuclear dipole moments is supposed to be different in the two cases. The overall agreement of the two data sets confirms the validity of the BPP theory and it shows that a single-barrier description is valid. Inversely, the activation energy of the τ_c correlation time can be determined assuming an Arrhenius behavior. τ_c was fitted to the Kubo-Tomita equation, $\tau_c = \tau_0 \exp(E_a/k_B T)$, and an additional, temperature-independent relaxation process was assumed with $\nu_0 = 0.4 \mu\text{s}^{-1}$. Fig. 3.17 reveals that this activated behavior can explain satisfyingly all our data points with $E_a/k_B = 462 \text{ K}$ and $\tau_c = 0.24 \mu\text{s}$. The latter fit corresponds to a rotational frequency of 9.6 MHz at room temperature, in accordance with the NMR results [65].

ESR measurements at this high-temperature regime (between T_{MI} and room temperature) prove the low-dimensional metallicity of EDT-BCO. The spin-susceptibility, shown in Fig. 3.20, exhibits a clear constant term at high temperatures, above $T_{\text{MI}} = 75 \text{ K}$. In polycrystalline

⁵Whereas both the low-temperature fitting function of Eq. 3.10 and the high-temperature function of Eq. 2.27 describes a mechanism with dynamic character, the low λ measured at low temperatures (shown later) exhibits a significantly faster fluctuation that is absent at the high-temperature points.

⁶The BPP theory assumes that the correlation time defined in Eq. 3.1 is an exponentially decaying one with $\exp(-t/\tau_c)$, which differs from the definition of the strong collision model used for μSR data.

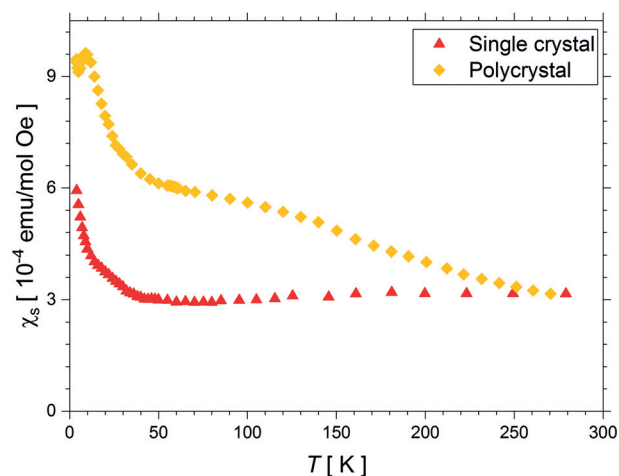


Figure 3.20 – Absolute spin-susceptibility in EDT-BCO as measured by X-band ESR studies. Red triangles correspond to spin-susceptibility of single crystals, yellow squares to χ_s of a polycrystalline sample. Both systems present a nearly constant Pauli spin-susceptibility above $T_{MI} = 75$. The slightly different temperature dependence originates probably from additional impurities in the polycrystalline sample.

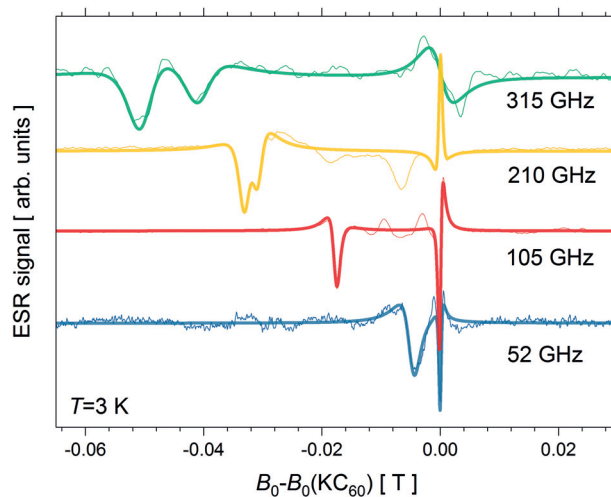


Figure 3.21 – ESR spectra in EDT-BCO at high frequencies at $T = 3$ K revealing a frequency dependence characteristic of paramagnetic ESR signals. The narrow line comes from KC_{60} , and serves as a g -factor reference. Solid lines are derivative Lorentzian fits to the spectra. Above 210 GHz, the ESR lines are split into two components coming from twinned crystals that cannot be resolved at lower frequencies.

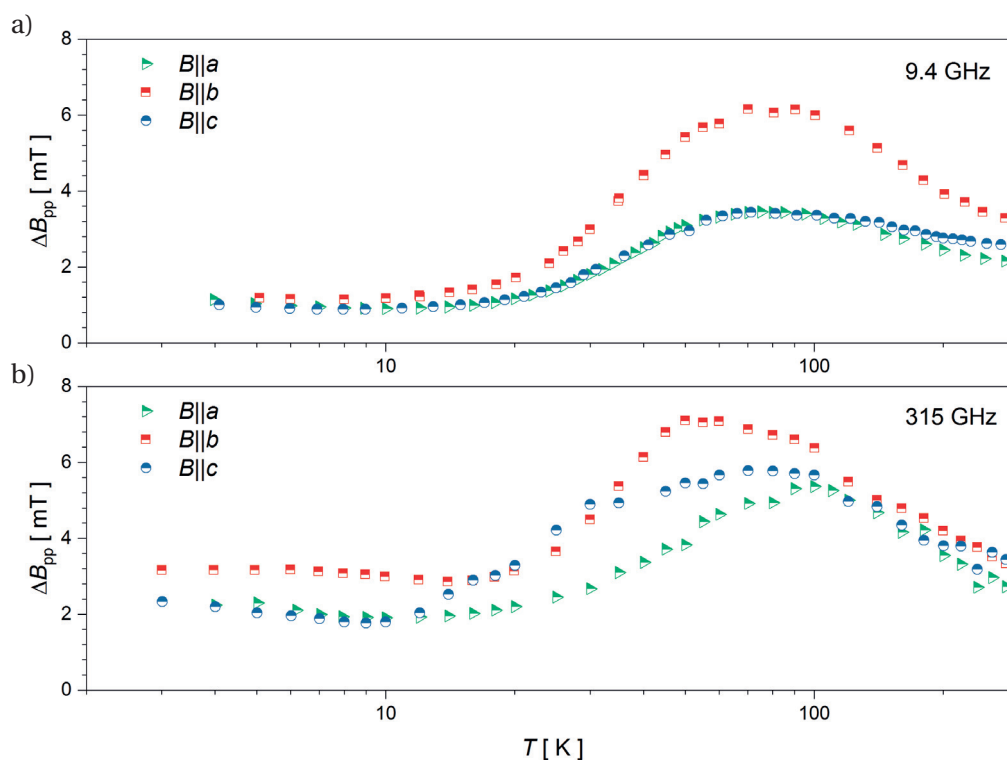


Figure 3.22 – ESR linewidths of EDT-BCO in the main crystallographic directions at 9.4 GHz (up) and at 315 GHz (down) displayed semilogarithmically. At all directions, a clear maximum of $\Delta B_{pp}(T)$ is found at $T_{MI} = 75$ K. The weak increase of the ESR linewidth at low temperatures stems from spin fluctuations provoked by the vicinity of the crossover region. The largest linewidth is measured parallel to the b direction, which is crystallographically equivalent to the b direction in κ -Ag (see Chapter 4).

samples (such as the ones used for μ SR studies), a slight increase of χ_s is found resulting from an increased concentration of impurities. The room-temperature angle dependence, displayed in Fig. 3.19 reveals the invalidity of the Elliott-Yafet mechanism. Relevantly, the ESR linewidth is the largest parallel to the b direction, which is the crystallographic direction perpendicular to the mirror plane of EDT-BCO. Thus, this is a direction perpendicular to the long direction of the EDT molecules⁷.

The larger linewidth in the b direction is present not only at room temperature but at all temperatures, as shown in Fig. 3.22 and in Fig. 3.23. This larger linewidth in the direction perpendicular to the reflection plane of the glide symmetry operation was found in other organics, such as κ -Cl. Interestingly, even the temperature dependence of the ESR linewidth is rather similar, with a maximum at 75 K, which was found to slightly depend on the cooling rate of the sample. In κ -Cl, low-frequency ESR studies found the maximum at the same temperature range, whereas high-frequency studies showed the effect of the DM interaction due to the proximity of the Néel temperature. In κ -Ag, I will show in Chapter 4 that there is a similar maximum at 50 K. This interesting phenomenon, which seems to be a common feature

⁷The other crystallographic direction perpendicular to the long direction of the EDT molecules is in-between a and c .

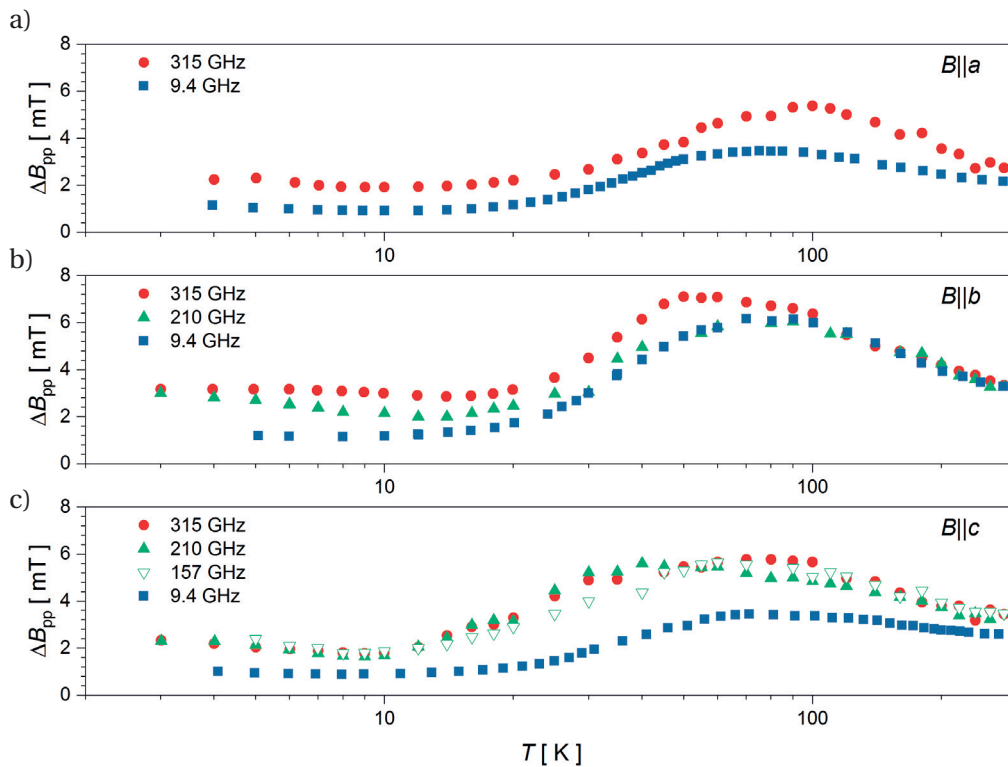


Figure 3.23 – Low-temperature ESR linewidth at several different frequencies in the main crystallographic directions ($B \parallel a$ (a), $B \parallel b$ (b), and $B \parallel c$ (c)) shown semilogarithmically. At high frequencies, the ESR linewidth is found to be independent of the frequency excluding the presence of antiferromagnetic fluctuations in the quantum disordered state. Note that slight changes of the temperature of the maximal ΔB_{pp} might stem from the cooling rate dependence of the disorder.

in magnetic (including QSL) systems has remained a puzzle. In κ -Cl and in κ -Cu it was related to the presence of inter-dimer dipole fluctuations [281, 282, 283]. Nevertheless, in the present case, the inter-dimer direction would be the a direction (instead of the b direction), excluding this explanation. Instead, in the present system, the maximum stems from the metal-insulator transition. Furthermore, the linewidth increase with decreasing temperature is characteristic of the observed low-dimensional metallic state [163, 206]. Thus, the maximum in ΔB_{pp} and its temperature dependence can be understood as the drop of charge-related fluctuations including a critical slowing down of the BCO rotors. In other systems, the C-N disorder in the inter-layer spacing might induce similar charge fluctuations [284, 285]. Regarding the difference found perpendicular and parallel to the reflection plane, I speculate that the crystal symmetry leads to discrepancy, and gives equal linewidths in the a and c directions. This simple assumption does not explain why the maximum is in the perpendicular direction, hence, further theoretical considerations are needed to provide better insight into this puzzling common behavior of organic QSL candidates.

As shown in Section 1.3.1, the relevance of the observed metal-insulator transition at a moderate temperature (or at a moderate pressure) is motivated by theoretical considerations that identified the quantum disordered state to emerge in weak Mott insulators close to

the Mott transition [87, 109]. In this sense, it does not play a crucial role whether the state at high temperatures is truly metallic or not. In a number of cases, such as in irradiated κ -Cl [150], despite the resistivity was found to display closely metallic behavior, the vicinity of the Mott transition was emphasized. Furthermore, studies under pressure in κ -type triangular lattice organics [67, 119] showed that the QSL state persists up to the phase boundary of the insulator-Fermi-liquid phase transition. Thus, the observation of a definite metallic resistivity in EDT-BCO under moderate pressures [65] is already sufficient for following a quantum critical state at low temperatures⁸.

3.4.2 ESR measurements in quantum critical state

To interpret the results of the low-temperature ESR experiments, it is needed to investigate whether the DM interaction (see Section 2.1.3) plays a role in the observed ESR lineshape. From the analysis of the crystal structure, I showed that there is no symmetry that would take the A cation to the B cation. The absence of inversion symmetry in the system implies that the DM interaction is expected to be present in the system. DFT calculations found that for both possible scenarios of the charge distribution, i.e., the quasi one-dimensional case with strong charge disproportionation and the two-dimensional one with strong dimerization a sizable DM interaction can be found in-between the neighboring spin-carrying molecules (dimers). These theoretical proposals can be contrasted to the low-temperature ESR linewidth data shown in Fig. 3.22 and Fig. 3.23.

In the one-dimensional case, a *uniform* DM interaction would be expected in the b -direction with a size of $|\mathbf{D}|/\mu_B = 0.26$ T. As in Cs_2CuCl_4 (an anisotropic triangular lattice that undergoes a dimensional reduction resulting in a one-dimensional QSL state), the uniform DM interaction boosts the $q = 0$ spinons by $q = D/Ja_0$ (J is the intrachain coupling and a_0 is the crystal lattice parameter). This splits the ESR lines into two lines causing a resonant field shift that reads

$$\Delta B_0 = \frac{\hbar\nu|\mathbf{D}|}{g\mu_B J}. \quad (3.9)$$

In the present material with the calculated exchange and DM values at the highest frequency (315 GHz) a shift of $\Delta B_0 \approx 5$ mT would be seen⁹. Furthermore, as shown in Fig. 3.23, linewidths in the b direction (as in other directions) are $\Delta B_{\text{pp}}(T = 3 \text{ K}) = 3$ mT at the lowest measured temperatures. This signifies that such a large shift due to splitting would be clearly visible in the ESR spectra. However, this was not observed (not shown).

Both in the one- and two-dimensional solutions, the *staggered* DM interaction would lead to a frequency-dependent (i.e., magnetic field-dependent) ΔB_{pp} -broadening and g -factor shift

⁸Given the striking similarities between all the ambient-pressure properties of EDT-BCO and the κ -type QSLs, it would be natural to expect a superconducting state at large enough pressures. Our studies are still on-going towards finding the superconducting state at high enough pressures.

⁹The expression only depends on the ratio D/J of the DM and exchange interactions, therefore, numerical errors of the separate energy ranges are not relevant.

while cooling the sample, and this broadening would depend on temperature, as well. As described by the Oshikawa-Affleck theory presented in Section 2.1.3, these effects depend on the angle, and are the largest for directions perpendicular to the staggered DM interaction. From a symmetry point of view, the glide plane symmetry operation gives $D_b = 0$ for the staggered DM interaction in the b direction. This is in line with the case of κ -Cl, where this restriction was theoretically predicted and measured [222, 286], and to κ -Ag, which was measured within the frame of the present thesis project (see Chapter 4). Thus, the DM interaction in EDT-BCO is perpendicular to the b direction, and it has to lie in the $a - c$ plane. Namely, in the one-dimensional case DFT concluded $\mathbf{D}/\mu_B = (0.18, 0, 0.76)$ T, whereas in the two-dimensional one it was $\mathbf{D}/\mu_B = (-0.12, 0, -0.43)$ T. Thus, in the b -direction, ESR measurements would be supposed to show the largest effect of these interactions. Nevertheless, the frequency dependence shown in Fig. 3.23 confirms that the change in-between 210 GHz and 315 GHz is not substantial, and the foreseen g -factor shift would be an order of magnitude smaller effect at the lowest temperatures as determined from Eq. 2.22. Regarding the temperature dependence of ΔB_{pp} , a slow broadening is found below 5-6 K, which corresponds to the crossover regime identified by μ SR experiments (see below). This weak effect is seen to be frequency-independent, unlike any field-dependent change expected in the presence of the DM interaction. To conclude, the effect of the DM interaction is not observed experimentally, it is probably suppressed by quantum fluctuations in the system.

Now I turn to the analysis of the low-temperature spin-susceptibility depicted in Fig. 3.20. Independently of the morphology of the samples, a very slow increase of χ_s is found experimentally below 75 K. In a distorted triangular lattice, the susceptibility decreases at low temperatures below a peak temperature T_p , slightly lower than the leading exchange interaction size ($T_p/|\theta_{CW}| \approx 0.2$ for the ideal triangular lattice) [158], which is absent in EDT-BCO. However, the increase is definitely slower than a Curie-like behavior, as $\chi_s(T = 4 \text{ K})/\chi_s(T = 75 \text{ K}) \approx 2$ (in single crystals). Fitting χ_s at the lowest temperatures to a Curie-component would yield a small impurity spin concentration of 0.6 % (single crystals), which would be a reasonable value even in the cleanest single crystals. Nevertheless, the robustly weak increase at this large temperature range and its lack of sample-to-sample variance amongst single crystals suggests that the increase is an intrinsic characteristic of the EDT-BCO crystal, and not related to defects created during the sample growth. A recent theoretical proposal [287] evidenced that the spin-susceptibility can differ from the rolling-over type behavior below T_p , and a minor upturn might happen in the case of medium bond-randomness in frustrated magnetic systems. In fact, bulk susceptibility measurements in X-ray irradiated κ -Cl uncovered a similar susceptibility upturn of $\chi_s(T = 4 \text{ K})/\chi_s(T = 75 \text{ K}) \approx 1.8(2)$ [150].

Unlike in other materials, such as Yb_4As_3 [288], where Dzyaloshinskii-Moriya interaction is large compared to J , I do not believe that the low-temperature increase of the susceptibility stems from the bond randomness of the DM interaction. Instead, in EDT-BCO, the intrinsic disorder of the stopping position and conformation of the BCO rotator provides a direct way

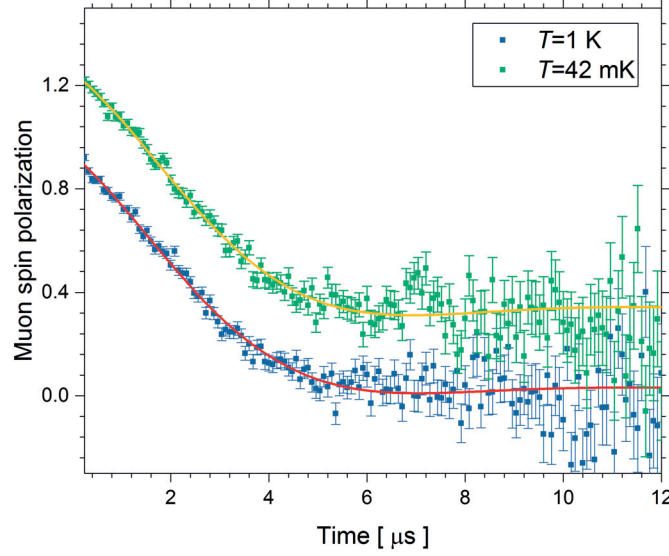


Figure 3.24 – Comparison of the time-dependent zero-field muon-spin polarizations in EDT-BCO at $T=1$ K and at $T=42$ mK. Solid lines are fit to Eq. 3.10. Data are offset for clarity. Note the apparent difference of these depolarization curves as compared to the strictly Kubo-Toyabe function defined in Eq. 2.26.

to introduce the bond-randomness, and to result in a low-temperature enhancement of χ_s ¹⁰.

3.4.3 μ SR measurements in the quantum critical state

As we saw above, ESR measurements gave an unambiguous proof of a magnetically fluctuating state down to 1.5 K. To unravel the low-temperature behavior of our system below 1.5 K, I opted for μ SR measurements at ISIS and at PSI¹¹.

Fig. 3.24 depicts ZF μ SR depolarization curves at low temperatures as measured at the ISIS facility. The most prominent observation is the absence of oscillations revealing the absence of a magnetically ordered fraction in the material. The corrected $A(t)$ of the ZF data was best fitted to a product form frequently used for representing coexisting dynamic and static fields in frustrated organic systems. At ISIS, where a pulsed source is used, the best fitting function reads

$$A(t) - A_0 = G_{KT}(\Delta, t) \cdot e^{-\lambda t}, \quad (3.10)$$

¹⁰I remark that in the plethora of theoretical descriptions, the approach of Biswas *et al.* [289] using spinful Majorana excitations offers a viable reasoning to explain χ_s . This model gives a power-law increase of the type $\chi_s \propto T^{-1/3}$, which is approximately valid in EDT-BCO in the narrow $4 \text{ K} < T < 75 \text{ K}$ regime. To contrast my data to this model, low-temperature specific heat or thermal conductivity studies would be required.

¹¹A polycrystalline sample with a mass of $m = 134$ mg was packed into a silver foil packet of size of $1 \times 1 \text{ cm}^2$. Before the experiment, 49 mg mass sample was measured in ESR (data not shown here) to check the material quality. To ensure that the μ^+ beam is stopped, the packet was covered with a further Ag stripe. The packet was glued to a fly-past mode sample holder at ISIS to achieve large enough mass per unit surface area.

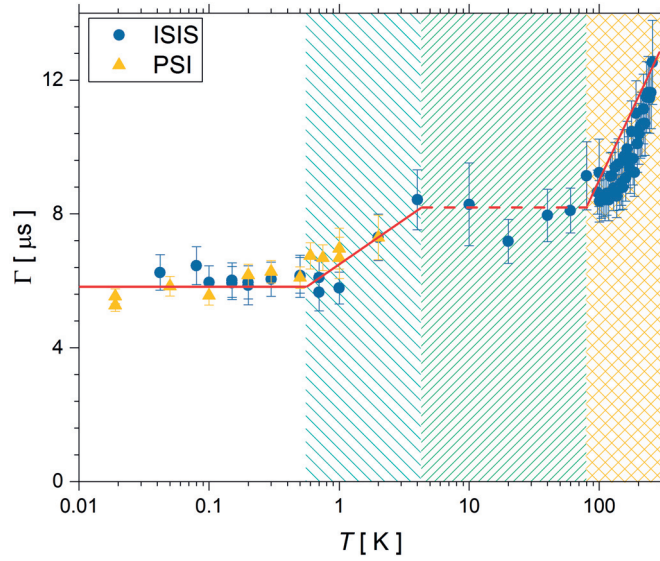


Figure 3.25 – Electronic spin fluctuation rate ($\Gamma = 1/\lambda$) in EDT-BCO from zero-field μ SR data from the fits to Eq. 3.10. Data measured at separate experiments in ISIS (circles) and in PSI (triangles) are shown together. The spin fluctuations barely change at low temperatures, indicative of the persistent dynamics in the quantum critical regime. Shaded areas highlight the crossover in a mid-temperature insulating regimes, and in the high-temperature metallic state. The muon spin relaxation in the high-temperature regime cannot be described using the relaxation function of Eq. 3.10, as it is driven by the BCO rotator component.

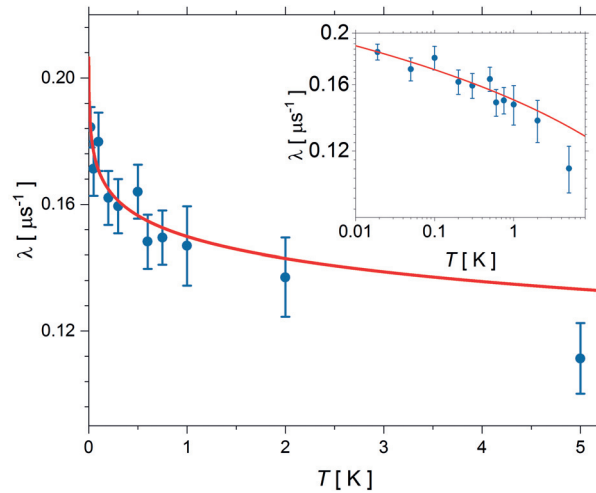


Figure 3.26 – Zero-field muon spin relaxation rate as found from PSI data as a function of temperature. The weak temperature-dependence of the fitted fluctuation rate provides a direct observation of the excitation spectrum, indicating a spin excitation spectrum dominated by the $q = \pi/a$ excitations with an intrachain coupling of $J/k_B = 482$ K. Inset: Same data and fit shown on a semilogarithmic scale.

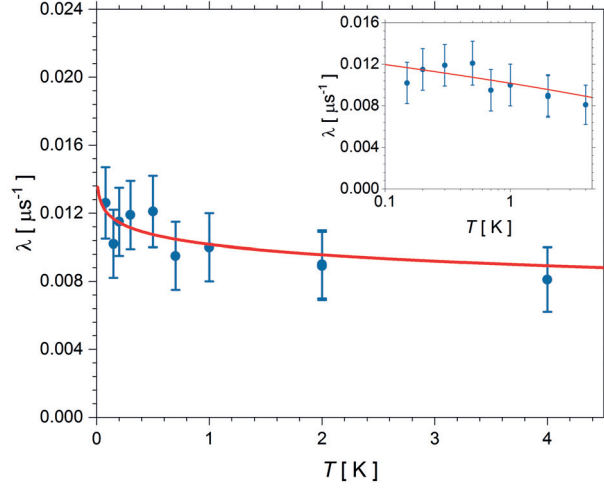


Figure 3.27 – Temperature dependence of the muon spin relaxation rate, λ , at an applied longitudinal field of $B_{LF} = 2$ mT at low temperatures deduced from fits to Eq. 3.13. The upturn of the spin fluctuations at the lowest temperatures indicate that $q = \pi/a$ fluctuations are predominant in the μ SR data of EDT-BCO. Inset: Same data and fit shown on a semilogarithmic scale. Note that the weak temperature dependence provides only an approximate value to the intrachain magnetic coupling.

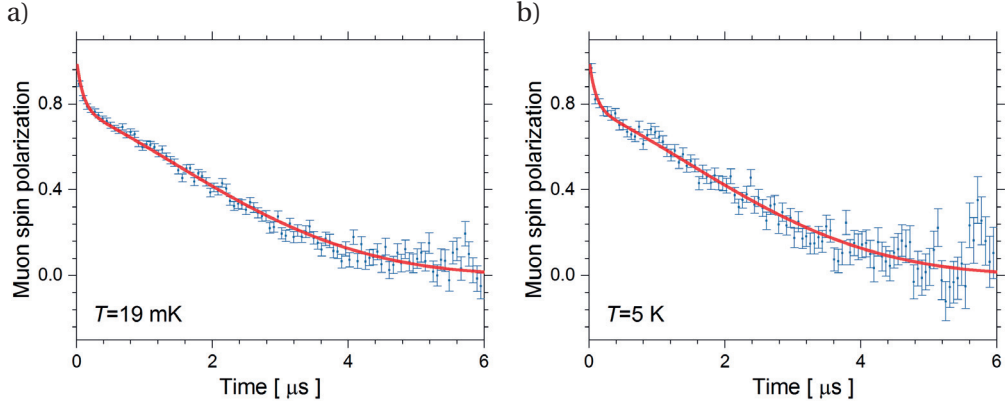


Figure 3.28 – Zero-field μ SR spectra at $T = 19$ mK (a) and $T = 5$ K (b). The fast depolarization component and its fraction is T -independent, indicating the absence of a magnetic transition and a small fraction of muonium.

where G_{KT} is the static Kubo-Toyabe function describing spatially random fields with many different frequencies overlapping. Δ is the distribution width of the depolarization rate of the static nuclear spin contributions, and λ that of the electronic spin fluctuations, as a signature of the persistent dynamics at low temperatures. While cooling, the temperature-dependent fits show an abrupt change of the nuclear dipole field contribution, with $\Delta = 0.52(2) \mu\text{s}^{-1}$ at high temperatures. At low temperatures, $\Delta = 0.247 \mu\text{s}^{-1}$ (MHz) is fixed at the base temperature, $T = 19$ mK. This value is consistent with a relaxation coming from the nuclear site contribution, and is close to the values found in other organic systems [71, 126, 290]. The dominating Kubo-Toyabe relaxation shows that the muons are mostly diamagnetic in our sample. The baseline, A_0 , is fitted at all temperatures separately to the ZF data as the small sample size might alter

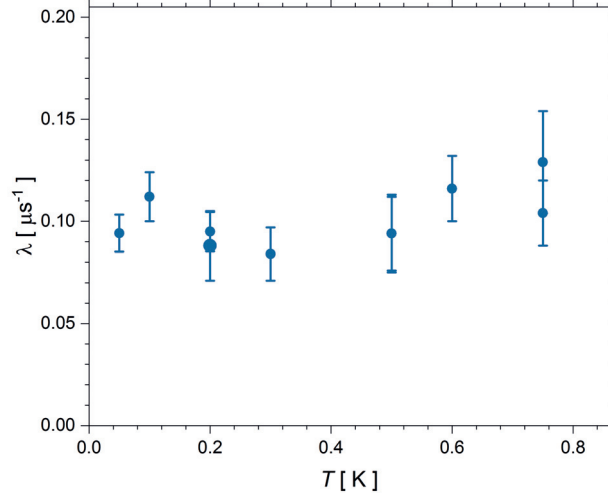


Figure 3.29 – Relaxation rates in a weak transverse field of $B_{\text{TF}} = 5$ mT at low temperatures as deduced from the fit to Eq. 3.12.

it as a function of temperature. The change of A_0 was, however, negligible as a function of temperature. It is noteworthy that at low temperatures the initial asymmetry did not reach the expected value of 0.25 corresponding to an exclusively diamagnetic contribution with zero magnetically ordered fraction in EDT-BCO.

Similarly to the presented fitting function of Eq. 3.10, coexisting static and dynamic magnetic fields were identified using the same fitting function by Pratt *et al.* [71] and Ohira *et al.* [126] to describe the muon spin polarization in κ -Cu. Furthermore, the same fitting function was applied to describe the ZF behavior in 1D spin-1/2 Heisenberg antiferromagnetic spin chains, such as $\text{Cu}(\text{pyz})(\text{NO}_3)_2$, $\text{Cu}(\text{pyz})_2(\text{ClO}_4)_2$ [291], and DEOCC-TCNQF₄ [290].

In Fig. 3.24, fits to Eq. 3.10 are shown at two temperatures. The fitted λ values are close at the two temperatures yielding $\lambda = 0.16 - 0.17 \mu\text{s}^{-1}$. Notably, both are significantly lower than the Δ originating from the static contributions. As described in Eq. 2.28, the low λ values correspond to the fast fluctuating limit at zero applied magnetic field. In fact, the expression identifies a relaxation rate that can be written as $\lambda = \Delta^2 \tau_c$, where τ_c is the spin correlation time. Thus, the λ values much smaller than the static contribution, expressed by Δ , point to a fast fluctuating spin system in our material.

The presence of partial or complete magnetic ordering in EDT-BCO could be evidenced from the critical behavior in the relaxation rate, $\lambda(T)$, as a function of temperature. It is therefore of crucial relevance to examine the measured ZF- λ to search for an increase in it. To follow the temperature dependence of $\lambda(T)$, an alternative measure, $\Gamma(T) = 1/\lambda(T)$, was introduced in Ref. [71] to look for critical properties and to identify the different temperature regimes in κ -Cu. In Fig. 3.25, the zero-field spin fluctuation rate, $\Gamma(T)$, is shown for EDT-BCO. It does not reveal any temperature region, where it would approach the zero value as a signature of magnetic ordering. In addition, it remains almost constant down to the base temperature

pointing to significant fluctuations at all temperatures (see below). A similar temperature dependence with a rather featureless low-temperature Γ was found in κ -Cu [71]. As explained therein, the presence of temperature-independent, persistent dynamics at all low-temperature points shows that the system stays in the fluctuating regime. Hence, it might be described as a quantum spin liquid state close to absolute zero (down to 20 mK).

As shown in Fig. 3.25, the almost constant fluctuation rate at low temperatures changes character at higher temperatures. Clearly, a rather slow change takes place below $T \approx 4$ K. As in κ -Cu [71], this mid-temperature change can be assigned to a crossover region. In QSLs, the temperature dependence of this fluctuation rate measured by the NMR or the μ SR fluctuation rates are expected to follow a power law $\Gamma(T) \propto T^w$ [292]. In two-dimensional QSLs, w equals η , the anomalous-dimension critical exponent reflecting the wavevector dependence of critical correlations at the critical point. Here, $w \approx 0.15$, close to the value of $w = 0.27$ found in κ -Cu. However, the two-dimensional critical behavior may be of limited importance in the present case (as it will be shown later). Regarding the observed changed nature of Γ , a related transition was found in the ESR spectra, which is an indication that it concerns all q values simultaneously (see below). One alternative explanation would be that below 0.5 K the correlation time of the temperature-independent channel with persistent dynamics limits the further increase of λ [293], leading to a constant relaxation time at lower temperatures.

In the high-temperature insulator regime, i.e., in the range of $4 \text{ K} < T < 75 \text{ K}$, Γ is seen to be constant. Above the metal-insulator transition, however, a rapid increase of Γ is observed, which is the signature of a high-temperature region better described with a slower fluctuation regime. There, the fast fluctuating limit is not valid anymore, and the μ^+ couples to the BCO rotator component (as discussed below in detail).

To examine the origin of the missing asymmetry as observed at the ISIS facility, additional ZF measurements were performed at the quasi-continuous source in PSI $S\mu$ S. Data measured at this site enables the identification of even fast relaxing components that decay within the deadtime of the pulsed source in ISIS. Thus, our measurements at PSI give relevant information about the existence of loss of muon polarization due to magnetic transitions or the significant muonium content. Fig. 3.28 depicts example zero-field μ SR spectra at two temperatures. The muon depolarization curves were fitted to

$$A(t) = A_1 G_{\text{KT}}(\Delta, t) \cdot \exp(-\lambda t) + A_{\text{Mu}} \exp(-\lambda_{\text{Mu}} t) + A_{\text{bg}} \exp(-\lambda_{\text{bg}} t). \quad (3.11)$$

Here, λ and λ_{Mu} fit the depolarization rates of muons in EDT-BCO and the fast depolarization of the muonium, respectively. The term $A_{\text{bg}} \exp(-\lambda_{\text{bg}} t)$ accounts for the muons that stop in the silver sample holder, with a slow, $\lambda_{\text{bg}} = 0.03 \mu\text{s}^{-1}$ relaxation rate. The fits to the μ SR depolarization curves in Fig. 3.28 show depolarization curves with a muonium fraction of $\sim 22\%$ pointing to a temperature-independent muonium fraction at the low-temperature regime. Importantly, the approximate values of the muonium fraction based on the longitudinal repolarization curves give similar values (see Fig. 3.14). Similarly to other organic compounds

with a large number of unsaturated bonds, all of the observed fast relaxation at short times is a result of the radical state depolarization, it is therefore independent of the magnetic behavior. Hence, it does not point to partial ordering [294]. This assignment is evidenced by the temperature-independence of the observed fraction and the unchanged depolarization rate seen in Fig. 3.28.

To analyze exclusively the fraction of the implanted species in the μ^+ state, transverse field measurements were performed at 5 mT and at 1 mT at low temperatures in PSI. These can be best fitted to

$$A(t) = A_1 \exp(-\lambda_{\text{TF}} t) \cdot \cos(\gamma_\mu B + \Phi_1) + A_{\text{bg}} \exp(-\lambda_{\text{bg, TF}} t) \cos(\gamma_\mu B + \Phi_2). \quad (3.12)$$

Here, B is the applied transverse magnetic field, Φ_1 and Φ_2 are phase shifts and λ_{TF} is the transverse relaxation rate. Fig. 3.29 shows that our measurements reveal an approximately temperature-independent depolarization with a weakly logarithmic behavior as a confirmation of the ZF data.

3.4.4 Spinon spectral density from μSR relaxation

To gain direct information of the QSL state, one needs to assess not only the absence of magnetic ordering but additional proof of exotic spinon excitations is required to unambiguously exclude any other possible state (as I presented in Section 1.3).

In Section 2.2.5, I emphasized that ESR technique is a powerful tool to measure the $q = 0$ excitations, whereas μSR is a local probe. Thus, it is not selective of the wavevectors, and it detects spin excitations for all the possible q values. The response valid to the full spectrum can be separated by the virtue of testing the temperature-dependence of the measured relaxation rate, $\lambda(T)$. In the case of a continuous spinon spectrum of a disordered quantum critical state in one dimension (see below discussion of the dimensionality), spectroscopically two relevant extrema, the contribution of $q = 0$ and $q = \pi/a$ excitations can be separated as $\lambda(T) = \lambda_{q=0}(T) + \lambda_{q=\pi/a}(T)$. Here, $\lambda_{q=0}$ gives a linear and quadratic [295] term, and $\lambda_{q=\pi/a}$ is constant but it displays logarithmic corrections of the type $\lambda_{q=\pi/a} \propto \sqrt{\ln(4.5J/k_B T)}$, where J is the intrachain magnetic coupling [296].

To test the spinon dynamics in EDT-BCO, one cannot use the relaxation rate measured at ZF in all cases, as it may be altered by the presence of a sizable nuclear contribution. The existence of a nuclear component can be excluded via the application of a small longitudinal field. In Fig. 3.27, the low-temperature relaxation rate is depicted in an applied longitudinal field of $B_{\text{LF}} = 2$ mT, which is expected to be independent of the nuclear component. As an additional result, these μSR measurements provide a further proof that the fitted ZF spin fluctuations do not only stem from the nuclear contribution but electronic spin fluctuations also play a role. As the nuclear fields, in general, are in the range of $B \approx 0.1 - 1$ mT, the electronic contribution can be measured using the present magnetic field value of $B_{\text{LF}} = 2$ mT, sufficiently larger than

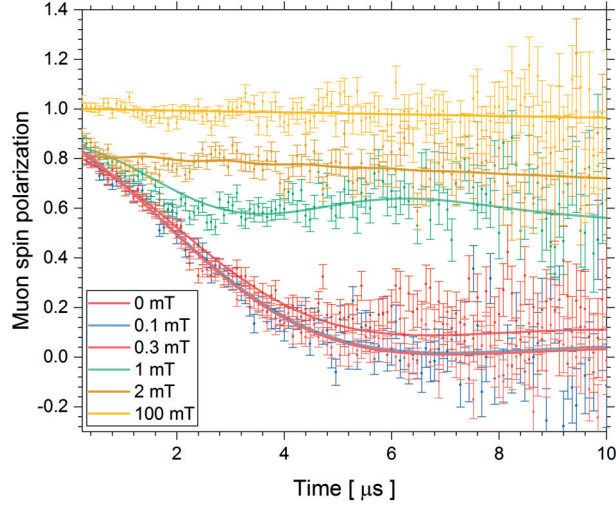


Figure 3.30 – Longitudinal field dependence of the muon depolarization at $T = 80$ mK. Solid lines are fits to the field dependence as defined in Eq. 3.13. Despite partial repolarization at low fields, which is largely due to a nuclear contribution and a transition from the one-dimensional to a three-dimensional relaxation, a significant depolarization is still preserved even at the highest applied longitudinal fields of $B_{LF} = 200$ mT, highlighting the persistence of fast electron spin fluctuations at the lowest temperatures. Note that application of large longitudinal fields leads to a repolarization of the muon asymmetry lost due to muonium formation in EDT-BCO.

the nuclear ones.

Both the data measured at ZF and that measured at $B_{LF} = 2$ mT are shown in Fig. 3.27 and in Fig. 3.26, respectively. The observed temperature dependences do not differ significantly. In both cases, the slow decrease of λ as a function of temperature is an indication that the $\lambda_{q=\pi/a}$ spin excitations are predominant in the present system. In addition, a fit to the λ values at $B_{LF} = 2$ mT yields a $J/k_B = 89(10)$ K and the zero-field data gives $J/k_B = 482(20)$ K. The latter agrees better with the values predicted from DFT calculations. The continuous change of λ while cooling is a confirmation of the shortening of the correlation time down to 19 mK. Thus, it reveals that the measured λ definitely arises due to the presence of prevailing dynamic spin fluctuations in EDT-BCO originating solely from the hyperfine coupling of the muons coupled to the quantum-entangled spin bath of the EDT layer.

3.4.5 Diffusive spin transport from μ SR relaxation

To further investigate the spin transport in the present quasi-one-dimensional QSL, μ SR measurements were performed at longitudinal applied fields (LF) in both facilities from 19 mK to 300 K. Determination of the nature of the spin transport requires the identification of the exact amplitude of the spin fluctuations at several temperatures and fields. Using the LF dependence, I can gain more information about the spin dynamics, and I can distinguish the dimensionalities of the given system. In addition, the LF data may provide insight whether the spin transport is diffusive or ballistic. For 1D diffusion, the spectral density is expected to follow

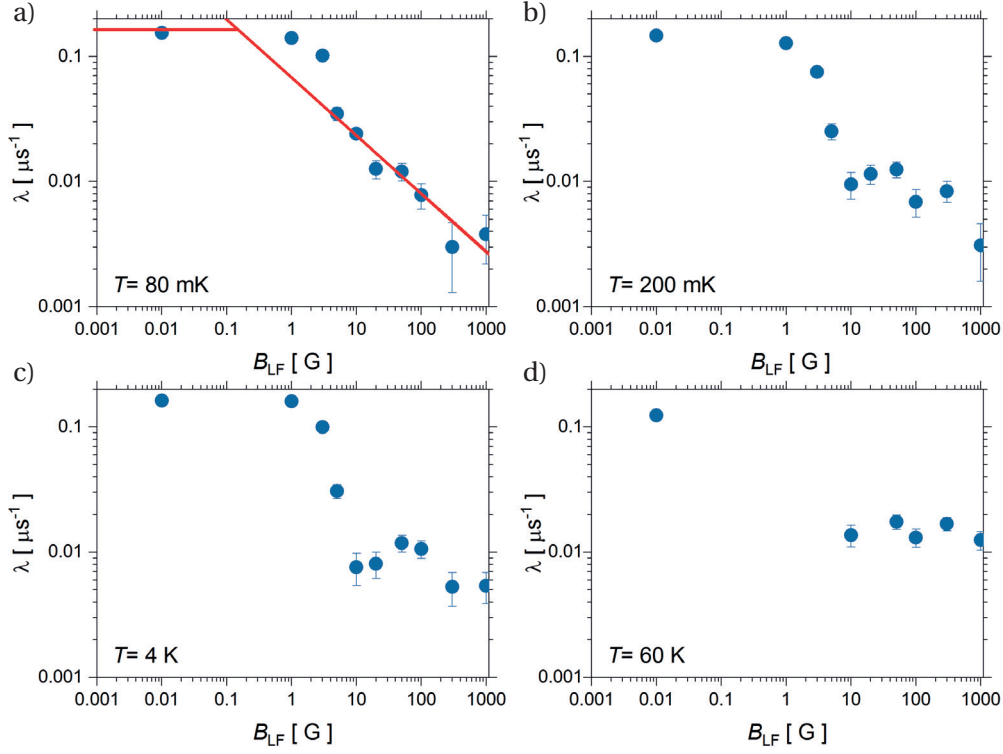


Figure 3.31 – Longitudinal field dependence of λ_{LF} at several temperatures from the quantum critical state to the high-temperature regime of the insulating state. The red lines at $T = 80$ mK illustrate the fit to the 1D diffusive spin transport with a low-field cutoff as a result of higher-dimensional diffusion at longer times. Note that the behavior is preserved up to 4 K, the highest point of the crossover temperature region.

$\lambda(B) \propto B^{-1/2}$, however, for ballistic transport it can be described by $\lambda(B) \propto \ln(J/\mu_B B)$ [295]. The 2D diffusive spin transport follows logarithmic behavior.

Data were acquired at both facilities, and, as discussed in Section 2.2.2, the pulsed source in ISIS results in a significant loss of time resolution as compared to the quasi-continuous source in PSI. However, the pulsed working principle has the advantage of allowing measurements even at longer times. The latter provides us essential information about the longitudinal field depolarization of the static component of our fitted depolarization curves, i.e., the Kubo-Toyabe function. In addition, it enables precise detection of the slow relaxations observed in organic compounds. In contrast, the weak depolarizations coupled to the Kubo-Toyabe function cannot be measured using a continuous source, such as $S\mu S$ in PSI. Thus, I neglect the discussion of the LF data measured at PSI, and I focus on the longitudinal field data from ISIS. As found in Eq. 3.10, the longitudinal field dependence was fitted to the integrated form of the longitudinal field Kubo-Toyabe function defined in Eq. 2.29 multiplied by the Lorentzian depolarization originating from the dynamic local fields in the system. The fitted expressions read

$$A(t) - A_0 = G_{KT,LF}(\Delta, t, B_{LF}) \cdot e^{-\lambda_{LF} t}. \quad (3.13)$$

Here, λ_{LF} , the relaxation rate of a Lorentzian behavior is expected to weakly depend on the longitudinal field, if it arises from a dynamic origin.

Fig. 3.30 depicts the muon spin depolarization for several different applied longitudinal fields at $T = 80$ mK together with fits to Eq. 3.13. The prevailing contribution to the muon depolarization, stemming from the Kubo-Toyabe function with a low Δ value, quickly repolarizes below $B_{\text{LF}} = 2$ mT. Nevertheless, as already seen in Fig. 3.27, a non-negligible fraction of λ_{LF} stays depolarized, even at an applied field of $B_{\text{LF}} = 200$ mT. The remaining depolarization, which clearly originates from a Lorentzian component, uncovers the persisting dynamics¹². The presented field dependence is markedly different from the one seen in inorganic two-dimensional QSLs, such as herbertsmithite (see Section 1.4.2) [114], where the simplicity of the crystal structure results in well-defined muon stopping positions with larger hyperfine coupling with the electron spin bath. Instead, the LF data is similar to the one found in κ -Cu [278], where two different relaxation rate components were identified, and explained by microscopic segregation inducing a quick repolarization at low applied longitudinal fields. Thus, these measurements are to be correlated with data in low-dimensional organic systems [226].

Indeed, the LF dependence shown in Fig. 3.31 is similar to previous data in 1D organic QSLs [290]. The low-temperature muon spin relaxation rate at longitudinal fields, λ_{LF} , is best described at high fields with the power law characteristics of the 1D diffusive transport. In contrast to the spin-1/2 Heisenberg chain systems with weak interchain coupling [290, 291], the power law of $n = 0.47(2)$ fitted here is much closer to the classical model than the anomalous $n = 0.25$ calculated numerically [297]. Furthermore, this finding of a strongly diffusive transport in EDT-BCO reveals a good agreement with the theoretical prediction of diffusive spin transport in systems with large interchain coupling [298]. In principle, this fit is an indirect proof that EDT-BCO, which is placed on the border of a two-dimensional quantum spin liquid state with a diffusive spin transport showing one-dimensional characteristics, presents a prime example of a quasi-one-dimensional quantum critical state.

At low fields, the relaxation rate exhibits a cutoff of the power law fit, from which the anisotropy of the spin diffusion can be determined. In a general ground, the muon can couple to the electronic spin density either by dipolar or by hyperfine interactions. The λ relaxation rate therefore follows

$$\lambda(B) = 1/20 [3D^2 f(\omega_\mu) + (5A^2 + 7D^2) f(\omega_e)]. \quad (3.14)$$

Here, the first term accounts for the dipolar coupling, with the Larmor frequency of the muon $\omega_\mu = \gamma_\mu B$. The second term measures the hyperfine interaction, where the Larmor frequency of the electron is $\omega_e = \gamma_e B$. The constant prefactors, A and D are the scalar and dipolar hyperfine coupling parameters. In this organic system, the assumption that $A \gg D$ is validated through the similarity with other organics. Thus, the second term becomes

¹²Longitudinal-field μ SR spectra, acquired at larger magnetic fields are not shown as the position of the muon beam changes with the magnetic field, leading to an artificial loss of the initial asymmetry.

predominant, yielding: $\lambda(B) = (A^2/4)f(\omega_e)$. The $f(\omega)$ function can be expressed in terms of the fast intrachain and the slow interchain diffusion rates, D_{\parallel} and D_{\perp} , respectively:

$$f(\omega) = \frac{1}{\sqrt{2D_{\parallel}D_{\perp}}} \left(\frac{1 + \sqrt{1 + (\omega/2D_{\perp})^2}}{2[1 + (\omega/2D_{\perp})^2]} \right)^n. \quad (3.15)$$

This equation describes a transition from a constant low- ω value of $(2D_{\parallel}D_{\perp})^{-1/2}$ to a power law behavior. For $n = 0.5$, as it is the case in the ideal 1D diffusive case, it yields $(2D_{\parallel}\omega)^{-1/2}$. In the time domain, a crossover from a one-dimensional diffusion to a higher-dimensional one can be calculated. Given that the scalar hyperfine coupling (A) is not known (muon level crossing measurements would be necessary to determine it), I can only infer the D_{\perp} slow diffusion rate using the low-field constant and high-field power law fits (see Fig. 3.31). I obtain $D_{\perp} = 1.5(5)$ MHz at 80 mK, and it shows very weak T dependence. For D_{\parallel} , I can give an estimate using the classical spin diffusion $(2/\pi)/J$, with the above calculated exchange coupling. This yields about $D_{\parallel}^{-1} \approx 0.3(1)$ ps for the fast intrachain diffusion rate. Using the diffusion rates, a strong anisotropy of $D_{\perp}/D_{\parallel} \approx 5(2) \cdot 10^{-7}$ is inferred. Nevertheless, using the classical spin diffusion model is far from optimal, as the presence of the disorder due to the BCO rotator component is expected to severely affect the spin diffusion. For example, dissipative coupling of quantum noise, such as the Brownian motion, was shown to induce dissipative friction on the spin chain currents in quantum spin chains [299, 300].

If the approximate value of the measured anisotropy is indeed the measure of the anisotropy of the spin diffusion rates, the proportionality of the diffusion rates and the exchange couplings provide a further insight into the ratio of the magnetic couplings. In fact, the strong anisotropy might indicate two different scenarios. It could be a manifestation of a strongly one-dimensional magnetic structure or a very slow interchain spinon transit at low temperatures. This one-dimensionality could be strengthened by the randomness provoked by the mechanical disorder of the BCO molecular rotators [299]. On the other hand, the experimental determination of the interchain spin diffusion rate would provide substantial further evidence, as the randomness of J (or any additional parameter to the present model) may invalidate the simple classical estimates used above [287].

3.4.6 Comparison of high-field and low-field quantum critical state

The ESR characterization is carried out in an applied magnetic field from 0.1 T up to 15 T, and the above presented μ SR measurements only assess the zero-field quantum critical state. Thus, to contrast these results, complementary high transverse field μ SR experiments are required. Fig. 3.32 shows the low-temperature comparison of the weak and high transverse field data, confirming that as high as at 1 T applied transverse magnetic field the sample remains in an unordered state. Application of a large magnetic field does not lead to a substantial broadening of the Fourier lineshape, and the lineshape stays symmetric even in 1 T. In addition, the line does not split into more components, revealing that no partially magnetically ordered fraction

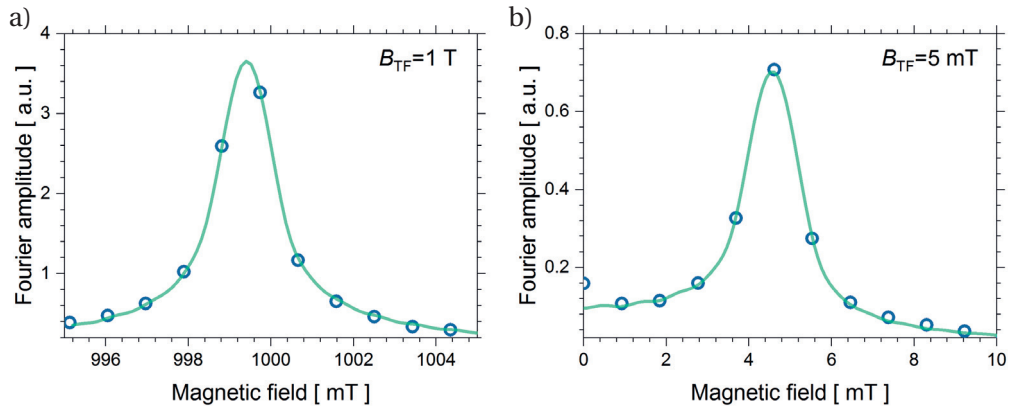


Figure 3.32 – Fourier power spectra of EDT-BCO in transverse magnetic fields of $B_{TF} = 5$ mT (a) and $B_{TF} = 1$ T (b) at $T = 19$ mK. The linewidth of the Fourier line does not increase significantly, giving $B_{rms} = 0.19$ mT at 5 mT and $B_{rms} = 0.57$ mT at 1 T, signaling the absence of a partial magnetic ordering.

shows up in the Fourier μ SR spectrum (as it was shown previously in kagome antiferromagnets [301]). In contrast to κ -Cu, where a partial antiferromagnetic ordering takes place at low fields according to the detailed transverse field μ SR studies [71]¹³, and the measured Fourier spectrum linewidth (B_{rms}) starts to slowly increase above 14 mT, here, only a weak increase of B_{rms} was found.

¹³As I will show in Chapter 4, the static magnetization found by TF- μ SR in κ -Cu is due to the DM interaction, and it does not necessarily originate from an ordered fraction.

4 Antiferromagnetic fluctuations in a QSL candidate

Since the discovery of the first nearly isotropic triangular lattice QSL candidate (κ -Cu) in 2003 [24] (followed by its sister compound, κ -Ag in 2016 [67]), it has been a major challenge to prove that the material is indeed the realization of a true quantum critical state hosting fermionic spinon excitations. The plethora of theoretical and experimental studies in the field boost further the experimental search for exotic behavior in the low-temperature quantum phase. Whereas the magnetic system has been shown to be sensitive to weak perturbations, the complexity of the theoretical descriptions is lagging behind to elucidate their roles separately and to explain the perplexing experimental observations. This is therefore of fundamental requirement for experimental studies to achieve a simplified picture and to identify the most important components.

In the following, I will present a multi-frequency ESR study of κ -Ag that resolves long-standing issues of the magnetic phase diagrams of its sister compound, κ -Cu. I will show that weak spin-orbit coupling, neglected before both experimentally and theoretically [71, 119], is large enough to lead to a Dzyaloshinskii-Moriya interaction that strongly affects the low-temperature magnetic phase diagram [68]. I present both ambient-pressure and high-pressure ESR investigations exploring a rather complex effect originating from the DM interaction.

4.1 Structure and NMR studies in triangular organics

The striking discovery of the QSL state in κ -Cu by Shimizu *et al.* [24], in an organic system synthesized first two decades earlier [124, 303] not only launched the new experimental research field of the two-dimensional QSLs, but it boosted a material design interest for other QSL candidates. This endeavor, motivated mainly by the criteria listed in Section 1.3.1, led to the realization of κ -Ag, a pressure-tunable spin liquid candidate.

These two systems are remarkably similar both structurally and in their physical properties. Fig. 4.1 *a-b* display the layered crystal structure of the sister compounds revealing a similar packing and almost equivalent tilt angles. Both show dynamic charge fluctuations in-between

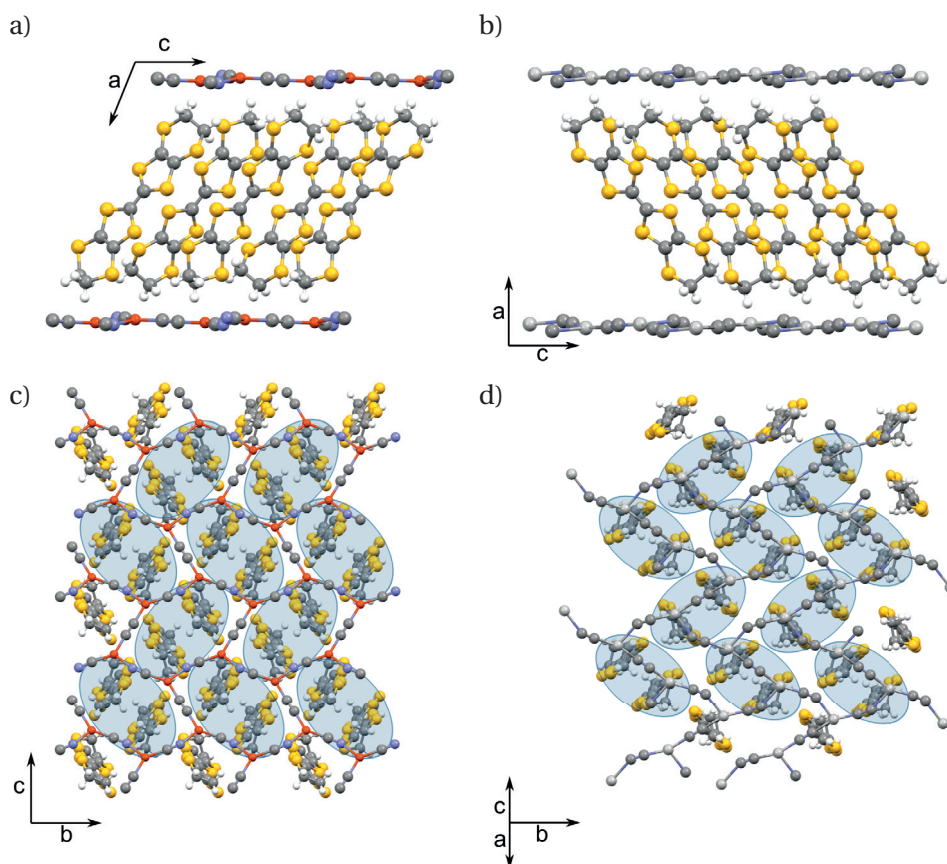


Figure 4.1 – Structural comparison of the sister compounds κ -Cu and κ -Ag. Crystal structures of κ -Cu (a) and κ -Ag (b) viewed along the b axis. Crystal structures obtained by the overlay of the anion layer on the ET conducting layer: c) κ -Cu viewed along the a axis and d) κ -Ag viewed along the $[101]$ direction. Figure adapted from Ref. [302].

the ET molecules down to low temperatures [304]. Furthermore, their symmetry properties are equivalent, both are monoclinic structures within the space group $P2_1/c$. Thus, a glide symmetry operation exists that involves a reflection across the $a - c$ plane (using b as the reflection plane) followed by a $\frac{1}{2}$ unit cell translation in the c direction [302, 305].

Nonetheless, the large ionic radius of Ag(I) as compared to Cu(I)¹ induces a change of the shape and size of the anion openings. Fig. 4.1c and d present the relation of the anion openings and the spin-bearing ET molecules. Relevantly, the *key-keyhole* relation of the ET molecules occurs to be different, possessing a key-on-hole type behavior for κ -Cu and a key-on-rim type for κ -Ag. These different patterns explain the slight deviation of the ET packing, and induce a narrower bandwidth and larger on-site Coulomb repulsion, i.e., an overall larger electron correlation, U/W , in κ -Ag. Furthermore, it leads to a slightly different anisotropy [302].

¹Whereas a number of experimental studies, including ESR investigations [306], faced severe difficulties due to presence of Cu(II) impurities, the absence of Ag(II) was confirmed in Ref. [302] and within the present project.

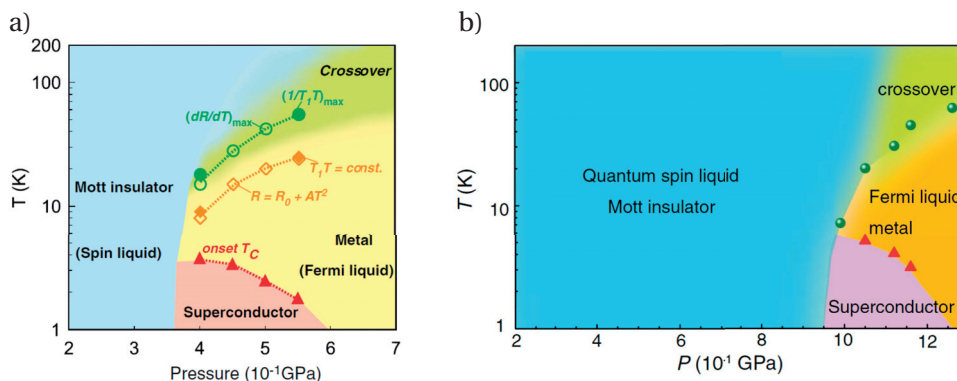


Figure 4.2 – Pressure-temperature phase diagram of the QSL sister compounds constructed on the basis of the resistance and NMR measurements under hydrostatic pressures in κ -Cu (a, figure taken from Ref. [118]) and in κ -Ag (b, figure taken from Ref. [67]) differing by a negative pressure offset of 0.6 GPa. The Mott transition is determined as the resistivity inflection point, $(d\rho/dT)_{\max}$. The upper limit of the Fermi-liquid region is defined as the deviation from $\rho_0 + AT^2$.

More generally, altering the anion layer induces considerable modification of the ground state magnetic and electronic properties. This change allows to tune from conducting [307] (and even superconducting [22]) to insulator state with antiferromagnetic [308, 309], spin-gapped [69], or QSL states. Regarding κ -Cu and κ -Ag, these minor divergences contribute to a phase diagram transformation that cannot be described with a simple chemical pressure. Although the ground state of both systems is a non-ordered QSL state next to a superconducting phase reached without a structural phase transition, the superconducting T_C is almost twice higher in κ -Ag than in κ -Cu (see Fig. 4.2).

4.1.1 Mott transition and superconducting state

Regardless of the minor structural dissimilarities, the phase diagrams depicted in Fig. 4.2 show a number of common peculiarities differing from other systems. In organic charge transfer salts, the Mott insulator-metal transition is a prime example of the so-called *bandwidth-controlled* Mott criticality [310, 97]. As a result of the absence of symmetry breaking, these systems offer *pure* Mott transitions. Hydrostatic pressure-dependent resistivity and NMR studies in other ET-compounds (such as κ -Cl) showed that this Mott transition possesses unconventional criticality [311, 312, 310]. Some of the theoretical studies seem, however, to confirm an unconventional Ising universality class of the resistivity data in κ -Cl highlighting that the global conductivity might depend on other singular observables such as the energy density [313].

In contrast, the Mott transition of κ -Cu was recently demonstrated to possess only an extremely weak first-order component using detailed transport experiments. As a result of Mott delocalization upon application of high pressure, the spinon Fermi surface turns into an electron Fermi surface [314]. The observed continuousness of the transition is in excellent

Chapter 4. Antiferromagnetic fluctuations in a QSL candidate

agreement with theoretical proposals based on large-scale numerical simulations and analytical bosonization that identify the phase transition as a Kosterlitz-Thouless-like one between the *spinon metal* and the Fermi-liquid metal [315, 316].

Furthermore, Anderson's first proposal of a QSL state in high- T_c systems [94] call the attention to the particular similarity of the phase diagrams of high- T_c superconductors and the phase diagram of organic QSLs [67, 118], the only systems accommodating neighboring QSL and superconducting states. Even if the phase diagram of other organic antiferromagnets, such as κ -Cl [311, 317], was identified to be analogous with that found in the high- T_c compounds, the antiferromagnetically ordered systems exhibit an important difference in the pressure-temperature plane, namely, the presence of a *reentrant* Mott transition [318, 319]. This phenomenon, i.e., the sign change of the dT/dp in organic antiferromagnets in the antiferromagnetic state was explained by the change of entropy differences through the simple Clausius-Clapeyron relation ($dT/dp = \Delta V/\Delta S$). Given the absence of magnetic ordering in κ -Cu and κ -Ag, a larger residual spin entropy remains in the spin liquid state as compared to the neighboring Fermi liquid, maintaining a slope $dT/dp > 0$ [320].

The superconducting state that was theoretically suggested to favor either $d_{x^2-y^2}$ pairing due to the triangular lattice distortion [321] or $d_{x^2-y^2} + is$ or p -wave pairing [135, 322] for the undistorted triangular case. ^{13}C -NMR data provided experimental evidence of a non- s -wave superconducting state [323], via finding cubic temperature dependence of the inverse relaxation time, T_1^{-1} , and the absence of the Hebel-Slichter relaxation peak [324, 325]. Furthermore, no pseudogap was found in the Fermi liquid state, unlike in the case of κ -Br [326].

4.1.2 Previous NMR investigations

The absence of magnetic ordering and the emergence of fermionic spinon excitations were first demonstrated using NMR spectroscopy, and only later confirmed from μSR data [71, 126]. Unlike NMR data of κ -Cl where the commensurate antiferromagnetic ordering with a magnetic moment of $0.45 \mu_B$ causes the splitting of the NMR lines [308, 327], no such splitting was observed in κ -Cu and κ -Ag in ^1H -NMR, and later on in ^{13}C -NMR data [24, 67, 119]. Both for κ -Cu and κ -Ag the static spin-susceptibility drops, but does not reach 0, confirming the presence of low-temperature excitations and the emergence of a disordered state. The temperature dependence of the susceptibility fits remarkably well to the theoretical estimate for triangular-lattice Heisenberg model [157], permitting the determination of the exchange coupling experimentally, and providing valuable data for theoretical calculations.

In κ -Ag, the static susceptibility, as expected theoretically [328], is found to be proportional to the spinon density of states, i.e., it scales inversely with the J exchange coupling, the spinon hopping amplitude. In contrast, the dynamic spin susceptibility, measured through $(T_1 T)^{-1}$ (see Eq. 3.4), unveils a sudden drop at the Mott transition in both compounds [118, 67], indicative of a reduction of $\chi''(\mathbf{q}, \omega)$ over the \mathbf{q} space. In the Mott insulator state above 30 K (above 10 K in κ -Cu), $(T_1 T)^{-1}$ points to a weak, power-law increase related to the weak evolution of

the antiferromagnetic correlation length, characteristic of triangular-lattice quantum antiferromagnets. Furthermore, $(T_1 T)^{-1}$ scales with J , approaching a $\sim T^2$ behavior, exhibiting a Korringa law for spin liquids. Remarkably, the low-temperature T_1^{-1} (from ^1H -NMR data) in κ -Ag conforms to slowing down of Lorentzian-type fluctuations below ~ 1 K.

Instead of the appearance of spontaneous moments, ^{13}C -NMR investigations provided evidence of small inhomogeneous, staggered moments [67, 119] but from these studies only the upper limits of $< 0.1 \mu_{\text{B}}$ (for κ -Cu) and $< 0.02 \mu_{\text{B}}$ (in κ -Ag) were extracted, and the exact field dependence of this magnetic moment remained an open question. This was later interpreted by Pratt *et al.* [71] as a signature of a weakly ordered antiferromagnetic state. Even if the staggered moments were speculated to originate from the DM interaction and not from phase segregation, neither the field dependence, nor the size of the DM effect were identified.

4.2 Ambient-pressure fluctuations in κ -(ET) $_2$ Ag $_2$ (CN) $_3$ as seen by ESR

The effect of the DM interaction was presented in κ -type QSLs, and it was clarified that no evidence of the DM interaction was found based on ^{13}C -NMR results in κ -Ag. It is in stark contrast to κ -Cl, in which ^{13}C -NMR was capable to identify the presence of staggered moments already above T_{N} [215]. These observations strongly contradict to each other, as exact diagonalization calculations showed that the size of the DM is similar in the two compounds [68]. Thus, I opted for multi-frequency ESR study in κ -Ag, to demonstrate how the low-temperature properties display a drastic influence of the DM interaction.

4.2.1 Low-field ESR measurements

To unravel the low-temperature behavior of κ -Ag close to the zero-field, low-frequency ESR measurements were performed. These experiments will later serve as a basis for comparison for high-field studies. To provide sufficiently detailed information of this field-range, 4 GHz (with a resonant field of 0.14 T), 9.4 GHz (corresponding to a resonant field of 0.33 T), and 35 GHz (corresponding to a resonant field of 1.2 T) studies were performed. ESR measurables, i.e., temperature dependence of the linewidth (especially, the low-temperature linewidth) and the spin-susceptibility did not show any difference at the three frequencies, slight changes of the magnetic field did not have any effect on them. This is an indication that at the investigated temperature regime (from 1.5 K to 300 K) the 9.4 GHz ESR data can be treated as the zero-field case, as this is still well below the applied field for studies at 35 GHz. Thus, for simplicity, only the 9.4 GHz investigations are shown in the following.

In κ -type charge transfer salts either one or two ESR signals are followed as a function of temperature (or frequency) and crystallographic orientation. As shown in the previous Section, each (ET) $_2$ dimer possesses one hole and this charge is significantly delocalized on the two molecules, inducing a truly dimerized structure. In the ESR experiment, the g -tensor principal values and axes of the crystals correspond to that of the (ET) $_2$ dimers. This not only facilitates

Chapter 4. Antiferromagnetic fluctuations in a QSL candidate

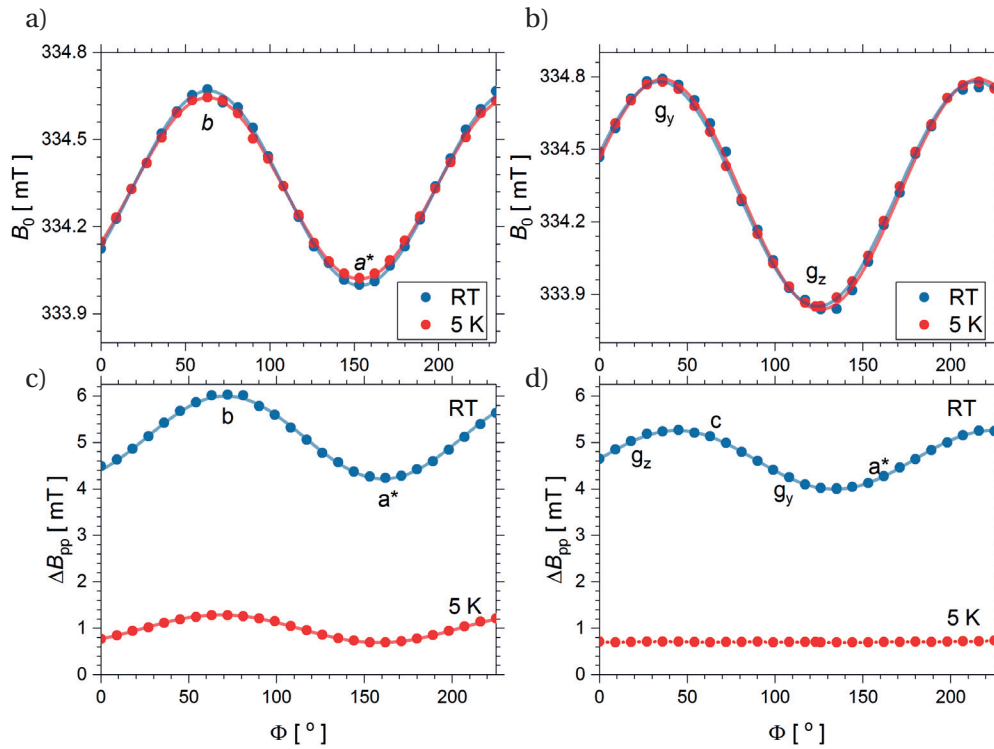


Figure 4.3 – 9.4 GHz ESR resonant field and linewidth angular dependencies at room temperature and at 5 K. As demonstrated here, the ESR line remains unchanged at low frequencies, as the staggered magnetization is almost zero. Angular dependence of the resonant field in the $a^* - b$ (a) and in the $a^* - c$ planes (b) is shown along with angular dependence of ΔB_{pp} in the $a^* - b$ (c) and in the $a^* - c$ planes (d).

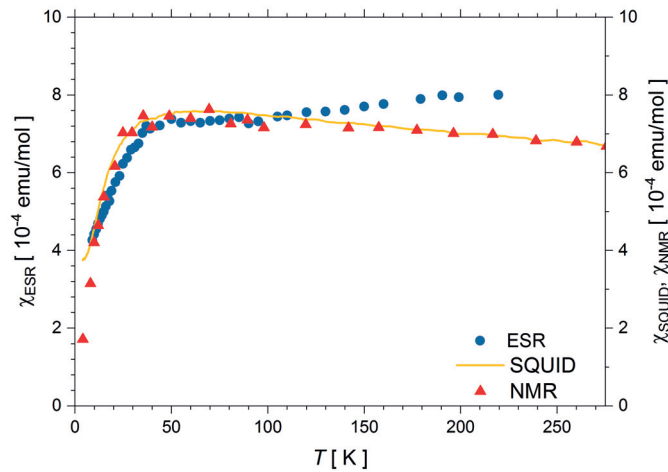


Figure 4.4 – Low-temperature spin susceptibility of κ -(ET) $_2$ Ag $_2$ (CN) $_3$ as measured by SQUID, ^{13}C NMR [67], and ESR measurements. The low-temperature ESR spin-susceptibility fits satisfactorily to the literature data.

the orientation of the crystals in practice but it also ensures that the layer stacking can be identified in the different crystals using ESR spectroscopy. Inversely, the layer stacking presents an additional experimental advantage in some κ -type charge transfer salts, such as κ -Cl and κ -Br, where subsequent layers of ET dimers (*A* and *B*) form a different angle with the inorganic anion layer. The two different *g*-factors of the different donor stackings related to *A* and to *B* layers lead to a splitting of ESR lines at certain angles [222]. Observation of this splitting, as I stressed in Section 2.1.3, serves as a measure of interlayer interaction in these compounds [222, 224]. In κ -Ag, however, the donor stacking (as in, e.g., κ -Cu(NCS)₂ [329]) is equivalent in consecutive layers. The above discussion has two relevant consequences: *i*) only one ESR line is followed at all temperatures and at all frequencies and *ii*) the interlayer interaction cannot be measured using ESR spectroscopy. Despite the lack of direct experimental proof of the interlayer interaction, I will assume it to be negligible based on its structural similarities with κ -Cl.

Fig. 4.3 depicts the angular dependence of the ESR line in X-band. Comparison of the room-temperature and the 5 K ESR signals reveals that the resonant field of the ESR signal does not change, indicating the absence of structural changes and that the signal observed at this temperature regime proves the absence of impurities in the compound. In addition, the observation of the staggered moment, μ_s , would signify that the staggered magnetization becomes sizable already at this low magnetic field but this is absent. Furthermore, the ESR linewidth closely follows the crystallographic orientation, indicating that there is no additional broadening due to the DM interaction at low temperatures. Clearly, the temperature-independent behavior of the overall ESR lineshape is a proof of the paramagnetic, unordered state. Above the antiferromagnetic phase transition, antiferromagnetic fluctuations would be expected to increase, as it was seen in κ -Cl [216, 330] (and in Section 3.2.2, where an ordered antiferromagnetic state was found in [BEDT-TTF]₂⁺[HO₂C-CC-BCP-CC-CO₂⁻] using ESR spectroscopy). In the present system, these fluctuations are not observed. Nevertheless, the ESR line could come from defects that are in the appropriate crystallographical positions in the bulk of the material.

To exclude the possibility that the ESR signal originates from structurally well-defined defects, as explained in the previous paragraph, the absolute ESR spin-susceptibility was determined. Figure 4.4 compares the susceptibility measured by ¹³C NMR, SQUID magnetization, and 9.4 GHz ESR. The microscopic probes, ¹³C-NMR and ESR measure a spin-susceptibility that fits together satisfactorily. It can be concluded that none of these methods include Curie contributions at low temperatures. SQUID magnetization measurements show, however, a low concentration of Curie impurities in the system. The similar spin-susceptibility measured by ESR and ¹³C-NMR reveal that the two-dimensional spin-1/2 triangular lattice structure of the (ET)₂ dimers is in the strongly frustrated regime, and it suggests that comparison of the staggered magnetic moments determined using the two methods is reasonable, as both methods have access to the $q = 0$ regime where the staggered magnetization is expected to give weight. Fitting the spin-susceptibility to the isotropic spin-1/2 Heisenberg triangular

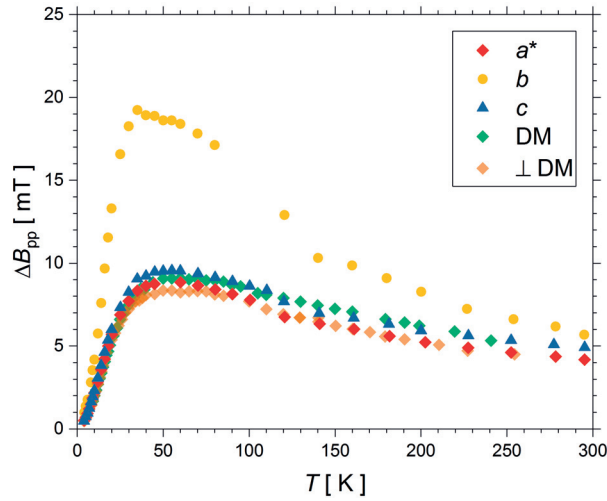


Figure 4.5 – Temperature dependence of the ESR linewidth in the crystallographic directions (a^* , b , and c), in the direction of the DM interaction (DM), and perpendicular to the DM interaction in the $a^* - c$ plane ($\perp \overrightarrow{\text{DM}}$). The maximum around 50 K is assigned to freezing of the C-N disorder [285].

lattice² yields $J/k_B=175$ K for the exchange coupling [157, 158]. Unlike in the case of hybrid molecular rotor systems discussed in Chapter 3, there is no intrinsic disorder in κ -Ag that would provide a low-temperature upturn in the spin-susceptibility. Thus, the weak disorder of the C-N positions in the anion layer does not give a substantial effect at low temperatures in κ -Ag. Disorder may be induced via X-ray irradiation as it was observed in other organic charge transfer salts [332].

As the spin-susceptibility shows a pronounced difference in EDT-BCO and in κ -Ag, it is interesting to examine the temperature dependence of the ESR linewidth. Fig. 4.5 shows the ESR linewidth from 4 K to room temperature at 9.4 GHz (0.3 T) in the crystallographic directions and parallel to the staggered component of the DM interaction. Discussed in detail in Section 3.4.2, ΔB_{pp} depicts an equivalent temperature dependence as the one observed in EDT-BCO and other κ -type salts [281], with *i*) a sizable maximum around 50 K and *ii*) larger linewidth in the direction perpendicular to the reflection plane of the glide symmetry operation (here, in the b direction). I explained the former with charge fluctuations, which, in the present case, is induced by the C-N disorder freezing, or it can be related to the inter-dimer dipole charge fluctuations [285]. The temperature of the maximum may be weakly depending on the cooling rate due to different paces of freezing of the disorder. In addition, $\Delta B_{pp}(T)$ further proves that the DM interaction does not come to play at low temperatures. In the a - c plane, the linewidth stays unchanged independently of the angle formed by DM (see Fig. 4.5).

²Quite remarkably, recent theoretical investigations showed that the dimer Heisenberg model, used for ~20 years [331], seems to be invalid. Despite strong dimerization of the ET molecules, the assumption that the same parameters describe the Heisenberg model of the monomer and the dimer structure was found to be misleading. This approach indicates that two-dimensional QSL materials are to be described as quasi-one-dimensional spin chains, and the spin liquid phase is remnant of Tomonaga-Luttinger physics of spin chains [223].

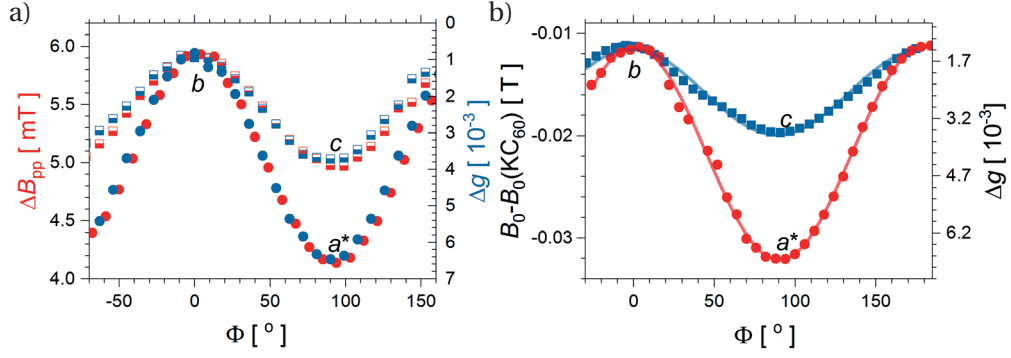


Figure 4.6 – Room-temperature angular dependence of the g -factor (left axis) and ESR linewidth (right axis) in the $a-b$ plane and in the $b-c$ planes at 9.4 GHz (a) and at 210 GHz (b). The high-field angular dependence agrees well with the low-field one. Solid lines are sinusoidal fits to the experimental data.

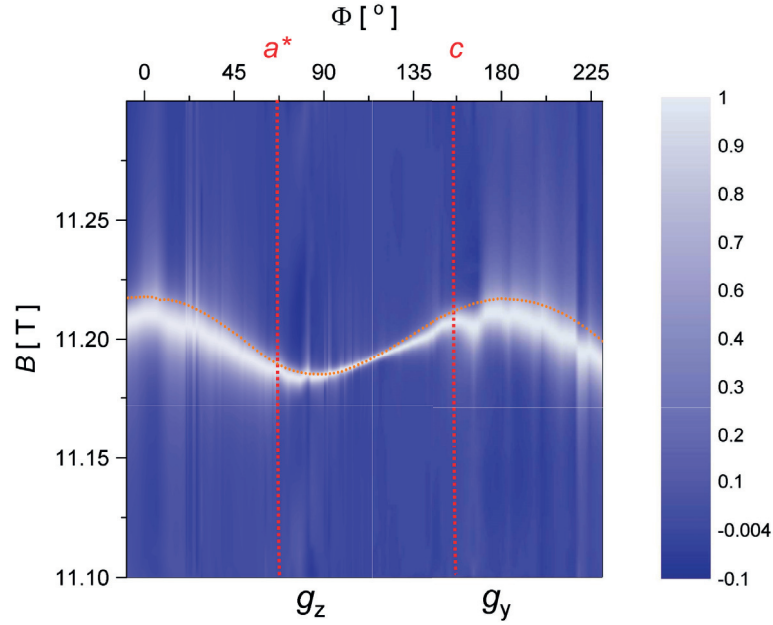


Figure 4.7 – Integrated ESR spectra (3D white area) of κ -(ET) $_2$ Ag $_2$ (CN) $_3$ in the a^*-c plane at 3 K at 315 GHz as a function of the angle formed with the crystallographic a direction. Resonant field of the ESR line at RT at 315 GHz (orange dots). Note that the main g -factor directions form an angle of $25(3)^\circ$ with the a^* and c directions.

4.2.2 High-field ESR measurements

In the following, I will discuss the high-frequency ESR measurements to observe the high magnetic field effects due to the DM interaction, and to identify the defects in the quantum spin liquid state, as it was done in the case of other QSLs, most recently in the inorganic herbertsmithite [333].

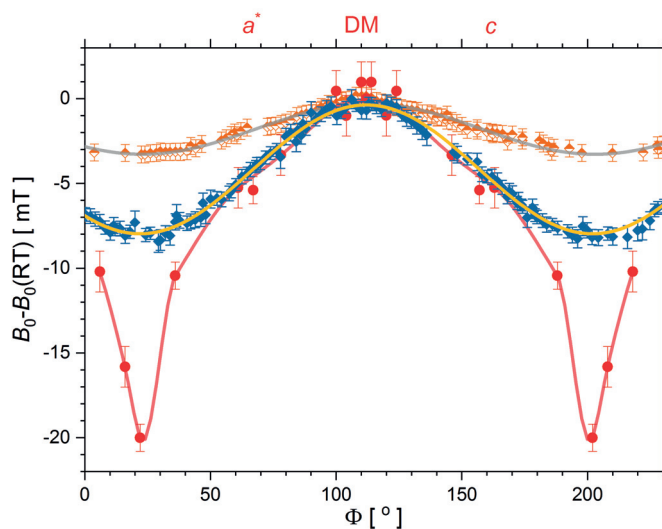


Figure 4.8 – Angle dependence of the low-temperature shift at 210 GHz (light brown squares), at 315 GHz (light blue squares), and at 420 GHz (red circles) as compared to the room-temperature resonant field. The solid lines at 210 GHz at 315 GHz are sinusoidal fits to the Oshikawa-Affleck theory explained in the text. The line at 420 GHz is a guide to the eye.

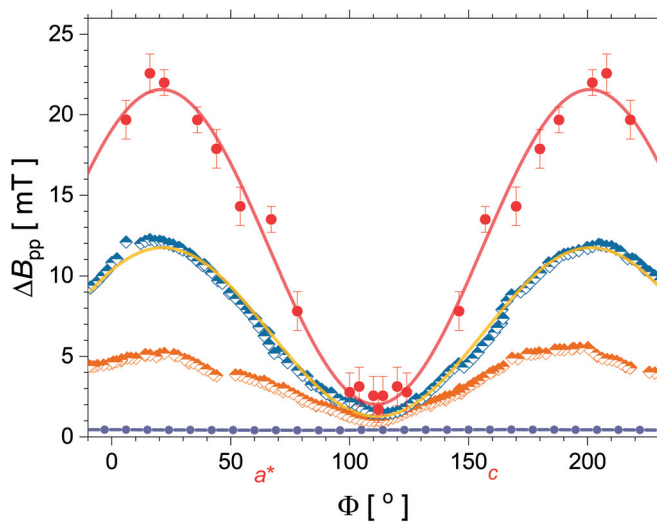


Figure 4.9 – ESR linewidth at 3 K at 420 GHz, 315 GHz, 210 GHz, and 9.4 GHz of κ -(ET)₂Ag₂(CN)₃ in the $a^* - c$ plane as a function of the angle formed with the crystallographic a direction. The solid green curve is a fit to the low-field limit of the Oshikawa-Affleck theory [219] as explained in the text.

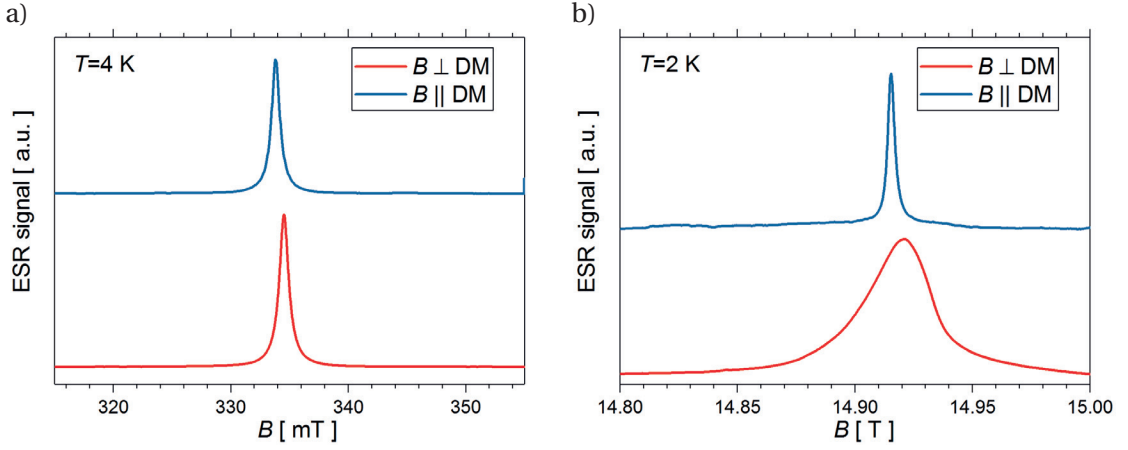


Figure 4.10 – Comparison of the low-temperature low-field and the high-field ESR lineshapes. *a)* ESR spectra at 9.4 GHz at 4 K in the directions parallel and perpendicular to the DM interaction. *b)* ESR spectra at 420 GHz at 2 K in the directions parallel and perpendicular to the DM interaction. Note that the lineshape at a magnetic field of $B_s = 14.8$ T is inhomogeneous, and not Lorentzian anymore.

Theoretical prediction of the DM interaction

Winter *et al.* [68] demonstrated that symmetry considerations imply that the staggered component of the DM interaction lies in the $a^* - c$ plane of the κ -Ag crystal structure. Namely, it was shown in Section 4.1 that the glide symmetry operation involves b as reflection plane. From this, a constraint can be obtained to the DM interaction: $\vec{D}_b = \vec{0}$ [286].

Furthermore, the exact cluster diagonalization calculations in Ref. [68] showed the *staggered* DM interaction to lie in the $a - c$ plane, forming an angle of 45° with both $(-a)$ and $(-c)$ directions, and indicating a value of $\mathbf{D}/\mu_B = (-4.3, 0, -4.3)$ T. The calculated values are close to the ones observed in other κ -salts, such as κ -Cl, κ -(ET) $_2$ B(CN) $_4$, and κ -Cu [68] and to the value experimentally observed in κ -Cl [222].

Given that gauging away completely the DM component in the 2_1 axis direction is not possible, it was found that a small spin gap of the order of $\Delta_s/k_B \approx 10 - 50$ mK is present in the system, in quite good accordance with the experimentally observed spin-gap of $\Delta_s/k_B = 3.5$ mK in κ -Cu [71].

Analysis of high-temperature ESR

To contrast the low-field and the high-field behavior of κ -Ag in the paramagnetic state, room-temperature angular dependence at 210 GHz was measured in κ -Ag and is shown in Fig. 4.6. Clearly, the ESR data measured at 9.4 GHz, and shown in Fig. 4.6*a* is in excellent agreement with the 210 GHz one in Fig. 4.6*b*. This demonstrates that the crystal is a perfect single crystal, and no splitting is observed due to the presence of twins or impurities. Furthermore, it signifies that in the absence of DM interaction the same temperature-dependent values are expected for all ESR measurables, independently of the magnetic field.

Importantly, the high-field ESR experiments presented focus only on the a - c plane for two reasons. Firstly, in the b direction a significantly larger linewidth was found already at 9.4 GHz that is difficult to compare with the smaller linewidth values measured in the a - c plane. In addition, $B \parallel b$ is known to be perpendicular to the DM interaction, i.e., the a - c plane does not only accommodate the direction of the DM interaction, it presents a plane where the angle formed by B and DM can be continuously tuned from 90° to 0° .

Low-temperature effects

Fig. 4.7 depicts a map of integrated ESR spectra in the $a^* - c$ plane at 3 K and at 315 GHz (corresponding to a $g = 2$ position of 11.1 T). For comparison, the resonant field positions found at room temperature (cf. Fig. 4.6b) are shown. Whereas the latter room-temperature data exhibits a clear sinusoidal dependence, the low-temperature, high-frequency data is not reminiscent of a harmonic dependence, a clear deviation can be identified. Downshift of the resonant field is followed by a clear broadening of the ESR line, as it is evident from the 3D mapping. It can be concluded already at this stage of the analysis that the broadening results in a linewidth 8-10 times larger at different angles. ΔB_{pp} is the narrowest, and the resonant field position shift is the smallest in the direction forming an angle of 45° with a^* and c . Thus, in accordance with the theoretical result, the DM interaction points in this direction. It is worth to note that the theoretical proposal described DM 180° away from this position but this sign cannot be differentiated experimentally.

In the following, I turn to the analysis of the observed low-temperature changes of the ESR lineshape. First, I examine the observed downshift of the resonant field position. In Fig. 4.8, this downshift is displayed as the deviation of the $T = 3$ K resonant field position from the room-temperature one at two frequencies, at 315 GHz and at 420 GHz in the $a - c$ plane. The deviation goes to zero at the angle where the magnetic field is parallel to DM, and it is maximal in directions perpendicular to it. Thus, the deviation has no relation to the g -factor of the crystal structure, it only depends on the angle formed by the DM interaction and the magnetic field. Remarkably, the increase of the frequency (and the magnetic field) induces a large increase of the shift. The same data already at 210 GHz (not shown) does not reveal significant deviation of the low-temperature resonant field. This strong, clearly non-linear frequency dependence of the staggered magnetization shows analogy with that observed in κ -Cl [216]. Interestingly, the 315 GHz data fits satisfactorily to a sinusoidal angle dependence, whereas the 420 GHz data points to a fast increase at angles deviating significantly from the $\overrightarrow{DM} \parallel B$ direction.

The resonant field downshift is followed by a fast increase of the measured ESR linewidth. Fig. 4.9 shows the data at 9.4 GHz ($T = 5$ K), 210 GHz, 315 GHz, and at 420 GHz ($T = 3$ K). As for the downshift, the angle dependence depends only on the angle formed by the DM interaction, and a strong, non-linear frequency dependence of the broadening is found. At the angle where $\overrightarrow{DM} \parallel B$, the broadening remains close to zero independently of the frequency ($\Delta B_{pp}(420 \text{ GHz}) - \Delta B_{pp}(9.4 \text{ GHz}) = 1.3 \text{ mT}$), whereas at angles where $\overrightarrow{DM} \perp B$, the broadening

leads to an order of magnitude larger linewidths. The angular dependencies appear to be well described with sinusoidal fits at all frequencies yielding a minimum in the direction $\vec{DM} \parallel B$ and a maximum at $\vec{DM} \perp B$.

To summarize our preliminary observations and to visualize the important change of the spectral shape of κ -Ag by the virtue of a large magnetic field, Fig. 4.10 compares the low-temperature (integrated) ESR lines at 420 GHz and at 9.4 GHz parallel and perpendicular to the DM interaction. At 9.4 GHz, the lineshape is Lorentzian in both directions and their overall linewidth does not differ significantly. Due to the angular dependence of the g -factor of the crystal that is followed even at the lowest temperatures, the ESR lines display a small shift of the resonant field position. In contrast, from the 420 GHz ESR lines only the one measured in the direction parallel to the DM interaction indicates a narrow Lorentzian lineshape. In the direction perpendicular to DM, instead of following a shift due to the g -factor of the $(\text{ET})_2$ dimers, a large downshift of the ESR lineshape is obtained, together with a significant broadening as explained above. In addition, the observed spectrum differs from the Lorentzian lineshape, it cannot be anymore identified by a linewidth and a g -factor, as the spectra become distorted at the highest magnetic fields and at the lowest temperatures.

These discrepancies could result from slight temperature inhomogeneities of the staggered magnetization across the crystal. However, I estimate that this would require a temperature difference at the order of 5-10 K at the two edges of a mm-size crystal to induce such a distortion of Lorentzian-shape ESR signals. More importantly, the distortion can be a signature of a more complicated excitation spectrum, as it was predicted by earlier works in one-dimensional systems [217, 220, 334]. As well, given that the ESR linewidth is a measure of the spectral density of the ESR signal, the inhomogeneous broadening provides information of the inhomogeneous magnetization of the system. This would imply that the quantum spin liquid state is not anymore in a long-range quantum-entangled state, instead, local islands are present with large staggered magnetization. This signifies that the 420 GHz resonant field downshift deviation from the sinusoidal field dependence may be a characteristic of the signal distortion, which results in a local staggered magnetization increase in some of the islands. This assumption is validated by the critically increasing shift (cf. Fig. 4.8) while reaching the positions closer to the $\vec{DM} \perp B$ direction. In this case, the intrinsic upturn of the staggered magnetization points to a state close to a phase transition in a strongly fluctuating regime. Nevertheless, the observed sinusoidal dependence of the ESR linewidth demonstrates that the overall spectral density does not increase fast at these magnetic fields, so the phase transition to the antiferromagnetic state is expected to occur at magnetic fields much larger than the maximal 15 T in my ESR experiments.

We saw that the broadening and the shift of the ESR line only depends on the field applied perpendicular to the DM interaction. Thus, it is reasonable to define the *staggered applied field* as:

$$B_s = \frac{hf}{g\mu_B} |\sin(\phi - \phi_{DM})| \quad (4.1)$$

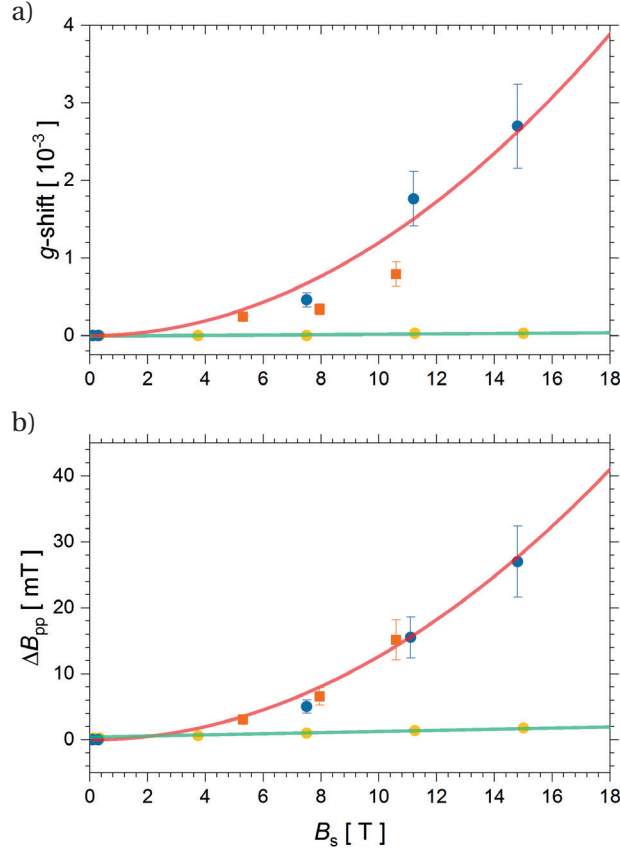


Figure 4.11 – Staggered magnetic field dependence of the ESR measurables. *a*) g -factor shift at 2 K ($\Delta g = g(2\text{ K}) - g(100\text{ K})$). Both $B \parallel a^*$ (tawny squares) and $B \perp \overline{DM}$ (blue circles) measurements are shown. The solid red line is a quadratic fit. For comparison, frequency dependence of the g -shift is shown for $B_s = 0$ ($B \parallel \overline{DM}$) (amber circles). *b*) Broadening of the ESR linewidth at 2 K. The solid curve is a quadratic fit. Both $B \parallel a^*$ (tawny squares) and $B \perp \overline{DM}$ (blue circles) measurements are shown. For comparison, frequency dependence of the linewidth is shown for $B_s = 0$ ($B \parallel \overline{DM}$) (amber circles).

Here $\phi - \phi_{DM}$ measures the angle formed by the DM interaction and the position of the applied magnetic field. Thus, B_s is zero in the direction $B \parallel \overline{DM}$, and it is maximal in directions perpendicular to DM: $B_s = \frac{hf}{g\mu_B}$. Relevantly, this definition is in line with the Oshikawa-Affleck theory (see Section 2.1.3), where the staggered field is the only parameter that identifies the effect of the DM interaction.

To confirm the validity of the above assumption, i.e., that B_s alone governs the broadening and the downshift, Fig. 4.11 and Fig. 4.12 recap the B_s -dependence of the resonant field shift and the broadening of ΔB_{pp} . In order to keep this representation harmonized with the Oshikawa-Affleck theory, Fig. 4.11 displays the resonant field downshift as a low-temperature g -factor shift compared to its room-temperature value. The frequency dependence measured in a broad regime is shown in Fig. 4.11 at $T = 2\text{ K}$ and in Fig. 4.12 at $T = 3\text{ K}$. Furthermore, the angular dependence at 315 GHz in the a - c plane is recalculated to B_s values (using Fig. 4.9), and is shown in Fig. 4.12 together with frequency-dependent data. Clearly, the experimental

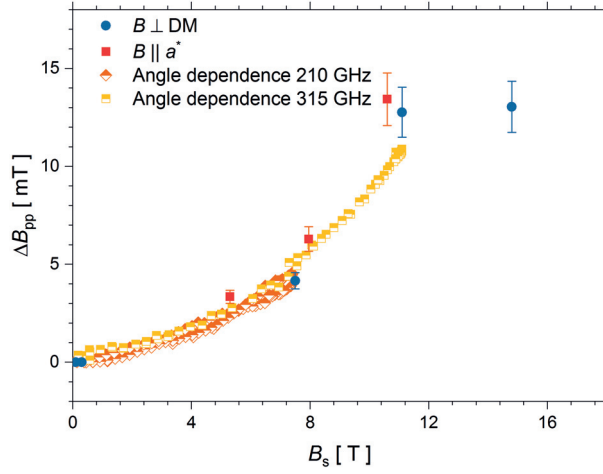


Figure 4.12 – Staggered magnetic field dependence of the linewidth of the ESR signal at 3 K at 210 GHz and at 315 GHz. The frequency dependence found for $B \parallel a^*$ (persian red squares) and $B \perp \overline{DM}$ (blue circles) fit well to our staggered field dependence calculated from the angle dependence (tawny squares).

data is a monotone function of B_s in both depictions, and the angular dependence, giving a quasi-continuous B_s -dependence, fits strikingly well the discrete B_s values of the frequency dependence. Overall, the non-linear fast increase is even more pronounced in these representations.

Nevertheless, knowledge of the magnetic field dependence alone is not enough to describe the relevance of the DM interaction via ESR spectroscopy, as the frequency dependence of the spin excitations may lead to an additional change of the ESR lineshape. Comparison of the maximal B_s field data with the case of $B_s = 0$ at the same frequency is shown in Fig. 4.11. Apparently, this baseline of the g -factor shift and the ΔB_{pp} -broadening yields an almost constant contribution. This means that the dominant contribution is in fact the DM interaction, the frequency-dependent effects present an order of magnitude smaller perturbation.

To investigate the $B_s = 0$ case more in detail, Fig. 4.13 presents g -factor shift and linewidth data separately. In contrast to the effect of the DM interaction, the g -factor remains constant, and a convincingly linear increase of the linewidth is found, in stark contrast with the above discussed non-linear dependence of the results. To reason the slow increase of ΔB_{pp} , several different scenarios may play a role. As in Chapter 3, the low-frequency small linewidth might originate from a *motional narrowing*-like behavior, i.e., the fast fluctuations in the QSL state might lead to a narrow ΔB_{pp} . Thus, high frequencies may partially decrease the strong entanglement and approach the frequency of the spin fluctuations. Alternatively, in κ -(ET)₂-Ag₂(CN)₃, a gapless spin liquid with a spinon Fermi surface, theoretical considerations expect the ESR lineshape to be similar to the two-dimensional Fermi gas [335].

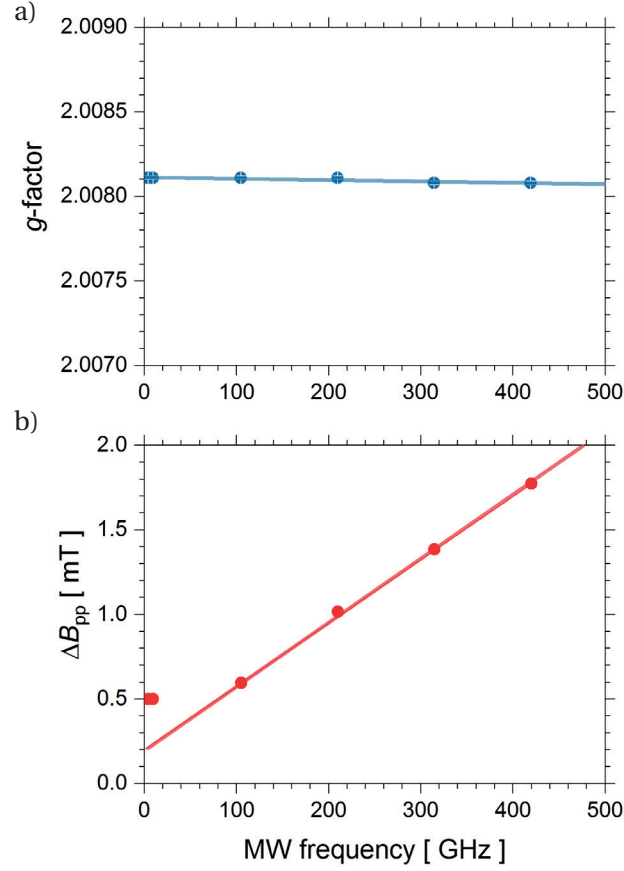


Figure 4.13 – Frequency dependence of the ESR measurables at $T = 2$ K at $B_s = 0$ (along with the 9.4 GHz and 4 GHz data measured at $T = 4$ K). *a*) Frequency dependence of the g -factor in the $B \parallel \vec{DM}$ direction. The solid line is a linear fit. *b*) Frequency dependence of the ESR linewidth at 2 K in the direction $B \parallel \vec{DM}$, the 4.1 GHz and 9.4 GHz experimental points were measured at 4 K. The solid line is a linear fit to the high-frequency points. Note the marked difference compared to $B_s \neq 0$ in Fig. 4.11.

Temperature dependence at high fields

To investigate the critical antiferromagnetic fluctuations, I turn to the analysis of the temperature dependence of ESR spectra. In Fig. 4.14 and in Fig. 4.15 the T -dependence is depicted at 315 GHz in two directions in the a - c plane, parallel and perpendicular to the DM interaction. At high temperatures, as it was presented in Fig. 4.6, the ESR lineshape is similar at both directions. Remarkably, the high-frequency linewidths display a different temperature dependence, to some extent, resulting in a maximum at different temperatures. This is a plausible result for the charge-fluctuation related ΔB_{pp} -maximum, as freezing of the fluctuations is sensed at different temperatures at different frequencies, analogously to the BPP theory.

The effect of the DM interaction comes into play below ~ 30 K. In the DM direction (see Fig. 4.14), the paramagnetic lineshape of the low-frequency ESR spectra is preserved at low temperatures (down to 1.5 K). This lineshape in the DM direction indicates the absence of antiferromagnetic fluctuations down to the lowest temperatures, and it demonstrates that the

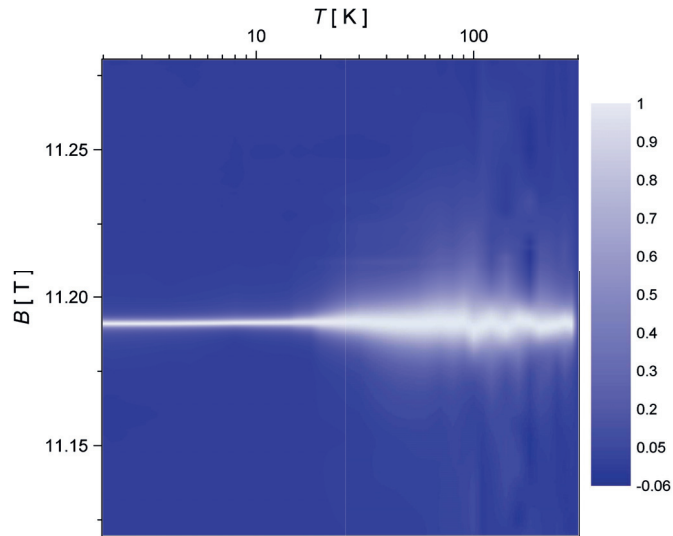


Figure 4.14 – Integrated ESR spectra of κ -(ET)₂Ag₂(CN)₃ as a function of temperature at 315 GHz in the $B \parallel \vec{DM}$ direction in a semilogarithmic scale. The linewidth maximum around 50 K observed at low frequencies is also seen at this frequency. At low temperatures, the ESR lineshape preserves its paramagnetic-like nature with an almost constant intensity.

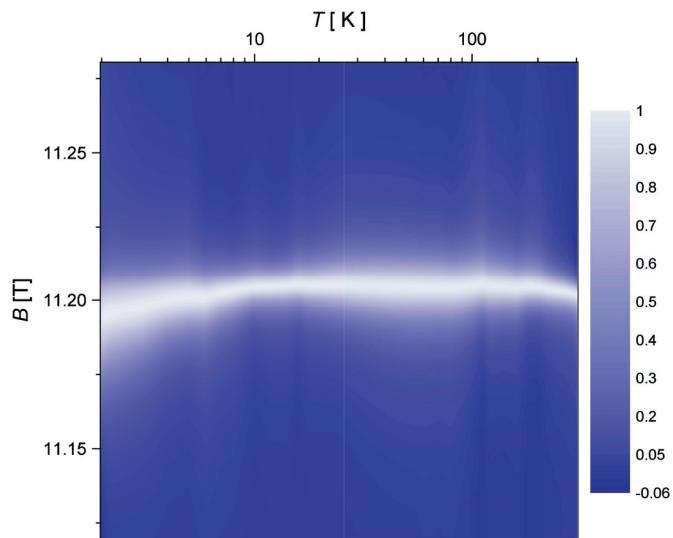


Figure 4.15 – Integrated ESR spectra of κ -(ET)₂Ag₂(CN)₃ as a function of temperature at 315 GHz in the $B \perp \vec{DM}$ direction (in the a - c plane) in a semilogarithmic scale. Note the slow shift of the spectral weight to lower magnetic fields, which indicates a linear change at the logarithmic scale.

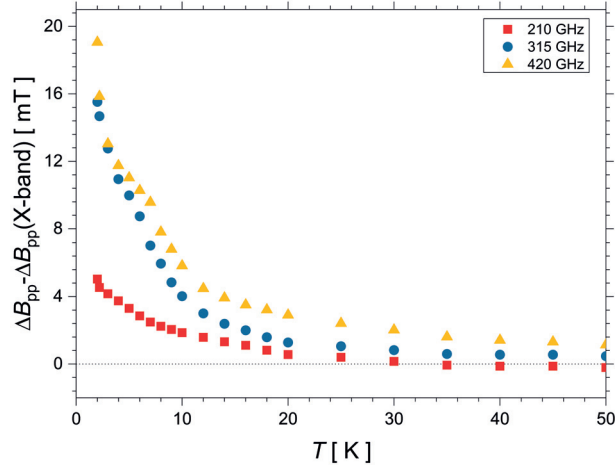


Figure 4.16 – Temperature dependence of the field-induced broadening measured as the difference of high-frequency and 9.4 GHz linewidths in the direction $B \perp \overrightarrow{DM}$. Note that the values below 4 K were calculated with $\Delta B_{pp}(9.4 \text{ GHz})$ at 4 K.

observed excitations of the QSL state are temperature-independent. As discussed in detail above, in the $B \perp \overrightarrow{DM}$ direction (see Fig. 4.15), a linewidth broadening evolves together with a shift of spectral weight to lower magnetic fields. Remarkably, temperature-evolution of the linewidth change turns out to be closely logarithmic as shown in Fig. 4.15.

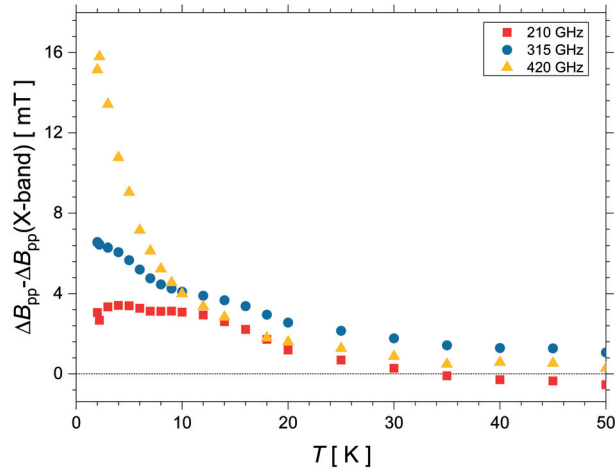


Figure 4.17 – Temperature dependence of the field-induced broadening measured as the difference of the high-frequency and 9.4 GHz linewidths in the direction $B \parallel a^*$ ($\overrightarrow{DM} \angle a^* = 45(3)^\circ$). Note that the values below 4 K were calculated with $\Delta B_{pp}(9.4 \text{ GHz})$ at 4 K.

It is essential to separate the effect of the DM interaction from the charge-fluctuation related linewidth maximum, which gives a significant component at intermediate temperatures, similarly to the case of $\kappa\text{-Cl}$ [216]. For this purpose, data with $B_s = 0$ is reasonable to be used as the baseline. It would be sensible to make use of experimental data at the same frequency with $B \parallel \overrightarrow{DM}$, however, this is not feasible due to the weak dependence of the ΔB_{pp} -maximum

(~50 K) on the angle in the a - c plane (not shown here). As the temperature dependence at high frequencies and at 9.4 GHz turned out to be very similar, comparison of the high-field and low-field ESR linewidth can be used, as well, to give a complete description of the effect solely originating from the DM interaction. Thus, the field effect can be determined at each temperature as

$$\Delta B_{pp,s} = \Delta B_{pp}(\text{high-frequency}) - \Delta B_{pp}(9.4 \text{ GHz}) \quad (4.2)$$

Fig. 4.16 and Fig. 4.17 summarize the calculated linewidth increase, $\Delta B_{pp,s}$ in two different directions in the a - c plane at different microwave frequencies. Fig. 4.16 corresponds to $B \perp \overrightarrow{DM}$, whereas Fig. 4.17 gives the frequency dependence of $\Delta B_{pp,s}$ for $B \parallel a^*$, i.e., perpendicular to the anion layer. The latter gives a factor $1/\sqrt{2}$ smaller B_s values at all frequencies, which results in visibly smaller broadening values. At each field, the T -dependence appears to show the same non-linear behavior as the one observed at the lowest temperatures previously. Thus, this proposed representation of the magnetic field effect is validated by the experimental data. Qualitatively, the temperature dependence seems to change character significantly at the highest frequencies (at 315 GHz and at 420 GHz for $B \perp \overrightarrow{DM}$ and at 420 GHz for $B \parallel a^*$).

$\Delta B_{pp,s}(T)$ as defined in Eq. 4.2 and the g -factor shift, defined as

$$\Delta g = g(\text{low temperature}) - g(\text{high temperature}) \quad (4.3)$$

proved to be convenient descriptions of the low-temperature DM effect. Fig. 4.18 visualizes these critical parameters as a function of the *staggered field*, B_s . Both maps present an increase of critical antiferromagnetic fluctuations with increasing magnetic field and decreasing temperature. The ESR linewidth turns out to be a more sensitive measure of the effect of the DM interaction pointing to fluctuations already at low magnetic fields. Remarkably, a sudden increase in both maps is found at magnetic fields above $B_s > 10$ T. The g -factor shift, i.e., the low-temperature field shift measured by ESR can be rescaled to a staggered magnetic moment, μ_s using the relation [216, 336]

$$\Delta g = g_0 \frac{D}{6B_s} \frac{\mu_s}{\mu_B} \quad (4.4)$$

Here, g_0 is the g -factor in the absence of the effect of the DM interaction. For our system, it corresponds to the high-temperature value. μ_s is the *staggered magnetic moment* upon the application of the magnetic field. Thus, the g -factor is directly related to the staggered moment, μ_s , and it predicts the formation of a field-induced antiferromagnetic state. Regarding the linewidth, as ΔB_{pp} measures the spectral broadening of the staggered component, physically Δg and ΔB_{pp} cannot be simply related. Nevertheless, the Oshikawa-Affleck theory [217, 219] connects the two parameters as given in Eq. 2.22. This field-independent, linear-in-temperature ratio ($\Delta B_{pp,sf}/\Delta g_{sf} \propto T$) suggests that at low temperatures Δg dominates but the linewidth can predict the critical fluctuations at higher temperatures. This is in perfect

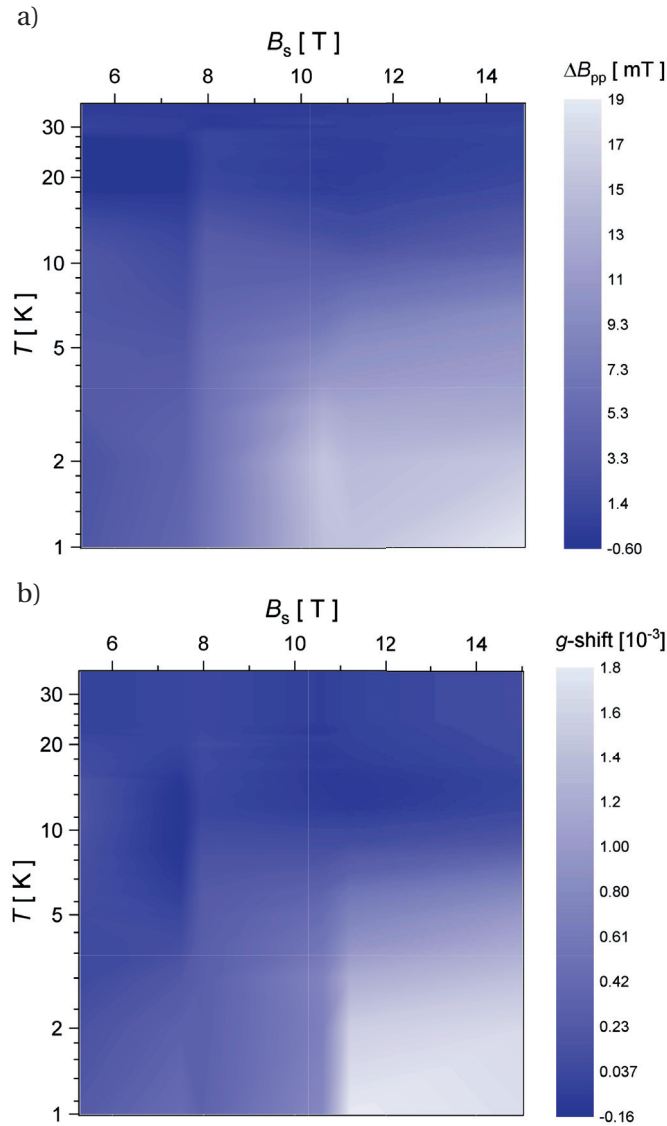


Figure 4.18 – Maps of the low-temperature *applied staggered field* (B_s) dependence of the ESR observables. *a)* The field-dependent component of the linewidth calculated as described in Eq. 4.2, i.e., $\Delta B_{pp}(B, T) - \Delta B_{pp}(B = 0.3 \text{ T}, T)$ (in units of mT). *b)* g -factor shift, Δg as compared to the g -factor at 100 K (in units of 10^{-3}). Both maps provide magnetic field-temperature phase diagrams that demonstrate that critical antiferromagnetic fluctuations increase significantly above $B_s > 10 \text{ T}$. Note that the values below 4 K were calculated with $\Delta B_{pp}(9.4 \text{ GHz})$ at 4 K.

4.2. Ambient-pressure AFM fluctuations

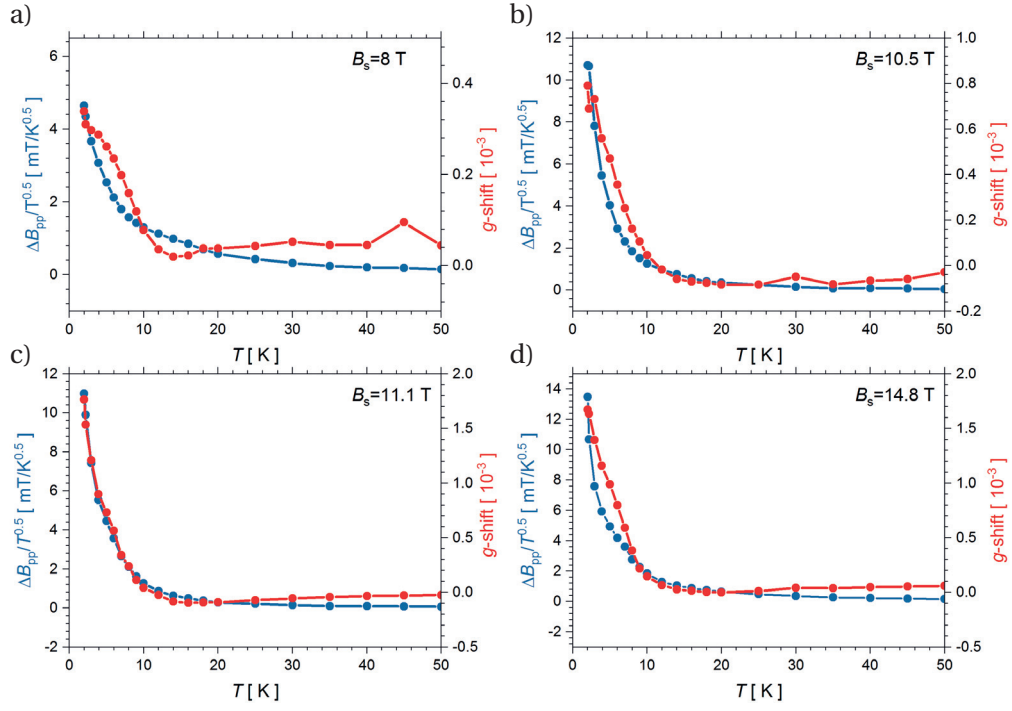


Figure 4.19 – Scaling of the linewidth to the g -factor shift a in the direction $B \parallel a^*$ ($B \perp \overline{DM} = 45^\circ$) at 315 GHz, $b) B \parallel a^*$ ($B \perp \overline{DM} = 45^\circ$) at 420 GHz, $c) B \perp \overline{DM}$ at 315 GHz, and $d) B \perp \overline{DM}$ at 420 GHz.

qualitative agreement with our finding of the linewidth increase being extended to higher temperatures, even to ~ 40 K, whereas Δg appears only below ~ 15 K. In addition, this explains the anomalously large Δg at very low temperatures (seen in Fig. 4.8).

Validity of the Oshikawa-Affleck theory

I concluded above that the observed low-temperature behavior is in qualitative accordance with the Oshikawa-Affleck model developed for one-dimensional systems. To elucidate how this model fits to the present two-dimensional system, I globally fitted the temperature-dependences and the frequency-dependences of the ESR observables in κ -Ag using the model characteristics given in Section 2.1.3.

To examine the frequency dependence, the B_s -dependence of the g -factor shift and the ESR linewidth is presented at $T = 2$ K in Fig. 4.11 and in Fig. 4.12. At this temperature and at this field range, the conditions of the Oshikawa-Affleck theory would give a transition from a quadratic to linear field dependence as shown in Eq. (8.17) and Eq. (8.12) of Ref. [219]. Nevertheless, the measured points in our data are better described with a quadratic curve (shown in Fig. 4.11), corresponding to the low-field limit of the theoretical approximation given in Eq. 2.21. Deviations from this quadratic behavior can only be observed above 10 T. Furthermore, the $\Delta B_{pp} \propto B_s^2$ dependence below 10 T is confirmed through the angle dependence at 210 GHz and at 315 GHz at a fixed temperature of $T = 3$ K (see Fig. 4.12). Thus,

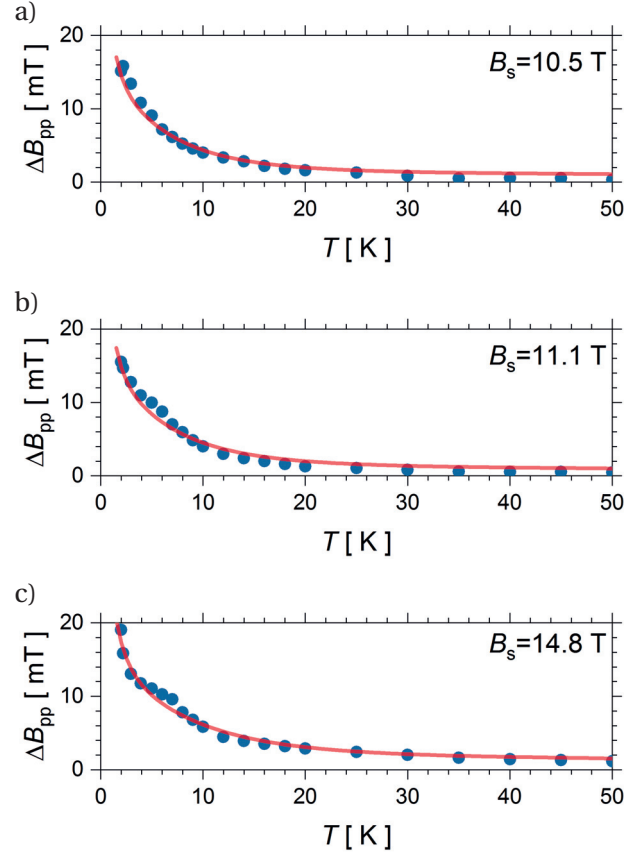


Figure 4.20 – Global fit to the temperature dependence of the staggered magnetic field-induced broadening *a*) at 420 GHz in the direction $B \parallel a^*$, *b*) at 315 GHz in the direction $B \perp \overrightarrow{DM}$, and *c*) at 420 GHz in the direction $B \perp \overrightarrow{DM}$ using the high-field limit of the Oshikawa-Affleck theory developed for one-dimensional systems (see Eq. 2.19 and Eq. 2.20).

all B_s dependences can be described by Eq. 2.21 with a constant $c = 1.2(5) \cdot 10^{-3}$, which is a crystal-dependent parameter, and as such, cannot be directly related to the size of the DM interaction. Assumably, the measured behavior can be understood as a more complicated transition from the quadratic to the linear field dependence in the two-dimensional case. It is noteworthy that I neglected the logarithmic correction of Eq. 2.19 and Eq. 2.20 in these fits. This approximation was found to simplify the numerical task and provide more precise approximations of the fitted parameters in several cases [219, 334].

Interestingly, the temperature dependence of the ESR data does not follow the exact dependence proposed by the low-field Oshikawa-Affleck theory. In fact, at low temperatures, the theory would suggest that the temperature dependence follows (see Eq. 2.21) $\Delta g \propto 1/T^3$ and $\Delta B_{pp} \propto 1/T^2$ after neglecting the logarithmic corrections. These imply that $\Delta B_{pp}/T \propto \Delta g$ would hold as a scaling relation. In our case, the linewidth is best described by $\Delta B_{pp} \propto T^{-0.5(1)}$, and the g -factor shift follows $\Delta g \propto 1/T$ at low fields, whereas Δg satisfies $\Delta g \propto 1/T^{0.5(2)}$ at the highest magnetic fields (above 10 T). All of these are in contradiction with the low-field limit³.

³The staggered susceptibility, χ_s , is defined as the linear magnetic response of the system to the staggered

Thus, I expect the scaling relation $\Delta B_{pp}/T^{0.5} \propto \Delta g$ to hold approximately at all temperatures and at all frequencies. Indeed, Fig. 4.19 shows that these scaling relations hold roughly. Despite the non-trivial relation of the T -dependent broadening and Δg , the identification of these scaling relations can provide substantial input for upcoming theoretical studies.

The above conclusions exposed that the temperature dependence of the linewidth can be better described in the high-field approximation, unlike the frequency dependence following closely the low-field approximation. Given that $k_B T < g_0 \mu_B B$ is satisfied in our highest field measurements in a large temperature range, the high-field limit is a reasonable approximation for our measurements. To demonstrate the excellent correspondance of the Oshikawa-Affleck theory and the experimental data, a global fit is shown in Fig. 4.20 to the high-field approximation fitting all three curves simultaneously to Eq. (8.6) of Ref. [219] using the corrections of Ref. [220] (see Eq. 2.19 and Eq. 2.20). This global fit yields $\lambda = 1.25(20)$ for the logarithmic correction and $c = (4.7(5)) \cdot 10^{-3}$ for the ratio of the coupling and the DM interaction using $J/k_B = 175$ K [67]⁴. Thus, the staggered component of the DM interaction is found to be well approximated with $D/\mu_B = 1.2(2)$ T, a value somewhat lower than the calculated one of 5.5 T [68]. As these fits were performed using a one-dimensional theoretical description, the difference does not contradict to the theoretically calculated staggered DM component to be valid, it rather demonstrates the limitations of our simplified model.

It is therefore useful to directly compare the present experimental results to those obtained from ESR measurements in other two-dimensional systems. In the case of κ -Cl [216], the system orders at a Néel temperature of 24 K. 10 K above the ordering temperature Δg reaches $\Delta g_{\kappa\text{-Cl}}(T = 34 \text{ K}) = 3 \cdot 10^{-3}$, at a staggered magnetic field of $B_s = 8$ T. At a similar field at 2 K, the present measurements in κ -Ag gave $\Delta g_{\kappa\text{-Ag}}(T = 2 \text{ K}) = 3 \cdot 10^{-4}$, an order of magnitude lower shift. As well, a similar difference is observed for the broadening of the ESR signal. Previous ESR measurements in κ -Cl [222], however, were consistent with the calculated DM values. Thus, the lower shift and the lower broadening in κ -Ag cannot be a result of a small staggered DM component. Instead, I speculate that the quantum critical state of κ -Ag suppresses the effect of the DM interaction, similarly to the case of EDT-BCO.

4.2.3 Comparison with ¹³C-NMR and μ SR

Determination of the staggered magnetic moment, μ_s , from Δg gives an opportunity to contrast these ESR results with ¹³C-NMR data, where the staggered magnetic moment remained unobserved [67]. Namely, non-linear effects in the shift of outer ¹³C sites were not seen. Thus, nonlinear dependence of the staggered magnetic moment on B_s found by ESR indicates that the linear shift observed in ¹³C-NMR measurements cannot be induced by the DM interaction.

field. Remarkably, the fitted temperature dependence satisfies the Curie relation $\chi_s \propto 1/T$ at fields below 10 T as assumed by Winter *et al.* [68].

⁴It is noteworthy that in the global fits, $c^2 J$ and λJ are fitted simultaneously to the temperature dependences, whereas η_0 , the constant is fitted for each curve, separately. Therefore, λ and c are scaled with the chosen J magnetic coupling.

To decrease the number of lines related to the different sites, ^{13}C -NMR data are acquired in the direction $B \parallel a^*$ leading to a factor $1/\sqrt{2}$ decrease of the B_s staggered field. Assuming that the staggered component of the DM interaction is close to the calculated value [68], $|\mathbf{D}/k_B| \approx 4.1$ K, and using the largest g -factor shift ($\Delta g \approx 3 \cdot 10^{-4}$, see Fig. 4.18), the expected staggered magnetic moment at 1.5 K and at the highest staggered field of the NMR measurements, ~ 6 T is: $\mu_s = 1 \cdot 10^{-3} \mu_B$, which is well below the sensitivity of the NMR measurements. It must be emphasized that determination of the shift in NMR data is a challenging task, as it would require the fit of a broad spectral component of the NMR spectra, which is overwhelmed by the narrow component of the inner ^{13}C sites [67]. However, at 15 T staggered field and at 1.5 K, the staggered magnetic moment measured by ESR increases to ($\Delta g = 1.7 \cdot 10^{-3}$) $\mu_s = 6 \cdot 10^{-3} \mu_B$. Based on the data found in NMR measurements in $\kappa\text{-(ET)}_2\text{-Cu[N(CN)}_2\text{]Cl}$ [215], this staggered magnetic moment would also be observable by NMR. Thus, high-field ^{13}C -NMR measurements can be proposed to clarify the discrepancy of the results of the two techniques, to verify experimentally the size of the staggered moment, and to follow the critical behavior at low temperatures. Notably, these very small magnetic moments are not thought to give rise to a phase transition as seen, e.g., in herbertsmithite [149], unless the low-temperature, high-field ($B_s > 10$ T) fast increase of Δg (and thus, μ_s) becomes even more dominant at lower temperatures. As the simplest approximation, the phase transition is expected at $B_c \approx (D_c - D)/\mu_B$, where $D_c \approx 0.1$ J is the critical DM interaction strength, where the quantum critical state is not anymore preserved in kagomé [148, 149]. In our case, this yields $B_c \approx 31$ T in $\kappa\text{-Ag}$ using the results of exact cluster diagonalization calculations. These considerations signify that the long-range antiferromagnetic order proposed theoretically in Ref. [148] is at magnetic fields (and temperatures) well above (well below) the studied regime. Therefore, it remains an open question for future studies whether the AFM resonance modes can be found using ESR spectroscopy.

Given the absence of a phase transition in ESR, it is interesting to compare the ESR data with the μSR results in $\kappa\text{-Cu}$ that suggest a phase transition, and the formation of a weakly antiferromagnetic state with unique properties at low fields of $B = 14$ mT [71]. The phase diagram of Pratt *et al.* [71] compiled of ^{13}C -NMR and μSR measurements was recently reanalyzed theoretically [68]. It was argued that the observed transition is a result of a crossover from a staggered field-induced magnetic moment to a uniform field induced magnetic moment. In fact, the crossover exponents in the phase transition region were perfectly described by these two regimes.

More recently, Isono *et al.* [140] demonstrated that the temperature- and field-dependence of the susceptibility ($\chi(T, H)$) determined from magnetic torque data in $\kappa\text{-Cu}$ exhibit exotic quantum critical scaling, which could not be explained by any previous theoretical models. As I show in Appendix B, the change of the susceptibility can be explained by the presence of the DM interaction found by ESR, and a closely Curie-like low-temperature increase of the susceptibility due to the intrinsic disorder of the system. Relevantly, the low-temperature, high-field Oshikawa-Affleck theory provides a closely perfect global fit to the magnetic torque data.

4.3 High-pressure antiferromagnetic fluctuations

As I presented in Section 4.1, in contrast to κ -Cu, the pressure tunable exchange coupling in κ -Ag ensures that systematic studies can be performed in a large pressure range in the spin liquid state. Furthermore, the phase transition from the spin liquid to the superconducting state is more easily reachable in κ -Ag, as the highest critical temperature is larger in this system (the maximum approaching $T_c \approx 6$ K), and the pressure range is more suited to our piston cylinder pressure cell (Section 2.1.2). The exotic phase diagram of κ -Ag allows to follow this phase transition, and it affords to test the previous assumptions on the effect of the DM interaction and on the ~ 50 K charge fluctuation-related maximum of the ESR linewidth.

I performed high-pressure ESR measurements in the $B \parallel a^*$ direction to follow these changes covering the phase diagram as a function of pressure and temperature⁵. As described above, this field direction corresponds to a staggered field of $B_s \approx B/\sqrt{2}$ at ambient pressure⁶. Given that the presence of any structural transition at high pressure would have been clearly visible from previous ^1H -NMR, ^{13}C -NMR, or resistivity investigations [67], or in previous detailed investigations in κ -Cu [314, 118], the DM direction is expected to remain unchanged in this pressure range. Along with the DM direction, the staggered field, B_s , is constant in the chosen a^* direction. Nevertheless, the size of the DM interaction and the ratio of DM as compared to the exchange interaction, J , strongly depend on the size of the transfer integrals. Indeed, theoretical calculations carried out in the case of an organic ferromagnet [337] demonstrate that the size of the DM interaction and that of the exchange interaction may be different. Here, I cannot rely on theoretical calculations, but I speculate that the examined pressure range is small enough to keep the D/J ratio constant. In particular, this hypothesis is reasonable in the low-pressure regime relevant in my low-temperature investigations.

4.3.1 High-temperature charge fluctuations at high pressure

Pressure-dependent transport investigations by Shimizu *et al.* [67] do not point to a phase transition close to room temperature up to the highest pressures (1.2 GPa) (see Fig. 4.2). Fig. 4.21 presents the ESR linewidth from detailed p -dependent ESR measurements at 260 K. ΔB_{pp} depicts a linear increase with pressure, proving the lack of phase transition in this pressure regime ($p < 1.5$ GPa). Importantly, the g -factor remains unchanged (not shown). As the intermolecular distance decreases with pressure, the linewidth, originating from charge fluctuations possesses a slow increase in this high-temperature paramagnetic insulator state. Remarkably, the linewidth possesses only a weak, pressure-independent field dependence demonstrating that the ESR signal does not originate from paramagnetic impurities and

⁵Given that the pressure of the Daphne 7373 oil, which is used as a pressure medium, has a temperature dependence that leads to a drop of 0.15 GPa between room temperature and 1.5 K, all low-temperature and high-temperature analyses are shifted by this value.

⁶Relevantly, the low-temperature effect of the DM interaction is decreased in this direction. Nevertheless, the ESR signal increases significantly if the sample is positioned on the microwave mirror, and the smaller low-temperature linewidth further improves the signal-to-noise ratio compensating the loss due to the high-pressure setup.

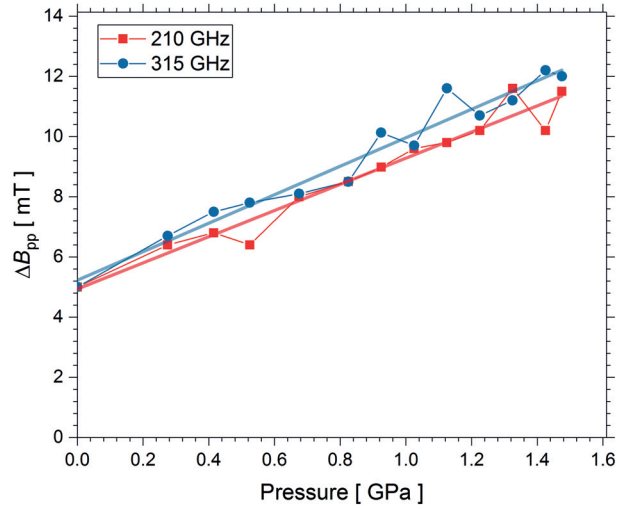


Figure 4.21 – Pressure dependence of the ESR linewidth at 210 GHz and at 315 GHz at 260 K. The weak pressure dependence stems from the decrease of intermolecular distance affecting the high-temperature charge fluctuations. Note that there is no sign of phase transition in the studied pressure regime.

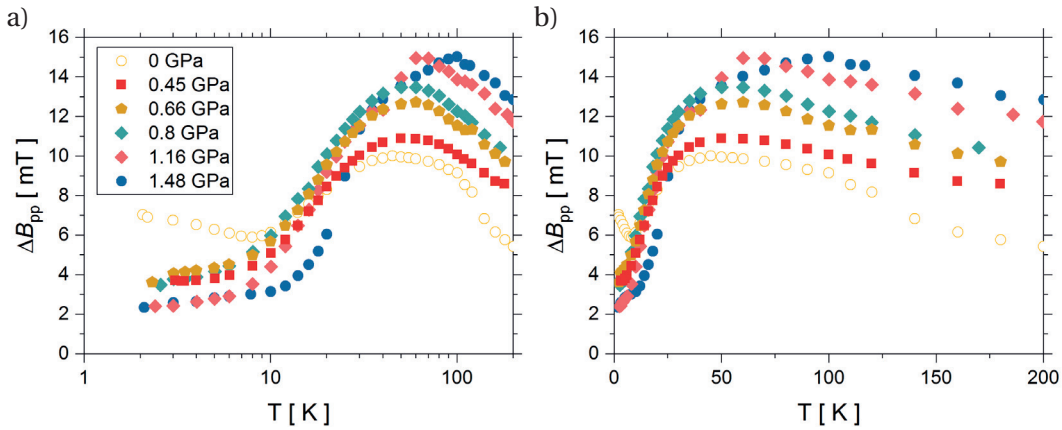


Figure 4.22 – Temperature dependence of the ESR linewidth at several different pressures at 315 GHz displayed in semilogarithmic (a) and linear (b) scales. The maximum of $\Delta B_{pp}(T)$ shifts to higher temperatures and shows increasing maximum value with increasing pressure. Note that the decrease of ESR linewidth at 1.48 GPa around ~ 20 K reveals the low-temperature metallic state.

further proving that the ambient-pressure state is preserved at high temperatures.

The pressure-dependent change of the charge disorder is most conveniently followed through the p evolution of the charge fluctuation-related ESR linewidth maximum observed at ~ 50 K in the ambient-pressure studies (cf. Fig. 4.5). In Fig. 4.22, $\Delta B_{pp}(T)$ is displayed at several different pressures. A similar *peak* is witnessed at all pressures, nevertheless, its exact temperature dependence is pressure-dependent: *i*) the maximum shifts to higher temperatures with increasing pressure, and *ii*) the maximum value of ΔB_{pp} increases with p . These variations are consistent with the increased electron mobility that moves the fluctuation maximum to

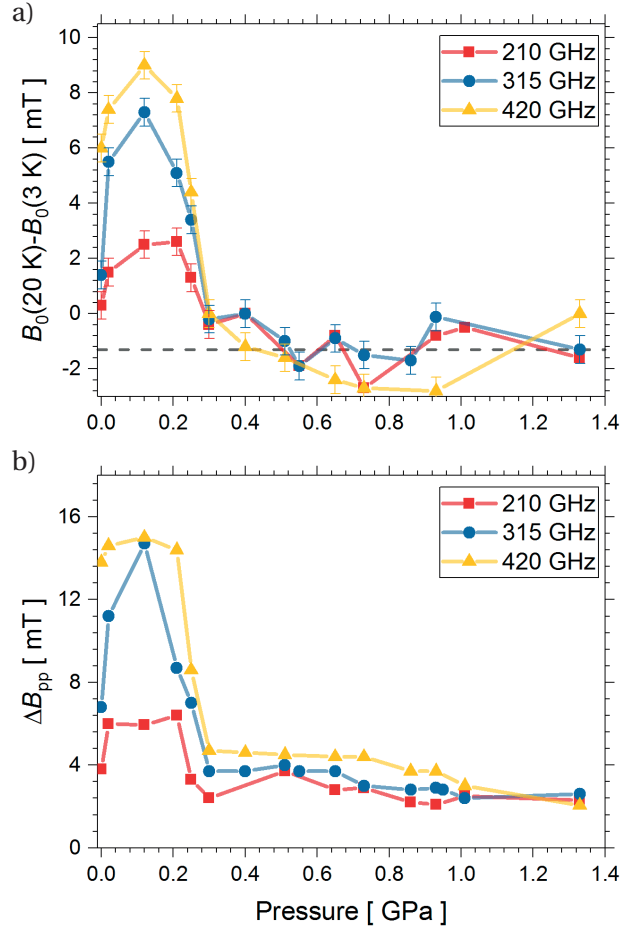


Figure 4.23 – Pressure dependence of the low-temperature ESR observables at 210 GHz, 315 GHz, and 420 GHz revealing the suppression of the effect of antisymmetric exchange at 0.35 GPa. *a)* Resonant field shift of the ESR signal at 3 K using the 20 K value as a reference. Note that the negative shift values agree with the g -factor anisotropy change found in κ -Cu in Ref. [140]. *b)* Frequency-dependent linewidth displaying three different pressure regimes dominated by the DM effect ($p < 0.35$ GPa), fast spin fluctuations ($0.35\text{ GPa} < p < 0.9$ GPa), and the metallic state ($0.95\text{ GPa} < p$).

higher temperatures. In addition, the decrease of interplane distances increases the effect of the anion layer C-N charge disorder upon the cation layer. Notably, both effects lead to the above described high-temperature linear-in-pressure increase of $\Delta B_{pp}(p)$.

4.3.2 Pressure-tunable antiferromagnetic fluctuations

In Section 4.2, I provided a detailed analysis of the AFM fluctuations emerging at low temperatures as a result of the DM interaction. In the following, I focus on the effect of hydrostatic pressure upon the low-temperature state.

Fig. 4.23*a* depicts the pressure dependence of the resonant field shift at 3 K compared to the 20 K value used as a reference at different frequencies. Interestingly, the resonant field shift

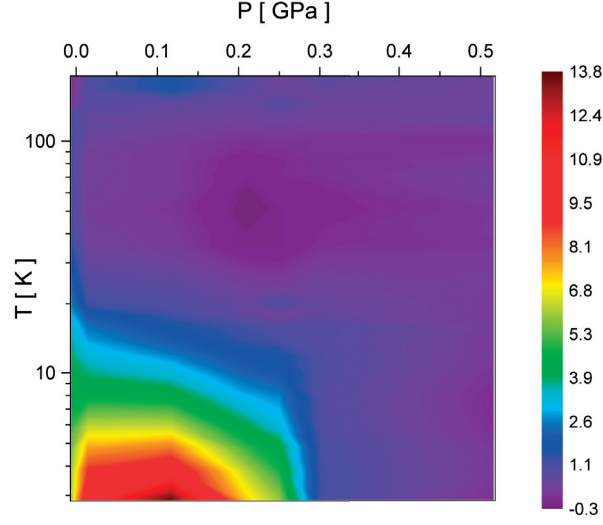


Figure 4.24 – Map of the pressure- and temperature-dependent broadening at 315 GHz. The linewidth at 9.4 GHz is subtracted to remove the effect of charge fluctuations: $\Delta B_{pp}(315 \text{ GHz}) - \Delta B_{pp}(9.4 \text{ GHz})$. Note the dome shape and the quick drop of the effect of the DM interaction at $\sim 0.3 \text{ GPa}$.

drops to below 0 at a moderate hydrostatic pressure of $p \approx 0.3 \text{ GPa}$. The surprising negative resonant field shift is reminiscent of the weak distortion found in magnetic torque data in $\kappa\text{-Cu}$ [140], which exhibited a clear 3° change of the g -factor principal axis from 30 K to 1.6 K. In Fig. 4.23b, the pressure dependence of the ESR linewidth, $\Delta B_{pp}(p)$ is shown at 3 K. Along with the resonant field shift decrease, the ESR linewidth, as the other fingerprint of the DM interaction, unveils a definite drop at the same pressure of $p \approx 0.3 \text{ GPa}$. At this pressure, the frequency (field) dependence of the linewidth alters from quadratic to linear (discussed below).

The meaningful drop of the DM effect at this pressure regime, away from the Mott transition and in the absence of any structural transition is a striking observation that remained unnoticed in previous ^1H -NMR and ^{13}C -NMR investigations. This experimental result is all the more compelling in Fig. 4.24. Therein, temperature and pressure dependence of the antisymmetric exchange-induced $\Delta B_{pp}(p, T)$ broadening are presented as defined in Eq. 4.2. The complicated pressure- and temperature-dependence of the DM effect, seen as a *dome*-shape pattern can be explained as the competition of two counteracting changes: *i*) increase of the J exchange interaction with pressure and *ii*) *strengthening* of low-temperature quantum fluctuations with decreasing U/t . As NMR studies showed and in line with expectations, the size of the exchange interaction increases significantly with pressure. It contributes to the increase of a g -factor shift and the broadening of the ESR signal as demonstrated by the high-field Oshikawa-Affleck approximation (see Eq. 2.19). This situation is perfectly resolved at pressures $0.15 \text{ GPa} < p$, exhibiting a definite increase of ΔB_{pp} in the mapping at the lowest temperatures.

4.3. High-pressure antiferromagnetic fluctuations

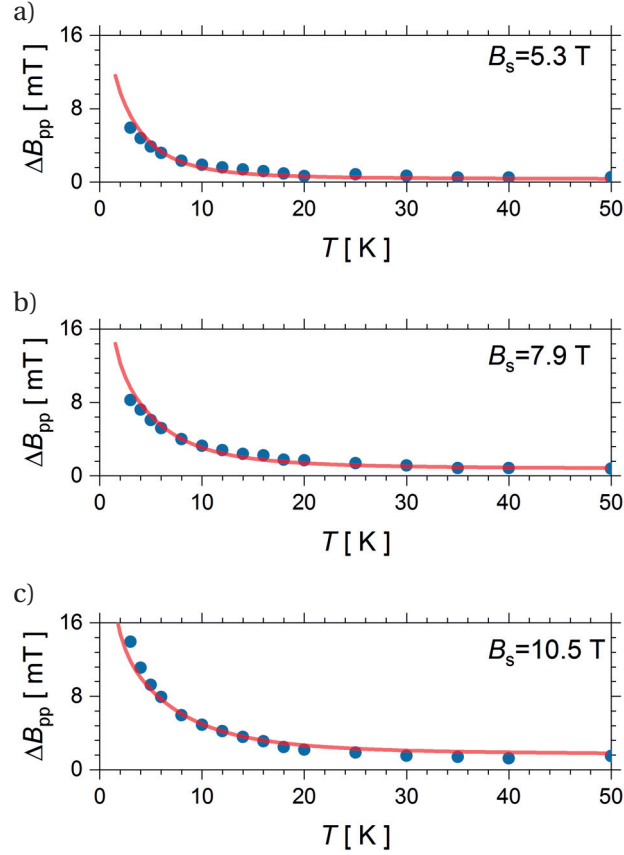


Figure 4.25 – Example of global fits to temperature dependence of the staggered magnetic field induced broadening at an applied hydrostatic pressure of $p = 0.21$ GPa in the direction $B \parallel a^*$ at 210 GHz (a), at 315 GHz (b), and at 420 GHz (c). As in Fig. 4.20 at ambient pressure, satisfying agreement is found with the high-field limit of the Oshikawa-Affleck theory.

Nevertheless, the map of Fig. 4.24 depicts a sudden drop of the broadening above $p > 0.3$ GPa. The increase of t induces a drop of U/t , moving κ -Ag away from an ordered phase. As it was calculated [120, 123, 338], and as it is shown in Fig. 1.5, the QSL state and the spiral-ordered state lie both in the same $t'/t \approx 1$ line, separated only by small negative chemical pressure. The antiferromagnetic low-temperature fluctuations are, thus, further strengthened by the vicinity of this ordered phase at ambient pressure in perfect agreement with theoretical proposals [339]. Decrease of U/t on the $t'/t \approx 1$ line engender a decrease of this *proximity*-phenomenon, and reduces the effect of the DM interaction despite the unchanged D/J ratio. This is in perfect accordance with the ambient-pressure result that the antiferromagnetic fluctuations are considerably smaller than it would be expected based on theoretical predictions of the DM interaction size.

To confirm the relevance of the two distinct effects and to separate their contribution to the ESR signal, I performed global fitting of the broadening of the ESR linewidth to the high-field limit of the Oshikawa-Affleck theory. Similarly to ambient pressure data (see Fig. 4.20), simultaneously fitting all data at the three available applied staggered magnetic fields, the theoretical

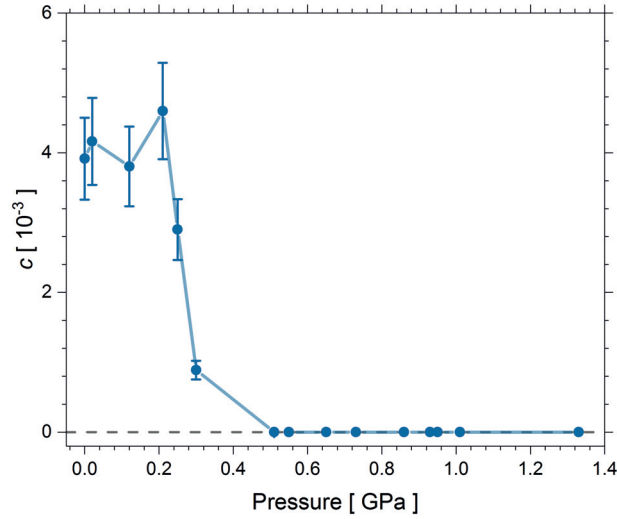


Figure 4.26 – Hydrostatic pressure dependence of the globally fitted c parameter measuring the staggered field induced by the DM interaction. The pressure dependence presents a clear decrease of the effect of the DM interaction with increasing pressure owing to increasing quantum fluctuations.

approximations were found to provide satisfying description of the experimentally observed broadening (see Fig. 4.25 as an example). I assumed a simple linear pressure dependence of J in-between the experimentally determined values. Based on the two-parameter global fits (utilizing $c^2 J/k_B$ and $\lambda J/k_B$ as fitting parameters), the pressure dependence of c can be deduced as displayed in Fig. 4.26. The depicted pressure dependence of c is selectively influenced only by the coupling of the electron spin system to the DM interaction, it is independent of the changes of J . Fig. 4.26 expresses a clear drop of the DM effect with increasing pressure, unambiguously proving the suppressed DM effect at pressures above $p > 0.3$ GPa. Thus, the *dome*-shape behavior is reduced to a continuously diminishing DM contribution upon the quantum fluctuating QSL state.

4.3.3 Absence of DM effect at moderate pressures

In the pressure regime between the antiferromagnetically fluctuating state and the Mott transition, i.e., at pressures $0.3 \text{ GPa} < p < 0.9 \text{ GPa}$, ESR measurements detect a strongly spin-fluctuating state with strong magnetic exchange interactions in the range of $J/k_B \approx 220 - 310 \text{ K}$. Fig. 4.27 illustrates that the field- (frequency-) dependence of the linewidth is linear at this pressure range, in marked contrast with the quadratic field dependence induced by the DM interaction and the frequency-independent linewidth seen in the metallic state. In addition, the g -factor remains constant as a function of frequency, in accordance with an unordered paramagnetic state. Similarly to the case of EDT-BCO presented in Section 3.4, I identify this state as a strongly quantum fluctuating one: the weak and clear frequency dependence of the linewidth can be explained as a *motional narrowing*-like effect, reminiscent of fast motions in the spin system. Remarkably, the analogy of the two different systems, i.e., the moderately

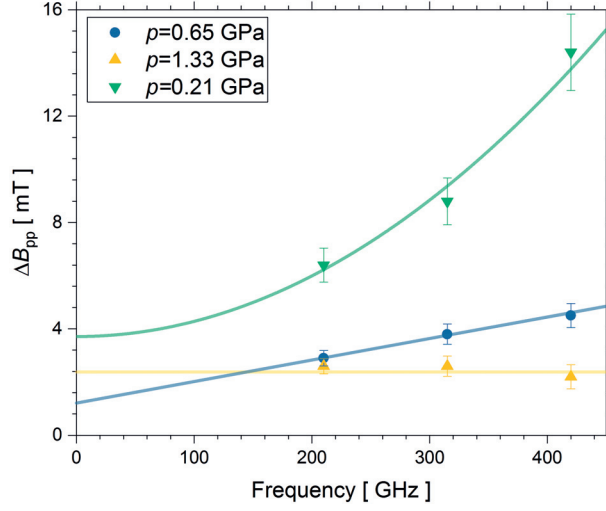


Figure 4.27 – Field dependence of the linewidth in three different pressure regimes: *i*) for $p < 0.3$ GPa ($p = 0.21$ GPa) DM-induced broadening can be identified with quadratic field dependence, *ii*) for $0.3 \text{ GPa} < p < 0.9$ GPa ($p = 0.65$ GPa) strong quantum fluctuations suppress the DM effect, and the field dependence is detected as *motional narrowing*, *iii*) for $0.9 \text{ GPa} < p$ ($p = 1.33$ GPa) constant-in-field ΔB_{pp} demonstrates a metallic state.

pressurized κ -Ag and the ambient-pressure EDT-BCO reveals that the effect of the disorder is non-negligible in κ -Ag [285], and it further illustrates that a sizable antisymmetric exchange can be suppressed in the QSL state.

4.3.4 Quasi-continuous Mott transition

Similarly to previous transport and NMR investigations presented in Section 4.1, high-pressure ESR measurements could not identify discontinuity of the transition. Relevantly, the phase transition from the insulator state to the Fermi liquid state is not followed by a change of the g -factor (not shown). Furthermore, the phase transition cannot be identified through the ESR linewidth ($\Delta B_{pp}(T)$): the temperature dependence does not provoke a jump of ΔB_{pp} as shown in Fig. 4.28. Along with previous NMR studies, the electronic spin system is found to be unaffected.

Given the detailed pressure dependence explored in the vicinity of the insulator-metal transition, absence of such a temperature-dependent behavior implies that the DM interaction does not induce a broadening at these pressures. Furthermore, there is no evidence of shift or a clear change of the susceptibility. Whereas the NMR investigations of Shimizu *et al.* in Ref. [67] proposed that the decrease of the low-temperature susceptibility at high pressures stems from the decrease of the q -space, I could not identify a sizable change of χ_s ⁷.

At pressures where the insulator-to-metal transition takes place at low enough temperatures

⁷Even though high-frequency ESR is not readily applicable to determine the χ_s due to the absence of microwave resonating components, the signal-to-noise ratio of the spectra provides a good approximation.

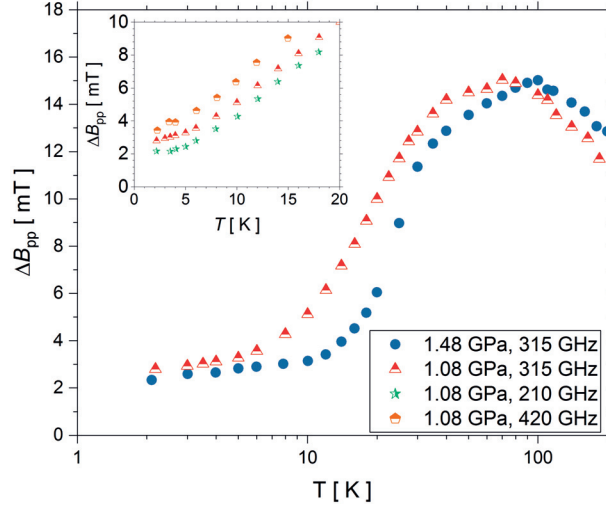


Figure 4.28 – ESR linewidth at the close vicinity of the Mott transition ($p = 1.08$ GPa) and in the metallic state ($p = 1.48$ GPa) revealing a quasi-continuous transition from the Fermi liquid to a *spinon metal* state. Inset: Frequency dependence of the linewidth at the Mott transition confirming the lack of a sudden linewidth change and indicating a linear frequency dependence of the linewidth most characteristic of the Mott insulator state.

(0.9-1 GPa), in principal, any of the fingerprints of the DM interaction could be seen. Remarkably, the lack of evidence for a significant DM component demonstrates that the QSL state is not perturbed by the antisymmetric exchange at pressures close to the Mott transition, the substantial effect of the DM interaction is strongly suppressed here. As we saw above, the role of the DM interaction is only identifiable spectroscopically at much lower pressures (below 0.3 GPa) and the present observation further highlights the relevance of this phenomenon.

4.3.5 Low-temperature superconducting and metallic state

As in other organic superconductor systems [23, 340], such as κ -Cu(NCS)₂ [341], the high-pressure superconducting state of κ -Cu [323] and κ -Ag [67] can only be explored in high-field measurements very close to the conducting layer. In these systems, the fluctuations of pancake vortices can only be suppressed in a very narrow angle regime where the conducting layer is parallel with the magnetic field. To lock the Josephson vortices into the anion layer in these weakly coupled superconducting layers, the upper limit of the angle between the external field, H and the conducting layer, i.e., the lock-in angle (θ_L) must be smaller than $H_{c1} < H \sin \theta_L$, where H_{c1} is the lower critical field [341]. In the present high-pressure ESR setup such precision cannot be achieved, thus, all ESR measurements were performed above the upper critical field, H_{c2} , in the normal state parallel to the a^* direction.

Despite the low H_{c2} insufficient for ESR studies and the difficulty of ESR studies in the superconducting state with only a few exceptions [342, 343], another characteristic of the superconducting state can be explored, namely, the magnetically modulated microwave absorption

4.3. High-pressure antiferromagnetic fluctuations

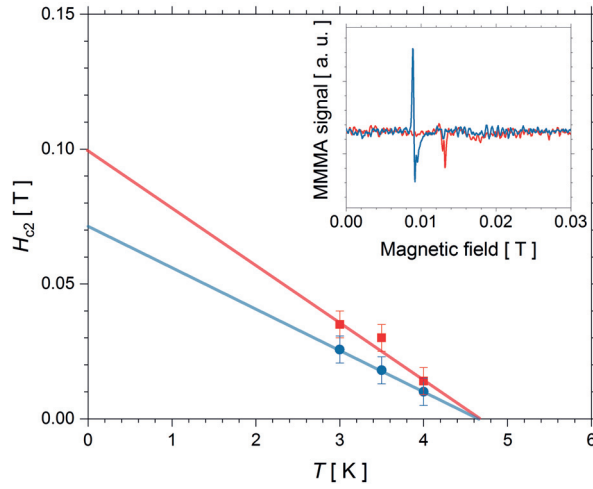


Figure 4.29 – Upper critical field in the high-pressure superconducting phase of κ -Ag at $p \approx 1.16$ GPa in the a^* direction as determined from the magnetically modulated microwave absorption (MMMA) signals. Red and blue points are measured in increasing and decreasing magnetic fields, respectively. Solid lines are linear fits to the experimental points indicating a critical temperature of $T_c \approx 4.7$ K and the zero-temperature upper critical field $H_{c2}(0) = 0.1$ T assuming linear temperature dependence of H_{c2} . Inset: MMMA signal measured in increasing and decreasing magnetic fields at $T = 4$ K and at 315 GHz.

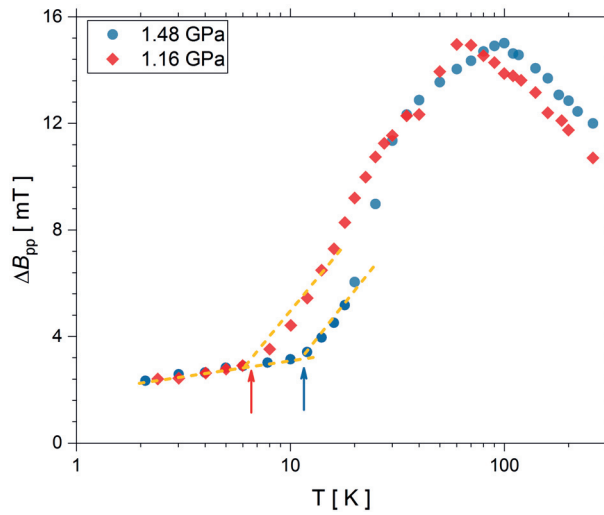


Figure 4.30 – ESR linewidth in the Fermi liquid state. ΔB_{pp} is independent of pressure, and increases linearly with temperature revealing a three-dimensional Fermi-liquid state. Dashed lines are fits to the temperature dependence of ΔB_{pp} , arrows indicate the extracted probable metal-insulator transition temperatures. Note that due to the presence of the charge fluctuation-related increase of the ESR linewidth, exact determination of the metal-insulator transition temperature is ambiguous.

(MMMA). This is a low-field signal, originating probably from microwave dissipation of the viscous fluxon motion [344]. Given that this method does not require the bulk percolation of the superconducting state, and low volume fractions of the superconducting state can be detected [210], it was applied for identification of new superconducting phases [345]. As in other organic superconductors [346, 347], the MMMA signal was detected in κ -Ag at $p = 1.16$ GPa as shown in the inset of Fig. 4.29. Remarkably, the temperature dependence of the MMMA signal permits to extract the upper critical field, H_{c2} at this pressure.

To extract the critical temperature and zero-temperature critical field ($H_{c2}(0)$) using the low-temperature MMMA data, I assumed a linear temperature dependence of the upper critical field. This approximation is strictly valid within the Bardeen-Cooper-Schrieffer (BCS) theory, nevertheless, it was recognized to provide a good approximation away from the T_c , even in multiband superconductors, e.g., pnictides [348, 349]. The linear fit yields a value of $T_c = 4.7$ K, as reported at similar pressures based on resistivity data [67]. The upper critical field of $H_{c2}(0) = 0.1$ T is a reasonable approximation, indicating an anisotropy in the range of 100 if compared with data in the conducting layer in κ -Cu [323].

In the Fermi liquid state, as we saw above, the ESR linewidth is independent of magnetic field (see Fig. 4.27), typical of three-dimensional metallic systems. In line with this, the temperature dependence of the ESR linewidth is characteristic of three-dimensional metals. As shown in Fig. 4.30, ΔB_{pp} displays a slow, linear increase at low temperatures, below the metal-insulator transition, T_{MI} (or metal-crossover state transition, see Fig. 4.2). Importantly, the T_{MI} transition temperature measured by ESR is in satisfying accordance with the transport data [67]. The similar slow increase of ΔB_{pp} and the resistivity suggest the probable validity of the Elliott-Yafet mechanism (see Section 2.1.3) at this narrow temperature regime.

5 Conclusions & outlook

Research in frustrated magnetism is still far from its maturation, and the experimental quest for Quantum Spin Liquids is considerably lagging behind theoretical works. This discrepancy, in some extent, originates from the thirty-year-long delay of the first experimental realization of an almost ideal triangular lattice (Anderson, 1973 [25], Shimizu *et al.*, 2003 [24]). More importantly, it is the peculiarity of the identification of the QSLs as *long-range quantum-entangled* systems. This intricate definition that requires the observation of non-local excitations necessitates an arsenal of experimental methods unmasking the low-temperature magnetic ground state from the search for magnetic ordering to the description of emergent exotic excitations. Thus, novel combinations of conventional microscopic magnetic methods are required

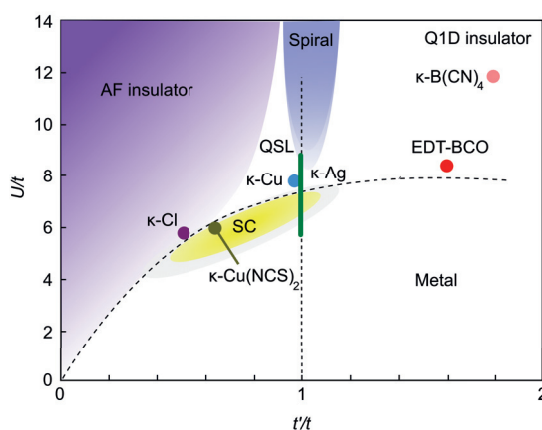


Figure 5.1 – Schematic phase diagram of two-dimensional organic charge-transfer salts. Investigations of the present PhD project are shown as a red dot (the hybrid conductor-rotor system of EDT-BCO, Chapter 3) and as a green line (κ -Ag, Chapter 4). The extension of the vertical line shows the change of U/t upon the application of hydrostatic pressure studied by high-field ESR. Note the proximity of the spiral-ordered phase to the ambient-pressure κ -Ag provoking large field-induced antiferromagnetic fluctuations. Due to its moderate anisotropy, EDT-BCO is placed far away from any ordered state, revealing a QSL state without antiferromagnetic fluctuations. The figure data and the original figure is taken from Ref. [69] (see Fig. 1.5).

to probe the intrinsic QSL behavior. During my PhD project, I employed multi-frequency ambient- and high-pressure Electron Spin Resonance and Muon Spin Rotation experiments to study geometrically frustrated magnetic organic materials and to analyze the electronic spin excitations. Remarkably, ESR signatures of two-dimensional organic QSLs were unknown prior to the present work. In particular, I concentrated on two organic charge-transfer salt families spanning from one-dimensional spin chains to two-dimensional isotropic triangular lattice systems, and I scrutinized the role of quenched *randomness*.

To examine the role of designed, well-controlled disorder, I performed detailed ESR analysis of hybrid conductor-rotor charge transfer salts. Anion layers are either a BCP or a BCO rotators, which freeze at random positions at low temperatures, engendering strong randomness in the crystal. This is further increased by different conformational forms in the case of the BCO rotator. In $[\text{EDT-TTF-CONH}_2]_2^+[\text{HO}_2\text{C-CC-BCP-CC-CO}_2^-]$, I found a strong-rung spin-ladder state on the dimers. At the freezing temperature of the BCP rotator, a presumably charge-ordered state is reached, leading to a spin-singlet state. In contrast to $[\text{EDT-TTF-CONH}_2]_2^+[\text{HO}_2\text{C-CC-BCP-CC-CO}_2^-]$, where the neighboring spin-ladders are separated due to their relation with the BCP rotator, the BCP components isolate the *A* and *B* spin chains in $[\text{BEDT-TTF}]_2^+[\text{HO}_2\text{C-CC-BCP-CC-CO}_2^-]$, and the interchain coupling remains rather weak ($J_1/k_B = 94$ K, and $J_2/J_1 = 7\%$). Nevertheless, stopping of the BCP units leads to three-dimensional antiferromagnetic order as manifested in antiferromagnetic resonance and supplementary $^1\text{H-NMR}$ data. Discrepancy of the Néel temperatures measured by the two techniques was interpreted as a result of the disordered potential arising due to the microscopic distribution of the BCP freezing angular positions.

Systems with BCO rotator layers do not realize long-range order due to their two-dimensional nature and increased low-temperature disorder. In $(\text{EDT-TTF-CONH}_2)_6^+[\text{O}_2\text{C-CC-BCO-CC-CO}_2^-](\text{CH}_3\text{OH})_2$, the high-temperature metallic state above 120 K produces impeded motion of the BCO components, which is freed in the insulator state, provoking an only weakly ordered antiferromagnetic state at low temperatures. Its sister compound, $(\text{EDT-TTF-CONH}_2)_2^+[\text{BABCO}^-]$ realizes a distorted triangular lattice QSL candidate. This discovery, confirmed using high-field ESR and μSR investigations, is the main result of the present Thesis project, as it is the first QSL with quasi-one-dimensional triangular lattice structure, a long-standing theoretical proposal (see Fig. 5.1, a modified version of Fig. 1.5) [350]. Exceptionally, freezing of the BCO motion induces development of a special, disordered spin liquid state, as highlighted by static spin-susceptibility. In contrast to irradiated $\kappa\text{-Cl}$ [150], however, the randomness is an intrinsic, designed component of the system. Despite the strong, $J/k_B = 365$ K exchange interaction, the absence of magnetic ordering and the presence of spin fluctuations was confirmed with μSR experiments down to 20 mK. As revealed by longitudinal-field μSR , one-dimensional diffusive spin excitations are predominant and the intrachain spin diffusion is weak. Temperature dependence of the muon spin relaxation rate indicates $q = \pi/a$ excitations to prevail at low temperatures. Even though EDT-BCO lacks the inversion symmetry, and DFT calculations point to the presence of a weak antisymmetric exchange in it, multi-frequency low-temperature ESR measurements does not display sub-

stantial field-induced non-linear broadening. Lack of the DM effect is in good accordance with Fig. 5.1, where EDT-BCO is located far from ordered phases.

The absence of the DM effect in EDT-BCO is in stark contrast with κ -(BEDT-TTF)₂Ag₂(CN)₃, the sister compound of the first organic QSL candidate, κ -(BEDT-TTF)₂Cu₂(CN)₃. The closeness of a spiral-ordered phase to κ -Ag (see Fig. 5.1) explains the strong antiferromagnetic fluctuations found at my ambient-pressure ESR measurements. However, upon application of hydrostatic pressure, U/t decreases, inducing the drop of the DM effect and leading to the disappearance of the staggered moments at low temperatures. Above 0.9 GPa, a clear, quasi-continuous Mott transition is observed towards a superconducting state both in the present high-pressure ESR and previous transport and NMR investigations [67]. In-between the DM-induced broadening and the Mott transition, the field dependence of the ESR linewidth is observed to follow a linear increase (as in EDT-BCO) proving the presence of fast electronic spin fluctuations.

In a broader context, the presence of antiferromagnetic fluctuations due to the DM interaction in κ -Ag answers the long-standing issue of importance of weak spin-orbit coupling in organic QSLs, which was first addressed theoretically only recently [68], and was neglected experimentally [71, 140]. Relevantly, comparison of the ambient-pressure κ -Ag, high-pressure κ -Ag, and EDT-BCO highlights pertinence and complexity of the problem. Thus, it is fundamentally relevant to separately study each QSL candidates using high-field ESR or ¹³C-NMR [215]. Furthermore, this illustrates the need for microscopic probes of the electronic spin system.

Additionally, strong effects of the Brownian rotor components upon the magnetic state of the hybrid conductor-rotor systems lay down substantial proof of the effect of inhomogeneous, local disorder upon the non-local state of QSLs. Discovery of a new organic charge-transfer family hosting possible QSL candidates augments the hope for a complete and generalized model of the two-dimensional Quantum Spin Liquids.

A Versatile detection in high-frequency ESR

Fig. A.1 presents multiple detection schemes used at our home-built high-field ESR setup. Apart from traditional field-modulation technique that became widespread to improve the signal-to-noise ratio, we have the capability to use frequency-modulation technique and microwave chopping technique. The former is possible as a result of absence of microwave resonant components. In Ref. [181], frequency modulation was achieved with the 100 MHz reference oscillator. As the 13.1 GHz phase-locked dielectric resonator oscillator (which was a bottleneck in the frequency modulation) is removed from our setup, and a 13.1 GHz reference oscillator is used instead, the latter can be applied for modulating the frequency, resulting in a

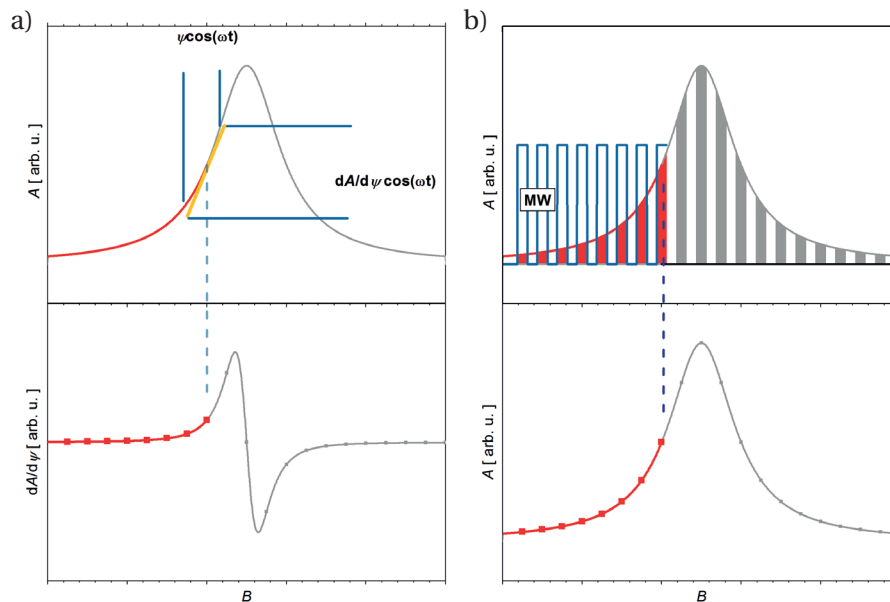


Figure A.1 – Detection schemes at the high-field multi-frequency ESR experimental setup in our laboratory *a*) Traditional field-modulation technique ($\Psi \equiv B$) and the frequency-modulation technique ($\Psi \equiv \omega$) using the same detection method, and measuring the derivative of the ESR signal. The absence of resonant microwave components in our setup allows using both methods. *b*) Microwave chopping detection scheme.

Appendix A. Versatile detection in HF-ESR

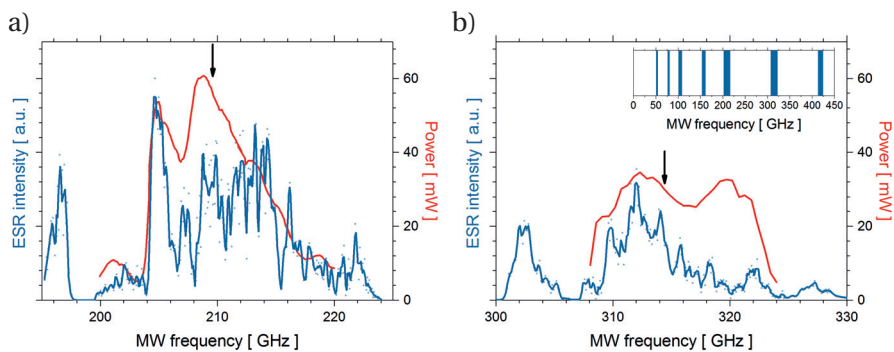


Figure A.2 – Demonstration of continuous tunability of the ESR frequency. ESR intensity measured using the ~ 210 GHz ($\times 16$) and the ~ 315 GHz ($\times 24$) doublers. Solid lines are smoothed curves serving as guides to the eye. Test MW power of the manufacturer is plotted for comparison (Virginia Diodes Inc.). The frequency was set by the MW signal generator, and field-modulation detection was used to measure the ESR signal. Arrows denote the $13.1 \text{ GHz} \cdot 16 = 209.6 \text{ GHz}$ (a) and the $13.1 \text{ GHz} \cdot 24 = 314.4 \text{ GHz}$ (b) points. Inset to b: Operating frequencies of the HF-ESR setup revealing quasi-continuous operation covering a large frequency range.

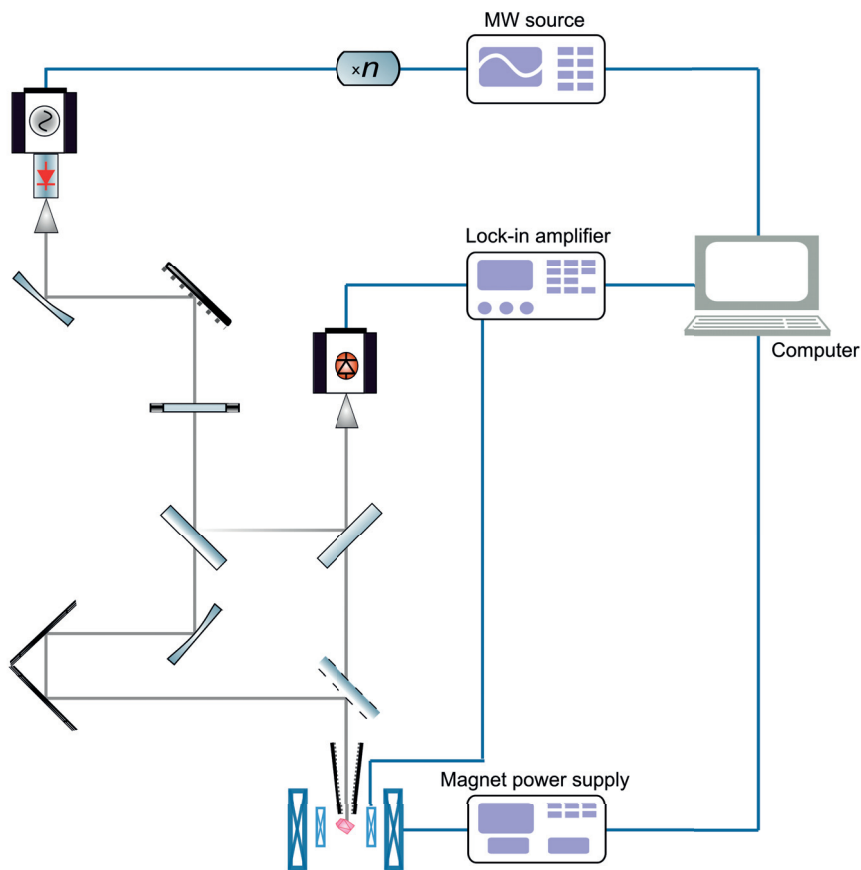


Figure A.3 – Block diagram of the quasi-optical induction mode high-frequency ESR developed in our laboratory.

much more flexible system.

For the microwave chopping technique, we use the modulating function of the reference oscillator. This technique proved to be particularly advantageous for detection of broad signals that are not detectable by field-modulation technique due to upper limits of the modulation amplitude (e.g., heating effects) or due to increased mechanical noise.

To demonstrate tunability of the operating MW frequency, I performed field-modulated ESR measurements using a KC_{60} reference sample. My room-temperature test results are summarized in Fig. A.2. Similar frequency-dependent measurements were repeated at low temperatures, yielding similar results. The ESR intensity approximately follows the test MW power found by the manufacturer but (due to the complexity of this high-frequency setup) some deviations can be identified. Most importantly, by tuning the MW frequency, the signal-to-noise ratio can be increased by about 50% accelerating time-consuming data collection. Furthermore, the frequency can be changed by about $\pm 5\%$ without significant loss of intensity. This characteristic may become useful in sensitive detection of field-induced effects.

B Analysis of magnetic torque data in $\kappa\text{-(ET)}_2\text{Cu}_2(\text{CN})_3$

In the following, I will comment on recent magnetic torque measurements in Ref. [140] that found a quantum critical behavior in the high-temperature low-field regime in $\kappa\text{-Cu}$. I will demonstrate that the DM interaction found using exact diagonalization calculations in Ref. [68], and ESR data presented in Chapter 4 explains a significant fraction of the field-induced drop of the spin-susceptibility as a consequence of the DM interaction in the QSL candidate $\kappa\text{-Cu}$.

Magnetic torque measurement serves as a unique method to determine the low-temperature susceptibility of organic quantum spin liquids, and it proved to provide an essential microscopic tool to single crystal studies on small samples [140, 351, 352]. It makes use of the small g -factor anisotropy ($g_1 - g_2$) of the cation layer, which directly relates the magnetic torque, τ , to the spin-susceptibility anisotropy in a given plane, $\Delta\chi$: $\tau \propto \Delta\chi$. Using rotation in a plane (here, $a^* - c$) perpendicular to a crystallographic direction (here, b), and applying the low-temperature g -factor anisotropy, temperature- and field-dependent changes of χ_s can be

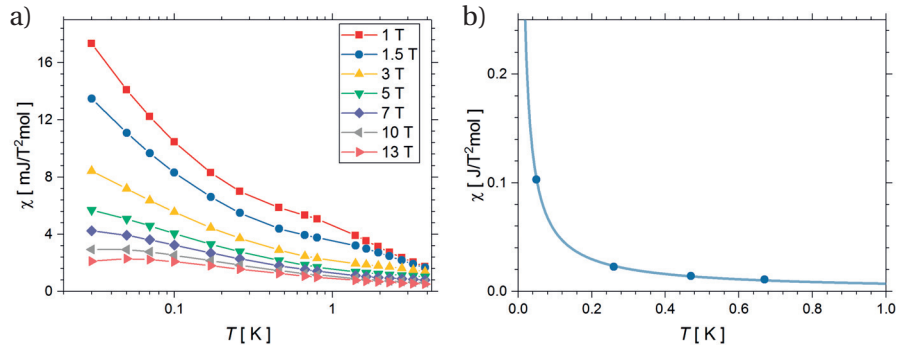


Figure B.1 – *a*) Simulation of the low-temperature susceptibility of $\kappa\text{-Cu}$ measured in Ref. [140] assuming the presence of DM interaction in $\kappa\text{-Cu}$. Zero-field susceptibility was fitted to $\chi \propto T^{-0.9}$, and high-field limit of the Oshikawa-Affleck theory was applied without logarithmic corrections, and using $\tilde{c} \approx 0.017$. *b*) Temperature dependence of zero-field susceptibility in $\kappa\text{-Cu}$ deduced from experimental magnetic torque data in Ref. [140] assuming validity of the Oshikawa-Affleck theory and presence of a DM interaction calculated in Ref. [68]. Solid line is a fit to $\chi \propto T^{-0.9}$.

Appendix B. Comparison of magnetic torque measurements

followed. In κ -Cu, magnetic torque measurements found exotic behavior, where two distinct regimes were identified: *i*) a *low-field, high-temperature* regime, where quantum critical increase of $\chi_c \propto T^{-0.8}$ was shown to hold, and *ii*) a *high-field, low-temperature* regime, where $\chi_c \propto H^{-0.8}$ was identified. Interestingly, low-field data did not follow the described scaling relations. Relevantly, the only anisotropy considered in the calculations was the g -factor anisotropy, the DM interaction was neglected. Furthermore, the plane of magnetic torque measurements corresponds to the plane of the ESR data shown in Chapter 4 in κ -Ag. This plane is perpendicular to the 2_1 axis, where the staggered DM interaction was found by exact diagonalization calculations [68].

As we saw in Chapter 4, the direction of the DM interaction is such that the g -factor anisotropy is decreased due to the staggered static magnetization. That is, in the direction with higher resonant field, the ESR line shifts down, and it remains unchanged in the directions with lower resonant field. Within a 1% precision, the Δg_{sf} -shift reduces completely the g -factor anisotropy. (Closeness of the g -tensor principle axes to the $B \perp DM$ and $B \parallel DM$ directions is demonstrated through the small crystallographic axis change found in Ref. [140].)

To present relevance of the DM interaction in the g -factor anisotropy drop, I compare at 2 K the two separate effects. In the magnetic torque measurements, based on published data, the susceptibility decrease found at 13 T as compared to 1 T is $\chi_\tau(13 \text{ T})/\chi_\tau(1 \text{ T}) = 68\%$. In the ESR measurements, the g -factor anisotropy decrease can only be observed above 1 T (above 35 GHz). I use rotation data at 315 GHz, i.e., in 11.1 T compared to 9.4 GHz data (at 0.33 T) that shows $\Delta g_{\text{anis, ESR}}(11 \text{ T})/\Delta g_{\text{anis, ESR}}(0.33 \text{ T}) \approx 63\%$. Even if these values seem to be close, the comparison is not complete for two reasons: *i*) the magnetic torque data was measured at higher fields than the ESR rotation, and *ii*) ESR was performed in κ -Ag, where theoretical calculations predict a somewhat larger DM: namely, $|\mathbf{D}_{\kappa\text{-Ag}}|/k_B = 4.1 \text{ K}$, in contrast to $|\mathbf{D}_{\kappa\text{-Cu}}|/k_B = 3.5 \text{ K}$. Taking into account these two counteracting differences, the size of the observed change is expected to remain in the same range. It is noteworthy that the field dependence could be calculated from the field dependence found from torque or ESR data but it is rather difficult to account for the DM interaction difference.

This signifies that the T - and H -dependent magnetic torque data can be utilized to test whether the low- or high-field Oshikawa-Affleck theory (see Eq. 2.19 and Eq. 2.21) is satisfied in κ -Cu, and it can be employed to confirm our findings from the measured ESR linewidth and g -factor shift. In this sense, the two distinct regimes found in magnetic torque data indicate a character change. At low temperatures and at high fields (barely available in our ESR measurements) the field dependence follows $\chi_c \propto H^{-0.8}$. As the staggered susceptibility is exactly the opposite of the critical susceptibility shifted by χ_0 , high-temperature susceptibility (leading to $\chi_{\text{staggered}} \propto H^{0.8}$) can be compared to the ESR linewidth change and g -factor shift at the highest fields and at the lowest temperatures. As I found a slowed-down increase of the ESR linewidth and g -factor shift, it is in agreement with a slower-than-quadratic behavior. Numerically, I performed a global fit to the field dependence of the critical susceptibility using Eq. 2.19 and Eq. 2.20, and the best fit was achieved with $\tilde{c} = 0.012(2)$ and $\tilde{\lambda} = 0.07(1)$

(from fits without the logarithmic correction, $\tilde{c} = 0.015(2)$)¹. These fits give a remarkably good qualitative field-dependence. Likewise, Oshikawa-Affleck fits reason why the low-field data differed from the power-law fitted at higher fields in Ref. [140]: the low-field data fits to a quadratic field-dependence, quite different from the high-field one, leading to a broken *scaling* at low fields.

From the Oshikawa-Affleck fits, one can extract the zero-field temperature dependence of the spin-susceptibility. As shown in the inset of Fig. B.1*b*, the temperature dependence barely differs from a Curie-like temperature dependence (best fitted with $\chi \propto T^{-0.9}$). Quite relevantly, the observed low-temperature χ_s measured with this microscopic method, which is sensitive to *g*-factor anisotropies, cannot stem from impurities, as the latter would be seen as having different *g*-factor principal axes. Instead, as in the case of X-ray irradiated κ -Cl [150] and for (EDT-TTF-CONH₂)₂⁺[BABCO⁻] (see Section 3.4), this slow increase can be assigned to an intrinsic disorder in κ -Cu [287]. Magnetic torque data therefore presents a demonstration of a universal low-temperature increase of susceptibility in spin-1/2 triangular lattice QSL candidate systems.

To demonstrate the agreement between the fitted data and experiments in Ref. [140], experimental results presented in Fig. 3*a* by Isono *et al.* were simulated assuming $\chi \propto T^{-0.9}$ and a coupling of $\tilde{c} \approx 0.017$. As shown in Fig. B.1*a*, our two-parameter simulation reproduces remarkably well all temperature-dependent torque data.

¹These simulated parameters cannot be directly compared with ESR results for two reasons: the crystal is not the same chemical composition, and fitted parameters are determined up to a constant factor.

Acknowledgements

I am very fortunate to have been surrounded by excellent people during my graduate years from whom I learned a lot and to whom I hereby would like to thank their invested time and effort.

Firstly, I would like to express my sincere gratitude to my supervisor, Prof. László Forró, for his continuous support since my first visit in Lausanne more than seven years ago. His motivation and his vision of science back our group in real scientific discussions. His multi-faceted scholar approach stimulates our enthusiasm. He accomplished to create a team of interdisciplinary researchers with diverse views and approaches, the combination of which contributes to the realization of revolutionary ideas in novel materials.

My sincere thanks also goes to my co-supervisor, Dr. Bálint Náfrádi, whose immense knowledge in physics always challenged me. His experimental approach and theoretical view towards broad areas provided great insight into all our common projects and his guidance gave me continuous support, and his hard-working attitude kept me focused. Together, we solved a great deal of problems making use of *Angelina* and *Shakira*, our favorite ESR instruments.

I would like to thank Prof. András Jánossy for steering me in the right direction in research during his numerous visits, and for sharing with me his one-of-a-kind expertise in ESR and in the field of organics.

I am grateful to Prof. Patrick Batail and Dr. Cécile Mézière for the perfect single crystals of hybrid conductor-rotor systems and the tremendous work to provide sufficient sample for the μ SR experiments. Our long-standing collaboration helped me to jump into new research areas in the forefront of organic chemistry and physics. I thank Dr. Pawel Wzietek for the NMR data that remained a cornerstone of our understanding of the hybrid materials. I am thankful to Prof. Gunzi Saito and to Dr. Takaaki Hiramatsu for the impurity-free single crystals of κ -(ET)₂Ag₂(CN)₃.

Besides my supervisors, I acknowledge all the thesis committee for their service and the exciting insights: Prof. Thierry Giamarchi, Prof. Patrick Batail, Prof. Henrik M. Rønnow, and the jury president, Prof. Nicolas Grandjean. I am grateful to Prof. Frédéric Mila for his four-year-long mentoring, which guided me through the challenging moments of my PhD. I thank Dr. Richárd Gaál for continuously sharing with me his experience and knowledge in all arising

Acknowledgements

difficulties in the lab and outside.

I would like to thank the help of all the Muon Group in ISIS Rutherford Appleton Laboratory, and the Bulk μ SR group in PSI S μ S facility for all the long night hours and the great impulses. I thank Evelyn, Nicole, and Anh for their assistance in all the arising administrative questions, and to Stéphane and Samuel for providing us liquid helium endlessly in the crucial moments of our experiments.

A special gratitude goes out to Endre, the insightful visionary of our team with whom we discussed intriguing experimental and philosophical problems be it day or night. I thank Péter Matus, the real-life NMR expert, and Andrzej for hours of analyses of ideas and ESR issues. My thanks goes to Márton *the Great* for providing the most relaxing moments and the sweetest chocolates.

I thank my office mate and friend, Lidia, for her meticulous corrections of the French version of my abstract and for creating an ideal ambiance in our office in the last years. I am indebted to my university classmate and fellow PhD fighter, Árpí, for his careful reading of all my thesis in a two-day run giving me numerous valuable comments.

I thank my fellow group- and labmates with whom we worked hard together on experiments and we shared a number of *easy* moments: thanks Maryam, Xavier, Konstantins, Edoardo, Dunja, Pavao, Anastasiia, and Dani! Thanks for the helpfulness of previous generations: Laurent, Massimo, Andrea, and Iness! Special thanks for the ideas of the seniors of our team: Alla, Luka, Sergiy, and Gaétan! I am grateful to my students and summer interns, Jeremy and the two Bences, for their passion and important input and to Prof. Ferenc Simon for his collaboration and for the great students we could cooperate with. And thanks to all the Hungarians in Lausanne and in Geneva: Dóri for sharing the office and thoughts, and Ági, Brigi, Nóri, Zsuzsi, Zsolti, Zsófi, Szabi, Kari, and Andreas for the inspiring and calming thoughts.

Last but not least I would like to thank my family for continuous encouragement throughout my years of study and through the process of researching. My parents, my sister and her family, all my relatives, and the family of Viki, in particular, the two Zsuzsas and her grandparents, allowed us to realize our own potentials. This accomplishment would not have been possible without them. I would like to express my profound gratitude to my wife and best friend, Viki. Her intellectual and loving companionship in the last ten years has been the source of my perseverance and my catalyst to improve. Her encouragement and patience has been the fundamental building block of my life from our arrival in Lausanne.

Finally, I thank all my collaborators and friends both at EPFL and outside for this amazing journey! With your support, I could have come to the end, and I hope to reciprocate it in the future!

Lausanne, 21 November 2017

P. Sz.

Bibliography

- [1] P. W. Anderson *et al.*, “More is different,” *Science*, vol. 177, no. 4047, pp. 393–396, 1972.
- [2] H. K. Onnes, “Further experiments with liquid helium,” in *KNAW, Proceedings*, vol. 13, pp. 1910–1911, 1911.
- [3] H. K. Onnes, “Investigations into the properties of substances at low temperatures, which have led, amongst other things, to the preparation of liquid helium,” *Nobel Lecture*, vol. 4, 1913.
- [4] J. Bardeen and W. H. Brattain, “The transistor, a semi-conductor triode,” *Physical Review*, vol. 74, no. 2, p. 230, 1948.
- [5] J. Bardeen and W. H. Brattain, “Physical principles involved in transistor action,” *Physical Review*, vol. 75, no. 8, p. 1208, 1949.
- [6] M. L. Cohen, “Essay: Fifty years of condensed matter physics,” *Physical Review Letters*, vol. 101, no. 25, p. 250001, 2008.
- [7] R. P. Feynman, “Simulating physics with computers,” *International journal of theoretical physics*, vol. 21, no. 6, pp. 467–488, 1982.
- [8] S. Haroche, “Nobel Lecture: Controlling photons in a box and exploring the quantum to classical boundary,” *Reviews of Modern Physics*, vol. 85, no. 3, p. 1083, 2013.
- [9] D. J. Wineland, “Nobel Lecture: Superposition, entanglement, and raising Schrödinger’s cat,” *Reviews of Modern Physics*, vol. 85, no. 3, p. 1103, 2013.
- [10] R. P. Feynman, “There’s plenty of room at the bottom,” *Engineering and Science*, vol. 23, no. 5, pp. 22–36, 1960.
- [11] “The nobel prize in chemistry 2016 - advanced information,” 2016.
- [12] P. Batail, “Introduction: molecular conductors,” 2004.
- [13] H. N. McCoy and W. C. Moore, “Organic Amalgams: Substances with Metallic Properties Composed in Part of Non-Metallic Elements.,” *Journal of the American Chemical Society*, vol. 33, no. 3, pp. 273–292, 1911.

Bibliography

- [14] W. Little, "Possibility of synthesizing an organic superconductor," *Physical Review*, vol. 134, no. 6A, p. A1416, 1964.
- [15] J. Ferraris, D. Cowan, V. t. Walatka, and J. Perlstein, "Electron transfer in a new highly conducting donor-acceptor complex," *Journal of the American Chemical Society*, vol. 95, no. 3, pp. 948–949, 1973.
- [16] M. J. Cohen, L. Coleman, A. Garito, and A. Heeger, "Electrical conductivity of tetrathiofulvalinium tetracyanoquinodimethan (TTF)-(TCNQ)," *Physical Review B*, vol. 10, no. 4, p. 1298, 1974.
- [17] F. Denoyer, F. Comès, A. Garito, and A. Heeger, "X-ray-diffuse-scattering evidence for a phase transition in tetrathiafulvalene tetracyanoquinodimethane (TTF-TCNQ)," *Physical Review Letters*, vol. 35, no. 7, p. 445, 1975.
- [18] L. Forró, *The Effect of Temperature, Disorder, and Pressure on the ESR Properties of Quasi-one-dimensional Organic Conductors*. PhD thesis, University of Zagreb, 1985.
- [19] D. Jérôme, A. Mazaud, M. Ribault, and K. Bechgaard, "Superconductivity in a synthetic organic conductor (TMTSF)₂PF₆," *Journal de Physique Lettres*, vol. 41, no. 4, pp. 95–98, 1980.
- [20] K. Bechgaard, C. S. Jacobsen, K. Mortensen, H. J. Pedersen, and N. Thorup, "The properties of five highly conducting salts:(TMTSF)₂X, X= PF₆⁻, AsF₆⁻, SbF₆⁻, BF₄⁻ and NO₃⁻, derived from tetramethyltetraselenafulvalene (TMTSF)," *Solid State Communications*, vol. 33, no. 11, pp. 1119–1125, 1980.
- [21] D. Jérôme, "Organic conductors: From charge density wave TTF-TCNQ to superconducting (TMTSF)₂PF₆," *Chemical Reviews*, vol. 104, no. 11, pp. 5565–5592, 2004.
- [22] H. Urayama, H. Yamochi, G. Saito, K. Nozawa, T. Sugano, M. Kinoshita, S. Sato, K. Oshima, A. Kawamoto, and J. Tanaka, "A new ambient pressure organic superconductor based on BEDT-TTF with T_c higher than 10 K ($T_c = 10.4$ K)," *Chemistry Letters*, vol. 17, no. 1, pp. 55–58, 1988.
- [23] T. Ishiguro, K. Yamaji, and G. Saito, *Organic superconductors*, vol. 88. Springer Science & Business Media, 2012.
- [24] Y. Shimizu, K. Miyagawa, K. Kanoda, M. Maesato, and G. Saito, "Spin Liquid State in an Organic Mott Insulator with a Triangular Lattice," *Physical Review Letters*, vol. 91, Sep 2003.
- [25] P. W. Anderson, "Resonating valence bonds: A new kind of insulator?," *Materials Research Bulletin*, vol. 8, no. 2, pp. 153–160, 1973.
- [26] H. Shirakawa, E. J. Louis, A. G. MacDiarmid, C. K. Chiang, and A. J. Heeger, "Synthesis of electrically conducting organic polymers: halogen derivatives of polyacetylene, (CH)_x," *Journal of the Chemical Society, Chemical Communications*, no. 16, pp. 578–580, 1977.

- [27] A. J. Heeger, "Nobel Lecture: Semiconducting and metallic polymers: The fourth generation of polymeric materials," *Reviews of Modern Physics*, vol. 73, no. 3, p. 681, 2001.
- [28] S. Roth, *One-dimensional Metals (Physics and Materials Science)*. VCH: Weinheim, 1995.
- [29] U. Lange, N. V. Roznyatovskaya, and V. M. Mirsky, "Conducting polymers in chemical sensors and arrays," *Analytica Chimica Acta*, vol. 614, no. 1, pp. 1–26, 2008.
- [30] H. Naarmann, "Polymers, electrically conducting," *Ullmann's Encyclopedia of Industrial Chemistry*, 2002.
- [31] A. Bernanose, M. Comte, and P. Vouaux, "A new method of emission of light by certain organic compounds," *Journal de Chimie Physique*, vol. 50, pp. 64–68, 1953.
- [32] C. W. Tang and S. A. VanSlyke, "Organic electroluminescent diodes," *Applied Physics Letters*, vol. 51, no. 12, pp. 913–915, 1987.
- [33] P. K. Weimer, "The TFT a new thin-film transistor," *Proceedings of the IRE*, vol. 50, no. 6, pp. 1462–1469, 1962.
- [34] H. Hoppe and N. S. Sariciftci, "Organic solar cells: An overview," *Journal of Materials Research*, vol. 19, no. 7, pp. 1924–1945, 2004.
- [35] H. W. Kroto, J. R. Heath, S. C. O'Brien, R. F. Curl, and R. E. Smalley, "C₆₀: Buckminsterfullerene," *Nature*, vol. 318, no. 6042, pp. 162–163, 1985.
- [36] H. Kroto, "Symmetry, space, stars, and c₆₀ (nobel lecture)," *Angewandte Chemie International Edition*, vol. 36, no. 15, pp. 1578–1593, 1997.
- [37] B. Miller, J. Rosamilia, G. Dabbagh, R. Tycko, R. Haddon, A. Muller, W. Wilson, D. Murphy, and A. Hebard, "Photoelectrochemical behavior of c₆₀ films," *Journal of the American Chemical Society*, vol. 113, no. 16, pp. 6291–6293, 1991.
- [38] M. Mikawa, H. Kato, M. Okumura, M. Narazaki, Y. Kanazawa, N. Miwa, and H. Shinohara, "Paramagnetic water-soluble metallofullerenes having the highest relaxivity for MRI contrast agents," *Bioconjugate Chemistry*, vol. 12, no. 4, pp. 510–514, 2001.
- [39] S. Iijima, "Helical microtubules of graphitic carbon," *Nature*, 1991.
- [40] S. J. Tans, A. R. Verschueren, and C. Dekker, "Room-temperature transistor based on a single carbon nanotube," *Nature*, vol. 393, no. 6680, p. 49, 1998.
- [41] A. Bachtold, P. Hadley, T. Nakanishi, and C. Dekker, "Logic circuits with carbon nanotube transistors," *Science*, vol. 294, no. 5545, pp. 1317–1320, 2001.
- [42] K. S. Novoselov, A. K. Geim, S. V. Morozov, D. Jiang, Y. Zhang, S. V. Dubonos, I. V. Grigorieva, and A. A. Firsov, "Electric field effect in atomically thin carbon films," *Science*, vol. 306, no. 5696, pp. 666–669, 2004.

Bibliography

- [43] K. Novoselov, "Nobel lecture: Graphene: Materials in the flatland," *Reviews of Modern Physics*, vol. 83, no. 3, p. 837, 2011.
- [44] I. Žutić, J. Fabian, and S. D. Sarma, "Spintronics: Fundamentals and applications," *Reviews of Modern Physics*, vol. 76, no. 2, p. 323, 2004.
- [45] S. Bae, H. Kim, Y. Lee, X. Xu, J.-S. Park, Y. Zheng, J. Balakrishnan, T. Lei, H. R. Kim, Y. I. Song, *et al.*, "Roll-to-roll production of 30-inch graphene films for transparent electrodes," *Nature Nanotechnology*, vol. 5, no. 8, pp. 574–578, 2010.
- [46] R. Raccichini, A. Varzi, S. Passerini, and B. Scrosati, "The role of graphene for electrochemical energy storage," *Nature Materials*, vol. 14, no. 3, p. 271, 2015.
- [47] S. Garaj, W. Hubbard, A. Reina, J. Kong, D. Branton, and J. Golovchenko, "Graphene as a sub-nanometer trans-electrode membrane," *Nature*, vol. 467, no. 7312, p. 190, 2010.
- [48] A. C. Ferrari, F. Bonaccorso, V. Fal'Ko, K. S. Novoselov, S. Roche, P. Bøggild, S. Borini, E. H. Koppens, V. Palermo, N. Pugno, *et al.*, "Science and technology roadmap for graphene, related two-dimensional crystals, and hybrid systems," *Nanoscale*, vol. 7, no. 11, pp. 4598–4810, 2015.
- [49] A. Lilja. <http://www.lateralmag.com/articles/?category=Issue+4>. [Online; accessed 5 September 2017].
- [50] Y. Galagan and R. Andriessen, "Organic photovoltaics: technologies and manufacturing," in *Third Generation Photovoltaics*, InTech, 2012.
- [51] D.-M. Sun, M. Y. Timmermans, Y. Tian, A. G. Nasibulin, E. I. Kauppinen, S. Kishimoto, T. Mizutani, and Y. Ohno, "Flexible high-performance carbon nanotube integrated circuits," *Nature Nanotechnology*, vol. 6, no. 3, pp. 156–161, 2011.
- [52] <http://www.arizonastateradiology.com/services/mri.html>. [Online; accessed 5 September 2017].
- [53] <http://www.jameshedberg.com/scienceGraphics.php?sort=graphene&id=graphene-transistor-3D-model>. [Online; accessed 5 September 2017].
- [54] <http://www.jameshedberg.com/scienceGraphics.php?sort=all&id=carbon-nanotube-long-3d-model>. [Online; accessed 5 September 2017].
- [55] <https://www.polymersolutions.com/blog/demand-grows-for-conductive-polymers/>. [Online; accessed 5 September 2017].
- [56] https://www.jmtour.com/about/photos_graphics/nanocars/. [Online; accessed 5 September 2017].
- [57] S. L. Lomonaco. <https://www.csee.umbc.edu/category/talks/page/39/>. [Online; accessed 5 September 2017].

- [58] https://en.wikipedia.org/wiki/Molecular_gyroscope. [Online; accessed 5 September 2017].
- [59] <https://en.wikipedia.org/wiki/Graphene>. [Online; accessed 5 September 2017].
- [60] <https://www.dreamstime.com/>. [Online; accessed 5 September 2017].
- [61] http://utw10193.utweb.utexas.edu/Archive/publications/journal_in_group.html/. [Online; accessed 5 September 2017].
- [62] T. Kudernac, N. Ruangsapapichat, M. Parschau, B. Macia, N. Katsonis, S. R. Harutyunyan, K.-H. Ernst, and B. L. Feringa, "Electrically driven directional motion of a four-wheeled molecule on a metal surface," *Nature*, vol. 479, no. 7372, p. 208, 2011.
- [63] T. R. Kelly, M. C. Bowyer, K. V. Bhaskar, D. Bebbington, A. Garcia, F. Lang, M. H. Kim, and M. P. Jette, "A molecular brake," *Journal of the American Chemical Society*, vol. 116, no. 8, pp. 3657–3658, 1994.
- [64] C. Lemouchi, C. S. Vogelsberg, L. Zorina, S. Simonov, P. Batail, S. Brown, and M. A. Garcia-Garibay, "Ultra-fast rotors for molecular machines and functional materials via halogen bonding: crystals of 1, 4-bis (iodoethynyl) bicyclo [2.2. 2] octane with distinct gigahertz rotation at two sites," *Journal of the American Chemical Society*, vol. 133, no. 16, pp. 6371–6379, 2011.
- [65] C. Lemouchi, C. Mézière, L. Zorina, S. Simonov, A. Rodríguez-Forteza, E. Canadell, P. Wzietek, P. Auban-Senzier, C. Pasquier, T. Giamarchi, and et al., "Design and evaluation of a crystalline hybrid of molecular conductors and molecular rotors," *Journal of the American Chemical Society*, vol. 134, no. 18, pp. 7880–7891, 2012.
- [66] P. Fendley, "Topological order from quantum loops and nets," *Annals of Physics*, vol. 323, no. 12, pp. 3113–3136, 2008.
- [67] Y. Shimizu, T. Hiramatsu, M. Maesato, A. Otsuka, H. Yamochi, A. Ono, M. Itoh, M. Yoshida, M. Takigawa, Y. Yoshida, and G. Saito, "Pressure-tuned exchange coupling of a quantum spin liquid in the molecular triangular lattice κ -(ET)₂Ag₂(CN)₃," *Physical Review Letters*, vol. 117, no. 10, 2016.
- [68] S. M. Winter, K. Riedl, and R. Valentí, "Importance of spin-orbit coupling in layered organic salts," *Physical Review B*, vol. 95, no. 6, 2017.
- [69] Y. Yoshida, H. Ito, M. Maesato, Y. Shimizu, H. Hayama, T. Hiramatsu, Y. Nakamura, H. Kishida, T. Koretsune, C. Hotta, and G. Saito, "Spin-disordered quantum phases in a quasi-one-dimensional triangular lattice," *Nature Physics*, vol. 11, no. 8, pp. 679–683, 2015.
- [70] L. Balents, "Spin liquids in frustrated magnets," *Nature*, vol. 464, no. 7286, p. 199–208, 2010.

Bibliography

- [71] F. L. Pratt, P. J. Baker, S. J. Blundell, T. Lancaster, S. Ohira-Kawamura, C. Baines, Y. Shimizu, K. Kanoda, I. Watanabe, and G. Saito, “Magnetic and non-magnetic phases of a quantum spin liquid,” *Nature*, vol. 471, no. 7340, pp. 612–616, 2011.
- [72] A. Kitaev and C. Laumann, “Topological phases and quantum computation,” *Les Houches Summer School, Exact methods in low-dimensional physics and quantum computing*, vol. 89, p. 101, 2009.
- [73] K. L. Hur, A. Soret, and F. Yang, “Majorana Spin Liquids, Superconductivity, Topology and Quantum Computation,” *arXiv preprint arXiv:1703.07322*, 2017.
- [74] Y. Zhou, K. Kanoda, and T.-K. Ng, “Quantum spin liquid states,” *Reviews of Modern Physics*, vol. 89, no. 2, p. 025003, 2017.
- [75] E. Pavarini, P. Coleman, and E. Koch, *Many-Body Physics: From Kondo to Hubbard*. Forschungszentrum Jülich, 2015.
- [76] G. Toulouse, “XVIII. Symmetry and topology concepts for spin glasses and other glasses,” *Physics Reports*, vol. 49, no. 2, pp. 267–272, 1979.
- [77] P. W. Anderson, “Spin glass I: A scaling law rescued,” *Physics Today*, vol. 41, no. 1, pp. 9–11, 1988.
- [78] A. Olariu, *Antiferromagnétisme frustré à deux dimensions : de la géométrie triangulaire dans NaCrO_2 à la géométrie kagomé dans $\text{Cu}_3\text{Zn}(\text{OH})_6\text{Cl}_2$* . PhD thesis, Université Paris Sud, 2008.
- [79] C. Lacroix, P. Mendels, and F. Mila, eds., *Introduction to Frustrated Magnetism*. Springer Berlin Heidelberg, 2011.
- [80] J. Sadoc and R. Mosseri, *Geometrical Frustration Monographs and Texts in Statistical Physics*. New York: Cambridge University Press, 1999.
- [81] P. Fazekas, *Lecture notes on electron correlation and magnetism*, vol. 5. World scientific, 1999.
- [82] P. Carretta, R. Melzi, N. Papinutto, and P. Millet, “Very-low-frequency excitations in frustrated two-dimensional $S=1/2$ Heisenberg antiferromagnets,” *Physical Review Letters*, vol. 88, no. 4, p. 047601, 2002.
- [83] R. Melzi, P. Carretta, A. Lascialfari, M. Mambrini, M. Troyer, P. Millet, and F. Mila, “ $\text{Li}_2\text{VO}(\text{Si},\text{Ge})\text{O}_4$, a prototype of a two-dimensional frustrated quantum Heisenberg antiferromagnet,” *Physical Review Letters*, vol. 85, no. 6, p. 1318, 2000.
- [84] J. S. Gardner, M. J. P. Gingras, and J. E. Greedan, “Magnetic pyrochlore oxides,” *Reviews of Modern Physics*, vol. 82, no. 1, pp. 53–107, 2010.

-
- [85] G. H. Wannier, “Antiferromagnetism. The Triangular Ising Net,” *Physical Review*, vol. 79, no. 2, pp. 357–364, 1950.
- [86] R. Moessner, S. L. Sondhi, and P. Chandra, “Phase diagram of the hexagonal lattice quantum dimer model,” *Physical Review B*, vol. 64, no. 14, 2001.
- [87] L. Savary and L. Balents, “Quantum spin liquids: a review,” *Reports on Progress in Physics*, vol. 80, no. 1, p. 016502, 2016.
- [88] P. Fazekas and P. W. Anderson, “On the ground state properties of the anisotropic triangular antiferromagnet,” *Philosophical Magazine*, vol. 30, no. 2, pp. 423–440, 1974.
- [89] D. A. Huse and V. Elser, “Simple Variational Wave Functions for Two-Dimensional Heisenberg Spin-1/2 Antiferromagnets,” *Physical Review Letters*, vol. 60, no. 24, pp. 2531–2534, 1988.
- [90] B. Bernu, C. Lhuillier, and L. Pierre, “Signature of Néel order in exact spectra of quantum antiferromagnets on finite lattices,” *Physical Review Letters*, vol. 69, no. 17, pp. 2590–2593, 1992.
- [91] M. Mambrini and F. Mila, “RVB description of the low-energy singlets of the spin-1/2 kagomé antiferromagnet,” *The European Physical Journal B*, vol. 17, no. 4, pp. 651–659, 2000.
- [92] C. Waldtmann, H.-U. Everts, B. Bernu, C. Lhuillier, P. Sindzingre, P. Lecheminant, and L. Pierre, “First excitations of the spin-1/2 Heisenberg antiferromagnet on the kagomé lattice,” *The European Physical Journal B*, vol. 2, no. 4, pp. 501–507, 1998.
- [93] M. Hermele, M. P. A. Fisher, and L. Balents, “Pyrochlore photons: The U(1) spin liquid in a $S=1/2$ three-dimensional frustrated magnet,” *Physical Review B*, vol. 69, no. 6, 2004.
- [94] P. W. Anderson, “The Resonating Valence Bond State in La_2CuO_4 and superconductivity,” *Science*, 1987.
- [95] G. Baskaran, Z. Zou, and P. W. Anderson, “The resonating valence bond state and high- T_c superconductivity: A mean field theory,” *Solid State Communications*, vol. 63, no. 11, pp. 973–976, 1987.
- [96] E. Fradkin and A. Auerbach, *Interacting Electrons and Quantum Magnetism*. Springer-Verlag, New York, 1994.
- [97] B. J. Powell and R. H. McKenzie, “Quantum frustration in organic Mott insulators: from spin liquids to unconventional superconductors,” *Reports on Progress in Physics*, vol. 74, no. 5, p. 056501, 2011.
- [98] I. Affleck and J. B. Marston, “Large- n limit of the Heisenberg-Hubbard model: Implications for high- T_c superconductors,” *Physical Review B*, vol. 37, no. 7, pp. 3774–3777, 1988.

Bibliography

- [99] N. Read and S. Sachdev, "Large- N expansion for frustrated quantum antiferromagnets," *Physical Review Letters*, vol. 66, no. 13, pp. 1773–1776, 1991.
- [100] X.-G. Wen, "Quantum orders and symmetric spin liquids," *Physical Review B*, vol. 65, no. 16, 2002.
- [101] A. Kitaev, "Anyons in an exactly solved model and beyond," *Annals of Physics*, vol. 321, no. 1, pp. 2–111, 2006.
- [102] A. Ramirez, "Strongly geometrically frustrated magnets," *Annual Review of Materials Science*, vol. 24, no. 1, 1994.
- [103] M. Levin and X.-G. Wen, "Detecting topological order in a ground state wave function," *Physical Review Letters*, vol. 96, no. 11, p. 110405, 2006.
- [104] A. Kitaev and J. Preskill, "Topological entanglement entropy," *Physical Review Letters*, vol. 96, no. 11, p. 110404, 2006.
- [105] K. Kanoda and R. Kato, "Mott Physics in Organic Conductors with Triangular Lattices," *Annual Review of Condensed Matter Physics*, vol. 2, no. 1, pp. 167–188, 2011.
- [106] J. T. Chalker, "Geometrically frustrated antiferromagnets: statistical mechanics and dynamics," in *Introduction to frustrated magnetism*, pp. 3–22, Springer, 2011.
- [107] H. Morita, S. Watanabe, and M. Imada, "Nonmagnetic insulating states near the Mott transitions on lattices with geometrical frustration and implications for κ -(ET)₂Cu₂(CN)₃," *Journal of the Physical Society of Japan*, vol. 71, no. 9, pp. 2109–2112, 2002.
- [108] I. Kézsmárki, Y. Shimizu, G. Mihály, Y. Tokura, K. Kanoda, and G. Saito, "Depressed charge gap in the triangular-lattice Mott insulator κ -(ET)₂Cu₂(CN)₃," *Physical Review B*, vol. 74, no. 20, 2006.
- [109] O. I. Motrunich, "Variational study of triangular lattice spin-1/2 model with ring exchanges and spin liquid state in κ -(ET)₂Cu₂(CN)₃," *Physical Review B*, vol. 72, no. 4, 2005.
- [110] M. S. Block, D. N. Sheng, O. I. Motrunich, and M. P. A. Fisher, "Spin Bose-Metal and Valence Bond Solid Phases in a Spin-1/2 Model with Ring Exchanges on a Four-Leg Triangular Ladder," *Physical Review Letters*, vol. 106, no. 15, 2011.
- [111] G. Chen, L. Balents, and A. P. Schnyder, "Spin-orbital singlet and quantum critical point on the diamond lattice: FeSc₂S₄," *Physical Review Letters*, vol. 102, no. 9, 2009.
- [112] G. Chen, R. Pereira, and L. Balents, "Exotic phases induced by strong spin-orbit coupling in ordered double perovskites," *Physical Review B*, vol. 82, no. 17, 2010.

- [113] H. O. Jeschke, F. Salvat-Pujol, and R. Valentí, “First-principles determination of Heisenberg Hamiltonian parameters for the spin-1/2 kagome antiferromagnet $\text{ZnCu}_3(\text{OH})_6\text{Cl}_2$,” *Physical Review B*, vol. 88, no. 7, 2013.
- [114] P. Mendels, F. Bert, M. De Vries, A. Olariu, A. Harrison, F. Duc, J. Trombe, J. Lord, A. Amato, and C. Baines, “Quantum magnetism in the paratacamite family: towards an ideal kagomé lattice,” *Physical Review Letters*, vol. 98, no. 7, p. 077204, 2007.
- [115] T. Itou, A. Oyamada, S. Maegawa, M. Tamura, and R. Kato, “Spin-liquid state in an organic spin-1/2 system on a triangular lattice, $\text{EtMe}_3\text{Sb}[\text{Pd}(\text{dmit})_2]_2$,” *Journal of Physics: Condensed Matter*, vol. 19, no. 14, p. 145247, 2007.
- [116] T. Itou, A. Oyamada, S. Maegawa, M. Tamura, and R. Kato, “Quantum spin liquid in the spin-1/2 triangular antiferromagnet $\text{EtMe}_3\text{Sb}[\text{Pd}(\text{dmit})_2]_2$,” *Physical Review B*, vol. 77, no. 10, 2008.
- [117] T. Itou, A. Oyamada, S. Maegawa, and R. Kato, “Instability of a quantum spin liquid in an organic triangular-lattice antiferromagnet,” *Nature Physics*, vol. 6, no. 9, pp. 673–676, 2010.
- [118] Y. Kurosaki, Y. Shimizu, K. Miyagawa, K. Kanoda, and G. Saito, “Mott transition from a spin liquid to a Fermi liquid in the spin-frustrated organic conductor $\kappa\text{-(ET)}_2\text{Cu}_2(\text{CN})_3$,” *Physical Review Letters*, vol. 95, no. 17, p. 177001, 2005.
- [119] Y. Shimizu, K. Miyagawa, K. Kanoda, M. Maesato, and G. Saito, “Emergence of inhomogeneous moments from spin liquid in the triangular-lattice Mott insulator $\kappa\text{-(ET)}_2\text{-Cu}_2(\text{CN})_3$,” *Physical Review B*, vol. 73, no. 14, 2006.
- [120] O. A. Starykh and L. Balents, “Ordering in spatially anisotropic triangular antiferromagnets,” *Physical Review Letters*, vol. 98, no. 7, 2007.
- [121] T. Pardini and R. Singh, “Magnetic order in coupled spin-half and spin-one Heisenberg chains in an anisotropic triangular-lattice geometry,” *Physical Review B*, vol. 77, no. 21, p. 214433, 2008.
- [122] H. Shinaoka, T. Misawa, K. Nakamura, and M. Imada, “Mott transition and phase diagram of $\kappa\text{-(BEDT-TTF)}_2\text{Cu}(\text{NCS})_2$ studied by two-dimensional model derived from ab initio method,” *Journal of the Physical Society of Japan*, vol. 81, no. 3, p. 034701, 2012.
- [123] S. Yunoki and S. Sorella, “Two spin liquid phases in the spatially anisotropic triangular Heisenberg model,” *Physical Review B*, vol. 74, no. 1, p. 014408, 2006.
- [124] T. Komatsu, N. Matsukawa, T. Inoue, and G. Saito, “Realization of Superconductivity at Ambient Pressure by Band-Filling Control in $\kappa\text{-(BEDT-TTF)}_2\text{Cu}_2(\text{CN})_3$,” *Journal of the Physical Society of Japan*, vol. 65, no. 5, pp. 1340–1354, 1996.
- [125] G. Saito, *Multifunctional conducting molecular materials*, vol. 100. Royal Society of Chemistry, 2007.

Bibliography

- [126] S. Ohira, Y. Shimizu, K. Kanoda, and G. Saito, "Spin liquid state in κ -(BEDT-TTF)₂Cu₂(CN)₃ Studied by muon spin relaxation method," *Journal of Low Temperature Physics*, vol. 142, no. 3-4, pp. 153–158, 2007.
- [127] S. Yamashita, Y. Nakazawa, M. Oguni, Y. Oshima, H. Nojiri, Y. Shimizu, K. Miyagawa, and K. Kanoda, "Thermodynamic properties of a spin-1/2 spin-liquid state in a κ -type organic salt," *Nature Physics*, vol. 4, no. 6, pp. 459–462, 2008.
- [128] S. Yamashita, T. Yamamoto, Y. Nakazawa, M. Tamura, and R. Kato, "Gapless spin liquid of an organic triangular compound evidenced by thermodynamic measurements," *Nature Communications*, vol. 2, p. 275, 2011.
- [129] M. Yamashita, N. Nakata, Y. Senshu, M. Nagata, H. M. Yamamoto, R. Kato, T. Shibauchi, and Y. Matsuda, "Highly Mobile Gapless Excitations in a Two-Dimensional Candidate Quantum Spin Liquid," *Science*, vol. 328, no. 5983, pp. 1246–1248, 2010.
- [130] M. Yamashita, N. Nakata, Y. Kasahara, T. Sasaki, N. Yoneyama, N. Kobayashi, S. Fujimoto, T. Shibauchi, and Y. Matsuda, "Thermal-transport measurements in a quantum spin-liquid state of the frustrated triangular magnet κ -(BEDT-TTF)₂Cu₂(CN)₃," *Nature Physics*, vol. 5, no. 1, pp. 44–47, 2008.
- [131] R. S. Manna, M. de Souza, A. Brühl, J. A. Schlueter, and M. Lang, "Lattice effects and entropy release at the low-temperature phase transition in the spin-liquid candidate κ -(BEDT-TTF)₂ Cu₂(CN)₃," *Physical Review Letters*, vol. 104, no. 1, 2010.
- [132] M. Poirier, S. Parent, A. Côté, K. Miyagawa, K. Kanoda, and Y. Shimizu, "Magnetodielectric effects and spin-charge coupling in the spin-liquid candidate κ -(BEDT-TTF)₂Cu₂(CN)₃," *Physical Review B*, vol. 85, no. 13, 2012.
- [133] M. Poirier, M. de Lafontaine, K. Miyagawa, K. Kanoda, and Y. Shimizu, "Ultrasonic investigation of the transition at 6 K in the spin-liquid candidate κ -(BEDT-TTF)₂Cu₂(CN)₃," *Physical Review B*, vol. 89, no. 4, 2014.
- [134] B. Kyung and A.-M. S. Tremblay, "Mott transition, antiferromagnetism, and d -wave superconductivity in two-dimensional organic conductors," *Physical Review Letters*, vol. 97, no. 4, 2006.
- [135] S.-S. Lee, P. A. Lee, and T. Senthil, "Amperean pairing instability in the U(1) spin liquid state with Fermi surface and application to κ -(BEDT-TTF)₂Cu₂(CN)₃," *Physical Review Letters*, vol. 98, no. 6, 2007.
- [136] T. Grover, N. Trivedi, T. Senthil, and P. A. Lee, "Weak Mott insulators on the triangular lattice: Possibility of a gapless nematic quantum spin liquid," *Physical Review B*, vol. 81, no. 24, 2010.
- [137] H. Li, R. T. Clay, and S. Mazumdar, "The paired-electron crystal in the two-dimensional frustrated quarter-filled band," *Journal of Physics: Condensed Matter*, vol. 22, no. 27, p. 272201, 2010.

- [138] S. Sebastian, N. Harrison, C. Batista, L. Balicas, M. Jaime, P. Sharma, N. Kawashima, and I. Fisher, "Dimensional reduction at a quantum critical point," *Nature*, vol. 441, no. 7093, pp. 617–620, 2006.
- [139] F. Pratt, "Superconductivity and magnetism in organic materials studied with μ SR," *Journal of the Physical Society of Japan*, vol. 85, no. 9, p. 091008, 2016.
- [140] T. Isono, T. Terashima, K. Miyagawa, K. Kanoda, and S. Uji, "Quantum criticality in an organic spin-liquid insulator κ -(BEDT-TTF) $_2$ Cu $_2$ (CN) $_3$," *Nature Communications*, vol. 7, p. 13494, 2016.
- [141] Y. Li, G. Chen, W. Tong, L. Pi, J. Liu, Z. Yang, X. Wang, and Q. Zhang, "Rare-earth triangular lattice spin liquid: a single-crystal study of YbMgGaO $_4$," *Physical Review Letters*, vol. 115, no. 16, p. 167203, 2015.
- [142] Y. Shen, Y.-D. Li, H. Wo, Y. Li, S. Shen, B. Pan, Q. Wang, H. C. Walker, P. Steffens, M. Boehm, Y. Hao, D. L. Quintero-Castro, L. W. Harriger, M. D. Frontzek, L. Hao, S. Meng, Q. Zhang, G. Chen, and J. Zhao, "Evidence for a spinon Fermi surface in a triangular-lattice quantum-spin-liquid candidate," *Nature*, vol. 540, no. 7634, pp. 559–562, 2016.
- [143] P. A. Lee, "An end to the drought of quantum spin liquids," *Science*, vol. 321, no. 5894, pp. 1306–1307, 2008.
- [144] J. S. Helton, K. Matan, M. P. Shores, E. A. Nytko, B. M. Bartlett, Y. Yoshida, Y. Takano, A. Suslov, Y. Qiu, J.-H. Chung, D. G. Nocera, and Y. S. Lee, "Spin Dynamics of the Spin-1/2 Kagome Lattice Antiferromagnet ZnCu $_3$ (OH) $_6$ Cl $_2$," *Physical Review Letters*, vol. 98, no. 10, 2007.
- [145] M. A. de Vries, J. R. Stewart, P. P. Deen, J. O. Piatek, G. J. Nilsen, H. M. Rønnow, and A. Harrison, "Scale-free antiferromagnetic fluctuations in the $S=1/2$ kagome antiferromagnet Herbertsmithite," *Physical Review Letters*, vol. 103, no. 23, 2009.
- [146] T.-H. Han, J. S. Helton, S. Chu, D. G. Nocera, J. A. Rodriguez-Rivera, C. Broholm, and Y. S. Lee, "Fractionalized excitations in the spin-liquid state of a kagome-lattice antiferromagnet," *Nature*, vol. 492, no. 7429, p. 406–410, 2012.
- [147] M. Norman, "Colloquium : Herbertsmithite and the search for the quantum spin liquid," *Reviews of Modern Physics*, vol. 88, no. 4, 2016.
- [148] O. Cépas, C. M. Fong, P. W. Leung, and C. Lhuillier, "Quantum phase transition induced by dzyaloshinskii-moriya interactions in the kagome antiferromagnet," *Physical Review B*, vol. 78, no. 14, 2008.
- [149] M. Jeong, F. Bert, P. Mendels, F. Duc, J. C. Trombe, M. A. de Vries, and A. Harrison, "Field-Induced Freezing of a Quantum Spin Liquid on the Kagome Lattice," *Physical Review Letters*, vol. 107, no. 23, 2011.

Bibliography

- [150] T. Furukawa, K. Miyagawa, T. Itou, M. Ito, H. Taniguchi, M. Saito, S. Iguchi, T. Sasaki, and K. Kanoda, "Quantum Spin Liquid Emerging from Antiferromagnetic Order by Introducing Disorder," *Physical Review Letters*, vol. 115, no. 7, 2015.
- [151] R. Coldea, D. A. Tennant, A. M. Tsvelik, and Z. Tylczynski, "Experimental Realization of a 2D Fractional Quantum Spin Liquid," *Physical Review Letters*, vol. 86, no. 7, pp. 1335–1338, 2001.
- [152] R. Coldea, D. Tennant, K. Habicht, P. Smeibidl, C. Wolters, and Z. Tylczynski, "Direct measurement of the spin Hamiltonian and observation of condensation of magnons in the 2D frustrated quantum magnet Cs_2CuCl_4 ," *Physical review letters*, vol. 88, no. 13, p. 137203, 2002.
- [153] R. Coldea, D. A. Tennant, and Z. Tylczynski, "Extended scattering continua characteristic of spin fractionalization in the two-dimensional frustrated quantum magnet Cs_2CuCl_4 observed by neutron scattering," *Physical Review B*, vol. 68, no. 13, 2003.
- [154] M. Kohno, O. A. Starykh, and L. Balents, "Spinons and triplons in spatially anisotropic frustrated antiferromagnets," *Nature Physics*, vol. 3, pp. 790–795, oct 2007.
- [155] M. Bocquet, F. H. Essler, A. M. Tsvelik, and A. O. Gogolin, "Finite-temperature dynamical magnetic susceptibility of quasi-one-dimensional frustrated spin-1/2 Heisenberg antiferromagnets," *Physical Review B*, vol. 64, no. 9, p. 094425, 2001.
- [156] T. Isono, H. Kamo, A. Ueda, K. Takahashi, A. Nakao, R. Kumai, H. Nakao, K. Kobayashi, Y. Murakami, and H. Mori, "Hydrogen bond-promoted metallic state in a purely organic single-component conductor under pressure," *Nature Communications*, vol. 4, p. 1344, 2013.
- [157] N. Elstner, R. R. P. Singh, and A. P. Young, "Finite temperature properties of the spin-1/2 Heisenberg antiferromagnet on the triangular lattice," *Physical Review Letters*, vol. 71, no. 10, pp. 1629–1632, 1993.
- [158] W. Zheng, R. R. P. Singh, R. H. McKenzie, and R. Coldea, "Temperature dependence of the magnetic susceptibility for triangular-lattice antiferromagnets with spatially anisotropic exchange constants," *Physical Review B*, vol. 71, no. 13, 2005.
- [159] E. Zavoisky, *Paramagnetic Absorption in Orthogonal and Parallel Fields for Salts, Solutions and Metals*. PhD thesis, Kazan University, Kazan, Russia, 1944.
- [160] C. P. Poole, *Relaxation in magnetic resonance*. Academic Press, 1971.
- [161] J. L. Zweier, "Measurement of superoxide-derived free radicals in the reperfused heart. Evidence for a free radical mechanism of reperfusion injury," *Journal of Biological Chemistry*, vol. 263, no. 3, pp. 1353–1357, 1988.

-
- [162] P. Szirmai, G. Fábián, B. Dóra, J. Koltai, V. Zólyomi, J. Kürti, N. M. Nemes, L. Forró, and F. Simon, “Density of states deduced from ESR measurements on low-dimensional nanostructures; benchmarks to identify the ESR signals of graphene and SWCNTs,” *physica status solidi (b)*, vol. 248, no. 11, pp. 2688–2691, 2011.
- [163] O. Chauvet, G. Oszlányi, L. Forro, P. W. Stephens, M. Tegze, G. Faigel, and A. Jànossy, “Quasi-one-dimensional electronic structure in orthorhombic RbC₆₀,” *Physical Review Letters*, vol. 72, no. 17, pp. 2721–2724, 1994.
- [164] B. Náfrádi, M. Choucair, K.-P. Dinse, and L. Forró, “Room temperature manipulation of long lifetime spins in metallic-like carbon nanospheres,” *Nature Communications*, vol. 7, p. 12232, 2016.
- [165] D. P. DiVincenzo, “Quantum computation,” *Science*, vol. 270, no. 5234, p. 255, 1995.
- [166] T. Takui, L. Berliner, and G. Hanson, *Electron Spin Resonance (ESR) Based Quantum Computing*, vol. 31. Springer, 2016.
- [167] P. Szirmai, G. Fábián, J. Koltai, B. Náfrádi, L. Forró, T. Pichler, O. A. Williams, S. Mandal, C. Bäuerle, and F. Simon, “Observation of conduction electron spin resonance in boron-doped diamond,” *Physical Review B*, vol. 87, no. 19, 2013.
- [168] C.-M. Park, S. Ramanathan, P. Morrow, and K. Cadien, “Integrated on-chip NMR and ESR device and method for making and using the same,” Sept. 25 2007. US Patent 7,274,191.
- [169] A. V. Matheoud, G. Gualco, M. Jeong, I. Zivkovic, J. Brugger, H. M. Rønnow, J. Anders, and G. Boero, “Single-chip electron spin resonance detectors operating at 50 GHz, 92 GHz, and 146 GHz,” *Journal of Magnetic Resonance*, vol. 278, pp. 113–121, 2017.
- [170] P. Zeeman, “The effect of magnetisation on the nature of light emitted by a substance,” *Nature*, vol. 55, no. 1424, p. 347, 1897.
- [171] P. Szirmai, “Electron spin resonance spectroscopy in boron-doped diamond,” Master’s thesis, Budapest University of Technology and Economics, 2013.
- [172] C. P. Slichter, *Principles of magnetic resonance*, vol. 1. Springer Science & Business Media, 2013.
- [173] N. Ashcroft and N. Mermin, *Solid State Physics*. HRW international editions, Holt, Rinehart and Winston, 1976.
- [174] P. Ehrenfest, “Bemerkung über die angenäherte gültigkeit der klassischen mechanik innerhalb der quantenmechanik,” *Zeitschrift für Physik*, vol. 45, no. 7-8, pp. 455–457, 1927.
- [175] F. Bloch, “Nuclear induction,” *Physical Review*, vol. 70, no. 7-8, p. 460, 1946.

Bibliography

- [176] E. M. Purcell, H. Torrey, and R. V. Pound, "Resonance absorption by nuclear magnetic moments in a solid," *Physical Review*, vol. 69, no. 1-2, p. 37, 1946.
- [177] R. R. Ernst and W. A. Anderson, "Application of Fourier transform spectroscopy to magnetic resonance," *Review of Scientific Instruments*, vol. 37, no. 1, pp. 93–102, 1966.
- [178] K.-D. Schmalbein and K. Holczer, "Electron spin resonance spectrometer," Nov. 1 1988. US Patent 4,782,296.
- [179] K. Holczer, D. Schmalbein, and P. Hofer, "Method of measuring pulsed electron spin resonance signals and pulsed electron spin resonance spectrometer," Apr. 30 1996. US Patent 5,512,829.
- [180] M. J. Junk, *Assessing the functional structure of molecular transporters by EPR spectroscopy*. Springer Science & Business Media, 2012.
- [181] B. Náfrádi, R. Gaál, A. Sienkiewicz, T. Fehér, and L. Forró, "Continuous-wave far-infrared ESR spectrometer for high-pressure measurements," *Journal of Magnetic Resonance*, vol. 195, no. 2, pp. 206 – 210, 2008.
- [182] B. Náfrádi, R. Gaál, T. Fehér, and L. Forró, "Microwave frequency modulation in continuous-wave far-infrared ESR utilizing a quasi-optical reflection bridge," *Journal of Magnetic Resonance*, vol. 192, no. 2, pp. 265 – 268, 2008.
- [183] E. J. Reijerse, "High-frequency EPR instrumentation," *Applied Magnetic Resonance*, vol. 37, no. 1-4, p. 795, 2010.
- [184] C. Poole, *Electron Spin Resonance: A Comprehensive Treatise on Experimental Techniques*. Courier Corporation, 1967.
- [185] G. Jeschke, "Instrumentation and experimental setup," in *ESR spectroscopy in membrane biophysics*, pp. 17–47, Springer, 2007.
- [186] J. A. Weil and J. R. Bolton, *Electron paramagnetic resonance: elementary theory and practical applications*. John Wiley & Sons, 2007.
- [187] G. Feher, "Sensitivity considerations in microwave paramagnetic resonance absorption techniques," *Bell System Technical Journal*, vol. 36, no. 2, pp. 449–484, 1957.
- [188] A. L. Barra, A. Caneschi, D. Gatteschi, and R. Sessoli, "High-frequency EPR spectra for the analysis of magnetic anisotropy in large magnetic clusters," *Journal of the American Chemical Society*, vol. 117, no. 34, pp. 8855–8856, 1995.
- [189] E. Rentschler, D. Gatteschi, A. Cornia, A. C. Fabretti, A.-L. Barra, O. I. Shchegolikhina, and A. A. Zhdanov, "Molecule-Based Magnets: Ferro- and Antiferromagnetic Interactions in Copper (II)- Polyorganosiloxanolate Clusters," *Inorganic Chemistry*, vol. 35, no. 15, pp. 4427–4431, 1996.

-
- [190] G. Smith, J. Lesurf, R. Mitchell, and P. Riedi, "Quasi-optical CW mm-wave Electron Spin Resonance spectrometer," *Review of Scientific Instruments*, vol. 69, no. 11, pp. 3924–3937, 1998.
- [191] P. J. van Dam, A. A. Klaassen, E. J. Reijerse, and W. R. Hagen, "Application of high frequency EPR to integer spin systems: Unusual behavior of the double-quantum line," *Journal of Magnetic Resonance*, vol. 130, no. 1, pp. 140–144, 1998.
- [192] J. C. G. Lesurf, *Millimetre-wave optics, devices and systems*. CRC Press, 1990.
- [193] A. Portis and D. Teaney, "Microwave Faraday rotation: design and analysis of a bimodal cavity," *Journal of Applied Physics*, vol. 29, no. 12, pp. 1692–1698, 1958.
- [194] J. Stankowski, A. Gal, M. Krupski, S. Waplak, H. Gierszal, *et al.*, "Microwave resonators for EPR studies at high hydrostatic pressure," *Review of Scientific Instruments*, vol. 47, no. 1, pp. 128–129, 1976.
- [195] O. Chauvet, A. Sienkiewicz, L. Forró, and L. Zuppiroli, "High-pressure electron-spin dynamics in disordered conducting polymers," *Physical Review B*, vol. 52, no. 18, p. R13118, 1995.
- [196] A. Sienkiewicz and M. Jaworski, "High hydrostatic pressure ESR manostats," *High Pressure Science and Technology*, vol. 5, no. 1-6, pp. 877–879, 1990.
- [197] A. Sienkiewicz, B. Vilenó, S. Garaj, M. Jaworski, and L. Forró, "Dielectric resonator-based resonant structure for sensitive ESR measurements at high-hydrostatic pressures," *Journal of Magnetic Resonance*, vol. 177, no. 2, pp. 261–273, 2005.
- [198] N. F. Mott, "The basis of the electron theory of metals, with special reference to the transition metals," *Proceedings of the Physical Society. Section A*, vol. 62, no. 7, p. 416, 1949.
- [199] J. Hubbard, "Electron correlations in narrow energy bands," in *Proceedings of the Royal Society of London A: Mathematical, Physical and Engineering Sciences*, vol. 276, pp. 238–257, The Royal Society, 1963.
- [200] F. J. Dyson, "Electron spin resonance absorption in metals. II. Theory of electron diffusion and the skin effect," *Physical Review*, vol. 98, no. 2, p. 349, 1955.
- [201] G. Feher and A. Kip, "Electron spin resonance absorption in metals. I. Experimental," *Physical Review*, vol. 98, no. 2, p. 337, 1955.
- [202] Y. Yafet, "g factors and spin-lattice relaxation of conduction electrons," *Solid State Physics*, vol. 14, pp. 1–98, 1963.
- [203] F. Beuneu and P. Monod, "The Elliott relation in pure metals," *Physical Review B*, vol. 18, no. 6, p. 2422, 1978.

Bibliography

- [204] R. J. Elliott, "Theory of the effect of spin-orbit coupling on magnetic resonance in some semiconductors," *Physical Review*, vol. 96, no. 2, p. 266, 1954.
- [205] Y. Yafet, "Conduction electron spin relaxation in the superconducting state," *Physics Letters A*, vol. 98, no. 5-6, pp. 287–290, 1983.
- [206] L. Forró, J. Cooper, G. Sekretarczyk, M. Krupski, and K. Kamarás, "Conduction electron spin resonance measurements on TTF-TNNQ and (TMTTF)₂BF₄ under hydrostatic pressure," *Journal de Physique*, vol. 48, no. 3, pp. 413–418, 1987.
- [207] Y. Tomkiewicz and A. Taranko, "Spin relaxations in quasi-one-dimensional organic conductors: tetrathiafulvalene (TTF) halides," *Physical Review B*, vol. 18, no. 2, p. 733, 1978.
- [208] P. Szirmai, I. Zivković, I. Djerd, H. Rønnow, L. Forró, and B. Náfrádi, "Magnetic structure of the double perovskite Ca₂MnTeO₆."
- [209] P. M. Chaikin and T. C. Lubensky, *Principles of condensed matter physics*. Cambridge University Press, 2000.
- [210] C. Coulon and R. Clérac, "Electron Spin Resonance: A Major Probe for Molecular Conductors," *Chemical Reviews*, vol. 104, no. 11, pp. 5655–5688, 2004.
- [211] I. Dzyaloshinsky, "A thermodynamic theory of 'weak' ferromagnetism of antiferromagnetics," *Journal of Physics and Chemistry of Solids*, vol. 4, no. 4, pp. 241–255, 1958.
- [212] T. Moriya, "Anisotropic superexchange interaction and weak ferromagnetism," *Physical Review*, vol. 120, no. 1, pp. 91–98, 1960.
- [213] P. Pincus, "Theory of magnetic resonance in α -Fe₂O₃," *Physical Review Letters*, vol. 5, no. 1, p. 13, 1960.
- [214] J. Rawson, A. Alberola, H. El-Mkami, and G. Smith, "Antiferromagnetic resonance studies in molecular magnetic materials," *Journal of Physics and Chemistry of Solids*, vol. 65, no. 4, pp. 727–731, 2004.
- [215] F. Kagawa, Y. Kurosaki, K. Miyagawa, and K. Kanoda, "Field-induced staggered magnetic moment in the quasi-two-dimensional organic Mott insulator κ -(BEDT-TTF)₂Cu[N(CN)₂]Cl," *Physical Review B*, vol. 78, no. 18, 2008.
- [216] Á. Antal, T. Fehér, B. Náfrádi, L. Forró, and A. Jánossy, "Two-dimensional magnetism in κ -(BEDT-TTF)₂Cu[N(CN)₂]Cl, a Spin-1/2 Heisenberg Antiferromagnet with Dzyaloshinskii–Moriya Interaction," *Journal of the Physical Society of Japan*, vol. 84, no. 12, p. 124704, 2015.
- [217] M. Oshikawa and I. Affleck, "Field-induced gap in $S = 1 / 2$ Antiferromagnetic chains," *Physical Review Letters*, vol. 79, no. 15, pp. 2883–2886, 1997.

- [218] I. Affleck and M. Oshikawa, "Field-induced gap in Cu benzoate and other $S = 1/2$ antiferromagnetic chains," *Physical Review B*, vol. 60, no. 2, pp. 1038–1056, 1999.
- [219] M. Oshikawa and I. Affleck, "Electron spin resonance in $S = 1/2$ antiferromagnetic chains," *Physical Review B*, vol. 65, no. 13, 2002.
- [220] S. Zvyagin, A. Kolezhuk, J. Krzystek, and R. Feyerherm, "Electron Spin Resonance in Sine-Gordon Spin Chains in the Perturbative Spinon Regime," *Physical Review Letters*, vol. 95, no. 1, 2005.
- [221] I. J. Hamad, A. E. Trumper, P. Wzietek, S. Lefebvre, and L. O. Manuel, " $1/T_1$ nuclear relaxation time of κ -(BEDT-TTF)₂Cu[N(CN)₂]Cl: effects of magnetic frustration," *Journal of Physics: Condensed Matter*, vol. 17, no. 50, pp. 8091–8102, 2005.
- [222] Á. Antal, T. Fehér, A. Jánossy, E. Tátrai-Szekeres, and F. Fülöp, "Spin Diffusion and Magnetic Eigenoscillations Confined to Single Molecular Layers in the Organic Conductors κ -(BEDT-TTF)₂ Cu[N(CN)₂]X (X= Cl, Br)," *Physical Review Letters*, vol. 102, no. 8, 2009.
- [223] B. Powell, E. Kenny, and J. Merino, "Dynamical reduction of the dimensionality of exchange interactions and the 'spin-liquid' phase of κ -(BEDT-TTF)₂Cu₂(CN)₃," *arXiv preprint arXiv:1704.05688*, 2017.
- [224] Á. Antal, T. Fehér, E. Tátrai-Szekeres, F. Fülöp, B. Náfrádi, L. Forró, and A. Jánossy, "Pressure and temperature dependence of interlayer spin diffusion and electrical conductivity in the layered organic conductors κ -(BEDT-TTF)₂ Cu[N(CN)₂]X (X=Cl,Br)," *Physical Review B*, vol. 84, no. 7, 2011.
- [225] B. Martinelli, "Volcanic tremor and short-term prediction of eruptions," *Journal of Volcanology and Geothermal Research*, vol. 77, no. 1-4, pp. 305–311, 1997.
- [226] S. J. Blundell, "Spin-polarized muons in condensed matter physics," *Contemporary Physics*, vol. 40, no. 3, pp. 175–192, 1999.
- [227] S. J. Blundell, "Muon-Spin Rotation Studies of Electronic Properties of Molecular Conductors and Superconductors," *Chemical Reviews*, vol. 104, no. 11, pp. 5717–5736, 2004.
- [228] S. L. Lee, R. Cywinski, and S. Kilcoyne, *Muon science: Muons in physics, chemistry and materials*, vol. 51. CRC Press, 1999.
- [229] P. D. De Reotier and A. Yaouanc, "Muon spin rotation and relaxation in magnetic materials," *Journal of Physics: Condensed Matter*, vol. 9, no. 43, p. 9113, 1997.
- [230] R. Kubo, "A stochastic theory of spin relaxation," *Hyperfine Interactions*, vol. 8, no. 4, pp. 731–738, 1981.
- [231] R. Hayano, Y. Uemura, J. Imazato, N. Nishida, T. Yamazaki, and R. Kubo, "Zero-and low-field spin relaxation studied by positive muons," *Physical Review B*, vol. 20, no. 3, p. 850, 1979.

Bibliography

- [232] A. Abragam, *Principles of Nuclear Magnetism (International series of monographs on physics)*. Clarendon Press, Oxford, 1961.
- [233] A. Keren, "Generalization of the Abragam relaxation function to a longitudinal field," *Physical Review B*, vol. 50, no. 14, pp. 10039–10042, 1994.
- [234] Y. Uemura, " μ sr relaxation functions in magnetic materials," *Muon Science. Muons in Physics, Chemistry and Materials (Bristol and Philadelphia, 1999)*, SHKSL Lee and ER Cywinski, Eds, vol. 51, pp. 85–114, 1999.
- [235] S. Cox, "Implanted muon studies in condensed matter science," *Journal of Physics C: Solid State Physics*, vol. 20, no. 22, p. 3187, 1987.
- [236] M. Gaboardi, A. Bliersbach, G. Bertoni, M. Aramini, G. Vlahopoulou, D. Pontiroli, P. Mauron, G. Magnani, G. Salviati, A. Züttel, and M. Riccò, "Decoration of graphene with nickel nanoparticles: study of the interaction with hydrogen," *J. Mater. Chem. A*, vol. 2, no. 4, pp. 1039–1046, 2014.
- [237] E. Roduner, "Polarized positive muons probing free radicals: a variant of magnetic resonance," *Chemical Society Reviews*, vol. 22, no. 5, pp. 337–346, 1993.
- [238] S. F. Cox and D. Sivia, "Spin-lattice relaxation in hyperfine-coupled systems: applications to interstitial diffusion and molecular dynamics," *Applied Magnetic Resonance*, vol. 12, no. 2, pp. 213–226, 1997.
- [239] S. Cox, "Muon spin relaxation studies of interstitial and molecular motion," *Solid state nuclear magnetic resonance*, vol. 11, no. 1, pp. 103–121, 1998.
- [240] J. Chakhalian, R. Kiefl, R. Miller, S. Dunsiger, G. Morris, S. Kreitzman, W. MacFarlane, J. Sonier, S. Eggert, I. Affleck, *et al.*, "Local magnetic susceptibility of the positive muon in the quasi-1D $S=1/2$ antiferromagnet KCuF_3 ," *Physica B: Condensed Matter*, vol. 326, no. 1, pp. 422–426, 2003.
- [241] P. L. Anelli, N. Spencer, and J. F. Stoddart, "A molecular shuttle," *Journal of the American Chemical Society*, vol. 113, no. 13, pp. 5131–5133, 1991.
- [242] J. D. Badjić, V. Balzani, A. Credi, S. Silvi, and J. F. Stoddart, "A molecular elevator," *Science*, vol. 303, no. 5665, pp. 1845–1849, 2004.
- [243] B. L. Feringa, "In control of motion: from molecular switches to molecular motors," *Accounts of chemical research*, vol. 34, no. 6, pp. 504–513, 2001.
- [244] V. Balzani, A. Credi, F. M. Raymo, and J. F. Stoddart, "Artificial molecular machines," *Angewandte Chemie International Edition*, vol. 39, no. 19, pp. 3348–3391, 2000.
- [245] M. C. Jiménez, C. Dietrich-Buchecker, and J.-P. Sauvage, "Towards synthetic molecular muscles: Contraction and stretching of a linear rotaxane dimer," *Angewandte Chemie*, vol. 112, no. 18, pp. 3422–3425, 2000.

- [246] N. Koumura, R. W. Zijlstra, R. A. van Delden, N. Harada, and B. L. Feringa, "Light-driven monodirectional molecular rotor," *Nature*, vol. 401, no. 6749, p. 152, 1999.
- [247] M. A. Garcia-Garibay, "Crystalline molecular machines: Encoding supramolecular dynamics into molecular structure," *Proceedings of the National Academy of Sciences of the United States of America*, vol. 102, no. 31, pp. 10771–10776, 2005.
- [248] D. Horinek and J. Michl, "Surface-mounted altitudinal molecular rotors in alternating electric field: Single-molecule parametric oscillator molecular dynamics," *Proceedings of the National Academy of Sciences*, vol. 102, no. 40, pp. 14175–14180, 2005.
- [249] J. Michl and E. C. H. Sykes, "Molecular rotors and motors: recent advances and future challenges," 2009.
- [250] C. A. Fyfe, *Solid state NMR for chemists*. CFC Press, 1983.
- [251] R. Kubo and K. Tomita, "A general theory of magnetic resonance absorption," *Journal of the Physical Society of Japan*, vol. 9, no. 6, pp. 888–919, 1954.
- [252] C. Lemouchi, K. Iliopoulos, L. Zorina, S. Simonov, P. Wzietek, T. Cauchy, A. Rodríguez-Forteza, E. Canadell, J. Kaleta, J. Michl, *et al.*, "Crystalline arrays of pairs of molecular rotors: correlated motion, rotational barriers, and space-inversion symmetry breaking due to conformational mutations," *Journal of the American Chemical Society*, vol. 135, no. 25, pp. 9366–9376, 2013.
- [253] J. Kaleta, J. Michl, C. Mézière, S. Simonov, L. Zorina, P. Wzietek, A. Rodríguez-Forteza, E. Canadell, and P. Batail, "Gearing motion in cogwheel pairs of molecular rotors: weak-coupling limit," *CrystEngComm*, vol. 17, no. 41, pp. 7829–7834, 2015.
- [254] G. Bastien, C. Lemouchi, M. Allain, P. Wzietek, A. Rodríguez-Forteza, E. Canadell, K. Iliopoulos, D. Gindre, M. Chrysos, and P. Batail, "Changing gears to neutral in a polymorph of one-dimensional arrays of cogwheel-like pairs of molecular rotors," *CrystEngComm*, vol. 16, no. 7, pp. 1241–1244, 2014.
- [255] C. Lemouchi, H. M. Yamamoto, R. Kato, S. Simonov, L. Zorina, A. Rodríguez-Forteza, E. Canadell, P. Wzietek, K. Iliopoulos, D. Gindre, *et al.*, "Reversible control of crystalline rotors by squeezing their hydrogen bond cloud across a halogen bond-mediated phase transition," *Crystal Growth & Design*, vol. 14, no. 7, pp. 3375–3383, 2014.
- [256] F. Camerel, G. Le Helloco, T. Guizouarn, O. Jeannin, M. Fourmigué, A. Fraçkowiak, I. Olejniczak, R. Świetlik, A. Marino, E. Collet, *et al.*, "Correlation between metal–insulator transition and hydrogen-bonding network in the organic metal δ -(BEDT-TTF)₄[2,6-Anthracene-bis(sulfonate)]·(H₂O)₄," *Crystal Growth & Design*, vol. 13, no. 11, pp. 5135–5145, 2013.
- [257] N. F. Mott and E. A. Davis, *Electronic processes in non-crystalline materials*. OUP Oxford, 2012.

Bibliography

- [258] K. Behnia, *Fundamentals of thermoelectricity*. OUP Oxford, 2015.
- [259] C. P. Landee and M. M. Turnbull, "A gentle introduction to magnetism: units, fields, theory, and experiment," *Journal of Coordination Chemistry*, vol. 67, no. 3, pp. 375–439, 2014.
- [260] G. Bastien, C. Lemouchi, P. Wzietek, S. Simonov, L. Zorina, A. Rodríguez-Forteza, E. Canadell, and P. Batail, "A crystalline hybrid of paddlewheel copper (ii) dimers and molecular rotors: Singlet-triplet dynamics revealed by variable-temperature proton spin-lattice relaxation," *Zeitschrift für anorganische und allgemeine Chemie*, vol. 640, no. 6, pp. 1127–1133, 2014.
- [261] D. L. Reger, A. Debreczeni, M. D. Smith, J. Jezierska, and A. Ozarowski, "Copper (ii) carboxylate dimers prepared from ligands designed to form a robust $\pi \cdots \pi$ stacking synthon: Supramolecular structures and molecular properties," *Inorganic Chemistry*, vol. 51, no. 2, pp. 1068–1083, 2011.
- [262] S. Sachdev and K. Damle, "Low temperature spin diffusion in the one-dimensional quantum O(3) nonlinear σ model," *Physical Review Letters*, vol. 78, no. 5, p. 943, 1997.
- [263] A. El-Ghayoury, C. Mézière, S. Simonov, L. Zorina, M. Cobián, E. Canadell, C. Rovira, B. Náfrádi, B. Sipos, L. Forró, *et al.*, "A neutral zwitterionic molecular solid," *Chemistry—A European Journal*, vol. 16, no. 47, pp. 14051–14059, 2010.
- [264] A. Štefančič, G. Klupp, T. Knaflič, D. S. Yufit, G. Tavcar, A. Potočnik, A. Beeby, and D. Arcon, "Triphenylide-based molecular solid—a new candidate for a quantum spin-liquid compound," *The Journal of Physical Chemistry C*, 2017.
- [265] D. Johnston, M. Troyer, S. Miyahara, D. Lidsky, K. Ueda, M. Azuma, Z. Hiroi, M. Takano, M. Isobe, Y. Ueda, *et al.*, "Magnetic susceptibilities of spin-1/2 antiferromagnetic Heisenberg ladders and applications to ladder oxide compounds," *arXiv preprint cond-mat/0001147*, 2000.
- [266] T. Moriya, "Nuclear magnetic relaxation in antiferromagnetics," *Progress of Theoretical Physics*, vol. 16, no. 1, pp. 23–44, 1956.
- [267] H. Alloul, *Introduction to the Physics of Electrons in Solids*. Springer Science & Business Media, 2010.
- [268] J. C. Bonner and M. E. Fisher, "Linear magnetic chains with anisotropic coupling," *Physical Review*, vol. 135, no. 3A, p. A640, 1964.
- [269] D. Johnston, R. Kremer, M. Troyer, X. Wang, A. Klümper, S. Bud'ko, A. Panchula, and P. Canfield, "Thermodynamics of spin $S=1/2$ antiferromagnetic uniform and alternating-exchange Heisenberg chains," *Physical Review B*, vol. 61, no. 14, p. 9558, 2000.

- [270] B. Keith, C. Landee, T. Valteau, M. Turnbull, and N. Harrison, "Erratum: Two-dimensional spin-1/2 rectangular Heisenberg antiferromagnets: Simulation and experiment," *Physical Review B*, vol. 84, no. 22, p. 229901, 2011.
- [271] B. Keith, C. Landee, T. Valteau, M. Turnbull, and N. Harrison, "Two-dimensional spin-1/2 rectangular Heisenberg antiferromagnets: Simulation and experiment," *Physical Review B*, vol. 84, no. 10, p. 104442, 2011.
- [272] M. Dumm, A. Loidl, B. Fravel, K. Starkey, L. Montgomery, and M. Dressel, "Electron spin resonance studies on the organic linear-chain compounds $(\text{TMTCF})_2X$ ($C = \text{S, Se}$; $X = \text{PF}_6, \text{AsF}_6, \text{ClO}_4, \text{Br}$)," *Physical Review B*, vol. 61, no. 1, p. 511, 2000.
- [273] B. Náfrádi, A. Olariu, L. Forró, C. Mézière, P. Batail, and A. Jánossy, "Spin dynamics in the $S=1/2$ antiferromagnetic chain compounds δ -(EDT-TTF-CONMe₂)₂X ($X = \text{AsF}_6, \text{Br}$): A multi-frequency electron spin resonance study," *Physical Review B*, vol. 81, no. 22, 2010.
- [274] B. Náfrádi, *Multi-Frequency High-Pressure Electron Spin Resonance Study of Low Dimensional Organic Conductors*. PhD thesis, Ecole Polytechnique Fédérale de Lausanne, 2009.
- [275] M. Dumm, A. Loidl, B. Alavi, K. Starkey, L. Montgomery, and M. Dressel, "Comprehensive ESR study of the antiferromagnetic ground states in the one-dimensional spin systems $(\text{TMTSF})_2\text{PF}_6, (\text{TMTSF})_2\text{AsF}_6$, and $(\text{TMTTF})_2\text{Br}$," *Physical Review B*, vol. 62, no. 10, p. 6512, 2000.
- [276] B. Náfrádi, Á. Antal, T. Fehér, L. Kiss, C. Mézière, P. Batail, L. Forró, and A. Jánossy, "Frustration-induced one-dimensionality in the isosceles triangular antiferromagnetic lattice of δ -(EDT-TTF-CONMe₂)₂AsF₆," *Physical Review B*, vol. 94, no. 17, p. 174413, 2016.
- [277] S. P. Gabuda, S. G. Kozlova, D. G. Samsonenko, D. N. Dybtsev, and V. P. Fedin, "Quantum Rotations and Chiral Polarization of Qubit Prototype Molecules in a Highly Porous Metal–Organic Framework: ¹H NMR T_1 Study," *The Journal of Physical Chemistry C*, vol. 115, no. 42, pp. 20460–20465, 2011.
- [278] S. Nakajima, T. Suzuki, Y. Ishii, K. Ohishi, I. Watanabe, T. Goto, A. Oosawa, N. Yoneyama, N. Kobayashi, F. L. Pratt, and et al., "Microscopic phase separation in triangular-lattice quantum spin magnet κ -(BEDT-TTF)₂Cu₂(CN)₃ probed by muon spin relaxation," *Journal of the Physical Society of Japan*, vol. 81, no. 6, p. 063706, 2012.
- [279] A. Kornilov, V. Pudalov, Y. Kitaoka, K. Ishida, G.-q. Zheng, T. Mito, and J. Qualls, "Macroscopically inhomogeneous state at the boundary between the superconducting, antiferromagnetic, and metallic phases in quasi-one-dimensional $(\text{TMTSF})_2\text{PF}_6$," *Physical Review B*, vol. 69, no. 22, p. 224404, 2004.

Bibliography

- [280] L. Zorina, S. Simonov, C. Mézière, E. Canadell, S. Suh, S. E. Brown, P. Foury-Leykian, P. Fertey, J.-P. Pouget, and P. Batail, “Charge ordering, symmetry and electronic structure issues and Wigner crystal structure of the quarter-filled band Mott insulators and high pressure metals δ -(EDT-TTF-CONMe₂)₂X, X=Br and AsF₆,” *Journal of Materials Chemistry*, vol. 19, no. 38, pp. 6980–6994, 2009.
- [281] Á. Antal, *Two Dimensional Spin Transport and Magnetism in Layered Organic Crystals*. PhD thesis, Budapest University of Technology and Economics, 2011.
- [282] C. Hotta, “Quantum electric dipoles in spin-liquid dimer Mott insulator κ -ET₂Cu₂(CN)₃,” *Physical Review B*, vol. 82, no. 24, 2010.
- [283] M. Abdel-Jawad, I. Terasaki, T. Sasaki, N. Yoneyama, N. Kobayashi, Y. Uesu, and C. Hotta, “Anomalous dielectric response in the dimer Mott insulator κ -(BEDT-TTF)₂Cu₂(CN)₃,” *Physical Review B*, vol. 82, no. 12, p. 125119, 2010.
- [284] M. Pinterić, M. Čulo, O. Milat, M. Basletić, B. Korin-Hamzić, E. Tafra, A. Hamzić, T. Ivek, T. Peterseim, K. Miyagawa, and et al., “Anisotropic charge dynamics in the quantum spin-liquid candidate κ -(BEDT-TTF)₂ Cu₂(CN)₃,” *Physical Review B*, vol. 90, no. 19, 2014.
- [285] M. Pinterić, P. Lazić, A. Pustogow, T. Ivek, M. Kuveždić, O. Milat, B. Gumhalter, M. Basletić, M. Čulo, B. Korin-Hamzić, et al., “Anion effects on electronic structure and electrodynamic properties of the Mott insulator κ -(BEDT-TTF)₂Ag₂(CN)₃,” *Physical Review B*, vol. 94, no. 16, p. 161105, 2016.
- [286] D. F. Smith, S. M. De Soto, C. P. Slichter, J. A. Schlueter, A. M. Kini, and R. G. Daugherty, “Dzyaloshinskii-Moriya interaction in the organic superconductor κ -(BEDT-TTF)₂Cu[N(CN)₂]Cl,” *Physical Review B*, vol. 68, no. 2, 2003.
- [287] K. Watanabe, H. Kawamura, H. Nakano, and T. Sakai, “Quantum spin-liquid behavior in the spin-1/2 random Heisenberg antiferromagnet on the triangular lattice,” *Journal of the Physical Society of Japan*, vol. 83, no. 3, p. 034714, 2014.
- [288] M. Oshikawa, K. Ueda, H. Aoki, A. Ochiai, and M. Kohgi, “Field-induced gap formation in Yb₄As₃,” *Journal of the Physical Society of Japan*, vol. 68, no. 10, pp. 3181–3184, 1999.
- [289] R. R. Biswas, L. Fu, C. R. Laumann, and S. Sachdev, “SU(2)-invariant spin liquids on the triangular lattice with spinful Majorana excitations,” *Physical Review B*, vol. 83, no. 24, p. 245131, 2011.
- [290] F. L. Pratt, S. J. Blundell, T. Lancaster, C. Baines, and S. Takagi, “Low-temperature spin diffusion in a highly ideal S=1/2 Heisenberg antiferromagnetic chain studied by muon spin relaxation,” *Physical Review Letters*, vol. 96, no. 24, 2006.
- [291] F. Xiao, J. S. Möller, T. Lancaster, R. C. Williams, F. L. Pratt, S. J. Blundell, D. Ceresoli, A. M. Barton, and J. L. Manson, “Spin diffusion in the low-dimensional molecular quantum Heisenberg antiferromagnet Cu(py₂z)(NO₃)₂ detected with implanted muons,” *Physical Review B*, vol. 91, no. 14, 2015.

- [292] Y. Qi, C. Xu, and S. Sachdev, "Dynamics and transport of the Z_2 spin liquid: Application to κ -(ET) $_2$ Cu $_2$ (CN) $_3$," *Physical Review Letters*, vol. 102, no. 17, 2009.
- [293] T. Lancaster, P. J. Baker, F. L. Pratt, S. J. Blundell, W. Hayes, and D. Prabhakaran, "Persistent dynamics in the $S=1/2$ quasi-one-dimensional chain compound Rb $_4$ Cu(MoO $_4$) $_3$ probed with muon-spin relaxation," *Physical Review B*, vol. 85, no. 18, 2012.
- [294] T. Lancaster, S. J. Blundell, M. L. Brooks, P. J. Baker, F. L. Pratt, J. L. Manson, C. P. Landee, and C. Baines, "Magnetic order in the quasi-one-dimensional spin-1/2 molecular chain compound copper pyrazine dinitrate," *Physical Review B*, vol. 73, no. 2, 2006.
- [295] S. Sachdev, "NMR relaxation in half-integer antiferromagnetic spin chains," *Physical Review B*, vol. 50, no. 17, p. 13006, 1994.
- [296] O. A. Starykh, R. R. P. Singh, and A. W. Sandvik, "Quantum critical scaling and temperature-dependent logarithmic corrections in the spin-half Heisenberg chain," *Physical Review Letters*, vol. 78, no. 3, pp. 539–542, 1997.
- [297] M. Žnidarič, "Spin Transport in a One-Dimensional Anisotropic Heisenberg Model," *Physical Review Letters*, vol. 106, no. 22, 2011.
- [298] J. Sirker, R. G. Pereira, and I. Affleck, "Diffusion and ballistic transport in one-dimensional quantum systems," *Physical Review Letters*, vol. 103, no. 21, 2009.
- [299] A. Caldeira and A. J. Leggett, "Quantum tunnelling in a dissipative system," *Annals of physics*, vol. 149, no. 2, pp. 374–456, 1983.
- [300] M. Bauer, D. Bernard, and T. Jin, "Stochastic dissipative quantum spin chains (I) : Quantum fluctuating discrete hydrodynamics," *arXiv pre-print arXiv:1706.03984*, 2017.
- [301] J. C. Orain, L. Clark, F. Bert, P. Mendels, P. Attfield, F. H. Aidoudi, R. E. Morris, P. Lightfoot, A. Amato, and C. Baines, " μ SR study of a quantum spin liquid candidate: the $S=1/2$ vanadium oxyfluoride kagome antiferromagnet," *Journal of Physics: Conference Series*, vol. 551, p. 012004, 2014.
- [302] T. Hiramatsu, Y. Yoshida, G. Saito, A. Otsuka, H. Yamochi, M. Maesato, Y. Shimizu, H. Ito, Y. Nakamura, H. Kishida, *et al.*, "Design and Preparation of a Quantum Spin Liquid Candidate κ -(ET) $_2$ Ag $_2$ (CN) $_3$ having a nearby Superconductivity," *Bulletin of the Chemical Society of Japan*, 2017.
- [303] U. Geiser, H. H. Wang, K. D. Carlson, J. M. Williams, H. A. Charlier Jr, J. E. Heindl, G. A. Yaconi, B. J. Love, and M. W. Lathrop, "Superconductivity at 2.8 K and 1.5 kbar in κ -(BEDT-TTF) $_2$ Cu $_2$ (CN) $_3$: the first organic superconductor containing a polymeric copper cyanide anion," *Inorganic chemistry*, vol. 30, no. 12, pp. 2586–2588, 1991.
- [304] Y. Nakamura, T. Hiramatsu, Y. Yoshida, G. Saito, and H. Kishida, "Optical properties of a quantum spin liquid candidate material, κ -(BEDT-TTF) $_2$ Ag $_2$ (CN) $_3$," *Journal of the Physical Society of Japan*, vol. 86, no. 1, pp. 014710–1, 2017.

Bibliography

- [305] T. Hiramatsu, Y. Yoshida, G. Saito, A. Otsuka, H. Yamochi, M. Maesato, Y. Shimizu, H. Ito, and H. Kishida, “Quantum spin liquid: Design of a quantum spin liquid next to a superconducting state based on a dimer-type ET Mott insulator,” *Journal of Materials Chemistry C*, vol. 3, no. 6, pp. 1378–1388, 2015.
- [306] K. Padmalekha, M. Blankenhorn, T. Ivek, L. Bogani, J. Schlueter, and M. Dressel, “ESR studies on the spin-liquid candidate κ -(BEDT-TTF)₂Cu₂(CN)₃: Anomalous response below $T=8$ K,” *Physica B: Condensed Matter*, vol. 460, pp. 211–213, 2015.
- [307] N. Drichko, R. Beyer, E. Rose, M. Dressel, J. A. Schlueter, S. Turunova, E. Zhilyaeva, and R. Lyubovskaya, “Metallic state and charge-order metal-insulator transition in the quasi-two-dimensional conductor κ -(BEDT-TTF)₂Hg(SCN)₂Cl,” *Physical Review B*, vol. 89, no. 7, p. 075133, 2014.
- [308] K. Miyagawa, A. Kawamoto, Y. Nakazawa, and K. Kanoda, “Antiferromagnetic ordering and spin structure in the organic conductor, κ -(BEDT-TTF)₂Cu[N(CN)₂]Cl,” *Physical Review Letters*, vol. 75, no. 6, p. 1174, 1995.
- [309] H. Ito, T. Asai, Y. Shimizu, H. Hayama, Y. Yoshida, and G. Saito, “Pressure-induced superconductivity in the antiferromagnet κ -(ET)₂CF₃SO₃ with quasi-one-dimensional triangular spin lattice,” *Physical Review B*, vol. 94, no. 2, 2016.
- [310] F. Kagawa, K. Miyagawa, and K. Kanoda, “Magnetic Mott criticality in a κ -type organic salt probed by NMR,” *Nature Physics*, vol. 5, no. 12, p. 880, 2009.
- [311] F. Kagawa, T. Itou, K. Miyagawa, and K. Kanoda, “Transport criticality of the first-order Mott transition in the quasi-two-dimensional organic conductor κ -(BEDT-TTF)₂Cu[N(CN)₂]Cl,” *Physical Review B*, vol. 69, no. 6, p. 064511, 2004.
- [312] F. Kagawa, K. Miyagawa, and K. Kanoda, “Unconventional critical behaviour in a quasi-two-dimensional organic conductor,” *Nature*, vol. 436, pp. 534–537, 2005.
- [313] S. Papanikolaou, R. M. Fernandes, E. Fradkin, P. W. Phillips, J. Schmalian, and R. Sknepnek, “Universality of liquid-gas mott transitions at finite temperatures,” *Physical Review Letters*, vol. 100, no. 2, p. 026408, 2008.
- [314] T. Furukawa, K. Kobashi, Y. Kurosaki, K. Miyagawa, and K. Kanoda, “Quasi-continuous transition from a Fermi liquid to a spin liquid,” *arXiv preprint arXiv:1707.05586*, 2017.
- [315] R. V. Mishmash, I. González, R. G. Melko, O. I. Motrunich, and M. P. Fisher, “Continuous Mott transition between a metal and a quantum spin liquid,” *Physical Review B*, vol. 91, no. 23, p. 235140, 2015.
- [316] T. Senthil, “Theory of a continuous Mott transition in two dimensions,” *Physical Review B*, vol. 78, no. 4, p. 045109, 2008.

- [317] S. Lefebvre, P. Wzietek, S. Brown, C. Bourbonnais, D. Jérôme, C. Mézière, M. Fourmigué, and P. Batail, “Mott transition, antiferromagnetism, and unconventional superconductivity in layered organic superconductors,” *Physical Review Letters*, vol. 85, no. 25, p. 5420, 2000.
- [318] Y. Shimizu, H. Akimoto, H. Tsujii, A. Tajima, and R. Kato, “Reentrant Mott transition from a Fermi liquid to a spin-gapped insulator in an organic spin-1/2 triangular-lattice antiferromagnet,” *Journal of Physics: Condensed Matter*, vol. 19, no. 14, p. 145240, 2007.
- [319] B. Powell and R. H. McKenzie, “Strong electronic correlations in superconducting organic charge transfer salts,” *Journal of Physics: Condensed Matter*, vol. 18, no. 45, p. R827, 2006.
- [320] A. Liebsch, H. Ishida, and J. Merino, “Mott transition in two-dimensional frustrated compounds,” *Physical Review B*, vol. 79, no. 19, p. 195108, 2009.
- [321] R. Clay, H. Li, and S. Mazumdar, “Absence of Superconductivity in the Half-Filled Band Hubbard Model on the Anisotropic Triangular Lattice,” *Physical Review Letters*, vol. 101, no. 16, p. 166403, 2008.
- [322] B. Powell and R. H. McKenzie, “Symmetry of the superconducting order parameter in frustrated systems determined by the spatial anisotropy of spin correlations,” *Physical Review Letters*, vol. 98, no. 2, p. 027005, 2007.
- [323] Y. Shimizu, H. Kasahara, T. Furuta, K. Miyagawa, K. Kanoda, M. Maesato, and G. Saito, “Pressure-induced superconductivity and mott transition in spin-liquid κ -(ET)₂Cu₂(CN)₃ probed by ¹³C NMR,” *Physical Review B*, vol. 81, no. 22, p. 224508, 2010.
- [324] L. Hebel and C. Slichter, “Nuclear relaxation in superconducting aluminum,” *Physical Review*, vol. 107, no. 3, p. 901, 1957.
- [325] L. Hebel, “Theory of nuclear spin relaxation in superconductors,” *Physical Review*, vol. 116, no. 1, p. 79, 1959.
- [326] K. Miyagawa, A. Kawamoto, and K. Kanoda, “Proximity of pseudogapped superconductor and commensurate antiferromagnet in a quasi-two-dimensional organic system,” *Physical Review Letters*, vol. 89, no. 1, p. 017003, 2002.
- [327] K. Miyagawa, A. Kawamoto, K. Uchida, and K. Kanoda, “Commensurate magnetic structure in κ -(BEDT-TTF)₂X,” *Physica B: Condensed Matter*, vol. 284, pp. 1589–1590, 2000.
- [328] O. I. Motrunich, “Orbital magnetic field effects in spin liquid with spinon Fermi sea: Possible application to κ -(ET)₂Cu₂(CN)₃,” *Physical Review B*, vol. 73, no. 15, 2006.
- [329] T. Nakamura, T. Nobutoki, T. Takahashi, G. Saito, H. Mori, and T. Mori, “ESR properties of κ -type organic superconductors based on BEDT-TTF,” *Journal of the Physical Society of Japan*, vol. 63, no. 11, pp. 4110–4125, 1994.

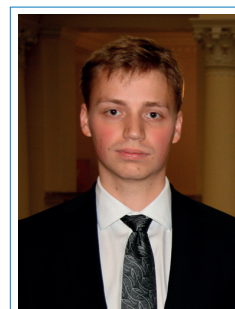
Bibliography

- [330] Á. Antal, T. Fehér, B. Náfrádi, L. Forró, and A. Jánossy, “Magnetic fluctuations above the Néel temperature in κ -(BEDT-TTF)₂Cu[N(CN)₂]Cl, a quasi-2D Heisenberg antiferromagnet with Dzyaloshinskii-Moriya interaction,” *physica status solidi (b)*, vol. 249, no. 5, pp. 1004–1007, 2012.
- [331] H. Kino and H. Fukuyama, “Phase Diagram of Two-Dimensional Organic Conductors: (BEDT-TTF)₂X,” *Journal of the Physical Society of Japan*, vol. 65, no. 7, pp. 2158–2169, 1996.
- [332] T. Sasaki, H. Oizumi, N. Yoneyama, N. Kobayashi, and N. Toyota, “X-ray irradiation-induced carrier doping effects in organic dimer–Mott insulators,” *Journal of the Physical Society of Japan*, vol. 76, no. 12, pp. 123701–123701, 2007.
- [333] A. Zorko, M. Herak, M. Gomilšek, J. van Tol, M. Velázquez, P. Khuntia, F. Bert, and P. Mendels, “Symmetry reduction in the quantum kagome antiferromagnet herbertsmithite,” *Physical Review Letters*, vol. 118, no. 1, p. 017202, 2017.
- [334] M. Oshikawa and I. Affleck, “Low-temperature electron spin resonance theory for half-integer spin antiferromagnetic chains,” *Physical Review Letters*, vol. 82, no. 25, p. 5136, 1999.
- [335] R. Glenn, O. A. Starykh, and M. E. Raikh, “Interplay of spin-orbit coupling and Zeeman splitting in the absorption lineshape of fermions in two dimensions,” *Physical Review B*, vol. 86, no. 2, 2012.
- [336] J.-B. Fouet, O. Tchernyshyov, and F. Mila, “Field-induced gap in ordered Heisenberg antiferromagnets,” *Physical Review B*, vol. 70, no. 17, p. 174427, 2004.
- [337] K. Thirunavukkuarasu, S. M. Winter, C. C. Beedle, A. E. Kovalev, R. T. Oakley, and S. Hill, “Pressure dependence of the exchange anisotropy in an organic ferromagnet,” *Physical Review B*, vol. 91, no. 1, p. 014412, 2015.
- [338] P. Hauke, T. Roscilde, V. Murg, J. I. Cirac, and R. Schmied, “Modified spin-wave theory with ordering vector optimization: spatially anisotropic triangular lattice and $J_1J_2J_3$ model with Heisenberg interactions,” *New Journal of Physics*, vol. 13, no. 7, p. 075017, 2011.
- [339] C. Griset, S. Head, J. Alicea, and O. A. Starykh, “Deformed triangular lattice antiferromagnets in a magnetic field: Role of spatial anisotropy and Dzyaloshinskii-Moriya interactions,” *Physical Review B*, vol. 84, no. 24, p. 245108, 2011.
- [340] T. Sasaki, N. Yoneyama, A. Matsuyama, and N. Kobayashi, “Magnetic and electronic phase diagram and superconductivity in the organic superconductors κ -(ET)₂X,” *Physical Review B*, vol. 65, no. 6, p. 060505, 2002.
- [341] K. Miyagawa, K. Kanoda, and A. Kawamoto, “NMR studies on two-dimensional molecular conductors and superconductors: Mott transition in κ -(BEDT-TTF)₂X,” *Chemical Reviews*, vol. 104, no. 11, pp. 5635–5654, 2004.

- [342] N. Nemes, J. Fischer, G. Baumgartner, L. Forró, T. Fehér, G. Oszlányi, F. Simon, and A. Jánossy, “Conduction-electron spin resonance in the superconductor K_3C_{60} ,” *Physical Review B*, vol. 61, no. 10, p. 7118, 2000.
- [343] F. Simon, A. Jánossy, T. Fehér, F. Murányi, S. Garaj, L. Forró, C. Petrovic, S. Bud’Ko, G. Lapertot, V. Kogan, *et al.*, “Anisotropy of superconducting MgB_2 as seen in Electron Spin Resonance and magnetization data,” *Physical Review Letters*, vol. 87, no. 4, p. 047002, 2001.
- [344] B. Raveau, C. Michel, M. Hervieu, J. Provost, F. Studer, J. Bednorz, and K. Muller, “Earlier and recent aspects of superconductivity,” *Springer Series in Solid State Sciences*, vol. 90, 1989.
- [345] A. Hebard, M. Rosseinsky, R. Haddon, D. Murphy, S. Glarum, T. Palstra, A. Ramirez, and A. Kortan, “Superconductivity at 18 K in potassium-doped C_{60} ,” *Nature*, vol. 350, no. 6319, pp. 600–601, 1991.
- [346] A. Zakhidov, A. Ugawa, K. Yakushi, K. Imaeda, H. Inokuchi, I. Khairullin, and P. Khabibulaev, “Low-field microwave absorption in organic superconductor κ -(ET) $_2$ [Cu(NCS) $_2$],” *Physica C: Superconductivity*, vol. 185, pp. 2669–2670, 1991.
- [347] P. Bele, H. Brunner, D. Schweitzer, and H. J. Keller, “Magnetically modulated microwave absorption (MMA) at low magnetic fields in (BEDT-TTF)-superconductors,” *Solid State Communications*, vol. 92, no. 3, pp. 189–193, 1994.
- [348] A. Pisoni, P. Szirmai, S. Katrych, B. Náfrádi, R. Gaál, J. Karpinski, and L. Forró, “Magnetotransport studies of superconducting $Pr_4Fe_2As_2Te_{1-x}O_4$,” *Physical Review B*, vol. 93, no. 9, p. 094519, 2016.
- [349] A. Pisoni, S. Katrych, P. Szirmai, B. Náfrádi, R. Gaál, J. Karpinski, and L. Forró, “Upper critical field, pressure-dependent superconductivity and electronic anisotropy of $Sm_4Fe_2As_2Te_{1-x}O_{4-y}F_y$,” *Journal of Physics: Condensed Matter*, vol. 28, no. 11, p. 115701, 2016.
- [350] E. Ghorbani, L. F. Tocchio, and F. Becca, “Variational wave functions for the $S=1/2$ Heisenberg model on the anisotropic triangular lattice: Spin liquids and spiral orders,” *Physical Review B*, vol. 93, no. 8, 2016.
- [351] D. Watanabe, M. Yamashita, S. Tonegawa, Y. Oshima, H. Yamamoto, R. Kato, I. Sheikin, K. Behnia, T. Terashima, S. Uji, and *et al.*, “Novel Pauli-paramagnetic quantum phase in a Mott insulator,” *Nature Communications*, vol. 3, p. 1090, 2012.
- [352] T. Isono, H. Kamo, A. Ueda, K. Takahashi, M. Kimata, H. Tajima, S. Tsuchiya, T. Terashima, S. Uji, and H. Mori, “Gapless Quantum Spin Liquid in an Organic Spin-1/2 Triangular-lattice κ -H $_3$ (Cat-EDT-TTF) $_2$,” *Physical Review Letters*, vol. 112, no. 17, 2014.

Péter Szirmai

EPFL SB IPHYS LPMC
1015 Lausanne, Switzerland
☎ (+41) 78 829 10 17
✉ peter.szirmai@epfl.ch
Nationality: Hungary (EU)



Education

- 2013–Present **PhD in Experimental Physics**, *Swiss Federal Institute of Technology (EPFL)*, Switzerland.
2011–2013 **MSc in Physics**, *Budapest University of Technology and Economics*, Hungary, *Scholarship of the Hungarian Republic*.
2008–2011 **BSc in Physics**, *Budapest University of Technology and Economics*, Hungary.

PhD Thesis

- Title *Frustration and Randomness: Magnetic Studies of Organic Quantum Spin Liquids*
Supervisor Prof. László Forró and Dr. Bálint Náfrádi (Laboratory of Physics of Complex Matter)
Detailed achievements
 - Discovered a new quantum spin liquid candidate, $[\text{EDT-TTF-CONH}_2]_2^+ \text{BABCO}^-$.
 - Investigated the exchange anisotropy and assessed the QSL state of $\kappa\text{-}[\text{BEDT-TTF}]_2\text{Ag}_2\text{CN}_3$.
 - Explored the phase diagram of $\kappa\text{-}[\text{BEDT-TTF}]_2\text{Ag}_2\text{CN}_3$.
 - Studied hybrid molecular conductor and rotor systems.

Experience

- 2013–Present **PhD student**, EPFL, Switzerland.
Group of Prof. László Forró
2012–2013 **Summer Intern**, UNIVERSITÄT WIEN, Austria.
Group of Prof. Thomas Pichler
2010–2011 **Summer Intern**, EPFL, Switzerland.
Group of Prof. László Forró
2010–2013 **Research Assistant**, TU BUDAPEST, Hungary.
Group of Prof. Ferenc Simon
2009–2010 **Research Assistant**, HUNGARIAN ACADEMY OF SCIENCES, Hungary.
Group of Prof. Attila Bóta

Awards

- 2016 Outstanding teaching assistant
2011–2013 Scholarship of the Hungarian Republic
2010 Scientific Conference of Hungarian University Students (3rd prize)

Publications

Scopus: 12 publications (lead author of 7), 75 citations, *h*-index: 5

Google Scholar: 16 publications (lead author of 8), 86 citations, *h*-index: 5

- **Szirmai, P.**, Hiramatsu, T., Saito, G., Forró, L., Náfrádi, B., *Magnetic field induced fluctuations in a quantum spin liquid κ -[BEDT-TTF] $_2$ Ag $_2$ (CN) $_3$* , in preparation
- **Szirmai, P.**, Pisoni, A., Gaál, R., Mézière, C., Batail, P., Forró, L., Náfrádi, B., *Mechanical disorder-induced quantum spin liquid in a two-dimensional triangular lattice*, in preparation
- **Szirmai, P.**, Spina, M., Horváth, E., Forró, L., Náfrádi, B., *All-optical THz-wave modulation using magnetic perovskites*, in preparation
- Náfrádi, B., **Szirmai, P.**, Spina, M., Pisoni, A., Mettan, X., Nemes, N. M., Forró, L., Horváth, E., *Tuning ferromagnetism at room temperature by visible light*, submitted to Nature
- Náfrádi, B., **Szirmai, P.**, Spina, M., Lee, H., Yazyev, O.V., Arakcheeva, A., Chernyshov, D., Gibert, M., Forró, L., Horváth, E., 2016, *Nature Communications*, 7, 13406
- **Szirmai, P.**, Stevens, J., Horváth, E., Ćirić, L., Kollár, M., Forró, L., Náfrádi, B., 2017, *Catalysis Today*, 284, p.146-152
- **Szirmai, P.**, Náfrádi, B., Arakcheeva, A., Szilágyi, E., Gaál, R., Nemes, N.M., *et al.*, 2017, *Catalysis Today*, 284, p.52-58
- **Szirmai, P.**, Márkus, B.G., Dóra, B., Fábrián, G., Koltai, J., Zólyomi, V., *et al.*, 2017, *Physical Review B*, 96, p.075133
- Pisoni, A., **Szirmai, P.**, Katrych, S., Náfrádi, B., Gaál, R., Karpinski, J. and Forró, L., 2016, *Physical Review B*, 93(9), p.094519.
- Pisoni, A., Katrych, S., **Szirmai, P.**, Náfrádi, B., Gaál, R., Karpinski, J., Forró, L., *Journal of Physics: Condensed Matter*, 28 (11), 115701
- Pisoni, A., Jacimovic, J., Náfrádi, B., **Szirmai, P.**, Spina, M., Gaál, R., *et al.*, arXiv:1604.05637
- Márkus, B.G., Szolnoki, L., Iván, D., Dóra, B., **Szirmai, P.**, Náfrádi, B., Forró, L., Simon, F., 2016, *Physica Status Solidi (B)*, 253(12), p. 2505-2508
- Márkus, B.G., Simon, F., Chacón-Torres, J.C., Reich, S., **Szirmai, P.**, *et al.*, 2015, *Physica Status Solidi (B)*, 252 (11), pp. 2438-2443
- **Szirmai, P.**, Fábrián, G., Koltai, J., Náfrádi, B., Forró, L., Pichler, T., Williams, O.A., Mandal, S., Bäuerle, C. and Simon, F., 2013, *Physical Review B*, 87(19), p.195132.
- **Szirmai, P.**, Horváth, E., Náfrádi, B., Micković, Z., Smajda, R., Djokić, D.M., Schenk, K., Forró, L. and Magrez, A., 2012, *The Journal of Physical Chemistry C*, 117(1), pp.697-702.
- **Szirmai, P.**, Pichler, T., Williams, O.A., Mandal, S., Bäuerle, C. and Simon, F., 2012, *Physica Status Solidi (B)*, 249(12), pp.2656-2659.
- **Szirmai, P.**, Fábrián, G., Dóra, B., Koltai, J., Zólyomi, V., Kürti, J., Nemes, N.M., Forró, L. and Simon, F., 2011, *Physica Status Solidi (B)*, 248(11), pp.2688-2691.

Conferences

Talks

- *Role of the Antisymmetric Exchange in QSLs*, ISCOM, Miyagi, Japan (2017)
- *Role of the Antisymmetric Exchange in QSLs*, SPS Meeting, Geneva, Switzerland (2017)
- *μ SR in a hybrid rotor-conductor QSL candidate*, Molecular Rotor Workshop, Prague, Czech Republic, Invited (2017)
- *Low-dimensional Rotor Dynamics*, Rotor Workshop, Angers, France, Invited (2016)

Presentations

- *All-optical THz-wave modulation using ferromagnetic $CH_3NH_3(Mn:Pb)I_3$ via low-fluence illumination*, HOPV17, Lausanne, Switzerland (2017)
- *Mechanical disorder-induced QSL in a triangular lattice*, SPS Meeting, Lugano, Switzerland (2016)
- *Magnetic field-induced fluctuations in a QSL*, MaNEP SWM, Diablerets, Switzerland (2016)
- *ESR study of the Dzyaloshinskii-Moriya interaction in a QSL*, ISCOM, Bad Gögging, Germany (2015)
- *EPR study of photoactive hydrogenated titania nanowires*, IWEPM, Kirchberg, Austria (2014)
- *ESR in superconducting boron doped diamond*, IWEPM, Kirchberg, Austria (2012)
- *DOS in potassium doped CNTs; a model system of biased graphene*, IWEPM, Kirchberg, Austria (2011)

Related professional experience

- Supervised and conducted research projects of Physics students and summer interns (1 PhD, 4 MSc, and 3 BSc students).
- Maintained and developed multi-frequency ESR spectrometers at EPFL.
- Referee for Phys. Rev. B.
- Wrote proposals to large facilities (EMFL, ISIS, PSI) and for Swiss and European grants.
- Managed a French-Swiss collaboration program (Germaine de Staël).

Teaching

- 2014– 2017 **Teaching Assistant**, EPFL, Physics of New Real Materials.
- Designed and developed course and examination
 - Tutored 30 Physics MSc students p.a.
- 2014–2017 **Head Teaching Assistant**, UNIVERSITÉ DE LAUSANNE, General Physics for Medical Students.
- Recruited and supervised 20 undergraduate TAs for > 600 students p.a.
 - Refined course and directed examination
- 2011– 2012 **Teaching Assistant**, TU BUDAPEST, Physics Laboratory.
- 2010– 2012 **Teaching Assistant**, TU BUDAPEST, General Physics for Bioengineering Students.

References

Prof. László Forró
SB IPHYS LPMC
EPF Lausanne
CH-1015 Lausanne
laszlo.forro@epfl.ch

Prof. Patrick Batail
Laboratoire MOLTECH-Anjou
Université d'Angers
FR-49045 Angers
patrick.batail@univ-angers.fr

Dr. Bálint Náfrádi
SB IPHYS LPMC
EPF Lausanne
CH-1015 Lausanne
nafradi@yahoo.com

Technical Skills

- Techniques Electron spin resonance (ESR), Muon Spin Rotation (μ SR), Raman spectroscopy, Magnetotransport, X-ray diffraction (XRD), Small-angle X-ray scattering (SAXS)
- Synthesis Vapor transport intercalation method, Liquid-phase intercalation, Hydrothermal growth
- IT Matlab, Wolfram Mathematica, Maple, \LaTeX , C, Visual Basic, LabVIEW, Solidworks, Blender

Languages

- Hungarian **Mother tongue.**
- English **Fluent**, C1.
- French **Fluent**, C1.
- German **Intermediate**, B1.